UNIVERSITY OF SOUTHAMPTON

Parametric Study and Modelling of the Dielectric Barrier Discharge Plasma Actuator for Flow Control

by
Sylvain Grosse

ORCID ID 0000-0002-0365-1357

A thesis submitted in partial fulfilment for the degree of Doctor of Philosophy

in the
Faculty of Engineering and Physical Sciences
School of Engineering

11th December 2019

UNIVERSITY OF Southampton

Research Thesis: Declaration of Authorship

Print name:	Sylvain Grosse

Title of thesis:	Parametric Study and Modelling of the Dielectric Barrier Discharge Plasma Actuator for Flow Control

I declare that this thesis and the work presented in it is my own and has been generated by me as the result of my own original research.

I confirm that:

1. This work was done wholly or mainly while in candidature for a research degree at this University;
2. Where any part of this thesis has previously been submitted for a degree or any other qualification at this University or any other institution, this has been clearly stated;
3. Where I have consulted the published work of others, this is always clearly attributed;
4. Where I have quoted from the work of others, the source is always given. With the exception of such quotations, this thesis is entirely my own work;
5. I have acknowledged all main sources of help;
6. Where the thesis is based on work done by myself jointly with others, I have made clear exactly what was done by others and what I have contributed myself;
7. Either none of this work has been published before submission, or parts of this work have been published as: [please list references below]:

Parametric investigation of the surface dielectric barrier discharge plasma actuator for future flow control, submitted and presented at The Future of Aerodynamics, organised by the Royal Aeronautical Society in Bristol (UK), from 24th to 26th July 2018

Parametric investigation and modeling of the dielectric barrier discharge plasma actuator for flow control, presented at the 12th European Fluid Mechanics Conference organised by the European Mechanics Society in Vienna (Austria), from 9th to 13th September 2018

Parametric investigation and modeling of the dielectric barrier discharge plasma actuator for flow control, paper in preparation for the Journal of Physics D: Applied Physics

Signature:	Sylvain Grosse	Date:	15 Jul. 19

Abstract

Dielectric Barrier Discharge (DBD) plasma actuators are widely studied in different applications such as flow control, de-icing, surface coating or surface cleansing. For instance, in their flow control use, flow reattachment can be achieved, or boundary layer control can be performed. DBD actuators can be used in different shapes or with different electric signals, which have different effects on the flow. However, the flow control abilities of the DBD are limited to low Reynolds numbers, with a lack of knowledge on the optimum design or a mathematical model to predict the optimum design of a DBD. Consequently, the following study focuses on the parametric investigation of the DBD actuator, in order to determine the relative significance of its design parameters, based on their effects on the momentum induced by the DBD in the airflow and on its electrical power consumption. Due to its lower power consumption and its ability to be used in different flow control cases, the AC driven DBD is focused on in the study. The momentum induced by DBD actuators is evaluated through the thrust generated devices, and the thrust over power ratio (or force efficiency) is used as a surrogate of the efficiency. A test rig has been created, in order to measure the small thrust induced by 10 cm wide DBDs. The test rig measures the thrust via a lever that amplifies the force generated by a DBD. The assessment of the new test rig demonstrates that its measurements of the thrust and power are accurate and repeatable. Nine design parameters of the DBD have been analysed with a Design of Experiment, using the data measured by the test rig. A fractional factorial design was employed with a resolution of IV, and a confidence level of 95%. The results show that mainly the electric parameters and the geometries of the dielectric and of the air electrode influence the thrust, power and force efficiency of DBDs. Firstly, a high voltage yields the greater thrust and force efficiency. Secondly, a high AC frequency results in a greater thrust but a smaller force efficiency. Thirdly, a short distance between the electrodes is need to reach a higher thrust and force efficiency. Finally, a thin and narrow air exposed electrode generates a greater thrust. The ranking of the parameters allows general guidelines to be drawn, that can be followed to achieve the best flow control performance of particular DBDs. The DOE derives models that can approximate the power consumption and force efficiency. The product of these two models provide reasonable estimates of the thrust generation, with a maximum inaccuracy of 0.9 mN/m. These models can be used to estimate the most suitable DBD design for a particular application. Then, the provided guidelines can be followed to achieve the highest force efficiency or thrust generation of this DBD.

Contents

List of Figures

List of Tables

Glossary

Nomenclature

C	Capacitance	F
C_0	Minimal capacitance of the DBD (plasma off)	F
C_{1A}	Electric capacitance of the plasma	F
C_{1B}	Electric capacitance of the air	F
C_{2A}	Electric capacitance of the dielectric beneath the plasma	F
C_{2B}	Electric capacitance of the dielectric beneath the air	F
C_{eff}	Effective capacitance of the DBD (plasma on)	F
d	Overall minimal distance between the electrodes	mm
D	Coefficient of charge diffusion	m^2/s
E	Magnitude of the electric field	V/m
$\mathbf{E}$	Vectorial form of the electric field	V/m
E_{b}	Breakdown electric field	V/m
e_{e}	Elementary charge (1.602×10^{-19} C)	C
e_{s}	Saturation vapour pressure	Pa
E_{s}	Minimum electric field for sustaining the plasma	V/m
$E(X)$	Effect of the input parameter X on the output Y	as Y
$\mathbf{F}$	Coulomb's force	N
f_{ac}	Frequency of the applied voltage	kHz
F_{b}	Total force exerted by the plasma on the free-stream	N
$\mathbf{f}_{\text{e}}$	Local electrical body force	N/m^3

F_{front}	Force per unit span induced by the wall jet at the front of the DBD	mN/m
f_{mod}	Modulation frequency	Hz
F^+	Reduced actuation frequency ($F^+ = f_{\text{mod}}/f_{\text{sep}}$)	
F_{rear}	Force per unit span induced by the wall jet at the rear of the DBD	mN/m
f_{s}	Sampling frequency	Hz
f_{sep}	Characteristic frequency of the separated flow ($f_{\text{sep}} = U_\infty/L_{\text{sep}}$)	Hz
F_x	Force per unit span induced by the wall jet at chord-wise location x	mN/m
g	Inter-electrode gap	mm
G	Gain of the load cell	mN/V
g_0	Standard gravitional acceleration (9.81 m/s^2)	m/s^2
H_0	Ambiant relative humidity	%
h_1	Thickness of the air exposed electrode	μm
h_2	Thickness of the encapsulated electrode	μm
I	Electric current	A
$\langle I \rangle$	Time average of the current	A
I^*	Complex current	A
j	Complex number: $j^2 = -1$	
$\mathbf{J}$	Current density	A/m^2
K	Free-stream velocity over drif velocity ratio	
L	Span of the electrodes	cm
L_{sep}	Characteristic length scale of the separated region	m
m_i	Calibration mass i placed in the test rig	g
$\mathring{m}$	Mass flow rate	g/s
MS_D	Mean square of dataset D	as D

M_Y	Matrix of the linear regression coefficients for the variable Y	
n	Number of observations	
N	Total number of tests of an experiment	
N_{EHD}	Electrohydrodynamic number	
n_+	Number of observations at the high value of variable X	
n_-	Number of observations at the low value of variable X	
p	Gas pressure	Pa
p_0	Atmospheric pressure	hPa
P_{A}	Average power consumed per unit span by a DBD	W/m
q	Charge density	$\mathrm{C/m^3}$
Q_i	Charge of particle i	C
r	Distance between the charged particles	m
R	Resistance	Ω
R_0	Specific gas constant of the air (287 J/kg·K)	J/kg·K
R^2	Coefficient of determination	
$\bar{R}^2$	Adjusted coefficient of determination	
$RMSE$	Root mean square of the errors	
R_p	Electric resistance of the plasma	Ω
$SE(X)$	Standardised effect of the input X on the output Y	
SS_D	Sum of squares of dataset D	as D^2
t	Thickness of the dielectric layer	mm
T	Gas temperature	K
T_0	Atmospheric temperature	K
T_{A}	Thrust per unit span generated by a DBD actuator	mN/m
$\mathbf{u}$	Velocity vector	m/s
u	Magnitude of the velocity	m/s
U_∞	Free-stream velocity	m/s

$u_{\max}$	Maximum velocity in the wall jet	m/s
V	Peak-to-peak electric voltage	$\mathrm{kV_{pp}}$
V_0	Amplitude of the voltage	V
v_d	Drift velocity of the charged species	m/s
v_i	Output voltage of the test rig for the calibration mass i	V
V^*	Complex votage	V
w_1	Width of the air exposed electrode	mm
w_2	Width of the encapsulated electrode	mm
X	General input parameter	
$X^{(\mathrm{c})}$	Input parameter X in its coded unit	
$X^{(\mathrm{u})}$	Input parameter X in its uncoded unit	as X
X_d	Array of the design parameters	
X_-	Minimum value of the input parameter X	
X_+	Maximum value of the input parameter X	
Y	General output parameter	
$\hat{Y}$	Predicted output parameter	as Y
$\overline{Y}$	Grand average of the output parameter Y	as Y
$z_{1/2}$	Wall jet thickness	mm
Z_{1A}	Complex impedance of the capacitance of the plasma	Ω
Z_{1B}	Complex impedance of the capacitance of the air	Ω
Z_{2A}	Complex impedance of the capacitance of the dielectric beneath the plasma	Ω
Z_{2B}	Complex impedance of the capacitance of the dielectric beneath the air	Ω
Z_{eq}	Equivalent complex impedance of the plasma	Ω
Z_p	Complex impedance of the resistance of the plasma	Ω
α	Factor of efficiency of the collisions in the plasma	C^{-1}
$\beta_{i(j)}$	Coefficient of the linear regression model	

δ	Dirac delta function	
Δz	Step between two heights over the wall	mm
ε	Electric permittivity	F/m
ε_0	Vacuum permittivity (8.854×10^{-12} F/m)	F/m
ε_r	Relative permittivity of the dielectric	
η	Force over power ratio	N/W
η_{A}	Force efficiency of a DBD actuator (thrust over power ratio)	μN/W
Γ_{A}	Thrust generated by a DBD actuator	mN
κ	Ion mobility	$\mathrm{m}^2/\mathrm{V{\cdot}s}$
μ	Gas viscosity	Pa.s
ν_e	Number density of the electrons	m^{-3}
ν_-	Number density of the anions	m^{-3}
ν_+	Number density of the cations	m^{-3}
ω	Angular frequency of the AC signal: $\omega = 2\pi f_{\mathrm{ac}}$	rad/s
Π_{A}	Average power consumed by a DBD actuator	W
ϕ	Electric potential	V
ϖ	Real time electric power consumption	W
ρ	Gas density	$\mathrm{kg/m}^3$
ρ_0	Gas density	$\mathrm{kg/m}^3$
σ_{e}	Electrical conductivity	S/m
σ_x	Standard error of of variable x	
τ	Time constant of a resistance-capacitance network: $\tau = RC$	s
Θ_{A}	Electric power scaling parameter	$\mathrm{s}^{0.5}/\mathrm{m{\cdot}V}^{2.5}$

Abbreviations

AC Alternate Current.
ANOVA Analysis of Variance.

BL Boundary Layer.

CAD Computer-Aided Design.

CD Corona Discharge.
CFD Computational Fluid Dynamics.

d.c. duty cycle.
DBD Dielectric Barrier Discharge.
DC Direct Current.
DDBD Double Dielectric Barrier Discharge.
DOE Design of Experiment.

EHD Electrohydrodynamics.

HV High Voltage.

ISA International Standard Atmosphere.

LDV Laser Doppler Velocimetry.
LE Leading Edge.

MEE-DBD Multiple-Encapsulated-Electrode DBD.
MHD Magnetohydrodynamics.

NARX Non-Linear AutoRegressive eXogenous.
NS-DBD Nano-Second(-Pulsed) DBD.

PCB Printed Circuit Board.
PI Proportional-Integral.
PID Proportional-Integral-Derivative.
PIV Particle Image Velocimetry.
PSJ Plasma Synthetic Jet.

RANS Reynolds-Average-Navier-Stokes.
rms root-mean-square.
RSM Response Surface Method.

SD Sliding Discharge.

TE Trailing Edge.

VG Vortex Generator.

ZNMF Zero-Net-Mass-Flux.

Acknowledgements

It is difficult to thank all the people who helped and showed support for the several years this project lasted. First, I would like to thank my supervisor, Dr. David Angland, for his advice and support throughout the study. Second, I want to thank all my colleagues and all the staff of the university who helped me with the technical work and questions I could have. Third, I want to thank my friends, who were there in difficult times, and brought moral support in times of crisis. More importantly, I want to thank my family, who were there all along, and never let me down, in good and hard times. Last but not least, I would like to particularly thank my friend Jeanne Blanchard, not only for all the help and advice she provided, but also for all her courage in life, and for being a truly inspirational person.

Chapter 1

Introduction

1.1 Description of the Problem

Due to the sustained growth of global aviation, it is essential to prepare the next generation of aeroplanes to limit their impact on the environment. When landing, high-lift surfaces, that are trailing-edge flaps and leading-edge slats, are big contributors to the increase in drag force and noise generation on the aircraft. However, they do have a key role in the increase in the lift-force in low-speed configurations and safe landing and take-off, and are thus crucial in these configurations. Current and future certification standards will also steer manufacturer towards quieter and cleaner aeroplanes. As a result, it is important to tackle the detrimental flow structures produced by the high-lift surfaces, and responsible for the rises in noise generation and fuel consumption.

A common solution consists in passive flow control, such as vortex generators. However, such a method implies the presence of the devices in all flight configurations, and especially during cruise, where they deteriorate the aerodynamic performance of the aeroplane. Consequently, active flow control is seen as a more viable solution. This control typically requires an energy source to work, and a feedback to optimise the control. When actuated, they need to be as effective as passive devices to control the airflow, and efficient enough not to consume more power than they allow to save. The main issue is to find an actuator that is also light and easy to maintain and install. That is the principal disadvantage of solutions such as blowing slots that require internal piping.

A suitable alternative lies in the utilisation of dielectric barrier discharge plasma actuators. They consist of, at least, two electrodes mounted on either side of a dielectric layer. By applying a high voltage of several kilovolts to the device, the air between the electrodes is ionised, meaning the electrons and charged species travel from one electrode to the other. Through viscous or thermal interaction with the free uncharged particles, the surrounding air is entrained and forms a wall jet in the close vicinity of the plasma. Other types of plasma actuators can be built, depending on the chosen configuration and power input, and each of the actuators presents particular characteristics, and takes advantage of different momentum transfer method. The present study

focuses on one type of plasma actuators: Alternate Current (AC) Dielectric Barrier Discharge (DBD) actuators (shortened as DBD actuators).

Even though DBDs have already been used for flow-control applications, their effectiveness is today too small for full scale applications. Different aspects of the design of DBDs have been reported, but studies predominantly observed isolated sets of design parameters. As a result, it is currently difficult to understand which of the design parameters predominantly influences the flow control performance of DBDs, and which design parameters to focus on when optimising a DBD actuator for flow control. Moreover, all combinations of design parameters were not tested. Therefore, it can be supposed some interactions between the design parameters exist, but were not met. Finally, even though some scaling laws exist, some discrepancies persist in the literature. Because of the lack of consensus on a definitive scaling of the flow control performance of the DBD with its design parameters, there is an absence of models to predict the power requirements and abilities to transfer momentum into the free-stream of particular DBDs.

1.2 Aims and Objectives

Consequently, the aim of the current work is to determine the relative significance of the impact of the design factors of the DBD plasma actuator on its flow control performance, and model the flow control performance of DBD actuators. As a result, the following objectives have to be fulfilled:

- Obtain a suitable test rig for direct thrust measurement, and arrange a test rig to acquire the thrust generation and power consumption of DBD actuators.
- Evaluate the effects of the DBD geometry and electric input on its flow generation abilities and power requirements, both for each isolated design variable, but also for the interactions between these variables.
- Rank the significant effects to determine the principal design parameters that influence the thrust generation and power consumption of DBDs.
- Produce simple mathematical models to predict the performance of particular designs of DBD, and verify the existing scaling laws that link the power consumption and thrust generation to the electrical signal.

The novel findings of the study are the ranking of the effects of the nine design parameters on the thrust generation, power consumption and force efficiency of the DBD actuator. The chosen analysis method also provides insights on the unexplored interactions between the design parameters. Finally, an attempt is given to model the thrust generation, power consumption and force efficiency of the DBD actuators through linear regression models.

1.3 Plan of the Study

In chapter two, an insight into the literature provides a better understanding of plasma actuation and its current abilities for flow control. Particularly, the physics responsible for the generation of a wall jet is discussed, along with other typical features of different types of plasma actuators. Besides, the lessons drawn from previous parametric studies and realised by different groups are introduced, and the different methods employed to assess their performance are detailed. The abilities of DBDs for flow and noise control are highlighted and compared with other flow-control techniques, in order to demonstrate their relevance for flow control.

In chapter three, the chosen analytical method is explained. The lessons drawn from the literature are highlighted, and the mathematical method employed to fulfil the objectives is introduced. The mathematical background of the selected method is explained, so that the reader can understand the following analysis.

In a chapter four, the experimental set up is detailed. The chosen design of the test rig is presented, along with its important features. The different apparatus that constitute the test rig are listed, and an error analysis is performed to assess its accuracy. Moreover, the predictable possible sources of errors are presented and discussed, so that their potential effects on the results are known.

Fourthly, the results are presented for the three selected output variables that are the thrust generated (chapter five) and the power consumed (chapter six) by the DBD actuators, and the thrust to power ratio of the actuators (chapter seven). In the three chapters, the mathematical suitability of the results is examined, and the discussion of the results links the captured effects to their most plausible physical ground, and to the observations reported through the literature. For each of the three output parameters, the first models are briefly presented.

Finally, in chapter eight, a small subset of DBD actuators is utilised at different voltages and frequencies of the input signal to verify the mathematical models derived through the analysis. Besides, the aerodynamics of the wall jet created by the plasma discharge are assessed, and the thrust generation is estimated from the aerodynamic measurements. The two experimental techniques are compared, and the acquired results are utilised to verify the scaling laws of the output variables reported in the literature.

1.4 Publications

1.4.1 Presentations

The Future of Aerodynamics, organised by the Royal Aeronautical Society
24^{th} to 26^{th} of July 2018 in Bristol, United Kingdom
Presentation: Parametric investigation of the surface dielectric barrier discharge plasma actuator for future flow control.

12th European Fluid Mechanics Conference, organised by the European Mechanics Society
9th to 13th of September 2018 in Vienna, Austria
Presentation: Parametric investigation and modeling of the dielectric barrier discharge plasma actuator for flow control.

1.4.2 Paper

Under review.
Journal of Physics D: Applied Physics
Title: Parametric investigation and modeling of the dielectric barrier discharge plasma actuator for flow control.

Chapter 2

Literature Review

Plasma actuators for flow control have been extensively studied in the past few decades. The current work focuses on the optimisation and modelling of the Dielectric Barrier Discharge (DBD) actuator in its flow control applications. Before starting the study, it is necessary to understand the physical mechanisms behind DBDs.

First, the formation of the plasma by the DBD and the different physical characteristics of the plasma must be understood. This also compromises the physical process through which momentum is transferred to the free-stream.

Secondly, the different methods employed to measure the performance of the actuator for flow-control applications must be reviewed. Thus, the most relevant measurement method can be selected in the current study.

Thirdly, different parameters have already been shown to influence the performance of the DBDs for flow control. As a consequence, these lessons must be emphasized, and especially the scaling laws that were proposed throughout the literature.

Finally, the flow control potential of DBD actuators is compared against several types of plasma actuators, and against more common fluidic or mechanic flow control devices.

2.1 Principle and Characteristics of the DBD Actuator

Several aspects of the plasma discharge must be explained here to better understand its physics and how it interacts with the free air around the actuator. Not only does the plasma produce an airflow, but it is also responsible for the emission of light, the radiation of temperature and the generation of an electric field.

2.1.1 Basic Principle

The DBD actuator consists of (refer to Figure 2.1):

1. an air-exposed electrode of width w_1 and height h_1,
2. an encapsulated electrode of width w_2 and height h_2 horizontally separated of the exposed electrode by a gap g,

3. a dielectric layer of thickness t and relative permittivity ε_r between the electrodes.

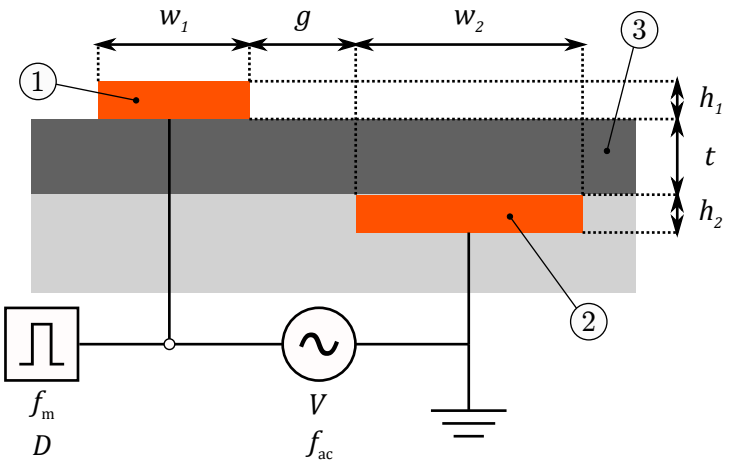

Figure 2.1: Geometry of a DBD actuator highlighting the air-exposed (1) and encapsulated (2) electrodes, and the dielectric layer (3).

In the case of an AC-DBD (the other types of plasma actuators are presented in Section 2.4), the electrodes are connected to an AC high-voltage power supply (amplitude V, frequency f_{ac}). Furthermore, the signal can also be modulated at the input, commonly with a pulse signal of frequency f_{m} and duty cycle D. Typically, the actuator is supplied with a sinusoidal AC electrical current of up to 20 kV (amplitude), at a frequency less than 10 to 15 kHz. As the current never exceeds a value of a few microamps to a few milliamps, the power consumption is relatively small.

Over one AC period, the electrons released by the air-exposed electrode travel towards the surface of the dielectric above the encapsulated electrode and back. When the voltage is in the negative going part of the cycle, the electrons are released in the air by the exposed electrode and thus ionise the particles. The negatively charged species are then repulsed towards the surface of the dielectric layer by the negatively charged exposed electrode. During the positive going half of a cycle, the electrons previously stored at the surface of the dielectric go back to the circuit thanks to the drift of the charged particles towards the positive exposed electrode. This process is highlighted in Figure 2.2 where both half cycles are displayed.

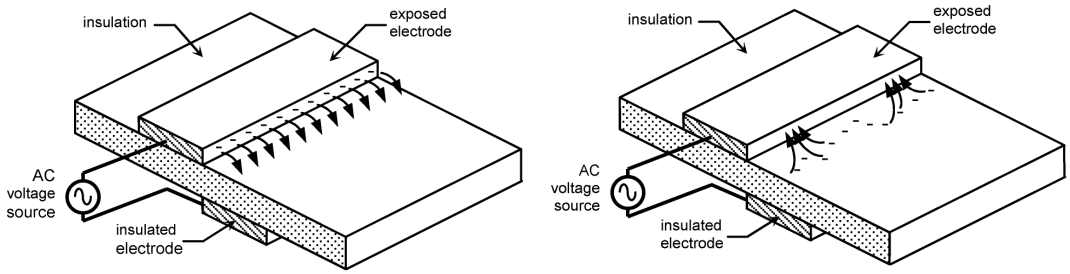

(a) (b)

Figure 2.2: DBD actuator during (a) the negative-going half cycle and (b) the positive going-half cycle (from Enloe et al. [1]).

As explained by Enloe et al. [1] and Corke et al. [2, 3], the plasma is obtained when the electric field between the electrodes exceeds a threshold value: $E > E_b$, where the subscript "b" stands for the breakdown value for the particular gas. It depends on both the actuator configuration and on the frequency of the signal. The plasma is then sustained as long as the voltage is kept over a second threshold value E_s, where $E_s < E_b$. The discharge quenches if the voltage reaches a steady state. Indeed, in this case, the charges, that travelled through the air and formed the plasma, have arrived at the dielectric surface (or exposed electrode) and cancel the electric field, thus preventing other charges to leave the exposed electrode (or dielectric surface). As explained by Roth [4], during this drift of the different charged particles, the electrons have little interaction with the free air, but the ions collide with the neutral molecules. This effect, called paraelectric by the author, can be seen as an electrostatic pressure in the plasma, acting on the neutral species, and that hence generates an airflow.

Corke and Enloe [1–3] added that the plasma lifetime is much smaller than the period of the AC voltage supplied to the actuator. They also observed that during one cycle of the AC current, the characteristics of the positive- and negative-going half cycles are different. Enloe et al. [1] describe the positive-going half cycle as "patchy". When the applied voltage is negative-going, the electrons leave the air exposed electrode and go towards the surface of the dielectric, and form a uniform discharge of weak streamers. Whereas, when it is positive-going, more numerous strong streamers are generated in the plasma, and result in the appearance of peaks in the current and in light emission. Thus the negative-going half cycle generates more body force on the surrounding gas and is less diffusive. Corke et al. [2, 3] identified two components of the actuator current. The conduction current can be defined as the charges going through the plasma due to its resistive behaviour, while the displacement current arises due to the capacitive component of the actuator.

Several authors have proposed simple electrical circuit to model the actuator. For instance, the circuit derived by Corke et al. [2] is reproduced in Figure 2.3. The plasma (branch "A" on the figure) is modelled both by a variable capacitor and a variable resistor, depending on the strength of the electric field and the gas mixture. The dielectric layer consists of the superposition of a constant capacitive components, and of variable capacitances varying with the plasma and air conditions (and thus with the applied voltage amplitude and frequency). The air (branch "B" on the figure) is also modelled as a variable capacitance, depending on its composition, on the extent of the plasma, and on the input voltage. More complex circuits exist [5] to model the actuator, and are particularly useful when simulating the plasma, but they will not be detailed here. In the present model, the surface of the dielectric material plays the role of an electrode.

When it comes to assessing the electrical power consumption, it has been found useful to utilise Lissajous figures (Q-U diagrams) [5–7]. The charge-versus voltage curves of DBDs have a parallelogram/almond shape. By integration, the area inside the four curves represent the power consumption of the device (an example of Lissajous

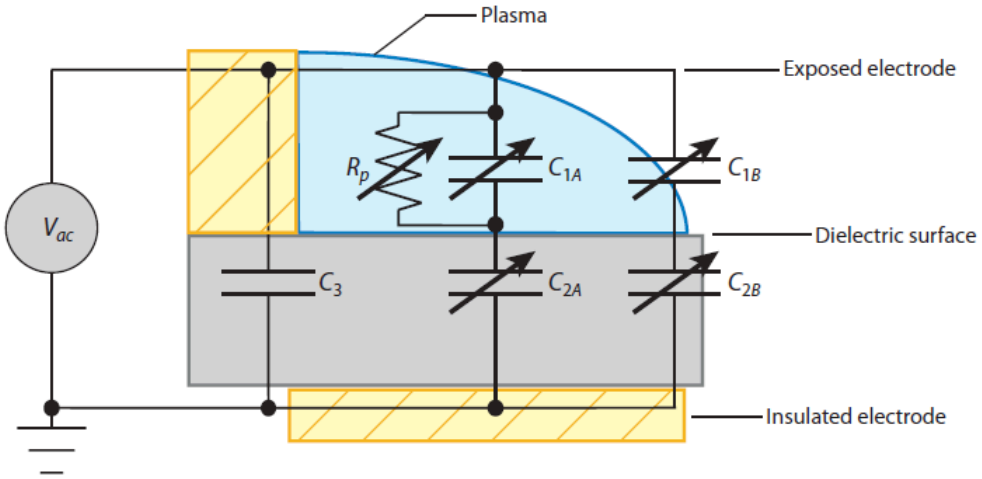

Figure 2.3: Lumped element circuit model (reproduced from [2]).

figure is presented in Figure 2.4). C_0 represents the pure capacitive component of the actuator (i.e. can be measured with a multimeter when the DBD is not connected to a power supply) while C_{eff} stands for the effective capacitance of the actuator. The maximum value for the capacitance of the plasma alone is $C_{\text{eff}} - C_0$, and C_{eff} has a close correlation with the plasma spatial extent. Kriegseis et al. [6, 7] determined that C_{eff} increased with the applied voltage, and that the value of C_{eff} was approximately the same for both half-cycles.

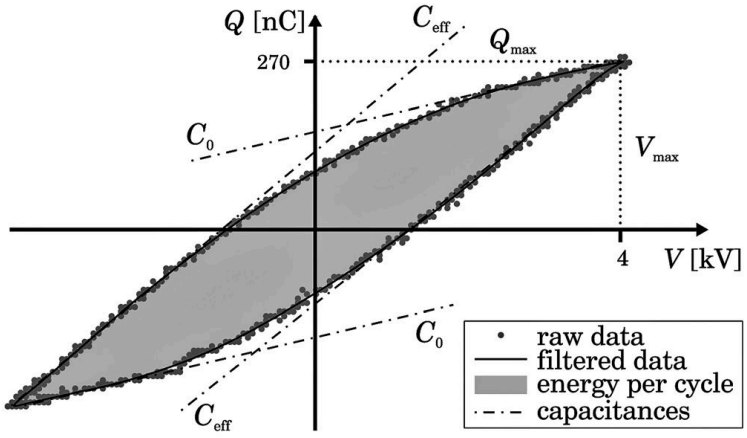

$$P_{\text{elec}} = f \oint Q(t)dV$$

Figure 2.4: Example of Lissajous figure (reproduced from [6]).

2.1.2 Plasma Physics

Concerning the plasma extent, several authors [1–3, 6, 8, 9] observed that it increases linearly with the applied voltage, but does not depend on the frequency. Also, the higher the voltage, the greater the speed of the discharge. However, the propagation speed is the same for both half cycles of the AC current. It was thus shown that the thrust created by the DBD was only the result of the asymmetrical geometry of

the device [1, 8]. The plasma never extends more than a few millimetres past the downstream edge of the encapsulated electrode.

The motion of the particles within the plasma is dominated by the electrostatic forces. As discussed by Enloe et al. [8], external potential are shielded through Debye shielding in the plasma region. However, Opaits et al. [10] measured the surface potential on the dielectric layer with an electrostatic voltmeter and observed that the charge extends downstream of the plasma. Such effect is certainly due to the non ideal behaviour of the plasma (some charged particles could leave the plasma region). They draw the conclusion that these particles more likely come from a deposition from the plasma rather than from the displacement of charges within the dielectric (since the charge mobility is low in such a material). They also remarked that the time average potential was positive, as confirmed by Enloe et al. [11]. It was seen as a consequence of the much higher mobility of the electrons compared to ions. The net result of this non-zero average potential is an asymmetry in the charge of the actuator over a cycle, that can be linked with the production of a flow by the DBD. Opaits et al. [10] suggested to find a configuration in which the electric field would be the strongest, as it would induce higher velocities in the free-stream. To avoid losses of energy downstream of the plasma, a strip of the encapsulated electrode was exposed. The effect was the cancellation of the potential downstream the electrode. Particular care was given to avoid any contact between the plasma and this exposed strip.

In addition, when the free-stream velocity cannot be neglected compared with the speed of the charged particles in the plasma, the electromechanical properties of DBD actuators can be modified. As emphasised by the work of Pavon et al. [12], at transonic flow regimes, the skew angle affects the breakdown voltage of the surrounding gas (here applied on a plasma array). It is considered to be a consequence of the stronger convective effects in the presence of a high speed flow, that tends to take away the metastable species, latter responsible for the formation of the plasma.

The light emission of the plasma can also be measured in order to obtain either its intensity (quantitative) or to differentiate the two regimes (streamer or glow discharge). As described by Kriegseis [6], the thrust generated by DBDs increases with the extent of the plasma, and also increases with the consumed power. For instance, Orlov [9] showed that the light emission scales with the amplitude of the applied voltage to the power 7/2, not dissimilar to some mechanical and aerodynamic properties of the device (cf. Section 2.1.5). Infra-red measurements have also been performed on DBD actuators [13] and provide the temperature of the exposed surface of the dielectric layer. Recording this parameter does not directly give the efficiency of the actuator, but its inefficiency. Indeed, for common DBD usages (in contrast with nanosecond-pulses or PSJs treated in Section 2.4), an increase in the gas or dielectric temperature is synonymous with greater losses.

The light emission can also be analysed through spectroscopy. Such process gives information about the light emission spectra and the related species in the plasma [14–18]. The plasma chemistry will not be discussed here as it goes beyond the primary

focus of the study. The main conclusion that is relevant to this study, is that the species in the plasma (ozone, nitrogen-oxides, and the different charged species) mainly emits ultra-violet light in the 300 nm to 450 nm spectrum. Thus, a plasma actuator can produce a wall jet, without an entirely visible plasma.

2.1.3 Plasma Equations

Plasma physics encompasses several fields of general physics. In essence, the electromagnetic properties of the charged species influence the behaviour of plasma as a fluid. Thermodynamics are also implied in the characteristics of plasmas. Finally, it is crucial to determine the chemical species formed and present in the plasma. The problem is very challenging, since these different fields interact in the formation and general behaviour of the plasma.

In Section 2.1.1, it was explained the plasma ignites when the electric field exceeds a breakdown threshold of the material. The ignition leads to the release of electrons in the conducting medium. If the loss of material from the electrode is neglected, many chemical reactions occur between the different molecules, electrons and photons. A detailed list of the chemical reactions has been drawn by Eliason et al. [19, 20]. However, the different reactions have various reaction times, which leads to several species recombining faster than others in the plasma. If the work of Eliason et al. [19, 20] focused on the ozone generation, spectroscopy studies, such as the work of Sanders et al. [14], highlighted the presence of different species generally brought by the reaction of nitrogen and oxygen, or the dissociation of water. For instance, Skalny et al. [21] reported the production of CO^{3-}, O^{3-}, HCO^{3-} and NO^{3-} in wet air for a negative corona discharge. On the other hand, Shahin [22] noticed the presence of H_3O^+, NO^+ and NO^{2+} for a positive corona discharge. Both studies highlighted the formation of water clusters around the charged species. These clusters are due to the polarity of the water molecule, which is an electric dipole.

In order to model the plasma, it is necessary to couple the typical Navier-Stokes equations to the Maxwell's equations. This field of physics is called Magnetohydrodynamics (MHD). However, its typical use involve strong magnetic field. In the case of DBD, the electromagnetic problem can be simplified to an electrostatic problem. In this situation, the study can be focused on Electrohydrodynamics (EHD). As described by Castellanos [23, 24], and latter summarised by Kourmatzis and Shrimpton [25, 26], an element of fluid of charge density q obeys the typical Navier-Stokes equation for the conservation of mass and momentum, by introducing a new body force term that depends on its electromagnetic characteristics:

$$\nabla \cdot \mathbf{u} = 0 \ , \tag{2.1}$$

$$\frac{\partial \mathbf{u}}{\partial t} + (\mathbf{u} \cdot \nabla)\,\mathbf{u} = -\frac{1}{\rho}\nabla p + \frac{\mu}{\rho}\nabla^2 \mathbf{u} + \frac{1}{\rho}\mathbf{f}_\mathrm{e} \ . \tag{2.2}$$

The above equations assume an incompressible flow. $\mathbf{u}$, p, ρ, μ and $\mathbf{f}_\mathrm{e}$ respectively

represent the velocity, pressure, density, viscosity and body force. The plasma body force for an electrostatic case can be described as:

$$\mathbf{f}_\mathrm{e} = q\mathbf{E} - \frac{1}{2}E^2\nabla\varepsilon + \nabla p_\mathrm{st} \ , \tag{2.3}$$

$$p_\mathrm{st} = \frac{1}{2}\varepsilon a E^2 \ , \tag{2.4}$$

$$a = \frac{\rho}{\varepsilon}\frac{\partial\varepsilon}{\partial\rho} \ , \tag{2.5}$$

where q, $\mathbf{E}$ and ε stand for the charge density of the element, the electric field and the permittivity of the element.

The electrical body force $\mathbf{f}_\mathrm{e}$ is composed of three terms. The first term ($q\mathbf{E}$) is the Coulomb force that acts on the element of charge density q. This term dominates over the other two in typical EHD problems, particularly for Direct Current (DC) electric fields. The second term ($-(1/2)E^2\nabla\varepsilon$) is called the dielectric force, and is due to the inhomogeneity of the medium. It becomes important when the electric field has an AC period, that is shorter that the charge relaxation time and/or ionic transit time. The charge relaxation time is the typical time scale, that describes the rate at which an initial charge placed at a point decays in a dielectric fluid. The ionic transit time scale represents the typical time taken by a charge to move to a characteristic distance due to electrical convection. As it is explained in Section 2.3.1, the plasma extent at the surface of the DBD usually reaches a maximum value, that mostly depends on the voltage and frequency of the electric current, as long as it is not constrained by the encapsulated electrode. This distance could be used as a typical length-scale for the plasma in this application. The final term (∇p_st) is the gradient of the electrostrictive pressure. It depends on the electrostriction parameter a, and is due to the inhomogeneity of the medium (i.e. the plasma). In a glow discharge in a gas, the charge distribution can be approximated as homogeneous. Therefore, this term should be negligible, in contrast with the filamentary discharge, where the plasma concentrates to strong streamers.

The electric field and space charge distribution obeys Gauss's and Faraday's laws, and the charge conservation equation. With the neglect of the magnetic field, these equations can be written as:

$$\nabla\cdot(\varepsilon\mathbf{E}) = q \ , \tag{2.6}$$

$$\nabla\times\mathbf{E} = 0 \ , \tag{2.7}$$

$$\frac{\partial q}{\partial t} + \nabla\cdot\mathbf{J} = 0 \ , \tag{2.8}$$

with $\mathbf{J}$ the density current. This last variable depends on the discharge. If the fluid is assumed to conduct the current homogeneously with a conductivity σ_e, the density current is given by Ohm's law:

$$\mathbf{J} = \sigma_\mathrm{e}\mathbf{E} + q\mathbf{u} \ . \tag{2.9}$$

The second term ($q\mathbf{u}$) here accounts for the contribution of the fluid velocity. The previous equation assumes the conduction is uniform in the fluid. On the contrary, if the fluid is assumed to be a perfect insulator ($\sigma = 0$) through which some ionic species flow with a coefficient of charge diffusion D, and a ion mobility κ, the current density equation becomes:

$$\mathbf{J} = \kappa q\mathbf{E} - D\nabla q + q\mathbf{u} \ . \tag{2.10}$$

More typically, DBDs actuator are simulated by using the electric potential ϕ that relates to the electric field by the following formula:

$$\mathbf{E} = -\nabla\phi \ . \tag{2.11}$$

Using Gauss's law (Equation 2.6) for a constant dielectric permittivity, the electric potential and the charge are linked by:

$$\nabla^2\phi = -\frac{q}{\varepsilon_r\varepsilon_0} \ . \tag{2.12}$$

Several authors [27–30] decomposed the charge density q into three components, in order to account for the participation of electrons and positive and negative ions. If e_e represents the elementary charge, and ν_+, ν_- and ν_e the number densities of the positive and negative ions, and of the electrons, the charge can be expressed as:

$$q = e_\mathrm{e} \cdot (\nu_+ - \nu_- - \nu_e) \ . \tag{2.13}$$

Although, Yamamoto and Fukagata [29] neglected the contribution of the electron, due to the much smaller momentum of electrons compared to ions.

Several assumptions can be made to simplify the problems, and model the plasma instead of simulating the discharge. As explained previously, the Coulomb force dominates the other force terms in EHD problems. Using Equations 2.3, 2.11 and 2.12, the EHD body force can be expressed as:

$$\mathbf{f}_\mathrm{e} \approx q\mathbf{E} \ , \tag{2.14}$$

$$\mathbf{f}_\mathrm{e} \approx \varepsilon_r\varepsilon_0\mathbf{E}\cdot\nabla\mathbf{E} \ . \tag{2.15}$$

For a one dimensional case, Equation 2.15 becomes:

$$\mathbf{f}_\mathrm{e} \approx \nabla\cdot\left(\frac{1}{2}\varepsilon_r\varepsilon_0 E^2\right) \ . \tag{2.16}$$

Equation 2.16 was proposed by Roth et al. [31]. For a gas, the relative permittivity ε_r can be approximated to one. It has been evidenced this model is only valid in a one-dimensional model [8]. Moreover, this model can only give an estimation of the force, since it does not compute the presence of the plasma [8], and its interaction with the neutral gas. Another model introduced by Shyy et al. [32], takes the plasma

generation into consideration:

$$\mathbf{f}_\mathrm{e} = f_\mathrm{ac}\, \alpha\, q\, e_\mathrm{e}\, \Delta t\, \delta\, \mathbf{E}\ . \tag{2.17}$$

In the above equation, α is the factor for the efficiency of the collisions between the charged and neutral particles, e_e is the charge of an electron, Δt is the time during which the plasma is ignited and δ is the Dirac delta function:

$$\begin{cases} \delta = 1 & \text{for } \|\mathbf{E}\| < E_\mathrm{b}\ , \\ \delta = 0 & \text{for } \|\mathbf{E}\| \geq E_\mathrm{b}\ , \end{cases}$$

where E_b is the breakdown electric field of the air. This model however relies on the assumption that the electric field strength decreases linearly between the exposed and encapsulated electrodes. Measurements performed by Enloe et al. [11] tend to agree with an exponential decay. It can be noted the previous equations neglect the thermal contribution of the plasma. Other contributions to the internal energy are described in the fourth chapter of the book of Castellanos [23]. The closure of the system of equations by be achieved by including equations such as the ideal gas equation of state:

$$p = \rho\, R_0\, T\ , \tag{2.18}$$

where p is the gas pressure in Pa, ρ is the gas density in kg/m^3, T is the temperature of the gas in K and R_0 is the specific gas constant in J/(kg·K). For instance, this model has been used by Zheng et al. [33] to simulate the shock wave generated by a nanosecond pulsed actuator, with good agreement with experimental results. This modelling is certainly sufficient to simulate the behaviour of the gas surrounding the discharge, but more complex models need to be employed in the plasma region, in order to capture the heat released by the chemical reactions, due to the ionisation of the gas.

Finally, the work realised in Toulouse by Boeuf, Callegari, Lagmich, Pitchford and Unfer [34–38] must be presented. Their model adds a surface charge term to Equation 2.13, in order to account for the electric charge of the dielectric surface. Moreover, the model computes the conservation equations for the number densities of the negative ions, positive ions and electrons. These continuity equations are not detailed in the current study, due to the large number of terms they include, and because a numerical analysis is beyond the scope of the present study. To summarise, the continuity equations include the diffusion, ionisation, attachment and recombination of the charged particles. Consequently, these equations provide informations about the production and disappearance of the charged particles, due to the different chemical processes that occur in the plasma. This model assumes a quasi-neutral plasma, where the number densities of the ions and electrons are close but not equal [34]. The quasi neutrality assumption indicate that the plasma discharge is composed of microscopic weak streamers. In the case of a neutral plasma (with equal number densities of the ions and electrons), the authors note that the body force is null [34]. The model was

used both with AC-DBD and Nano-Second(-Pulsed) DBD (NS-DBD) configurations. When coupled to the Navier-Stokes equations with including the energy equations, this model of the force distribution enables the study of the flow-field produced by the two types of plasma actuators [39].

2.1.4 Induced Airflow

Over the past decades, plasma DBD actuators have been extensively studied for flow control applications. As explained previously, the free air around the plasma is entrained, because of the collisions of its neutral species with the charged particles that are trapped in the plasma. Therefore the DBD actuator generates a wall jet. Wang et al. [40] provide an overview of the different utilisations of the DBD, which are further discussed in Section 2.6. A wall jet is created on the dielectric surface, showing a similar velocity profile to that obtained with blowing slots. Murphy et al. [41] reported the velocity profile close to the wall agrees with a Glauert laminar wall jet [42]. In the few milliseconds after the ignition of the DBD in quiescent conditions, a starting vortex is generated by the actuator, and rolls over the surface. This phenomenon was studied by Whalley and Choi [43]. They observed the motion of the starting vortex created by the actuator, downstream and away from the wall as the ignition was sustained. The radius of the vortex was also seen to increase as it rolled out. If the ignition is sustained long enough, the wall jet becomes the only visible feature in the flow-field. Furthermore, the experiment revealed that the momentum added to the flow increased linearly over the time, indicating a constant plasma body force. Nevertheless, other sets of experiments performed at different atmospheric conditions prove that other flow types can arise. Below 27.7 kPa, Che et al. [44] found three possible flow-fields. In addition to the tangential wall jet at the highest pressure (27.7 kPa), a vertical jet leaving the surface was captured at lower pressure (22.4 to 14.6 kPa), and a vortical flow developed at the lowest pressure (3.25 to 1.0 kPa). The maximum tangential velocity is typically encountered below 1 mm from the wall at the edge of the exposed electrode, but its location moves further away from the wall as the jet travels downstream and thickens [5, 44]. Both the starting vortex and the wall jet are presented in Figure 2.5.

2.1.5 Electro-Mechanical Properties

In terms of performance, it was usually noted by numerous authors that the thrust generated by the actuator, the electrical power consumption and the maximum velocity induced in the flow-field depends on the applied voltage to the power 7/2 [1–3, 7, 8, 45]. Moreover, Kriegseis et al. [7] found that the electrical power consumption scales with the frequency to the power 3/2. Thus, they proposed the following scaling law:

$$\frac{\Pi_A/L}{f_{ac}^{3/2}\,V^{7/2}} = \Theta_A = \text{cst}, \tag{2.19}$$

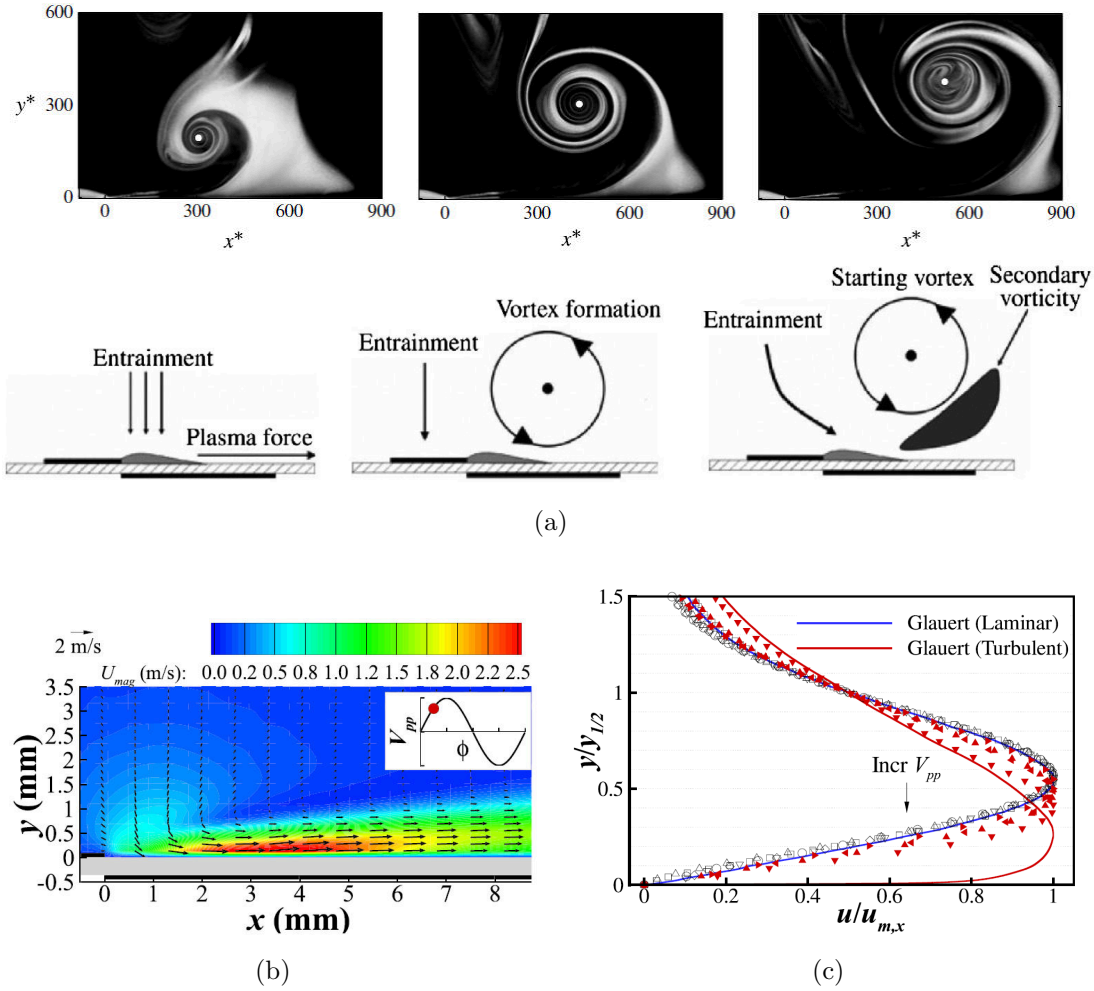

Figure 2.5: Typical airflow generated by DBD actuators: (a) smoke flow visualisation of the starting vortex in quiescent air (reproduced from [43]) , and (b, c) velocity profile of the wall jet (reproduced from [41]). Note: this coordinate system is not used in the current study.

where Π_A is the electrical power consumption by the actuator, L is the span of the electrodes and f_{ac} and V are respectively the frequency and amplitude of the applied voltage. They also defined the resonance frequency of a DBD actuator as the frequency of the applied voltage at which the phase shift between the applied voltage and the charge is maximum. Actuating the DBD at this frequency increased the electrical efficiency, that is defined as the electric power consumed by the actuator, divided by the input electric power. The electrical input power includes the actuator, and its high-voltage power supply. As a result, the resonance frequencies also depends on the utilised High Voltage (HV) power supply.

However, there is some discrepancy in the literature concerning this scaling law. Pons et al. [5, 46] captured a quadratic relationship between the power and the difference between the maximum voltage and a reference voltage. This reference voltage is a threshold below which the actuator does not generate an airflow. The maximum induced velocity scales linearly with this same voltage difference in their study. As

a result, the maximum induced velocity scales with the square root of the consumed electrical power. Murphy et al. [41] added that the maximum tangential velocity first scales as $V^{2.4}$ at the edge of the exposed electrode and scales as $V^{3.5}$ downstream. They also determined that the body force scales as a power law of the amplitude of the applied voltage, with an exponent depending on the applied voltage. Two regimes were found over or below 10 kV_{pp}, and this difference was hypothesised to be caused by the laminar-to-turbulent transition for the wall jet.

The plasma body force comes from the collisions of the neutral air particles with the charged particles of the plasma, thus adding momentum to the free-stream. Roth [4] calls this force paraelectric. He adds a "peristaltic" body force can be generated by triggering electrostatic waves over an array of DBDs. This conclusion is however unclear, and it has not been evidenced by other studies. In order to obtain the thrust of the actuator, one must not neglect to subtract the viscous losses occurring at the wall downstream of the actuator [6, 43], since up to 30% of the overall induced momentum can be dissipated by wall friction [47]. Several scenarios are usually considered to describe the time evolution of the force acting on the DBD. The push-push characterisation is typically retained [8, 48], in which the plasma first pushes on the free air, and then the opposite charges within the plasma push on the exposed electrode. Nevertheless, when friction losses are taken into account, a push-pull characterisation can also be valid [49] (since the contribution of the positive-going half cycle is less). These results highlight the importance of differentiating the plasma force acting on the air, and the total thrust of the actuator. Enloe et al. [50, 51] evidenced the greater contribution of the negative-going half cycle to the overall force. They found that this half cycle produced approximately 95% of the total thrust of the actuator. This leads to a PUSH-push model (the first "PUSH" representing the greater contribution of the negative-going half cycle).

The overall efficiency can be measured using several definitions. For instance, Krigseis et al. [6] used the force production efficiency defined as:

$$\eta = \frac{F_b}{\Pi_A} \ . \tag{2.20}$$

However, since F_b is the thrust or body force and Π_A the consumed power, this parameter is not non-dimensional but expressed in N/W.

2.2 Measuring the Performance of the DBD Actuator

Several of the characteristics described in the previous section were assessed experimentally. Consequently, a brief overview of the commonly employed measurement techniques must be drawn, so that the most relevant way to evaluate different DBDs is established.

Overviews of the different methods used in the characterisation of plasma actuator as been published by Benard and Moreau [52] and Kotsonis [53]. They will be detailed

in the following paragraphs.

As discussed by Kriegseis et al. [54], power losses occurs at different stages (see Figure 2.6):

- The power input corresponds to the overall electric power that is supplied to the device.
- The actuator power differs, due to the losses that occurs in the plasma. It can for instance be drawn from a Lissajou figure (refer to Section 2.2.3) obtained by voltage and current measurements realised in the electric circuit.
- The fluid mechanic power is lower than the actuator power, due to the losses that occur in the transformation of the actuator power into momentum (for example due to friction).
- The power savings correspond to the power transmitted to the flow when considering how efficiently the DBD is installed and actuated for a given application. The power savings need to be judged for each application, depending on the goal of the actuation.

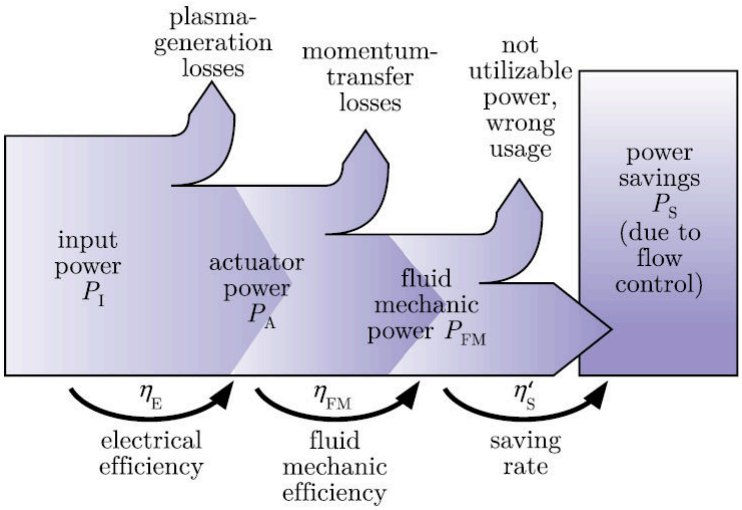

Figure 2.6: From initial electrical power to final power savings of a DBD actuator (reproduced from [54]).

The actuator power is the focus of most studies to determine the power consumed by the actuators. On the other hand, the fluid mechanics efficiency is generally estimated, as an output, by measuring the force generated by the DBDs and the actuator power. The thrust measurement can be replaced in some cases with different techniques giving more information on the plasma discharge, such as its extent, temperature or light emission. These different methods are discussed in the following sections, while the flow control abilities of DBD are introduced in Section 2.6.

2.2.1 Light Emission

As discussed in the previous section, light emission can be chosen to measure the performance of a DBD. Enloe et al. [1, 6, 8] measured the light emission as a surrogate for the plasma density. Kriegseis et al. [6] observed that the effective capacitance of an actuator increases almost linearly with the plasma length. They also proved the power consumption and thrust generation increases with the plasma extent. The relationship between the force generation and the plasma extent is not straightforward. Thus, it is necessary to record other quantities to verify the results and link them with the aerodynamic performance of the actuator.

Infra-red measurements [13] give the temperature of the air-exposed surface of the dielectric. The main issue is to derive the plasma temperature from the thermal characteristics of the dielectric material from which the measurement originates, and to make sure the test is run for a long enough time to reach a thermal equilibrium state. The recorded temperature is a time average quantity, and cannot provide any information on the time-evolution of the plasma. Also, it is difficult to compare different DBD configurations, since an improvement in the velocity leads to different convective effects, and thus affects the surface temperature.

Another possible technique consists in analysing the light spectra of the plasma, and coupling it with chemical properties [14], and thermal properties [14, 55] through spectroscopy. As this technique provides the plasma temperature, it is theoretically possible to calculate the temperature of the dielectric [55]. The induced temperature increases along with the induced velocity, however, no clear relationship has been drawn between them yet. It should be kept in mind that increasing the temperature also means an increase in the power consumption, which is itself linked to the supplied voltage, and so the induced velocity. The chemistry of the plasma will not be detailed in the present study. The main possible drawback is the ozone and nitric-oxide generation by the plasma. The reactions in the plasma mainly produce dark violet to ultra-violet light [14–18].

2.2.2 Electrostatic Potential

Two main arrangements have been reported to assess the electric potential at the surface of the dielectric layer. Opaits et al. [10] measured the surface potential through an electrostatic voltmeter. It is a non-intrusive way to assess the electric potential of the surface of the dielectric material, however, the electrostatic probe needs to be placed close to the surface making simultaneous aerodynamic measurements infeasible. It was observed that a significant positive charge deposition occurs downstream of the plasma. A non-intrusive surface potential measurement technique was assessed by Enloe et al. [11]. The electric potential at the surface of the dielectric was derived thanks to a V-dot probe array coupled to operational amplifier integrators. The probes simply consists of strips of the encapsulated electrode, that are electrically isolated from the electrode. The main drawback of this method lies in the fact that it makes the design of the DBD

more complex, as the V-dot probes are integrated into the encapsulated electrode. The potential of the exposed surface of the dielectric can be derived for the probes. The drift of the charged particles, and resulting entrainment of the neutral gas must be derived from the distribution of potential. This could be achieved through different equations and models, as described in Section 2.1.3. The study concluded on the dependency of the charge distribution on the dielectric material properties (thickness and permittivity) and the HV signal amplitude and frequency. Moreover, it was observed the electric field in the close vicinity of the exposed electrode oscillates between positive and negative values, and that it takes a small positive value further downstream. If a suitable relationship is found between an aerodynamic property of the actuator and the surface potential, better control could be obtained with DBD actuators.

2.2.3 Electrical Measurement

In order to assess the efficiency of the actuators, it is imperative to obtain the consumed electrical power. Utilising the definition of the electrical power (i.e. multiplying the current by the voltage) is difficult, since recording the intensity is not straightforward, and the signal-to-noise ratio is likely to be high [7]. Thus, a capacitor is usually placed at the encapsulated electrode so that, by measuring the voltage, the electrical charge Q can be calculated. Utilising a shunt capacitor instead of a shunt resistor helps to reduce the signal-to-noise ratio as the charge is an analogous integration of the current. A Lissajous figure (or Q-V cyclogram) can be drawn. The electrical power is derived by integration of the surface enclosed by the diagram. Kriegseis et al. [7] also highlight that the chosen capacitor should be as ideal as possible (i.e. its capacitance must be constant over the range of applied voltages), with a capacitance high enough to reduce the signal to noise ratio, but low enough not to interfere with the actuator. In their experiments, the probe capacitance was chosen such that $C_p \gg C_a$ where the subscripts p and a respectively designate the probe and the actuator. Note that $C_a = C_0 + C_{\text{eff}} > C_0$ (as explained in Section 2.1.1). Using Lissajous figures to calculate accurate and time depending values of the electrical power consumed by the DBDs has become very common [5, 6, 13, 17, 53, 56]. This technique however requires a high sampling frequency, and is only relevant if real time quantities are needed. In the present study, average values of the thrust and power are employed. Therefore, this set up is not necessary for the present study.

2.2.4 Aerodynamic and Mechanical Measurement

When it comes to assessing the force produced by the actuator, multiple techniques have been utilised. Several authors directly recorded the force of DBDs mounted vertically on high precision balances [57–59]. The main advantage of this method is its simplicity. However, the actuator needs to be mounted on a stand to keep the force sensors away from the high voltage sources. As the measured forces are small, this can lead to the use of highly expensive equipment, having a large enough dynamic range (to measure the

mass of the DBD, the stand, and the thrust) with good resolution. To overcome this problem, it is possible to use a lever arrangement [6, 60] in which the plasma actuator blows transversally to an arm that amplifies the force recorded at the other end of the lever. In this case, the balance does not have to sustain the mass of the support. However, a careful calibration is required to set the system in mechanical equilibrium, and make sure the friction does not create a hysteresis in the measurements. The generated force is generally less than 40 mN/m of electrode span and increases as a power law of the peak-to-peak applied voltage. Generally, the force is also less than 25 mN/m below 20 kV_{pp} [6, 41, 47, 57, 59, 61]. The previous estimation is limited to designs of DBD close to the employed geometries and electric supply used in the current study (see Chapter 4).

Such data are usually compared with aerodynamic measurements to find the coupling between the mechanical performance and the flowfield generated by an actuator. Durscher et al. [57] assessed several experimental methods to determine the thrust created by a DBD actuator. Direct thrust measurement from a balance was compared with thrust derived from Particle Image Velocimetry (PIV) data. The PIV velocity field was also compared to Pitot probe measurements in the boundary layer, in order to verify the possible interaction of the seeding particles with the plasma. Since the utilised Pitot probe was metallic, the measurements could only be performed downstream of the plasma (2.5 to 3.5 cm), since it would interact with the plasma otherwise. Nevertheless, both total pressure and PIV data showed good agreement. The PIV study proved that the size of the control volume taken around the actuator is particularly important to accurately calculate the thrust. The starting point of this volume was set at the upstream edge of the exposed electrode on the horizontal axis, and inside the dielectric on the vertical axis (0.5 mm). Then, its height was not found to have any noticeable influence on the calculated thrust, as long as it was more than 1 cm. However, the thrust strongly depended on the width of the control volume, and this dependency was strengthened as the applied voltage rose. The final recommendation was to extend it 35 mm downstream of the downstream edge of the encapsulated electrode (i.e. one times the width of this electrode in their study).

Laser Doppler Velocimetry (LDV) has also been employed by Benard et al. [62, 63], in order to determine the flow-field produced by DBDs. Using LDV, it was possible to analyse the time dependence of the wall jet. The authors observed an increase in the maximum induced velocity with the frequency of the voltage source, and confirmed the asymmetry of the flow-field created during the positive and negative half cycles of the AC signal [63]. The negative going half-cycle was observed to create a higher maximum velocity in the wall jet.

By measuring the plasma extent, Durscher et al. [57] found an empirical linear relationship between the minimum width that had to be chosen for the control volume and the plasma extent on the one hand, and between the thrust generated by the DBD and the plasma extent on the other hand. When processing PIV data, it is also crucial to utilise the correct set of governing equations. Kriegseis et al. [47] compared

several methods used by other authors to compute the force acting on the actuator. On the first hand, several models were derived from the Cauchy momentum equation by neglecting certain terms. On the other hand, other models were based on the steady 2D Navier-Stokes equations for an incompressible flow. All the methods showed some agreement with the data, but had the tendency to increase the actuator thrust compared to balance measurements. The assumptions on the wall friction, the pressure term and the body force in the momentum equation must be carefully chosen. In their study, no particular method stood out from the rest for the calculation of the total force acting on the actuator. The results of the study demonstrated that using the Cauchy momentum equation with neglecting the wall-shear stress gave slightly better results, with a better accuracy. However, this improvement was not significant, and the neglect of the wall shear stress is not physically justified.

Other works rely on the measurement of momentum addition by the DBDs. Porter et al. [64] used a pendulum arrangement to measure the thrust generated by an annular DBD actuator. By recording the position of a laser beam created by a pointer attached to the pendulum, the angular deviation (and hence acceleration) was estimated, and then the equivalent force was derived. A similar principle was employed by Enloe and coworkers [48, 50]. In this case, two identical DBDs were blowing on both blades of a propeller-like configuration. Thus, by knowing the friction in the central shaft, and by measuring the angular displacement due to the actuators, it was possible to determine the angular velocity and acceleration, and consequently, to derive the momentum and thrust added by the DBDs. Abe et al. [59] directly measured the momentum by making the actuator blow through a converging channel, and by recording the exit airspeed. Nevertheless, this test rig necessitates taking into account the effect of the converging walls and losses due to friction.

Due to the relative simplicity of thrust measurement techniques, they are preferred to assess the overall performance of DBD actuators. However, as it has been highlighted in the previous section, the thrust and the plasma body force are not the same, due to the presence of skin friction at the wall. Thus, it is common to see such methods compared with PIV or Pitot probe data. The main issue with the latter two techniques is their possible interaction with the plasma generation process.

2.3 Parametric Studies on the DBD Actuator

As represented in Figure 2.1, several parameters can be tuned when designing a DBD:

- shape of the electrodes,
- width of the electrodes w_1 and w_2,
- thickness of the electrodes h_1 and h_2,
- thickness of the dielectric layer t,
- (horizontal) gap between the electrodes g,
- material used as a dielectric, especially, its relative permittivity ε_r.

To these geometrical and material parameters can be added electrical variables that can be more easily modified:

- wave-form of the applied voltage,
- voltage amplitude V and frequency f_{ac} of the electric signal,
- wave-form of the modulating signal,
- frequency f_m of the modulating signal.

Finally, the atmospheric conditions around the actuator influence its flow control characteristics.

Using the measurement techniques explained in the previous section, many of these parameters have already been evaluated in previous studies. The results led to the discovery of several scaling laws. Since the present study aims at optimising DBDs, a review of the past findings concerning the actuator is thus required, in order to determine the significant parameters and their effects on the flow-control performance of the DBD actuator. The present study aims at confirming and ranking these significant parameters. Consequently, the results of the study highlight the design parameters that need to be focused on and the ones that can be neglected, when optimising the DBD actuator.

2.3.1 Geometry and Material of the Electrodes

Concerning the exposed electrode, it has been observed that reducing its thickness h_1 intensifies the thrust of the actuator [8, 59]. In addition, Abe et al. [59, 65] assessed a mesh-type exposed electrode. This alteration of the electrode increases the electric field, and the results revealed a subsequent increase in the induced velocity. Debien et al. [66] compared rectangular and wire type electrodes. The main motivation was to make the amplitude and the number of the streamers in the discharge lower. The streamers are sparks in the plasma, that concentrate the charged species. Reducing the number of streamers make the plasma more uniform, with a lower power consumption, and a greater ability to transfer momentum to the airflow. Decreasing the diameter of the wire reduced the amplitude of the peaks in the current evolution during the positive-going half cycle of the voltage (hence, weakened the streamers). For diameters below 25 μm, a filament-free regime was obtained during the positive-going half cycle. However, the number of current peaks (i.e. streamers) increased during the negative-going half cycle. The power consumed by wire electrodes was shown to be greater than with rectangular electrodes (up to 20%). Nevertheless, as the applied voltage rose, the trend did not hold and, above an amplitude of 18 kV (36 kV_{pp}), thick wires resulted in less power-consumption. For the same power input, decreasing the diameter of the wire enhanced the thrust produced by the device. The wire-to-plate configuration was consequently more effective than the plate-to-plate configuration. This result suggests a lower width of the exposed electrode w_1 can improve the thrust generation as well as a thin electrode. This was also observed by Hoskinson et al. [67], who determined

that the efficiency was proportional to the diameter to the power 3/4. Wire electrodes generated a thicker velocity profile at the wall with a greater suction towards the wall than the plate electrodes. Also, the recirculation produced by the wall jet was captured downstream of a plate air-exposed electrode, but upstream of the wire exposed electrode, and the size of the created vortex decreased with a smaller diameter of the electrode. In general, it was observed that the wire air electrodes were more efficient than rectangular electrodes. The main disadvantage of the wire-type electrode is that it requires more advanced and less accurate production techniques, in order to produce the DBD. In order for the inaccuracies imparted to the manufacturing of the actuators to be negligible, a rectangular-type electrode can be preferred. A rectangular electrode also enables to assess the significance of the width of the exposed electrode.

Enloe et al. [8] determined that increasing the width of the encapsulated electrode w_2 leads to an increase in the maximum induced velocity until reaching a plateau. As the maximum velocity is reached at the end of the plasma region, this might be explained by the fact that the plasma extent should not be constrained by the size of this electrode. This phenomenon was observed by other authors [45, 68–70]. Thus the size of the encapsulated electrode should be small enough (particularly in an array) not to interfere with the other actuators, but long enough not to limit the plasma extent.

Several works proved that the gap between the electrodes had a strong effect on the maximum velocity induced by a DBD actuator [2, 69, 70]. A small positive gap (i.e. the electrodes apart from each other) can enhance the performance of the DBD. Negative gaps or "high" positive gaps (over 5 mm) usually reduce the maximum attainable velocity.

Hoskinson et al. [67] also found that the material of the exposed electrode did not have any effect on the performance of the DBD.

2.3.2 Thickness and Material of the Dielectric

Modifying the configuration of the dielectric layer directly changes the capacitance of the DBD. Thus it can influence the performance both by allowing it to reach higher induced velocities, and by reducing the losses through the dielectric material. It was observed that a thick dielectric layer of low relative permittivity [45] increases the maximum obtainable thrust, even if a thin layer [69] of high permittivity [45] can produce a higher thrust at low voltage. Thomas et al. [45] highlight a saturation of the actuator as soon as the discharge has transitioned from a uniform glow discharge to a filamentary discharge of streamers. At saturation, increasing the voltage or frequency has a limited impact on the thrust generation, but increases the power consumption. For a given DBD, the higher the frequency, the lower the obtainable voltage before reaching saturation. At a given voltage and frequency, a thinner dielectric with a higher permittivity was found to produce more thrust. The saturation thrust was observed to increase almost linearly with the supplied voltage, but to decrease approximately as the inverse of the frequency. Corke, Enloe and Wilkinson [2] showed that the capacitance

of the DBD decreases with a thicker dielectric layer. They add that the capacitance is proportional to ε_r/t, where t is the thickness and ε_r the relative permittivity of the dielectric material. The power loss through the layer (associated with heating) is proportional to $f_{ac}\varepsilon_r/t$. Consequently, reducing this ratio might be necessary to reach a higher efficiency. This tends to confirm the observation of Murphy et al. [41], who found that the electrical power consumption scaled with $1/t$ in their experiment. However, decreasing t increases the maximum induced velocity by the actuator [41, 69, 70]. As a result even if the efficiency improves with thicker layers, the effectiveness of the actuator for flow control can decrease with such a configuration. As the dielectric layer gets thinner, it can also sustain lower voltages and create more filamentary discharges [69–71]. As it will be seen in the next section, this might be an issue, since the effectiveness of the DBDs is enhanced when using a higher voltage. Finally, these effects are strongly dependent on the operating conditions [65], which means that the best configurations found at sea level may not be suitable at different flight conditions.

2.3.3 Electrical Parameters

When varying the power supply inputs, it has been shown that increasing the applied voltage increases the induced velocity, and hence the thrust, even for different atmospheric conditions [2, 59, 66, 69–73]. As presented in the previous section, the thrust, maximum induced velocity and electrical power consumption typically scale approximatively with the applied voltage to the power of 7/2. However, other scaling laws have been reported in the literature [46]. This can be due to the location at which the capillary tube is placed during the measurements, as proven by Murphy et al. [41]. Details about these scaling laws can be found in Section 2.1.5. Another source of discrepancy lies in the amplitude of the applied voltage. For instance, Thomas et al. [45] agreed on the 7/2-power law below 50 kV_{pp}, but then found that the thrust scales as the applied voltage to the power of 2.3 above this amplitude. This phenomenon was found to occur just before the saturation point described in Section 2.3.2.

Abe et al. [59] reported an almost linear increase in the thrust and power with the AC frequency. Nevertheless, it is commonly observed that the applied frequency affects the performance of the actuator negligibly compared to the applied voltage. Even if the linear trend is not commonly reported, the augmentation of the thrust and induced velocity with the frequency is typically agreed on [45, 69, 70]. Besides, depending on the configuration of the DBD, there seems to exist an optimal (resonance) frequency, leading to better efficiency [7]. For voltages and frequencies that are too high, the maximum induced velocity plateaus [69, 70] due to the saturation detailed by Thomas et al. [45].

Moreover, several works focused on assessing the effects of different wave-forms on the performance of the device. Corke et al. [2] determined that the efficiency of DBD was maximised with sawtooth signals. Rectangular waveforms provided the worse efficiency. Sinusoidal waves had a lower efficiency compared to triangular waveforms.

Enloe et al. [1] highlighted that, for the same power consumption, negative-going sawtooth signals produced a more uniform discharge and induced more thrust than positive-going ones. As explained by Balcon et al. [74], this is due to the fact that the exposed electrode mostly acts as a cathode with a negative sawtooth. As seen previously, this leads to a more uniform discharge, and hence, a higher induced velocity, with a thinner velocity profile at the wall, but sustained further downstream. Abe et al. [65] also analysed this phenomenon by using both sinusoidal and triangle wave-forms for which they could control the slopes of the half cycles. They were also able to investigate positive and negative sawtooth signals (with modifying the slopes of the triangle wave-form), and "squashed" sine wave-forms, for which either the positive or negative slope was much higher than the other. They concluded that both half cycles are important for generating thrust with a sine wave-form, and that the steeper the positive-going slope, the higher the momentum transfer.

2.3.4 Atmospheric Conditions

The performances of DBDs were assessed for different atmospheric conditions. Abe et al. [59] and Benard et al. [72] highlighted that a drop in atmospheric pressure leads to a greater plasma extent and power consumption, and to a reduction in the number of current peaks. Benard added that the intensity of the current peaks was reduced at higher pressure. For encapsulated electrodes that are too short (for which the width constrains the plasma extent), the maximum induced velocity was less than with a wider encapsulated electrode. Abe et al. [65] also noticed that the thrust produced by the DBD first increases with the atmospheric pressure up to a peak value before dropping. This last remark holds in several gas mixtures including air. This peak was located between 750 and 800 hPa. Moreover, it was found that the power consumption was more in nitrogen than it is in air, and that it is lower in carbon dioxide. As explained by Falkenstein and Coogan [75], this is due to the higher electronegativity of oxygen, that attracts the electrons more than nitrogen. In addition, Kriegseis et al. [76] note that the discharge intensity increases when the atmospheric pressure drops. This might explain the greater power consumption mentioned previously. When assessing the effects of a flow-field, an adverse influence on the performance of the DBD was observed, for all atmospheric pressures. Benard et al. [73] also investigated the impact of humidity on the discharge. Raising the relative humidity tends to make the number of current peaks more numerous during the positive-going half cycle while less abundant during the negative-going half cycle. The minimum power consumption was reached for a relative humidity of 85%, and increased as soon as the humidity became lower or greater than this value. However, over 85% of relative humidity before reducing, the increased power consumption could be explained by the test conditions, since water started to deposit on the actuator.

As stated previously, Kriegseis et al. [76, 77] have focused on the impact of the free-stream velocity on DBD. The performance of a DBD for a certain output variable was

calculated as the ratio of the output parameter at non-zero free-stream velocity, over its value in quiescent conditions [77]. Their work focussed on three parameters: the power consumption, the capacitance and the plasma extent. An increase in the free-stream velocity decreases all three output parameters [12, 76]. Losses of up to 10% below Mach 0.2 and up to 30% below Mach 0.5 were captured for the power consumption compared to the consumption in quiescent conditions [77]. Since the thrust was found to increase with the plasma length [6], a non-zero free-stream velocity could lead to a reduction of the thrust generated by DBDs. A scaling parameter was thus proposed, in order to take the free-stream velocity into account. The number K [77], is quite similar to the Mach number, but is based on the velocity of the charged species in the plasma:

$$K = \frac{U_\infty}{v_\mathrm{d}} \ , \tag{2.21}$$

where v_d represents the drift velocity, i.e. the characteristic velocity of the species within the plasma. Yet, it can be difficult to assess this speed practically. The proposed model defines $v_\mathrm{d} = \kappa E$, with κ being the ion mobility, and E the electric field. Typically, $\kappa \approx 2.05$ to 2.10×10^{-4} m^2/V·s for common International Standard Atmosphere (ISA) conditions [78], but it can take higher values for smaller atmospheric pressures and relative humidities [78, 79] (estimated to a drop of approximately 6.6×10^{-7} m^2/V·s per percent of humidity, and a drop of approximately 3.6×10^{-7} m^2/V·s per hPa of atmospheric pressure from [78]). Again, the electric field is not easy to derive. Thus, one can use $E_0 = V/d$, where d represents the dielectric thickness and V the voltage amplitude. As a result, the drift velocity can be estimated using:

$$v_\mathrm{d} = \kappa \frac{V}{d} \ . \tag{2.22}$$

The higher the value of K, the more the DBD is affected by the free-stream. Even if the induced airflow weakens as the free-stream velocity increases, the plasma wall jet can still reduce the skin friction at the wall. It can be noted that the K number does not give any information on the actual momentum transfer to the airflow, it simply is a measure of the effect of the free-stream velocity on its performance. That is a reason why the electro-hydrodynamic number N_EHD can be preferred when the momentum transfer to airflow inertia ratio is of primary interest [80, 81]:

$$N_\mathrm{EHD} = \frac{\langle I \rangle}{\kappa L \rho_0 U_\infty^2} \ , \tag{2.23}$$

where $\langle I \rangle$ is the time average of the electrical current, L the span of the electrodes, ρ_0 the air density, and U_∞ the free-stream velocity. The higher the electro-hydrodynamic number, the greater the flow-field will be affected by the actuator. Together, K and N_EHD provide a measurement of the DBDs efficiency drop and actual effectiveness in a flow-field. Consequently, it is possible to estimate how much the free-stream influences the DBD, and vice versa, how much the latter alters the airflow. The work led by Pavon et al. [12] suggests that, when taking the skin friction into account, the force

production actually increases with free-stream velocity in a co-flow configuration. The counter-flow configuration displayed constant performance. In conclusion, the free-stream velocity seems to deteriorate the ability of the DBD to induce an airflow, but at the same time, improve its ability to reduce skin friction. One parameter that has not been mentioned here is the effect of free-stream turbulence on the performance. To the writer's knowledge, there is currently no work focusing on this particular aspect.

2.4 Other Types of Plasma Actuators

If standard linear AC DBD actuators have been chosen in the present study, it must be mentioned that other plasma actuators exist. They have each their advantages and disadvantages, and benefit from different discharge types. They have all displayed abilities for flow control, and are studied by various groups. First the corona discharge actuator is introduced. Although it can generate an airflow, this type of actuator consumes more power and has a less stable plasma discharge than the DBD. Several types of actuators rely on the DBD, by using three-dimensional geometries, such as plasma synthetic jets, or multiple-encapsulated-electrode actuators. This types of actuators could benefit from the optimisation of the single linear DBD. Moreover, it is possible to take advantage of thermal effects by employing the nano-second pulse actuator that is triggered by nano-second pulses from a voltage source. Nevertheless, its usage is typically reserved for the control of boundary layer transition, particularly in high-speed flows (supersonic or hypersonic). It is unknown whether the optimisation of the DBD and the Nano-Second(-Pulsed) DBD (NS-DBD) are linked. Finally, encapsulated both electrodes was studied. If it does generate an airflow, it is however much weaker than the wall jet obtained with a standard DBD. Consequently, if other types of plasma actuators can be utilised for flow control, the DBD actuator appears a better solution for low speed flow control, with the possibility to modify its geometry, and employ in different applications.

2.4.1 Corona Discharge

Dielectric barrier discharge were not the first plasma actuators utilised for flow control. Corona Discharge (CD) actuators are similar, but with both electrodes exposed to the air, and they are typically supplied with a Direct Current (DC) signal. Several flow regimes were reported with corona discharge. In addition to the glow and filamentary regimes [82] previously described, Moreau et al. [82, 83] report the "spot type" regime, in which the discharge is limited to visible spots on the high-voltage electrode. The spot regime only produces a negligible airflow. By increasing the electric field, the discharge transition to the streamer corona regime, showing a thin sheet of ionised air between the electrodes. The authors indicate this regime is unstable, and it can rapidly be transformed into the more beneficial glow discharge by increasing the electric field. The glow discharge allows to pass a higher electric current (hence increasing the flux of

charged particles) and is more stable. Finally, the filamentary regime occurs at higher electric field, with the current propagating through long filaments, and making the discharge uncontrollable. As explained by Moreau [82], the discharge is more stable when the diameter of the anode is lower than the diameter of the cathode. The current has two components in a corona discharge. The continuous component is due to the drift of the ions, and can be met in both glow and streamer regimes, however, the alternative component only exists in the streamer regime. Moreau adds that using AC voltage does not bring any advantage compared with DC voltage for corona discharges. As it has been reported by several authors [82, 84, 85], the maximum induced velocity increases with the applied current intensity. Nevertheless, increasing the current also makes the discharge less homogeneous [85]. The airflow is induced by a suction occurring at the anode [82]. Consequently, the momentum is added to the gas originating from above the anode. Corona discharge alone has already been successfully applied to control the separation on expansion corners [85, 86].

By comparison, if the maximum induced velocity is nearly the same for DBD and CD actuators, the obtained velocity profile is usually thicker with a corona discharge, and the maximum velocity is located closer to the wall for DBDs [84]. It is possible to couple both actuators, and make a Sliding Discharge (SD) actuator. In this configuration, an encapsulated electrode is placed between the two exposed electrodes, as presented by Moreau et al. [83]. Both DC and AC current components are applied to the circuit. In their experiments, Moreau et al. [83] applied a superposition of an AC and DC signals to one of the exposed electrodes, whereas the other two electrodes were grounded. The goal is to overcome the disadvantages of the corona discharge and DBD configurations. The corona actuators tend to be highly sensitive to the environment, and the DBDs result in greater peaks in power consumption. The authors concluded that the sliding discharge acted like the combination of both actuators. However, the maximum induced velocity was less than with a single DBD. A positive DC current shifted the maximum velocity away from the wall, whereas a negative DC component made the velocity profile thicker, yet with a maximum induced velocity closer to the reachable value with a standard DBD. A positive DC component was also found to induce a higher airspeed and increased the mass flow rate for the same power consumption [87].

2.4.2 Multiple Encapsulated Electrodes

As explained in Section 2.1.2, reducing the losses of electric charges in the jet is expected to increase the performance of the actuator. As a consequence, Berendt et al. [88] tested a "floating electrode" configuration, where a saw-like or smooth floating electrode was placed between the HV and ground electrodes. First the performance of a saw-like DBD was compared to a standard smooth DBD. The saw-like electrode was found to induce a higher maximum velocity than the smooth configuration, particularly for "low" voltages. Then, two scenarios were assessed. On the one hand, both the HV and ground electrodes were insulated on the lower side of the dielectric, while the floating electrode

(not connected to any electric potential) was placed on the air-exposed side and between the connected electrodes. Alternatively, the HV electrode was encapsulated on the lower side of the dielectric, whereas the floating and ground electrodes were located on the exposed side, the ground electrode behind encapsulated in a simple layer of Kapton tape. The saw-like floating electrode generated a higher maximum velocity in these scenarios. However, the floating DBD induced lower maximum velocity in the free-stream than the common DBD. Another three-electrode design was assessed by Benard, Mizuno and Moreau [89]. The air-exposed electrode was placed over a wide grounded encapsulated electrode, and a second HV encapsulated electrode was placed on the front side of the HV air-exposed electrodes. It appeared that this configuration greatly reduced the back-flow on the front side of the DBD actuator. The HV encapsulated electrode also allowed a slight reduction in the power consumption. These effects were even more pronounced with higher applied voltage. This configuration was particularly interesting in a DBD array, as it minimised the losses due to the backward-facing flow between every successive stages.

A more "traditional" Multiple-Encapsulated-Electrode DBD (MEE-DBD) simply comprises other ground electrodes downstream of the usual DBD configuration. Erfani et al. [90–93] focused on MEE-DBDs having one HV exposed electrode and three encapsulated ground electrodes downstream. The ground electrodes were each buried at different depths from the actuator surface. An optimisation method was employed in order to determine the most suitable geometry and power settings [90]. A Response Surface Method (RSM) led to an increase of 36.5% in the maximum induced velocity, compared with an equivalent DBD actuator, for a power consumption 11.7% lower [91, 92]. The optimisation process brought to the following geometric and electric parameters [90]:

- First encapsulated electrode: depth 245 μm, width 5 mm.
- Second encapsulated electrode: depth 470 μm, width 40 mm.
- Third encapsulated electrode: depth 210 μm, width 5 mm.
- Input voltage: 16 kV_{pp}.
- AC frequency: 14 kHz.

The previous results depend on the nature of the dielectric layer. It should be noted that the optimum input voltage was actually the upper limit of the assessed range of values. As a consequence, a higher applied voltage could result in a further improvement. The power consumption was however not part of the optimisation. This indicates that the most effective configuration found in the end of the study might not be the more efficient configuration encountered during the experiment. It should also be highlighted that the induced velocity was dependent on two-factor interactions between the applied voltage and the first grounded electrode depth and width [93]. As a consequence, the optimisation of the actuator must take the interactions of the design parameters with the electric variables into consideration, in order to draw meaningful results.

2.4.3 Plasma Synthetic Jet

A Plasma Synthetic Jet (PSJ) is a wall Zero-Net-Mass-Flux (ZNMF) jet directed perpendicular to the wall. Several methods have already been employed to obtain PSJs. An overview is provided by Wang et al. [40].

When two standard or SD DBD actuators are oriented such that they blow against each other, a vertical jet can be formed. This is the case for both linear and circular actuators, such as presented on Figure 2.7 (a) and (b). This vertical jet is responsible for the appearance of a contra-rotating vortex pair [94], that rolls up until they break down. In the linear case, it is even possible to incline the jet by simply reducing the amplitude or frequency of the voltage of one of the exposed electrodes [95]. As showed by Luo [96], such actuators have flow-control abilities, for example around cylindrical bodies. In this study, a standard DBD was also placed in a cavity, in order to blow vertically through a slot on a flat plate, and control the transition of a boundary layer.

However, plasma spark jets have been proven to be more effective for flow control, and easier to install due to their size [97]. A plasma spark jet actuator consists of a small cylindrical cavity, in which an electrode delivers the electric energy in a very short time (few nanoseconds), causing a sudden heating of the gas in the cavity. A schematic is provided in Figure 2.7 (c). The hot gas mixture expands and is thus expelled from the cavity at very high speed. This configuration has been utilised by several groups

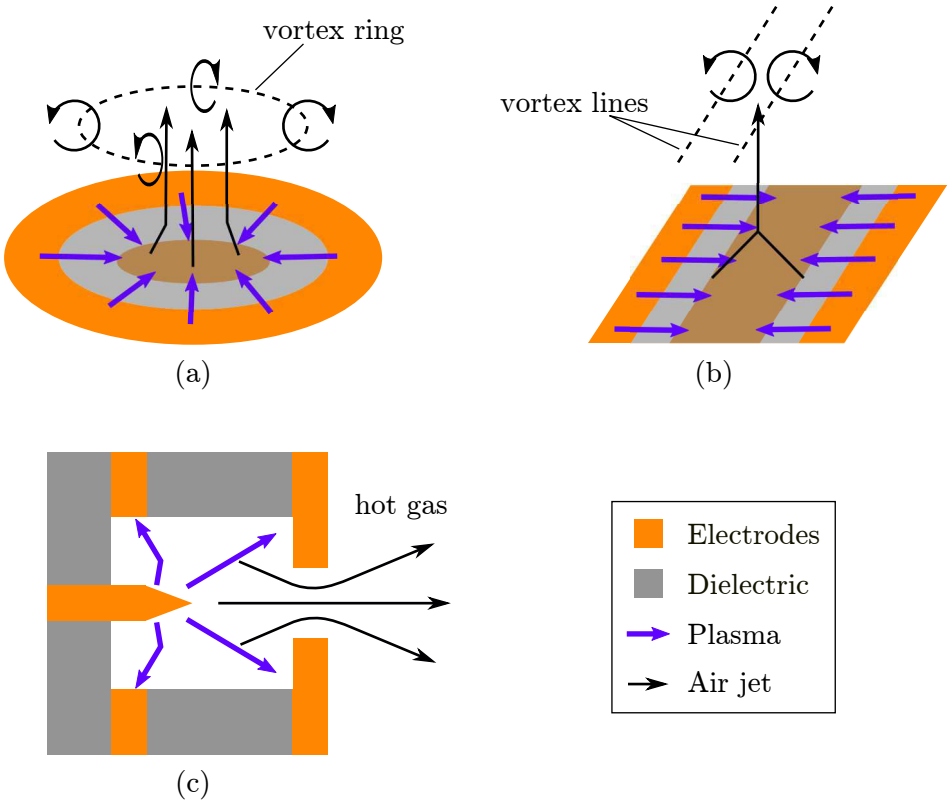

Figure 2.7: Plasma Synthetic Jet (PSJ) actuators: (a) ring actuator, (b) symmetrical linear actuator and (c) spark jet actuator.

[97, 98] and can produce almost supersonic exit velocities. Wang et al. [99] were able to visualise the shock-wave generated by a three-electrode spark jet actuator. The shock-wave spreads from the exhaust at the speed of sound. The jet then slows down, as a result of the mixing with the free air, leading to higher level of turbulence. However, such device still requires holes to be drilled in the wall. Moreover, the effects of spark jet actuators is very local due to their small size.

2.4.4 Nanosecond Pulse Actuator

The Nano-Second(-Pulsed) DBD (NS-DBD) actuators use the same geometry as regular DBDs, but are supplied with a high voltage consisting of a series of very short pulses. The fast heating of the gas near the exposed electrode generates micro-shock-waves that can interact with the boundary layer [39]. The criteria that determines whether the actuator is in an electro-hydrodynamic mode (i.e. DBD) or a shock-wave mode (i.e. NS-DBD) is the voltage slew rate. For NS-DBDs, the high-voltage discharge is usually realised within 10 to 100 ns. If heating implies power losses for DBDs, it is essential for NS-DBDs to work. The heating and corresponding density jump at the electrode results in the induced shock-wave being made visible using shadowgraphy [100]. It seems that positive voltage pulses are more efficient than negative ones. Benard et al. [100] also describe the different stages of a cycle. The shock-waves generated by the actuator were observed to travel at the speed of sound. Therefore, these actuators can be considered as aeroacoustic actuators and might reveal of interest for the control of boundary layer transition. Zhao et al. [33, 101] observed the shock-wave and flow generated by NS-DBDs. A semi-circular shock-wave is produced at the rear edge of the exposed electrode by the sudden discharge, and propagates. As the shock moves away from the wall, a weak vortex pair then forms near the centre of the shock. It was found that the higher the pulse amplitude in voltage, the stronger the shock wave, but also, the faster it decays. NS-DBDs do not need to be in a simple linear configuration. For instance, a sliding-discharge geometry can be used by connecting both exposed electrodes to the pulse source [102]. Such a configuration generates two interacting circular shock waves, each propagating from the edge of its native electrode.

2.4.5 Double Dielectric Barrier Discharge

Another evolution of the DBD actuator is the Double Dielectric Barrier Discharge (DDBD). In this configuration, both electrodes are encapsulated. Hoskinson et al. [67] determined that a HV wire electrode was also more efficient for DDBD devices. These actuators require a greater voltage so that plasma is formed. Due to the higher capacitance represented by the double encapsulation, the efficiency of the DDBD was found lower than for a DBD. In fact, the force production is up to five times lower with the DDBD actuators [58]. It was finally found that for both configurations, the force scales as an exponential of $-d/l$, where d is the active (HV) electrode diameter, and l is a fitting constant with the dimension of a length.

2.5 Three-Dimensional DBD and Plasma Array

The different plasma actuators discussed previously highlight the vast field of applications for these devices. If their 2D characteristics have been studied, several studies have also investigated three-dimensional configurations and their effects. These geometries, as it will be seen, can generate more complex flow-fields, and thus, may be used for different flow-control applications.

2.5.1 Plasma Vortex Generators

The previous studies focused on simple linear geometries blowing in quiescent air or parallel to the flow. Consequently, the induced flow-fields were two-dimensional. Nevertheless, 3D vortical flows can be obtained by changing the DBD orientation in the flow. For instance, Jukes et al. [103] utilised linear DBD actuators as Vortex Generators (VGs). This was achieved by changing the skew angle, i.e. between the directions of the wall jet and the free-stream. It was observed that the circulation addition from the plasma was linear along the DBD span. The greater the plasma velocity, the higher the induced circulation. Increasing the span of the device generated larger vortices. The optimum value of the skew angle was found to be 90° (actuator perpendicular to the flow). Several DBD vortex generators were assessed for two cases: counter- and co-rotating vortices. The circulation addition is lower for co-rotating vortices. However, they tend to spread more quickly over the chord than counter-rotating vortices. Hence, the effects of counter-rotating vortices are more localised. Overall, a counter-rotating configuration seemed more suitable, as long as the plasma velocity was at least equal to 20% of the free-stream velocity.

2.5.2 Serpentine DBD

Instead of placing localised vortex generators, it is also possible to design serpentine actuators. Riherd and Roy [104] define serpentine DBD actuators, as DBDs which shape are ruled by parametric function, periodic in some direction. Mainly, sine/circular, triangle and square wave-forms have been applied to the actuators, as represented in Figure 2.8. Wang et al. [105] and Roy and Durscher [106] investigated several kind of serpentine actuators in quiescent conditions. Their results proved that 3D designs greatly increase the plasma body force on the free air. For these configurations, pinching effects occur at the troughs, while spreading effects happen at the crests. The overall consequence is the creation of a vortical sheet (see Figure 2.9). Increasing the applied voltage was proven to induce a higher velocity without much changes in the velocity profile. It was also remarked that the power consumption of these actuators was higher than for linear geometries, which is not surprising since, for the same span, they present a greater wetted area. The jet angle in the pinching zone was found to scale with the maximum induced velocity by the plasma [104]. The shape of the actuator was found to mainly affect the reachable speed of the vertical component of the velocity

by the actuator [105]. The shape that induced the strongest vortical structure was the rectangle pattern. This can be explained by the fact that two plasma jets exactly face each other in this configuration, in a direction perpendicular to the flow-field. The sine pattern had slightly less ability to induce vertical velocity, and the triangle pattern generated slightly more vertical velocity than the simple linear actuator, but not as much as the circular and square geometries. Serpentine actuators present streaks having much higher velocities than DBD. This device was found to be efficient for several control cases. Sawtooth electrodes [107] and rake electrodes [108] have also been tested, and show similar results. They were successfully used for flow control at low Reynolds numbers.

(a) Circular. (b) Triangular. (c) Square.

Figure 2.8: Three common types of serpentine DBD actuators.

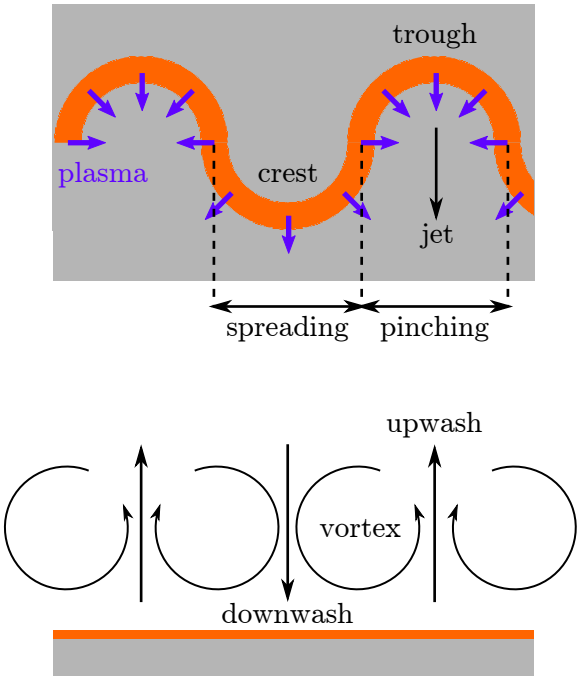

Figure 2.9: Schematic of the flow-field produced by a serpentine actuator: (top) horizontal jet and (bottom) vertical cross section of the vortical flow.

2.5.3 Plasma Array

DBD arrays (or cascades) consist of a succession of DBD actuators placed one behind another, so that the flow induced by one actuator interacts with the next stage. Roth [4] assessed several arrays and showed the validity of the concept for flow control on a NACA 0015 aerofoil. As previously explained (see 2.1.5), the peristaltic force can entrain the electrostatic wave across the stages of the array in order to improve the velocity generation.

Durscher and Roy [109] compared a DBD array with other DBD or MEE-DBD designs. When used in phase, several stages can actually reduce the force over consumed power ratio of the actuator. If placed face-to-face, two DBDs can be used as a PSJ [68]. In this case, the jet can be inclined at different angles by supplying the two stages with different input signals. Such configurations have also been investigated by Neretti et al. [95]. Only a two stage array was employed in the study, and could be set to blow in the same or opposite directions. The configuration in which the actuators blew in the same direction did not modify the maximum speed in the induced wall jet compared with a single actuator. However, this configuration increased the thickness of the wall jet. In the configuration with the discharges facing each other, a synthetic jet was observed perpendicular to the wall. The angle between the jet and the wall was tuned by modifying the voltage supplied to each of the actuators, and the authors found a relationship between the voltages supplied to each stage and the angle between the jet direction and the wall. A limited number of parameters have been assessed on arrays. It is sometimes observed that the thrust does not increase proportionally with the number of actuators [45]. But some simple control cases have shown it is possible to use plasma arrays for flow control. For instance, the damping of Tollmien-Schlichting waves have been demonstrated on a NACA aerofoil [110]. Placing the array in the span-wise direction on a plate (electrodes parallel to the chord), Whalley et al. [111] demonstrated it is possible to generate span-wise travelling waves within the turbulent boundary layer in order to influence turbulence events. The actuators were found to create stream-wise vortices in the near wall region, resulting in overall span-wise waves, and the creation of stream-wise ribbons of low speed in the viscous sublayer. Using a DBD actuator at its resonance frequency yields an increase in the maximum induced velocity and of the power consumption (see Section 2.1.5). Zadeh et al. [112] highlighted this frequency is modified when placing two DBDs in array. Thus, the optimisation of a single DBD do not lead to the optimisation of an array composed of different stages of this same DBD.

2.6 Flow Control Cases Using Plasma Actuators

Several studies have already highlighted the flow control abilities of DBD actuators. Because the maximum velocity they induce is currently relatively low (up to 8 to 10 m/s), these experiments and simulations are usually limited to low Reynolds numbers

(up to a few hundred thousands). Besides, modulating the signal can be quite useful for separation control, and decreases the power consumption of the actuator, as it is ignited for a shorter time on average. If the force production is unchanged or improved by the modulation, this can lead to a non-negligible enhancement of the actuator efficiency. An overview of plasma actuators for flow-control is given by Kriegseis et al. [113].

2.6.1 Boundary Layer Transition

Kurz et al. [110] utilised a modulated signal at the Tollmien-Schlichting wave frequencies to control the boundary layer transition on a symmetrical aerofoil. Since plasma actuators can be controlled at high frequencies, it was possible to move the transition upstream. Hence, such configurations could help to control separation at certain flight conditions. Similar conclusions were drawn numerically. It has been shown that DBDs are able to damp boundary layer streaks [114], by reducing the turbulent kinetic energy in the boundary layer. Plasma actuation is able to correct the surface discontinuities in the wing geometry (such as protruding panels leading to surface excrescence) [115]. In the work of Rizzetta et al. [115], the laminar flow region was widened, resulting in a drag reduction up to 70% of the uncontrolled case.

2.6.2 Separation Control

Benard et al. [116–118] placed a linear DBD actuator on a NACA 0015 aerofoil and determined that, even if quasi-steady actuation is able to tackle separation, an unsteady modulation at the natural frequency present in the flow is the most effective. The aforementioned natural frequency of the separation f_{sep} is defined as U_∞/L_{sep}, with U_∞ the free-stream velocity, and L_{sep} the length of the separated region. The modulation frequency f_{mod} was observed to produce the higher gain in lift and loss in drag when reaching the reduced frequency $F^+ = f_{\text{mod}}/f_{\text{sep}}$ of unity. The duty cycle for which this actuation was optimised was between 40 and 50%. The main effect of the control was to lock the structures convected in the wake of the wing at the control frequency. This led to organised Kelvin-Helmoltz instabilities accompanying the flow reattachment.

A linear DBD was used by Little et al. [119–121] to control the separation on the flap of a supercritical aerofoil. In agreement with Benard et al. [116–118], they determined that an unsteady actuation at the natural flow frequency of the separation on the flap ($F^+ = 1$) led to greater improvement than quasi-steady actuation. A duty cylcle in the range of 50% to 60% gave an optimised control. They concluded that an actuation at the hinge of the flap on the leading-edge of the flap is more effective than an actuation from the trailing-edge of the main element. Burst modulation was proven more effective as well than amplitude modulation to control flow separation on the flap.

Many other works tend to confirm these results [68, 107, 122–124]. The DBDs are useful only when placed near the point of turbulent separation, or slightly upstream. The actuation does not have any strong impact on the pre-stall regime. However, by delaying the occurrence of separation (at higher angle of attack), the actuator is able

to delay stall. In the post-stall regime, unsteady momentum transfer still improves the performance of an aerofoil.

Riherd et al. [104] and Rizetta et al. [125] simulated the flow-field around aerofoils equipped with serpentine actuators. In this configuration, unsteady actuation revealed more effective than quasi-steady blowing as well. A 45% duty cycle provided an optimised configuration. When comparing linear and serpentine DBD effects, it was found that linear DBD locked the structures in the flow-field at the modulation frequency, whereas the serpentine actuator did not. It instead moved the transition upstream, and added momentum to the flow through a vortical sheet. As explained previously, other devices, such as CD actuators [85, 86], were also proven to be able to tackle separation on an expansion corner.

Other applications focused on control over circular cylinder [126], backward-facing step [127], and delta wing [128]. In the different cases, separation control was possible, in order to either reduce the strength or cancel vortex shedding [126], reattach the flow sooner [127], or increase the lift in the post-stall region [128]. A linear DBD can also be set to act like a virtual Gurney flap [129], so that circulation is increased over the wing. To do so, the actuator needs to be placed to blow in a counter-flow configuration near the trailing edge of the aerofoil. Such a geometry triggers transition, thus, depending on the location of the device, other applications could arise.

2.6.3 Noise Control

Some groups focused on the control of noise around different bodies. For instance, Rossiter modes can be controlled in cavities, resulting in a reduction in both broadband and tonal noise [130]. Flow control is also possible around cylindrical bodies [96], in order to lock the vortex shedding. For instance, an attenuation of 5 to 10 dB has been reported by Kopiev et al. [131]. Chappel [132, 133] controlled the tip vortex on wings, and the noise generated by leading edge slats. The main tonal noise on the tested slat was reduced by 20 dB. A slight decrease of the wing tip broadband noise was also achieved. Another application consists in the control over wing sections [134]. The actuation led to a lowering of the tonal noise at the trailing edge, through the control of the boundary layer in the latter study. It should be remarked that the previous studies were limited to Reynolds number of a few hundred thousands, due to the lack of control authority of current DBDs.

2.6.4 Control System

The main issue for flow control with plasma actuators remains to find a suitable closed-loop model. After noticing the adverse effects of an airflow on the power consumption, Kriegseis et al. [135] utilised the power consumption of the actuator as a feedback for its control, in order to adapt to changes in the free-stream velocity. However, this control revealed inefficient for strong velocity variations. It was latter concluded that the drop in control authority with increasing free-stream airspeed must be considered in a

control strategy, as DBDs are typically tested at low velocities [77]. By using arrays of skin-friction sensors, Hanson et al. [136] were able to control boundary layer streaks at different free-stream velocities using a Proportional-Integral (PI) controller. The same results were obtained by Dadfar et al. [137], who used a numerical approach to show the ability of their system to control the streaks. A slope-seeking model was utilised experimentally by Benard et al. [138]. Their closed-loop model relied on lift measurements, in order to control the applied voltage amplitude. If the results showed some robustness for the tested configuration (adaptation to step changes in the Reynolds number), the lift force is not an obvious quantity that can be recorded in flight. Dandois and Pamart [139] numerically implemented a control system using a wall pressure sensor providing a feedback from the wake of the actuator on an expansion ramp to control separation. More recently, Francioso et al. [140, 141] achieved successful flow control around a turbine blade model, using a DBD coupled to a micro-mechanical capacitive pressure sensor. The turbulence intensity was attenuated, leading to a reduction of the separation area. The small size of the sensor and its accuracy makes it a viable choice for future applications.

2.7 Flow Control Cases Using Other Devices

If plasma actuators are relatively recent in their application for flow control, other techniques have already been studied for decades. Particularly, blowing slots have been commonly focused on in numerous applications. In order to confirm the viability of plasma actuators for flow control, it is necessary to compare them with these other flow control devices.

Ternoy et al. [142] introduced several flow control techniques investigated at ONERA over several years. They can be classified into two categories: mechanical and fluidic actuators. Mechanical actuators control the flow through the interaction with a solid boundary (e.g. deployable VG) whereas fluidic actuators only control the flow by injecting or sucking gas from the flow-field. The main disadvantages that can be found for most of these actuators is the need to alter the internal structure, in order to integrate them to the wing.

Blowing slots have been particularly studied in the past decades [143–146]. It was shown that the most effective locations for introducing the excitation are the leading edge of the main element, and the leading edge of the flap. It also appeared that unsteady actuation is more beneficial than steady blowing, and that the optimal frequency is usually the natural frequency of the flow (i.e. $F^+ = 1$). The required momentum addition to reattach the flow can be significantly less with an unsteady actuation. It was brought forward that the reduced frequency makes more sense when based on the length of the separated region (L_{sep}, or the distance between the separation point and the leading-edge, since they are more indicative of the periodic phenomena occurring in the flow. However, Brunet [144] remarked that a higher actuation frequency was most suitable in their case to reach a full reattachment. The effects of the two jet

velocity components were analysed for 2D cases. The vertical component of the velocity is responsible for the formation of vortices, while the tangential component adds momentum to the boundary layer. For non-zero skew angles, the lateral component acts as a cross-flow, thus leading to the formation of vortices. Naveh et al. [147] assessed simple analytical models to determine the actuation that must be applied on a three-dimensional case, from two-dimensional data. These models were validated, and it was concluded that the sweep angle does not have an adverse effect on the control of separation. Seifert and Pack [148] reported that the control was not as efficient in transonic flows, and could even prove detrimental. Indeed, the blowing slot tends to generate a shock wave when actuated in this situation. Moreover, to be applied on actual aircraft configurations, any flow control device would have to accommodate to the sweep angle. It is usually agreed that flow control is more effective at low Reynolds number [146, 148].

Greenblatt et al. [149] presented the results of several past experiments. Acoustic excitation, flapping ailerons and blowing slots were investigated. Overall, it seemed that actuation at the natural frequency present in the flow is more effective (vortex shedding, boundary layer instabilities, etc.). Nevertheless, higher frequencies reduce the need for addition of momentum, or allow the separation to be controlled when the flap angles are large. Yet, at over ten times the natural frequency of the flow, the actuation did not bring any improvement. The effects of the actuation were predominantly seen in post-stall regime. Finally, it was concluded that the optimum excitation frequency does not depend on the Reynolds number.

These results and the findings described in Section 2.6.2 show good agreement, confirming DBD actuators could be used in replacement of other type of devices, given they can reach at least the same flow control abilities. It is clear that plasma actuators share similar behaviour with other fluidic or mechanic flow control devices. If the way they induce momentum in the flow differs, the flow-control abilities of the DBDs are comparable to those of other types of actuators. For instance, the device increases in control authority when placed in the vicinity of the point of flow separation, e.g. for a flap, on its leading-edge. Unsteady actuation is much more efficient for flow control, and the optimal actuation frequency is the natural flow frequency (i.e. $F^+ = 1$). The actuation does not have much effect in the pre-stall regime, but can greatly improve the performance of an aerofoil at post-stall angles of attack. Plasma actuators also showed their ability to control boundary layer transition.

2.8 Summary

Overall, the DBD actuators can be used for the same applications as other flow control devices (e.g. jets, piezoelectric devices, micro-flaps), but they have less constraints in their installation. However, DBDs are currently too weak for full scale applications. Moreover, the present scaling laws are not widely used, or verified. Nevertheless, scaling laws would mean a better understanding of the DBD actuators. They would also make

it easier to design DBDs for particular flow control applications. Also, studies on DBDs and MEE-DBDs have shown that the performance of the actuators for flow control are impacted by two-factor interactions between electric and geometric parameters. However, all the possible interactions were not systematically investigated. All the reported effects of the design parameters of DBDs on the flow control ability lack a general ranking as well, in order to determine the parameters of primary importance to optimise DBDs for particular application. In addition, it would be beneficial to provide a complete baseline, for comparison with further improvements brought to DBDs (such as MEE-DBDs). Thus, it was decided to perform a parametric study, in which different geometric and electric parameters will be varied, in order to improve the understanding of their independent, and coupled, effects on the behaviour of the single linear AC-DBD actuator (simply called DBD in the rest of the study).

Chapter 3

Presentation of the Analytical Method

In the present chapter, the analytical method used in this study is explained. First, the informations found in the literature and relevant to the present study are summarised to highlight the more significant design parameters. Secondly, the input and output variables of the problem are introduced, in order to provide the frame of the study. Thirdly, the chosen analytical method is discussed. Its usage is justified in relation to the objectives of the present work, and its main features are briefly presented. Finally, the analytical method is fully explained, so that its underlying principles can be understood. The different mathematical processes are presented, and are illustrated by simple examples.

3.1 Introduction to the Parametric Study

3.1.1 Summary of the Literature

As seen in Section 2.3, different parameters affect the electric and fluid mechanic characteristics of DBDs. The thrust and power consumption depend on the plasma formation. Thus, it is reasonable to assume they are both influenced by the characteristic capacitances of the DBD, C_0 before ignition and C_{eff} after ignition. The capacitance is function of the geometry of the DBD, of the utilised material, and of the electrical input. Moreover, the plasma formation is also impacted by atmospheric conditions such as the humidity, the nature of the gas, the static pressure, and the free-stream velocity. Some interactions between the design parameters are discussed in the literature. However, there has not been a systematic study of all of the interactions. Moreover, the effects of all the parameters and interactions have not been given a ranking, in order to determine the leading phenomena for the optimisation of the DBD actuator. Mostly, different studies focus on a small subset of parameters at a time. The present study compares different DBD configurations, in order to improve the knowledge on the effects of several geometrical and electrical parameters on the DBD performance,

and to determine which of these parameters are of primary importance when designing such an actuator. First, let us summarise the different effects of the parameters on the thrust generation and power consumption of the DBD, that are reported in the literature. For more details, the author encourage the reader to refer to Section 2.3.

3.1.1.1 Thrust Generation

The major effect on the thrust generation that is reported in the literature belongs to the voltage. Numerous authors [41, 45, 59, 66, 69–73] observed the thrust that is induced by the DBD increases for a greater voltage. A growth in the frequency of the signal was also determined to increase the thrust [45, 69, 70]. The geometry was found to impact the thrust significantly. A wire electrode was particularly captured to create more thrust than a rectangular electrode, and the lower the diameter, the greater the thrust [7, 59, 66]. The encapsulated electrode was not determine to influence the thrust generation significantly. The encapsulated electrode was determined to importantly influence the thrust only if it constrains the plasma [7, 45, 68–70]. In such cases, the thrust increases as the electrode becomes wider, until reaching a plateau. An inter-electrode gap of 0 to 5 mm was observed to increase the thrust generation [69, 70]. A negative or greater gap led to a loss of thrust. A thin dielectric proved to increase the generation of thrust at fixed voltage [69], but a higher voltage can be applied on a thick dielectric, which results in a greater thrust generation [45]. Besides, this parameters interact with the permittivity of the dielectric, the voltage and the frequency, through the saturation of the DBD [45]. At saturation, the thrust cannot be further increased with higher voltages or frequencies. Lower saturation voltage and frequency are obtained with thicker dielectric or higher permittivity. However, a stronger dielectric (thicker or of high permittivity) can sustain a stronger voltage before reaching its electric breakdown. Consequently, the ranking of the effects of the voltage, frequency, dielectric thickness and permittivity needs to be determined, in order to conclude on which combinations parameters generates the more thrust. Finally, mainly two atmospheric conditions have been reported to affect the thrust. A higher free-stream velocity was proved to decrease the plasma extent and consumed power of the DBD [12, 76], and the thrust was found to reach a maximum value at an atmospheric pressure between 750 and 800 hPa [65]. The scaling laws of the thrust generation against the design parameters that have been reported in the literature are summarised in Table 3.1.

Several works focused on the maximum velocity reached by the wall jet that is induced by the actuators. A greater velocity is the sign of a greater momentum transfer of the plasma to the airflow. Consequently, a higher maximum velocity can be linked to a greater thrust generation. The maximum induced velocity was found to increase with a higher voltage [1, 3, 7, 8, 41]. The maximum velocity was also determined to increase with a higher frequency [45, 69, 70]. Finally, a thin dielectric layer was observed to increase the maximum velocity [41, 69, 70]. The scaling laws of the thrust generation and maximum velocity against the design parameters that have been reported in the

literature are summarised in Table 3.1.

Parameter	Scaling law	References
Voltage V	$T_A \propto V^{2.3}$ if $V > 50$ kV_{pp}	[45]
Voltage V	$T_A \propto V^{3.5}$ if $V \leq 50$ kV_{pp}	[45]
Voltage V	$T_A \propto V^{3.5}$	[3]
Voltage V	$T_A \propto V^a$ with $3.6 \leq a \leq 4.6$	[41]
Voltage V	$u_{max} \propto V^a$ with $2.4 \leq a \leq 3.5$	[41]

Table 3.1: Reported scaling laws of the thrust generation T_A and maximum induced velocity u_{max}.

3.1.1.2 Power Consumption

In different studies, the power consumption was typically affected by the same parameters that influence the thrust generation. A greater voltage increases the power consumption [1, 3, 5, 7, 8, 46]. A higher frequency also results in an increase of the power consumed by the DBD [7]. The power reduces with a thicker dielectric layer [41]. The geometry of the exposed electrode was found to influence the power consumption. A wire electrode was utilised and a lower diameter increased the power consumption [66] and the force over power ratio [67]. Therefore, the width and thickness of the air electrode can be expected to have a greater impact on the thrust generation than on the power consumption. The atmospheric pressure also affects the power, with a lower consumption at higher pressure [59, 72]. Finally, a greater humidity was determined to decrease the power consumption below 85% of relative humidity [73]. The behaviour is unclear over 85%, due to the test conditions of the study.

Parameter	Scaling law	References
Voltage V	$P_A \propto V^a$ with $3.35 \leq a \leq 3.42$	[1]
Voltage V	$P_A \propto V^2$	[5, 46]
Voltage V	$P_A \propto V^{3.5}$	[7, 41]
Voltage V	$P_A \propto V^{3.35}$	[8]
Frequency f_{ac}	$P_A \propto f_{ac}^{1.5}$	[7]
Dielectric thickness t	$P_A \propto 1/t$	[7]

Table 3.2: Reported scaling laws of the power consumption P_A.

3.1.1.3 Atmospheric Conditions

If the effects atmospheric conditions are not considered in present study, they were found to impact the performance of DBDs. Consequently, it is necessary to determine the possible noise these parameters generate in the data, because they are uncontrolled parameters. Unsurprisingly, the nature of the gas is of critical importance to the

plasma formation. More electronegative species, such as oxygen, tend to decrease the power consumption of the actuator [75]. The power consumption is reduced, and the maximum induced velocity is increased for an increasing humidity up to 70-85% [73]. The density of air is also altered by humidity. A more precise relationship than the usual ideal gas law is used to derive the density. As described in the book of Barlow et al. [150]:

$$\rho_0 = \left(\frac{0.0034847}{T_0}\right)\left(p_0 - 0.003796 \times H_0 \times e_s\right) \ , \tag{3.1}$$

where T_0 is the ambient temperature in K, p_0 is the atmospheric pressure in Pa, H_0 is the relative humidity in %, and e_s is the saturation vapour pressure given by the formula:

$$e_s = 1.7526 \times 10^{11} \times \exp\left(\frac{-5315.56}{T_0}\right) \ . \tag{3.2}$$

In the case of an inflow in a co-flow configuration, it has been determined that the momentum transfer from the plasma to the free gas is reduced [77]. However, when including the effect of skin friction, it appears the actuator could be more effective as the reduction in skin friction can be greater than the loss of plasma force [12]. Kriegseis et al. [77] suggested the use of the number K for scaling the actuator parameters in a moving free-stream:

$$K = \frac{U_\infty}{v_\mathrm{d}} \ , \tag{3.3}$$

where v_d represents the drift velocity. It can be estimated through:

$$v_\mathrm{d} = \kappa \frac{V}{t} \ , \tag{3.4}$$

where t is the dielectric thickness, V the applied voltage amplitude and κ the ion mobility. The higher the K number, the more the DBD looses its capacity to generate a force.

In order to scale the ion mobility with the atmospheric pressure and humidity, an equation can be derived from the work of Asano et al. [78], in which the ion mobility is scaled for different atmospheric conditions. The reference is taken as 40% humidity and 743 Torr (990.6 hPa) where $\kappa \approx 2.0 \times 10^{-4}\,\mathrm{m^2/(V{\cdot}s)}$. Based on the mobility versus humidity plot, on average, a gain of $6.6 \times 10^{-7}\,\mathrm{m^2/(V{\cdot}s)}$ is observed for every percent loss of relative humidity. A square fit is also employed to determine the trend of the ion mobility versus pressure curve. By taking the aforementioned reference point into consideration, it is approximated that:

$$\kappa \approx \left[2.00 + 6.60 \times 10^{-3}\left(40 - H_0\right) + 4.47 \times 10^{-6}\left(p_0^2 - 990.6^2\right) + \ldots \right.$$
$$\left. \ldots - 1.10 \times 10^{-2}\left(p_0 - 990.6\right)\right] \times 10^{-4} \ , \tag{3.5}$$

where p_0 is the atmospheric pressure in hPa, and H_0 is the relative humidity in % of relative humidity.

The K number can be coupled to the electro-hydrodynamic number N_EHD [80, 81],

in order to scale the impact of the DBD force into the airflow:

$$N_{\mathrm{EHD}} = \frac{\langle I \rangle}{\kappa L \rho_0 U_\infty^2} \ , \tag{3.6}$$

where $\langle I \rangle$ is the time average of the electrical current, L is the span of the electrodes, ρ_0 is the density of the air, U_∞ is the free-stream velocity, and κ is the ion mobility. The electro-hydrodynamic number represents the ratio of the electrical body force over the inertial force. If it is close to zero, the inertial force dominates, and the fluid is unaffected by the discharge. The greater the number, the greater the impact of the ionic wind on the surrounding gas.

3.1.1.4 Unexplored Parameters

Other parameters have not been investigated. For instance, the effect of turbulence on the effectiveness and efficiency of the DBDs has not been studied. However, given the current findings regarding the performance of DBDs in the presence of a free-stream, it could be interesting to investigate the scaling of the power consumption and thrust generation based on a K_{turb} parameter. This modified K number depends on the fluctuation velocity u' instead of the mean free-stream velocity U_∞ (see Equation 2.21).

Besides, the sound field generated by DBDs is not systematically assessed. Particularly, the correlation of the noise generation with the power consumption and thrust generation is necessary in order to make conclusions on the noise control abilities of the DBD.

3.1.2 Geometric and Electric Design Parameters of the DBD

Many parameters can have significant effects on the flow control performance of the actuator (see Figure 2.1 on page 6):

- Geometric parameters: the height and width of the exposed (h_1 and w_1) and encapsulated (h_2 and w_2) electrodes, the thickness of the dielectric (t), the shapes of the electrodes and gap between the electrodes (g).

- Material parameters: the resistivity of each of the electrodes and the relative permittivity of the dielectric ε_r.

- Electric parameters: the frequency (f_{ac}), the peak to peak amplitude of the voltage (V), and the waveform (duty cycle, rise time, fall time, function).

As a result, if the shape of the electrodes is not modified (use of wire or mesh electrodes for example), this would result in the investigation of fifteen independent parameters.

The DBDs are made by using common Printed Circuit Board (PCB) processes and materials, in order to make sure the production of all actuators stays consistent. Thus, the available values for the different parameters are limited to a few discrete levels. The electrode material can only be copper, due to the difficulty to replace this metal,

and due to the low importance of this parameter for the thrust generation and power consumption of the actuator [67]. Moreover, the investigation of the waveform is not included as part of the present Design of Experiment (DOE) study, and the work focuses on a standard sine-wave. This choice is motivated by the wider ranges of references that focus on sine-waves, allowing for more significant comparisons of the findings with the literature. It can be noted a negative going triangle wave could further improve the performance of the DBDs for flow control [2].

In conclusion, nine factors are retained in the present study: h_1, h_2, t, w_1, w_2, g, ε_r, V and f_{ac}. A summary of the high and low values is found in Appendix A (Table A.1). The chosen high and low values are discussed in chapter 4 with the description of the utilised experimental apparatus.

3.1.3 Output Parameters of the Parametric Study

The raw parameters, that are measured with the test rig, are the induced thrust Γ_{A} (in mN), the real time voltage V (in kV) and current I (in mA). From these measurements, the three output parameters analysed in the study can be determined.

The thrust Γ_{A} directly provides the information on the momentum injection ability of the actuator. A higher thrust indicates a greater momentum transfer to the surrounding gas. By recording the thrust, the friction losses occurring on the surface of the DBD are taken into account in the results.

By definition, the power consumption Π_{A} is derived by integration of the product of current and voltage over n period(s):

$$\Pi_{\mathrm{A}} = \frac{f_{\mathrm{ac}}}{n} \int_0^{n/f_{\mathrm{ac}}} V(t) \cdot I(t)\, \mathrm{d}t \ . \tag{3.7}$$

Thereafter, both parameters can be combined to get the force efficiency η_{A}:

$$\eta_{\mathrm{A}} = \frac{\Gamma_{\mathrm{A}}}{\Pi_{\mathrm{A}}} \ . \tag{3.8}$$

For more representative results, it is typical to scale these quantities with the span of the electrodes L. Hence, the study focuses on the thrust generation per unit span T_{A} (in mN/m), the power consumption per unit span P_{A} (in W/m) and force efficiency η_{A} (in μN/W) defined by:

$$T_{\mathrm{A}} = \frac{\Gamma_{\mathrm{A}}}{L} \ , \tag{3.9}$$

$$P_{\mathrm{A}} = \frac{\Pi_{\mathrm{A}}}{L} \ , \tag{3.10}$$

$$\eta_{\mathrm{A}} = \frac{T_{\mathrm{A}}}{P_{\mathrm{A}}} \ . \tag{3.11}$$

3.2 Design of Experiment Approach

3.2.1 Motivation

A high number of parameters are assessed in the parametric investigation. Moreover, they can only take certain discrete values. Due to the time required to manufacture all the necessary actuators, and to minimise uncertainties associated with manufacturing, they all need to be produced in advance. As a result, many optimisation processes involving the creation of the different DBDs as the data are collected are excluded. With the high number of parameters included in the study, a Response Surface Method (RSM) would lead to more than 150 actuators and tests, which is practically infeasible. Therefore, it has been decided to use a Design of Experiment (DOE) approach. The method provides a ranking of the effects of the design parameters on the chosen output variables. It can both rank previously observed trends and highlight new phenomena. Moreover, the DOE method draws simple mathematical modelling of the output variables, even though it is unable to fully capture complex non-linear mathematical laws between the input and output parameters.

The following sections provide the details of the selected method. If the reader requires an insight in the general process of the Design of Experiment, an introduction is presented in section 3.3, and applied to a simple example. The practical design of the DBDs and the chosen values for each of the parameters are discussed in Section 4.1.1.

3.2.2 Employed Design

The main objective of a DOE study is to determine the effects of different parameters (typically called factors) on a desired output variable, especially in the presence of hard-to-change parameters, that can only take predefined values. In this study, this means by assessing the effects of the previously mentioned nine parameters on the thrust generation and power consumption of a DBD actuator. One of the advantage of DOE is its relatively small test matrix, allowing to study many parameters. It is typically utilised at the beginning, so that the significant effects and factors can be determined. More advanced methods can be used subsequently to focus on the significant factors alone.

The DOE works by assigning two values (typically called levels) to each parameter. A test matrix is derived to assess all the possible combinations of low and high values of the different parameters. In the case where all the possible combinations of values of the factors are included in the test matrix, the design is called a full factorial design. A full 2-level factorial design grows as 2^n sets of values of the factors, with n being the number of factors. One set of levels of the factors is usually called a run. For the nine parameters that are retained, the test matrix would reach 2^9 independent runs, so 512 tests. This number of runs is impractical, since it requires a large number of actuators, and a long time to acquire all the data, specifically if the tests are repeated for greater accuracy. The solution to the problem consists in using a fractional factorial design.

3.2.3 Fractional Experiment and Aliasing

A fractional factorial design can be built by allowing certain effects to be confounded. The confounding (also called aliasing) occurs if the analysis of the DOE cannot determine whether an effect is the results of one or another parameter. For a typical two-level full factorial designs of n factors, the total number of needed tests is 2^n. For a fractional design, the test matrix is fractioned by a power of two, named k, so results 2^{n-k} runs instead. A run is a particular set of values of the factors. For instance, for a three factor design, if a one-half fraction is used, the number of runs is 2^{3-1} or 4, instead of a full factorial design of 8.

It is typical to rank the different designs by resolution, given in Roman numerals. The resolution gives the level of aliasing that exists in the study. The chosen design is a sixteenth fraction. In total, it includes 2^{9-4} so 32 runs. This design corresponds to a resolution of IV. This means that main effects are confounded with three-factor interactions, and that two-factor interactions can be confounded with other two-and three-factor interactions. The main effects are the effects of the isolated parameters. The two-factor interactions arise when the influence of one factor on the output parameter depends on one other interacting factor. Similarly, a three-factor interaction occurs if the influence of one factor on the output parameter depends on the other two interacting factors. The program Minitab is utilised to draw a randomised test matrix from a standard Plackett-Burman design, applied to the given nine factors. The software provides the alias table for the chosen design. The alias table is given in Table 3.3. It highlights the main effects (of single parameters), but also two-factor interactions and three-factor interactions that are confounded. The three-factor interactions are highlighted in red in the table, but are not focused on in this study. The main effects and two-factor interactions are respectively highlighted in blue and green. For instance, the main effect of the height of the encapsulated electrode h_2 is not aliased with two- and three-factor interactions. On the other hand, the interaction between the widths of both electrodes $w_1 \times w_2$ is aliased with the interaction between the dielectric thickness and permittivity $t \times \varepsilon_r$. The table is not fully analysed here, however, the aliases are discussed in the analysis of the results. The test matrix is presented in Table A.2.

3.2.4 Test Matrix

The created test matrix is randomised to reduce the possibility that an unexpected outside parameter (eg. atmospheric condition) impacts the results. Consequently, every actuator is referenced by a standard non-randomised number (shortened as "Std. No." in Table A.2), and a randomised run number (shortened as "Run No." in Table A.2). Unless stated otherwise, the randomised run numbers is used to refer to each run. In total, 32 runs are required to reach the desired resolution (Runs 1 to 32). Each one of these runs is repeated two more times, in order to raise the confidence in the results. The repeats simply consist in the same test matrix repeated twice (Runs 33 to 96). When planning the experiments, one obvious possible external variable that

Main effects								2-factor interactions								3-factor interactions			
w_1	+	$w_2 \times t \times \varepsilon_r$	+	$g \times t \times V$	+	$h_1 \times t \times f_{\mathrm{ac}}$													
w_2	+	$w_1 \times t \times \varepsilon_r$	+	$g \times \varepsilon_r \times V$	+	$h_1 \times \varepsilon_r \times f_{\mathrm{ac}}$													
g	+	$w_1 \times t \times V$	+	$w_2 \times \varepsilon_r \times V$	+	$h_1 \times V \times f_{\mathrm{ac}}$													
h_1	+	$w_1 \times t \times f_{\mathrm{ac}}$	+	$w_2 \times \varepsilon_r \times f_{\mathrm{ac}}$	+	$g \times V \times f_{\mathrm{ac}}$													
h_2																			
t	+	$w_1 \times w_2 \times \varepsilon_r$	+	$w_1 \times g \times V$	+	$w_1 \times h_1 \times f_{\mathrm{ac}}$													
ε_r	+	$w_1 \times w_2 \times t$	+	$w_2 \times g \times V$	+	$w_2 \times h_1 \times f_{\mathrm{ac}}$													
V	+	$w_1 \times g \times t$	+	$w_2 \times g \times \varepsilon_r$	+	$g \times h_1 \times f_{\mathrm{ac}}$													
f_{ac}	+	$w_1 \times h_1 \times t$	+	$w_2 \times h_1 \times \varepsilon_r$	+	$g \times h_1 \times V$													
$w_1 \times w_2$	+	$t \times \varepsilon_r$	+	$g \times h_2 \times f_{\mathrm{ac}}$	+	$h_1 \times h_2 \times V$													
$w_1 \times g$	+	$t \times V$	+	$w_2 \times h_2 \times f_{\mathrm{ac}}$	+	$h_1 \times h_2 \times \varepsilon_r$													
$w_1 \times h_1$	+	$t \times f_{\mathrm{ac}}$	+	$w_2 \times h_2 \times V$	+	$g \times h_2 \times \varepsilon_r$													
$w_1 \times h_2$	+	$w_2 \times g \times f_{\mathrm{ac}}$	+	$w_2 \times h_1 \times V$	+	$g \times h_1 \times \varepsilon_r$	+	$\varepsilon_r \times V \times f_{\mathrm{ac}}$											
$w_1 \times t$	+	$w_2 \times \varepsilon_r$	+	$g \times V$	+	$h_1 \times f_{\mathrm{ac}}$													
$w_1 \times \varepsilon_r$	+	$w_2 \times t$	+	$g \times h_1 \times h_2$	+	$h_2 \times V \times f_{\mathrm{ac}}$													
$w_1 \times V$	+	$g \times t$	+	$w_2 \times h_1 \times h_2$	+	$h_2 \times \varepsilon_r \times f_{\mathrm{ac}}$													
$w_1 \times f_{\mathrm{ac}}$	+	$h_1 \times t$	+	$w_2 \times g \times h_2$	+	$h_2 \times \varepsilon_r \times V$													
$w_2 \times g$	+	$\varepsilon_r \times V$	+	$w_1 \times h_2 \times f_{\mathrm{ac}}$	+	$h_1 \times h_2 \times t$													
$w_2 \times h_1$	+	$\varepsilon_r \times f_{\mathrm{ac}}$	+	$w_1 \times h_2 \times V$	+	$g \times h_2 \times t$													
$w_2 \times h_2$	+	$w_1 \times g \times f_{\mathrm{ac}}$	+	$w_1 \times h_1 \times V$	+	$g \times h_1 \times t$	+	$t \times V \times f_{\mathrm{ac}}$											
$w_2 \times V$	+	$g \times \varepsilon_r$	+	$w_1 \times h_1 \times h_2$	+	$h_2 \times t \times f_{\mathrm{ac}}$													
$w_2 \times f_{\mathrm{ac}}$	+	$h_1 \times \varepsilon_r$	+	$w_1 \times g \times h_2$	+	$h_2 \times t \times V$													
$g \times h_1$	+	$V \times f_{\mathrm{ac}}$	+	$w_1 \times h_2 \times \varepsilon_r$	+	$w_2 \times h_2 \times t$													
$g \times h_2$	+	$w_1 \times w_2 \times f_{\mathrm{ac}}$	+	$w_1 \times h_1 \times \varepsilon_r$	+	$w_2 \times h_1 \times t$	+	$t \times \varepsilon_r \times f_{\mathrm{ac}}$											
$g \times f_{\mathrm{ac}}$	+	$h_1 \times V$	+	$w_1 \times w_2 \times h_2$	+	$h_2 \times t \times \varepsilon_r$													
$h_1 \times h_2$	+	$w_1 \times w_2 \times V$	+	$w_1 \times g \times \varepsilon_r$	+	$w_2 \times g \times t$	+	$t \times \varepsilon_r \times V$											
$h_2 \times t$	+	$w_2 \times g \times h_1$	+	$w_2 \times V \times f_{\mathrm{ac}}$	+	$g \times \varepsilon_r \times f_{\mathrm{ac}}$	+	$h_1 \times \varepsilon_r \times V$											
$h_2 \times \varepsilon_r$	+	$w_1 \times g \times h_1$	+	$w_1 \times V \times f_{\mathrm{ac}}$	+	$g \times t \times f_{\mathrm{ac}}$	+	$h_1 \times t \times V$											
$h_2 \times V$	+	$w_1 \times w_2 \times h_1$	+	$w_1 \times \varepsilon_r \times f_{\mathrm{ac}}$	+	$w_2 \times t \times f_{\mathrm{ac}}$	+	$h_1 \times t \times \varepsilon_r$											
$h_2 \times f_{\mathrm{ac}}$	+	$w_1 \times w_2 \times g$	+	$w_1 \times \varepsilon_r \times V$	+	$w_2 \times t \times V$	+	$g \times t \times \varepsilon_r$											

Table 3.3: Alias table for the present study.

could potentially impact the results, is the presence of the epoxy glue to join the runs presenting different electrode thickness (further detailed in Section 4.1.1). An Analysis of Variance (ANOVA) (explained in Section 3.3.5) can indicate whether the presence of the glue has an effect on the results.

The following section provides a detailed explanation of the DOE method, the mathematical processes underlying it are developed and applied to a simple example.

3.3 Introduction to the Design of Experiment Method

This section provides a brief introduction to the Design of Experiment (DOE). It is based on the book of Anderson and Whitcomb [151]. The features relevant for the present work are detailed, in order to ease the understanding of the analysis of the results in the next chapter.

3.3.1 Factors, Levels and Designs.

The goal of the DOE analysis is to determine the effects of different parameters (generally called **factors**) on an output variable (usually called **response**). The factors are each assigned a low and a high values (named **levels**). It is usual to express the levels in their coded unit: -1 for the low level and $+1$ for the high level. The analysis of the results is commonly performed on the coded units. This use of only two levels for each factor is practical when studying **hard-to-change** factors, which are factors that can only take a set of discreet values.

The next step in the DOE is to derive a test matrix. This is performed by choosing a **design**, as it has been presented in Sections 3.2.2 and 3.2.3. A fractional factorial design is usually preferred to a full factorial design, because it reduces the number of runs that are required to perform the analysis. Plackett-Burman designs are commonly employed. These are drawn by allowing any possible combination of levels of any pair of factors to occur the same number of times in the test matrix. An example of Plackett-Burman design is given in Table 3.4 for four factors (A, B, C and D) having two levels ($+$ and $-$). In the table, for example, the four possible combinations of levels ($++$, $+-$, $-+$, $--$) for the pair B and C are each present three times.

After a design is obtained, it is common to randomise the runs, as for the design displayed in Table 3.4. Randomisation is a first step towards avoiding an external unforeseen phenomenon to affect the results. This is further described in the next section.

3.3.2 Confounding and Protection against External Sources of Errors.

The first risk of utilising a standard design in its original run order, is due to the repetitive pattern existing in the non-randomised design. One run originally differs from its predecessor from only a few levels. If an uncontrollable and/or unexpected external parameter was to affect the output variable (eg. atmospheric conditions), two

A	B	C	D
+	+	+	−
−	−	−	+
+	+	−	+
+	−	+	−
−	−	−	−
−	+	+	−
−	+	−	−
+	−	−	−
−	−	+	+
−	+	+	+
+	−	+	+
+	+	−	+

(a)

A	B	C	D	A	B	C	D
+	+	+	+	...	...	...	...
+	+	+	−	−	+	+	+
+	+	−	+	−	+	+	−
+	−	+	+	−	+	−	+
+	+	−	−	−	−	+	+
+	−	+	−	−	+	−	−
+	−	−	+	−	−	+	−
+	−	−	−	−	−	−	+
...	...	...	...	−	−	−	−

(b)

Table 3.4: Plackett-Burman (a) and full factorial (b) design for four factors and two levels.

successive runs would show a difference that would be attributed to the small number of changing factors. The randomisation of the runs avoids repeating patterns in the final test matrix. Consequently, a possible external parameter is more likely to affect the results for very different runs, and ends up being treated as noise in the results.

Another possibility if the external parameter(s) can be identified consists in using blocks. The data of each block are corrected by subtracting the difference between the mean of the subset of data of the block and the grand average of the full set of data. It is however difficult to judge how the blocks should be designed for the current study. The risk is ending with too many blocks, leading to an over-correction of the results.

In order to increase the accuracy of the results, the runs can simply be repeated. For instance, the runs are tested three times in the current work. This number of repeats keeps the size of the test matrix below a hundred runs, which is the maximum of tests that can be realised with the test rig in the time frame of the study.

The main deficiency of DOE is its limitation to linear relationships between the input and output parameters. A direct consequence of choosing two levels for each factor is the lack of information between the two extrema. A situation where the output variable has a non-linear trend between two points is not rare. One method to provide some information about non-linearity in the response over the tested ranges is by introducing centre points. They are special runs with all level set at the midrange value. They avoid using an expensive three level design, but provide an insight into whether the response follows a linear trend between the two levels for every factors. They are nevertheless difficult to realise if several factors are difficult to change (i.e. can only take discreet values).

Employing a fractional factorial design has one primary drawback that is **aliasing** (or confounding). First the notion of **interaction** must be explained. Mathematically, an interaction between several factors arises when the product of these interacting

factors modifies the response significantly. In the results, an interaction is visible when the effect produced by one factor is different when an interacting factor jumps from one level to the other. For example, let us consider an experiment of measuring the weight on two objects of distinct mass on the Earth and the Moon. From Newton's second law, the weight increases linearly on both astronomical bodies, but at different rates:

$$W = m \cdot g_0 \ , \tag{3.12}$$

where W is the weight of the object, m is its mass and g_0 is the local acceleration of free fall of the astronomical body. If the factors of the experiment are the gravitational accelerations at the surface of the bodies and the masses, it will become clear the weight of an object on Earth increases at a higher rate compared to the weight of the same mass on the moon. In this case, the gravitational acceleration and mass have a positive interaction, since an increase in either one of the factors lead to a higher increase rate in the response (the weight) with regards to the second factor. To come back to fractional design, let us consider the DOE study for three factors (A, B and C) with two levels for each factor (+1 and −1 in coded units). A full factorial design is given in Table 3.5. The columns AB to ABC are the interactions between the factors, and are simply obtained by multiplying the columns of the interacting parameters. In Table 3.5, each column contains the same number of low and high levels. A fractional factorial design is shown in Table 3.6 with a 1/2 fraction. The last column exclusively contains high levels, meaning the interaction ABC cannot be distinguished from the effect of a parameter of constant value (i.e. which cannot have an effect since it never changes). In such a situation, the number of interactions is counted (here three) and indicates the **resolution** as a Roman numeral (here resolution III).

A	**B**	**C**	**AB**	**AC**	**BC**	**ABC**
−	−	−	+	+	+	−
+	−	−	−	−	+	+
−	+	−	−	+	−	+
+	+	−	+	−	−	−
−	−	+	+	−	−	+
+	−	+	−	+	−	−
−	+	+	−	−	+	−
+	+	+	+	+	+	+

Table 3.5: Full factorial design with three factors and two levels.

A	**B**	**C**	**AB**	**AC**	**BC**	**ABC**
−	−	+	+	−	−	+
+	−	−	−	−	+	+
−	+	−	−	+	−	+
+	+	+	+	+	+	+

Table 3.6: Fractional factorial design with three factors and two levels.

All the interactions involving fewer factors than the resolution cannot always be fully trusted. As an other example, let us consider a fractional factorial design for four factors and two levels. With a 1/2 fraction, a resolution IV can be achieved, meaning the interaction ABCD is confounded with a constant. The test matrix for the design is given in Table 3.7. The two factor interactions are shown in the table, and placed so that they highlight the aliasing between the interactions. Due to the fraction, the same pattern can be found in the levels for the pairs of interactions AB and CD, AC and BD, and AD and BC. Consequently, the aliases make it impossible to mathematically determine if an observed change in the response is due to either one of the aliased interactions. This is the reason why it is important to provide the alias table for any fractional factorial design.

A	**B**	**C**	**D**	**AB**	**CD**	**AC**	**BD**	**AD**	**BC**
−	−	−	−	+	+	+	+	+	+
+	−	−	+	−	−	−	−	+	+
−	+	−	+	−	−	+	+	−	−
+	+	−	−	+	+	−	−	−	−
−	−	+	+	+	+	−	−	−	−
+	−	+	−	−	−	+	+	−	−
−	+	+	−	−	−	−	−	+	+
+	+	+	+	+	+	+	+	+	+

Table 3.7: Fractional factorial design with four factors and two levels.

3.3.3 Effects.

In a DOE, an **effect** has a specific meaning. It refers to the change in the mean of the response provoked by a factor or interaction of factors. To illustrate, lets consider the thought experiment already used, involving the weight of an object on the Earth and Moon. In this example study, lets consider solid cubes of mass A in kg on a body of gravitational acceleration B in m/s^2. Another factor can be introduced for the sake of the example, the volume of the object C in litres. Since the cubes are assumed to be solids, C is constant on both astronomical bodies. Since both the volume and mass of the object are set, the solids used in the experiment need to be made of different materials which have different densities. Since this study is only an example, the experiment is assumed to be feasible, either by finding the correct materials, or by allowing the solid to be hollow and filled with vacuum. The mass A of the object can take the levels 1 or 5 kg. If the gravitational acceleration of the Earth is approximately 9.81 m/s^2 at sea level, this constant needs to be known for the Moon. The data provided by the NASA [152] can be utilised, and give an acceleration of approximately 1.63 m/s^2 on the Moon. The levels for the volume C are either 1 or 5 l. A full factorial design such as Table 3.5 can be utilised. Table 3.8 provides the final design for the example, with two responses. The first output variable Y_1 corresponds to the weight obtained in an ideal scenario, where the measured weight coincides exactly with Equation 3.12.

The second response Y_2 represents the weight that is measured with an instrument, with a standard deviation of 5% of the value. It is obtained by multiplying the ideal case by random numbers (one per measurement), that follows a normal distribution with a mean of 1 and standard deviation of 0.05.

Run	**A**	**B**	**C**	**AB**	**AC**	**BC**	**ABC**	$\mathbf{Y_1}$	$\mathbf{Y_2}$
1	1	1.63	1	1.63	1	1.63	1.63	1.63	1.62
2	5	1.63	1	8.15	5	1.63	8.15	8.15	7.33
3	1	9.81	1	9.81	1	9.81	9.81	9.81	9.37
4	5	9.81	1	49.1	5	9.81	49.1	49.1	49.0
5	1	1.63	5	1.63	5	8.15	8.15	1.63	1.70
6	5	1.63	5	8.15	25	8.15	40.8	8.15	8.42
7	1	9.81	5	9.81	5	49.1	49.1	9.81	9.15
8	5	9.81	5	49.1	25	49.1	245	49.1	51.0
$\mathbf{E_1}$	22.9	24.5	0.00	16.4	0.00	0.00	0.00	**Mean**	
$\mathbf{E_2}$	23.5	24.9	0.73	17.3	0.80	0.14	0.29	17.2	17.2

Table 3.8: Design and effects of the example, where $A = m$ in kg, $B = g_0$ in m/s^2, C the volume in l, $Y_1 = m \cdot g$ in N, and $Y_2 = Y_1 \pm 5\%$ in N.

An effect is defined as the change in the mean of the response due to one factor or interaction jumping from its low to high level. For a factor A and response Y, with a design where A is at its high level n_+ times and at its low level n_- times (normally $n_+ = n_-$), the effect E is given by:

$$E(A) = \frac{1}{n_+}\left(\sum_{A=+1} Y\right) - \frac{1}{n_-}\left(\sum_{A=-1} Y\right) \quad . \tag{3.13}$$

In Table 3.8, the effects E_1 and E_2 are respectively calculated for the responses Y_1 and Y_2 for all the factors and their interaction. For instance, the effect of the mass (factor A) on the ideal case (Y_1) can be calculated as:

$$E_1(A) = \frac{8.15 + 49.1 + 8.15 + 49.1}{4} - \frac{1.63 + 9.81 + 1.63 + 9.81}{4} \approx 22.9 \text{ N}.$$

In the case of an interaction, the coded units must be considered (see Table 3.5). As an example, the effect of the interaction between the mass and gravitational acceleration (AB) is derived through the formula:

$$E_1(AB) = \frac{1.63 + 49.1 + 1.63 + 49.1}{4} - \frac{8.15 + 9.81 + 8.15 + 9.81}{4} \approx 16.4 \text{ N}.$$

Mathematically, the effect of an interaction determines if the mean of the response is altered, between two sets of tests having either both factors high or low, or one factor high and one low. If there is no interaction, the effect is zero.

3.3.4 Selecting the Significant Factors.

In the thought experiment, the response Y_1 is ideal, which is rarely the case. It is more common that the measurements contain errors, as it is shown for the response Y_2. This error transpires in the effects. In Table 3.8, the effects of C, AC, BC and ABC take non-zero values due to the errors. These effects are relatively small in this example, yet, for larger errors it is legitimate to determine a way to discriminate false positives.

First, the important factors and interactions must be extracted. A **half-normal plot** of the effects can fulfil this purpose. The creation of a half-normal plot requires three steps:

1. The absolute value of the effects of the seven factors and interactions are sorted in ascending order.

2. The 0 to 100% cumulative probability is divided in seven (number of factors and interactions) equal segments of 14.28%.

3. The sorted factors and interactions are each assigned a midpoint of a segment, still in ascending order.

If the effects were the result of errors that follow a normal distribution, the representation of the effects with the seven equally spaced data would follow a perfect line on the plot. This is the reason why the data are always represented in this manner on the half-normal plot. The numerical values for the example are given in Table 3.9. The half-normal plot of the effects is displayed in Figure 3.1. On the x-axis, it shows the absolute value of the effects. On the y-axis, the probability is scaled as the cumulative distribution function of a normal distribution. As a consequence, a line on the half-normal plot follows a normal distribution. The effects that falls in line on the plot follow a normal distribution, and can thus be ignored since they could be due to random error. Figure 3.1 demonstrates the effects of BC, ABC, C and AC fall in line with a normal distribution, and are hence statistically insignificant.

Order	**Effect**	**Absolute value of the effect**	**Cumulative probability**
1	BC	|0.14|	7.14%
2	ABC	|0.29|	21.4%
3	C	|0.73|	35.7%
4	AC	|0.80|	50.0%
5	AB	|17.3|	64.3%
6	A	|23.5|	78.6%
7	B	|24.9|	92.9%

Table 3.9: Cumulative probability of the seven sorted effects.

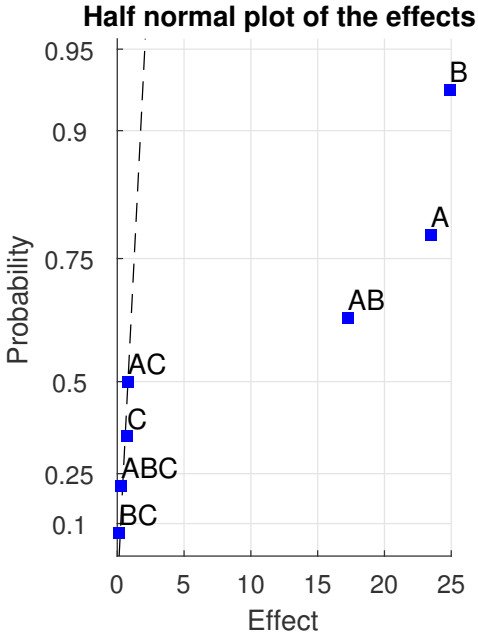

Figure 3.1: Half-normal plot of the effects.

3.3.5 Model, Residuals and Analysis of Variance.

It is typical to employ an **Analysis of Variance (ANOVA)** to determine whether the correct effects are ignored in a DOE study. Using the analysis performed with the half-normal plot, the statistically significant effects that do not follow a normal distribution are retained in the analysis, and form what is called the **model** (here, B, A and AB). On the other hand, the effects that have been found to follow a normal distribution are judged statistically insignificant, and they form the **residuals** (**also called residual terms or effects** to distinguish from the residuals of a linear regression).

The next step in the ANOVA consists in calculating the sums of squares of the model and residuals. The sum of squares SS_A of the effect of the parameter A on the response Y is defined as:

$$SS_A = n_+ \left(\frac{1}{n_+} \sum_{A=+1} Y - \frac{1}{N} \sum Y \right)^2 + n_- \left(\frac{1}{n_-} \sum_{A=-1} Y - \frac{1}{N} \sum Y \right)^2 , \quad (3.14)$$

where n_+ and n_- are the number of runs where the factor A is respectively at its high (+1) and low (-1) levels, and N is the total number of runs. It should be noted that the average of the response over all the runs, here defined by:

$$\overline{Y} = \frac{1}{N} \sum Y \ , \quad (3.15)$$

is commonly called the **grand average** (or grand mean) of the quantity Y. For a balanced two-level factorial design, such as employed in the example and main study:

$$n_+ = n_- = \frac{N}{2} \ . \quad (3.16)$$

Consequently, Equation 3.13 yields:

$$E(A) = \frac{1}{N/2}\left(\sum_{A=+1} Y - \sum_{A=-1} Y\right) \ . \tag{3.17}$$

It can be noted that the two sums of the response at the high and low levels of A simply forms the overall sum of the response for all the runs when they are added:

$$\sum Y = \sum_{A=+1} Y + \sum_{A=-1} Y \ . \tag{3.18}$$

Therefore, Equation 3.17 yields:

$$\frac{1}{2}\,E(A) = \frac{1}{N}\sum Y - \frac{1}{n_-}\sum_{A=-1} Y = \frac{1}{n_+}\sum_{A=+1} Y - \frac{1}{N}\sum Y \ . \tag{3.19}$$

Using Equations 3.14, 3.16 and 3.19, it can be determined that the sum of squares of the effect $E(A)$ of the factor A, with a design containing N runs is (see [151]):

$$SS_A = \frac{N}{4}\,E(A)^2 \ . \tag{3.20}$$

The sums of squares of the effects simply need to be added for the model and residuals:

$$\begin{aligned} SS_{\text{model}} &= SS_{\text{B}} + SS_{\text{A}} + SS_{\text{AB}} \ , \\ &= \frac{8}{4}\left(24.9^2\right) + \frac{8}{4}\left(23.5^2\right) + \frac{8}{4}\left(17.3^2\right) \ , \\ &= 1137 + 1103 + 596 = 2936 \ , \end{aligned}$$

$$\begin{aligned} SS_{\text{residuals}} &= SS_{\text{AC}} + SS_{\text{C}} + SS_{\text{ABC}} + SS_{\text{BC}} \ , \\ &= \frac{8}{4}\left(0.80^2\right) + \frac{8}{4}\left(0.73^2\right) + \frac{8}{4}\left(0.29^2\right) + \frac{8}{4}\left(0.14^2\right) \ , \\ &= 1.3 + 1.1 + 0.2 + 0.0 = 2.5 \ . \end{aligned}$$

The degrees of freedom need to be taken into account in the next calculation. Each effect is a mean between two values of the response (for each level), and thus has a degree of freedom of two. The sum of squares of a quantity diminishes the degree of freedom of the quantity by one. Consequently, for a two-level factorial design, the degree of freedom of the model or the residuals equals the number of effects contributing to the model or residuals. For instance, three effects contribute to the model, hence it has a degree of freedom of three. The mean square can be derived by dividing the sum of squares by the degree of freedom. Dividing the mean square of the model (or model term) by the mean square of the residuals produces an F-value. Critical F-values can be calculated with the degrees of freedom of the numerator (model) and denominator (residuals), and the confidence level at which the null hypothesis must be rejected. The null hypothesis corresponds to the case where the effects retained in the model cannot

be distinguished from measurement errors. For example, for the degrees of freedom of the model (3) and residuals (4), and with a probability of 0.1%, the F-value is 56.18 (right-tail F-value in Excel). This means that the F-value of any effect in the model and of the model itself needs to exceed 56.18 to be 99.9% confident to be significant. The different calculations are shown in Table 3.10.

Source	**Sum of squares**	**Degree of freedom**	**Mean square**	**F value**
Model	2936	3	979	1548
B	1237	1	1237	1956
A	1103	1	1103	1744
AB	596	1	596	943
Residuals	2.5	4	0.6	
Total	2938	7		

Table 3.10: ANOVA table for the thought experiment.

For a more complex design (fractional factorial, with repeats or centre points, blocks or non-orthogonal test matrix), the effects are usually replaced by the **standardised effects**. A standardised effect is a t-value of the null hypothesis. The standardised effect $SE(X)$ of a factor X that has an effect $E(X)$ is:

$$SE(X) = \frac{|E(X)|}{\sqrt{MS_{\text{residuals}}\left(\frac{1}{n_+} + \frac{1}{n_-}\right)}} \ , \tag{3.21}$$

where $MS_{\text{residuals}}$ corresponds to the mean square of the residuals, n_+ and n_- are the numbers of runs for which X has a high level(+) or low (−) level. The standardised effects can be analysed in the same manner as the effects. The standardised effects are t-values obtained with a two-tailed t-test. As a consequence, they can be compared to a critical t-value of the residuals. The degree of freedom is four for the residuals in the current example. With a typical confidence level of 95% ($\alpha = 0.05$), the critical two-tailed t-value for a degree of freedom of four is 2.8. The higher the confidence level, the higher the critical t-value. For instance, with a 99.9% confidence, a standardised effect needs to exceed 8.6 to be statistically significant. The standardised effects calculated for the present example are presented in Table 3.11. In this table, it can be seen that the standardised effects of the model terms all exceed the threshold t-values of 2.8, while the standardised effects of the residuals are less or equal to 1.41.

For a high number of factors, it is more common to utilise two visual aids. First, the **half-normal plot** of the standardised effects confirms the neglected effects fall in line with a normal distribution. Secondly, a **Pareto chart** (i.e. a bar chart of the effects, sorted by absolute values of the effects) of the standardised effects shows the most significant effects, and helps to compare the standardised effects to the critical

Source	Mean square	Effect	Standardised effect
Model	979		
B	1237	24.87	44.23
A	1103	23.48	41.76
AB	596	17.27	30.71
Residuals	0.6		
AC	1.3	0.80	1.41
C	1.1	0.73	1.29
ABC	0.2	0.29	0.52
BC	0.0	0.14	0.25

Table 3.11: Standardised effect of the factors and interactions.

t-value. Both graphs are presented in Figure 3.2 for the given example. In Figure 3.2b, the standardised effects of the model (B, A and AB) are all greater than the critical value of 2.8.

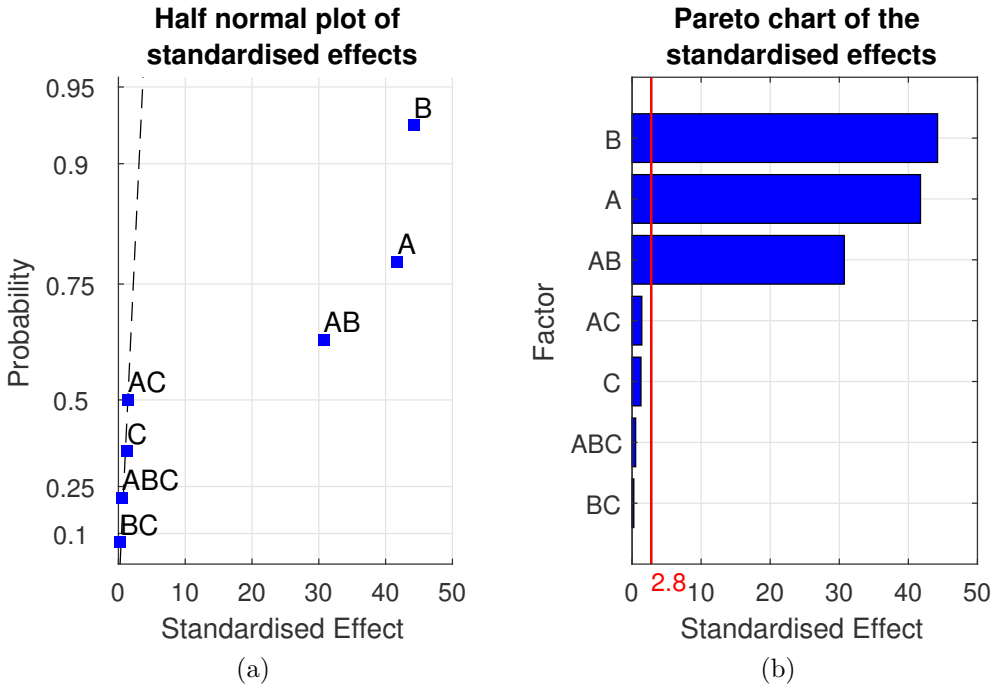

Figure 3.2: Half-normal plot (a) and Pareto chart (b) of the standardised effects.

3.3.6 Visualising the Effects.

After identifying the significant factors and interactions, their effects on the response can be analysed. The effect of a single factor is called a main effect, and the effect of an interaction between the factors is called an interaction effect. Two visual aids are

particularly useful for that purpose.

The **main effect plot** of a factor shows the change in the mean value of the response due to the change of the level of a factor. The x-axis provides the value of the factor, and the y-axis shows the value of the mean of the response for each level of the factor. For instance, Figure 3.3 is the main effect plot for the mass A on the response Y_2 in the employed example. The mean of the response is 5.46 N at the low level of A (1 kg), and 28.94 N at the high level of A (5 kg). The effect can be derived by calculating the difference: $28.94 - 5.46 = 23.48$ N. The grand mean of the response (i.e. the mean over all the runs) is typically displayed on a main effect plot for comparison purpose.

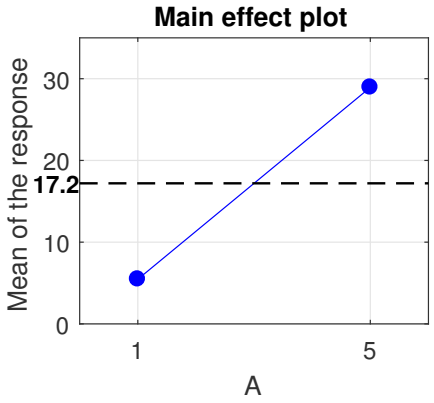

Figure 3.3: Main effect plot of the factor A (mass in kg).

The **interaction plot** is similar to the main effect plot. However, it displays two curves. The x-axis corresponds to the level of the first factor, while each curve relates to a level of the interacting factor. The interaction plot of the interaction AB of the present example study is shown in Figure 3.4. For a significant interaction, the two lines have different slopes, as it is the case here. If the interaction is insignificant, the alteration of the mean of the response due to one of the factors is not dependent on the level of the second factor, as a consequence, the segments are parallel. In Figure 3.4, the weight of the object increases even more if the gravitational acceleration of the planetary body rises. In such case, the interaction is positive. If the opposite phenomenon is observed (i.e. the weight increases less with regards to the mass as the acceleration increases), the interaction is negative.

3.3.7 Linear Regression Model.

With a two-level design, it is possible to build a linear regression model to estimate the response for a given set of values of the factors. For a response Y depending on the factors X_i $(1 \leq i \leq n)$, the predicted response $\hat{Y}$ is:

$$\hat{Y} = \beta_0 + \sum_{1 \leq i \leq n} \beta_i X_i + \sum_{\substack{1 \leq i \leq n \\ i < j \leq n}} \beta_{ij} X_i X_j \ , \tag{3.22}$$

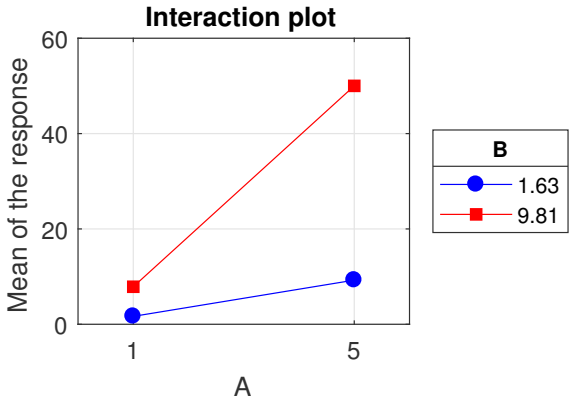

Figure 3.4: Interaction plot of the interaction AB.

where β_i and β_{ij} are the model coefficients. It can be noted that the β_{ij} is a triangular matrix, with $\beta_{ij} = 0$ if $1 \leq j \leq i$. The linear regression model can however exclude some of the factors if they are found insignificant in the ANOVA. For instance, the model for the weight in the example is:

$$\hat{Y} = \beta_0 + \beta_1 A + \beta_2 B + \beta_{12} AB \ . \tag{3.23}$$

The coefficients can be derived from the effects. β_0 is the average of the response for all the runs (17.2 for the example in Table 3.8). The other coefficients (β_i and β_{ij}) are half of the corresponding effects, if the factors are expressed in their coded units (-1 and $+1$). For instance, the model of the weight for the thought experiment (in the coded units) is:

$$\hat{Y} = 17.2 + 12.5\, B + 11.8\, A + 8.65\, AB \ .$$

However, a model given in the uncoded units of each factors is more useful. For a particular factor X which can take the coded values $X^{(\mathrm{c})} = +1$ or -1, and the uncoded values $X^{(\mathrm{u})} = X_+^{(\mathrm{u})}$ or $X_-^{(\mathrm{u})}$, the uncoded value depends on the coded value by a linear relationship:

$$X^{(\mathrm{u})} = \left(\frac{X_+^{(\mathrm{u})} - X_-^{(\mathrm{u})}}{2} \right) X^{(\mathrm{c})} + \left(\frac{X_+^{(\mathrm{u})} + X_-^{(\mathrm{u})}}{2} \right) \ . \tag{3.24}$$

Equation 3.24 can be used to express the coded value as a function of the uncoded value:

$$X^{(\mathrm{c})} = \frac{2\, X^{(\mathrm{u})} - X_+^{(\mathrm{u})} - X_-^{(\mathrm{u})}}{X_+^{(\mathrm{u})} - X_-^{(\mathrm{u})}} \ . \tag{3.25}$$

Equation 3.25 can be utilised in Equation 3.22 to obtain the model of the response in the more convenient uncoded units.

3.3.8 Validity of the Results and Response Transformation.

The analysis presented previously relies on several mathematical assumptions, in order for the results to be valid. The linear regression model that is drawn from the ana-

lysis can be verified with the standard tools. For that purpose, the errors between the model prediction ($\hat{Y}$) and the experimental data (Y) need to be assessed. The difference between the experimental data and the model predictions ($Y - \hat{Y}$) are typically called **residuals**. They must not be confused with the residual effects presented in the previous paragraphs. The coefficient of determination R^2 gives an overall estimation of the goodness of fit of the predictions of the model and the experimental results. Lets consider a response Y for which the experimental data Y_i have a mean $\overline{Y}$. A model of the experimental data derives the predictions $\hat{Y}_i$. In these conditions, the R^2 coefficient is given by:

$$SS_{\text{residuals}} = \sum_i \left(Y_i - \hat{Y}_i\right)^2 \ , \tag{3.26}$$

$$SS_{\text{total}} = \sum_i \left(Y_i - \overline{Y}\right)^2 \ , \tag{3.27}$$

$$R^2 = 1 - \frac{SS_{\text{residuals}}}{SS_{\text{total}}} \ . \tag{3.28}$$

In the ideal case, the predictions perfectly match the experimental data, leading the sum of squares of the residual to be zero, and consequently, the R^2 coefficient reaches the value of one. The adjusted R^2 can be preferred in a DOE. The adjusted R^2 ($\bar{R}^2$) also judges whether the model contains an excess of input variables, that are unnecessary for the model to fit the data. It can be calculated from the R^2 value through:

$$\bar{R}^2 = 1 - \left(1 - R^2\right) \frac{n-1}{n-m-1} \ , \tag{3.29}$$

where n is the total number of data points (96 runs in the present parametric study of the DBD) and m is the number of input variables in the model. The more input variables contribute to the model, the less the adjusted R^2. The R^2 and adjusted R^2 can be equal in the case where the model is a constant ($m = 0$). It can also be negative if the number of terms in the model exceeds the number of data points, which indicates there is a high risk of using too many variables in the building of the model. Finally, the root-mean-square of the error ($RMSE$) can be used to determine the mean deviation of the predicted data from the measurements:

$$RMSE = \sqrt{\frac{1}{n} SS_{\text{residuals}}} \ . \tag{3.30}$$

For a detailed analysis of the goodness of fit, four plots can be drawn. For the current example, the number of residuals is equal to the number of runs: 8. It is difficult to analyse the residuals for such a low number of cases. Besides, the error is previously simulated as a percentage of the response. Representing the error as a percent of the response is useful to exacerbate the effects of errors in a DOE analysis. However, this method is unrealistic, because most equipment have an absolute error, typically given as a percent of the full scale of the apparatus. As a result, a new

response Y_3 is calculated in order to produce clear examples.

The new response Y_3 considers a regression model for the experiments with a hundred points homogeneously distributed between the two extremum of the response: $1.63 \times 1 = 1.63$ N and $9.81 \times 5 = 49.05$ N. The experimental data are simulated by adding an error factor that is randomly generated, but follows a normal distribution probability density function with a mean of 0 N (no error) and a standard deviation of 3 N. As a result, 95% of the errors is found within a $\pm$ 9 N range around the analytical values. A standard first degree polynomial is fitted to the simulated experimental points in Matlab. The coefficient of determination for this linear regression model is 0.9583. This example does not represent a proper DOE analysis. However, it demonstrates the four common residual plots, that can be used to verify the goodness of the model.

The four residual plots are showed in Figure 3.5. They are:

(a) The **normal probability plot of the residuals**,

(b) The **histogram of the residuals**,

(c) The **residuals versus fitted values** plot,

(d) The **residuals versus orders of the observation**.

It is expected that the residuals of the predictions are normally distributed. The normal probability plot compares the probability distribution of the residuals to the cumulative probability of a normal distribution. In Figure 3.5a, the distribution of the hundred residuals follows an almost linear pattern with a few outliers for the negative residuals. Over 10% of probability, the data fall in line with a normal distribution. In addition, the histogram of the residuals, as presented in Figure 3.5b, can be employed to verify the normal distribution assumption. Furthermore, it highlights the possible skewness (asymmetry) of the distribution. Both should be as negligible as possible to respect the normal distribution assumption.

The residuals versus fitted values plot is utilised to confirm the constant variance assumption. The original data in the example would breach this assumption, as the residuals are linearly depending on the fitted values. In a proper DOE, the residuals of the model are required to be independent from the fitted values. In the hundred-point example, the residuals obey a normal distribution of constant standard deviation by construction, hence they have a constant variance (square of the standard deviation). In such a case, as displayed in Figure 3.5c, the residuals should not demonstrate any dependency over the fitted values. In this figure, the residuals are evenly distributed in an almost chaotic fashion without any clear trend.

The last type of plot that can be looked upon to assess the goodness of fit is the distribution of the residuals against the observation order (i.e. order in which the data are obtained). It indicates whether the residuals are correlated with each other, for instance, through an unexpected external variable affecting the response. The residuals

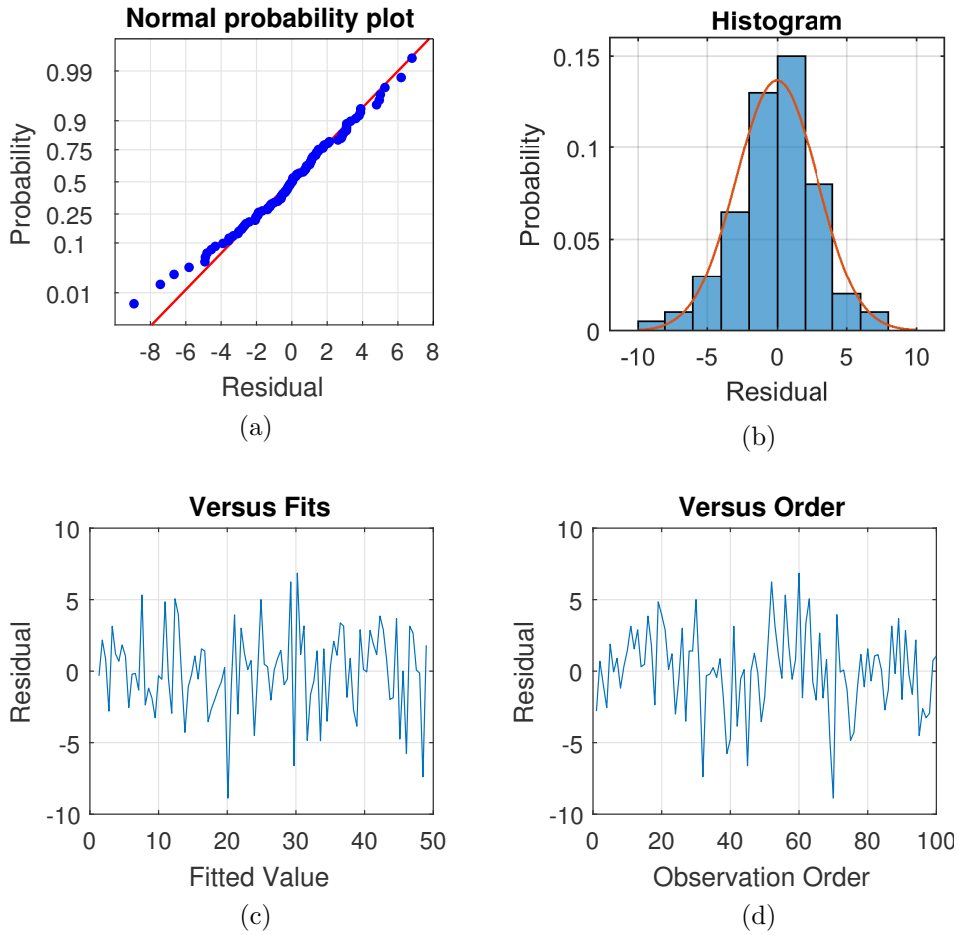

Figure 3.5: Residual plots for the thought experiment: (a) normal probability plot, (b) histogram, (c) residuals versus fits, and (d) residuals versus observation orders.

versus order plot for the current example is displayed in Figure 3.5d. As for the residuals versus fitted values plot, there should be no clear trend, and the distribution should be noisy.

In many cases, the response cannot be analysed directly. It is common to encounter a normal probability plot displaying an 'S' shape. In this situation, a simple solution can be utilised so that the residuals obey the assumptions: performing a **response transformation**. The output parameter is first transformed by applying a growing monotonic function to the data, which are then employed as the response. Three transformations are usually considered: the square root, the natural logarithm and the opposite of the inverse of the output parameters. However, programs such as Minitab comes with other mathematical tools, for instance, the Box-Cox transformation, which allows for a higher ranges of power laws. Nevertheless, the Box-Cox method that is utilised by Minitab only works for positive data. The Box-Cox transformation is explained in [153], but will not be detailed here, as it is not used to draw results in the current study. The main outcome of the transformation of the response is the ability of the DOE model to predict some non-linearity in the results.

A better way to assess any non-linear effect in the results consists in employing

centre points in the design. Centre points are distinct runs with all their factors set at the midrange values. The problem comes with hard-to-change factors which can only take discreet values. In the thought example, it is easy to imagine setting a midrange value of 3 kg for the mass used in the experiment. However, finding a third planetary body with the exact midrange value for the gravitational acceleration (5.72 m/s^2) would be very difficult. Many of the factors in the current study are hard to change due to the available material and fabrication process. As a consequence, the analysis of a run with centre points is not explained further.

3.4 Summary

The current chapter has presented the nine input parameters and three output parameters of the study. Namely, the input variables are the width (w_1) and height (h_1) of the air exposed electrode, the width (w_2) and height (h_2) of the encapsulated electrode, the inter-electrode gap (g), the relative permittivity (ε_r) and thickness (t) of the dielectric layer, and the frequency (f_{ac}) and the peak-to-peak voltage (V) of the AC sine wave. The three output variables are the thrust generation per unit of electrode span (T_A), the power consumption per unit of electrode span (P_A) and the force efficiency (η_A) (also known as the thrust to power ratio). Furthermore, the present chapter has introduced the Design of Experiment employed to analyse the data. The chosen design is a fractional factorial design, of resolution IV. It is formed by a test matrix of 32 independent combinations of the input variables, all being tested experimentally three times. The design enables the main effects of each of the input parameters to be studied, and gives some insights about the two-factor interactions. The aliases present in the current study have been provided in Table 3.3. Finally, a general presentation of DOE has been provided, and can be referred to, in order to understand the complete analyses of Chapters 5, 6 and 7.

The factors retained in the study are further described in the next section, along with their levels and accuracies. In addition, the equipment utilised to acquire the responses is described and the accuracy of the recordings is presented.

Chapter 4

Design and Accuracy of the Force Measurement Test Rig

The present chapter presents the dedicated test rig that has been produced for the measurement of the small force generated by DBD actuators. First, the design of the DBDs that are studied is introduced. The levels taken by the nine parameters are discussed, along with the reasons that led to these choices. As a result, the maximum force that can be expected to be recorded is estimated. Secondly, the design of the test rig that has been created to measure the thrust lower that this maximum threshold is presented. The measurement method and used apparatus are discussed, and the accuracy of the test rig is assessed. Thirdly, the equipments that are employed to obtain aerodynamic measurements, in order to verify the results of the test rig are introduced. Finally, the repeatability of the measurements is analysed, along with the possible external sources of error that have been found in the study.

4.1 Design of the DBD Actuators

First, the levels of the nine design parameters need to be introduced. Since the test rig is designed to measure the thrust of these DBD, their maximum thrust generation must be estimated.

4.1.1 Practical Design of the DBDs

Common PCB fabrication methods and material were utilised to produce the DBDs. Thus, the geometric and material-related factors can only take certain predefined levels. Moreover, the use of wire electrodes would make the design less accurate, and could bring additional sources of error, if a particular glue is utilised to bound the electrode to the dielectric. As a consequence, the study focuses on linear DBDs, which have rectangular electrodes.

Given the available materials for the dielectric, it was decided to use common FR4 epoxy laminate (ε_r = 4.42 at 250 MHz down to 4.36 at 2 GHz) and PTFE laminate

(Taconic TLP-3, $\varepsilon_r = 2.33 \pm 0.03$ at 10 GHz with an estimated loss of 0.03 at 1 GHz). For each material, standard thickness were chosen: 0.8 mm for the thinner DBD and 3.2 mm for the thicker DBD (accuracy for the thickness: +10%, −0%). In the case where the copper thickness differs between the electrodes, the actuator is formed of two PCBs stuck to each other with an epoxy glue. As the manufacturing method demands at least a 0.5 mm gap between the copper tracks and the edges of the dielectric, the minimum gap is 1 mm. It was thus decided that the gap between the two electrodes can vary between 1 and 5 mm, since this range could positively affect the results [69].

Both electrodes are made out of copper. The standard copper thickness are 1 and 2 oz., which corresponds to 35 and 70 μm ($\pm$10%) respectively. The width of the exposed electrode will vary from 0.5 to 5 mm. These values were chosen to reduce fragility due to the production (the minimum producible copper track size is 0.125 to 0.250 mm), and to enable the study of rectangular and filamentary electrodes. The encapsulated electrode is 1 to 5 cm wide. As seen in different studies [1, 6, 102], the typical plasma extent does not exceed 8 mm from the edge of the exposed electrode. Thus, the width of 10 mm should not constrain the plasma. The 50 mm wide buried electrode was chosen, so that other possible effects of the variable can be assessed. It was decided to allow a margin of 5 mm between the edges of any electrode, and the edges of the dielectric. This safety margin enables the use of nylon screws, in order to fix the DBDs to the test rig. As a result, the width (or chord) of all the DBDs hereby studied correspond to the widest case of a 5 mm exposed electrode, a 50 mm encapsulated electrode, a 5 mm inter-electrode gap and two safety margins of 5 mm. Hence the chord of the DBDs is 70 mm in total. The span of the electrodes was chosen to be 100 mm, with two margins of 5 mm of dielectric on each side (110 mm span in total for the PCB). DBDs similar to the ones studied here, and supplied with comparable voltage and frequency ranges were found to generate 20 to 40 mN/m of thrust [1, 41, 47, 57, 59]. Consequently, the electrode span should be enough to generate a measurable thrust without exceeding the load cell threshold (see Sections 4.2.1 and 4.2.2). For all the designs, the location of the upstream edge of the encapsulated electrode on the DBD is kept constant, 55.5 mm from the downstream edge of the DBD (see Figure 4.1). If applicable, the epoxy glue is stuck at this location. The geometry of the DBDs utilised in the current study is showed in Figure 4.1. An example of two plain configurations is provided in Figure 4.2 to give an idea of the widest and narrowest values of the electrodes widths and gap. The schematic also shows the marking for the screw holes and the DBD "name" (details in Appendix A).

The encapsulated electrode is insulated using a standard solder resist mask (relative permittivity of approximately 4.5 and thickness of approximately 20 μm). Due to some mistakes in the production of certain epoxy boards, the solder resist was placed on the top layer of some of the epoxy PCBs. Thus, an extra layer of dielectric material stands on top of the encapsulated electrode for several DBDs. Nevertheless, it was decided to keep these PCBs in the study, as the solder resist mask has a dielectric constant comparable to the epoxy beneath it, and its thickness lies within the error margin for

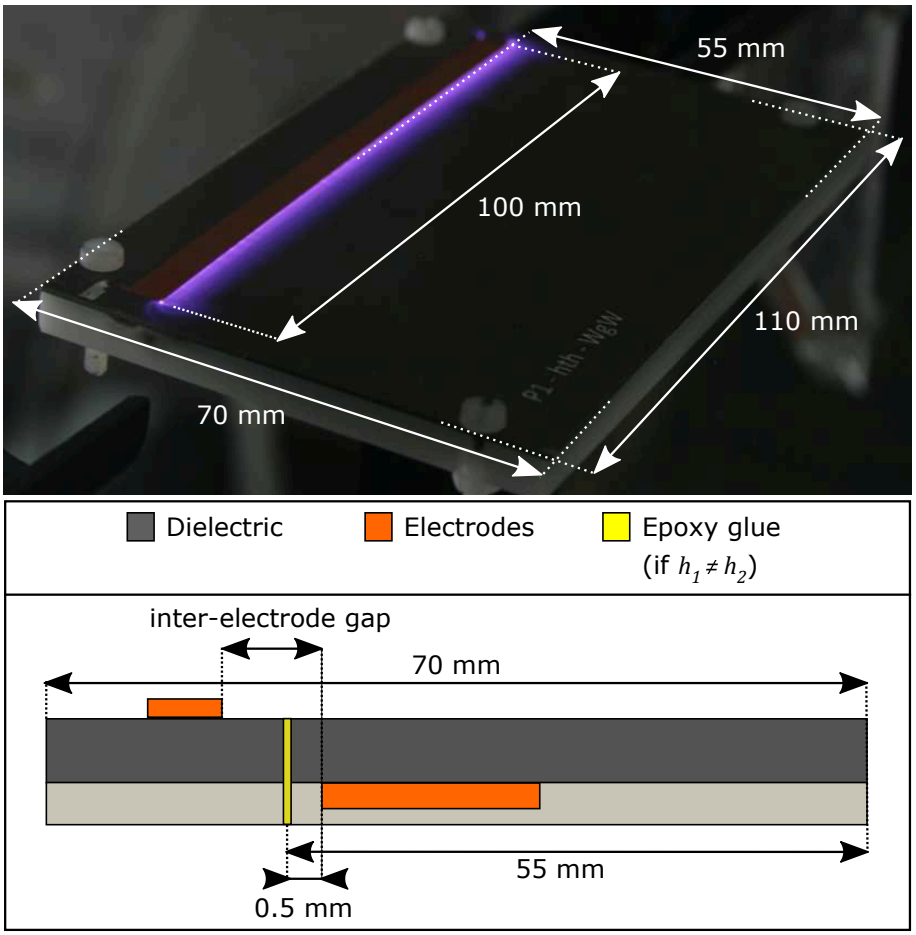

Figure 4.1: Dimensions of the DBD used in the study.

the dielectric board thickness (±10%). Kapton tape was then used in order to cover the encapsulated electrode for these particular DBDs, in order to avoid the formation of plasma on the buried electrode.

Eight actuators are shown in Figure 4.3. One DBD having the solder mask on the incorrect side is displayed on the bottom right corner. The presence of the solder resist (green layer) downstream of the exposed electrode can be seen. Each electrode is soldered to a thin copper wire (0.050 mm core diameter, 0.063 mm external diameter with the polyester insulation). This thin wires were not found to impact the measurements in the experiment. It must be remarked that the wires that are connected to the DBDs in Figure 4.3 are not the aforementioned wires. The model showed in Figure 4.3 was latter found to greatly affect the results, and was replaced by the described model of copper wire. The wires are soldered at their free ends to small squares of copper tape (strip folded in two to stuck on its glue layer, area less than 0.25 to 1 cm^2), allowing a constant and stronger grip for the crocodile clips connected to the HV power supply. In Figure 4.3, both the PTFE (left column of actuators) and epoxy (right column) are presented. The top four DBDs have thicker dielectric layers (3.2 mm), while the bottom four have thinner layers (0.8 mm). Two-part (glued) versions of the actuators are also shown with boards number 1, 10, 19 and 11 (run numbers that can be found

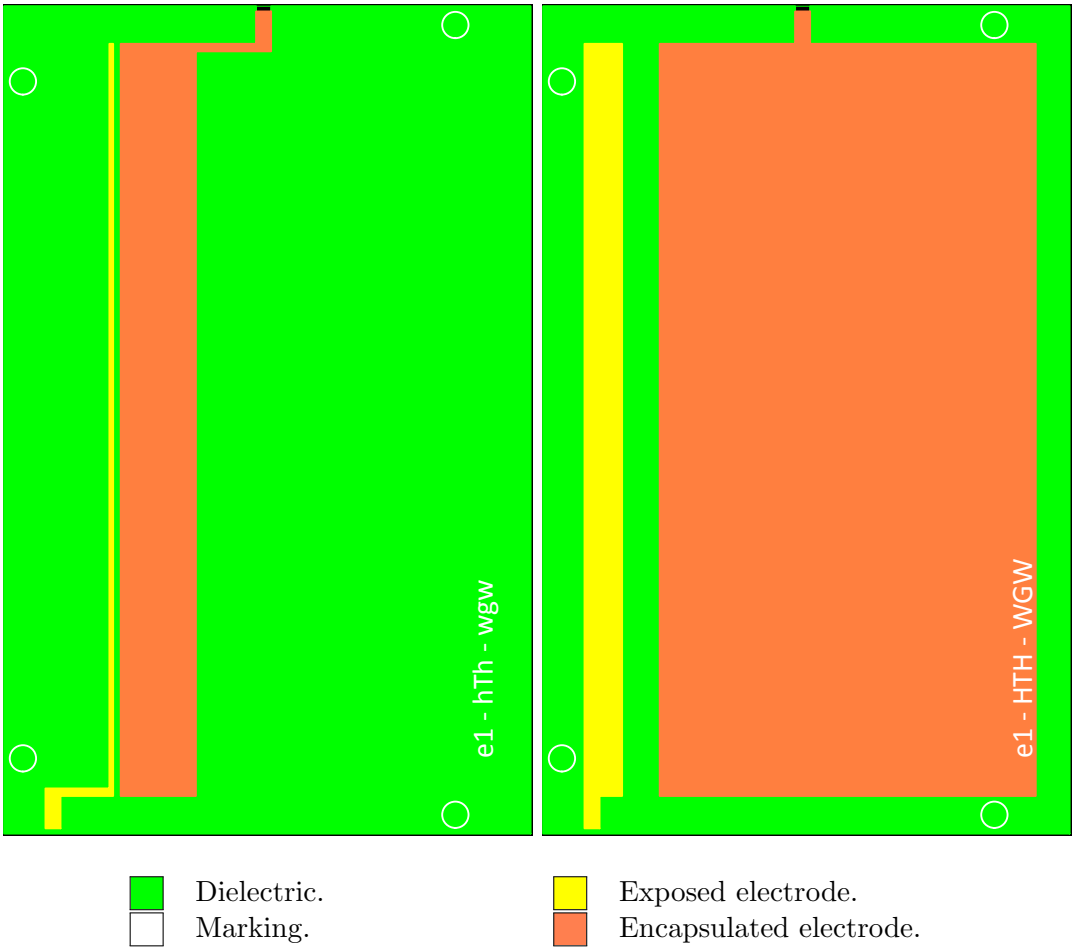

Figure 4.2: Two DBD designs showing the narrowest (left) and widest (right) electrodes and gaps (scale 1:1).

in Table A.2). For instance, light reflection can be seen on the epoxy glue of number 10. Number 11 corresponds to one of the designs for which the solder resist mask was placed on the wrong side of the dielectric layer. Thus, as can be seen on Figure 4.3b, Kapton tape was used to insulate the bottom electrode, resulting in the orange colour on the bottom side of some actuators.

4.1.2 High-Voltage Power Supply

4.1.2.1 HV Amplifier

A Trek Model 20/20C-HS high-voltage amplifier was used. It can deliver a signal with up to 20 kV of amplitude (40 kV_{pp}) at a current of 20 mA_{rms} (up to 60 mA peak for 1 ms). The amplifier has an in-built voltmeter and ammeter, which can acquire the data within 0.1% and 1% respectively of the DC full scales. As a result, the power is 1% accurate. The current monitor has a -3 dB bandwidth, and can hence capture a frequency ranging from DC up to more than 20 kHz. As it can be observed in the current measurements realised by different groups [1, 5, 66, 69], the frequency of the streamers in the plasma can exceed this value. The current monitor is hence unable to

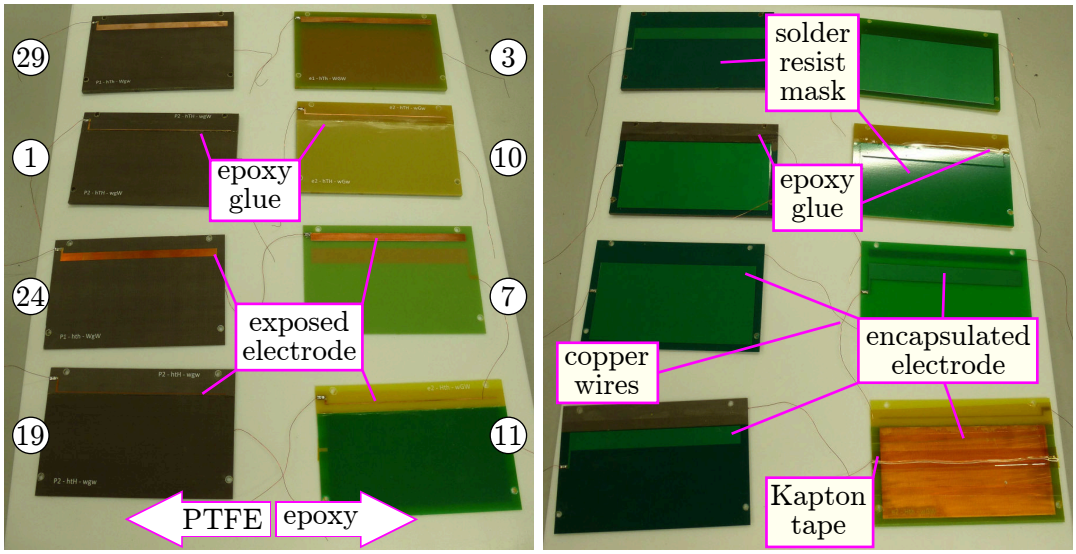

(a) (b)

Figure 4.3: Eight different DBDs, air-exposed electrode up (a), and down (b), numbered by run number (refer to Appendix A).

detect the streamers. In order to obtain more accurate time dependent measurements, a probe capacitor or resistor would need to be employed between the encapsulated electrode and the electric ground. The voltage would then need to be recorded with an oscilloscope connected to the employed data acquisition system. Due to the complexity of the installation, lack of of the necessary equipment, and since the thrust and power are time averaged in the present study, the voltage and current measurements from the amplifier monitors are used in the present work. Knowing the voltage and current limitations of this model of amplifier, it is important to bear in mind its capability depends on the electrical load to which it is connected. The distortion plot for the Trek 20/20C-HS is shown in Figure 4.4. In the case where the voltage and frequency requirements is too high for a given load, the amplifier has two options: tripping the device so that it does not deliver current, or limiting the output voltage. In the present study, the tripping mode was selected.

4.1.2.2 Function Generator

The amplifier intensifies the signal coming from a B&K Precision 4010A function generator. The device can provide with up to 20 V_{pp} at a frequency ranging from 0.2 Hz to 2 MHz. It has the ability to generate sine, square and triangle waves, at a variable duty cycle (d.c.) of 15 to 85%.

4.1.2.3 Voltage and Frequency Limitations

The low and high values of the voltage and frequency in the DOE need to be such that the plasma ignites without reaching dielectric breakdown, or without reaching the maximum power of the amplifier. Initial tests indicated plasma typically appeared

at approximately 6 to 9 kV_{pp} at frequencies between 0.5 and 2.5 kHz, with a few actuators expected to have a higher capacitance (thick dielectric of epoxy with a long inter-electrode gap).

Moreover, for a pure capacitive load supplied with an AC voltage, the electric current increases with the voltage amplitude, the frequency and the capacitance. Consequently, for a high capacitance, using high frequency and voltage can make the current reach the full scale of the amplifier. The capacitance of the designs of DBDs employed in the present study must hence be estimated, in order to make sure that the chosen levels for the voltage and frequency do not exceed the amplifier abilities. When reaching its maximum current, the amplifier either switches off, or limits the voltage so that the maximum current is met. For instance, the distortion plot of the Trek 20/20 is given in Figure 4.4.

Different studies either directly reported the capacitance of the utilised DBDs, or provided Lissajous figures (charge-voltage diagram) which enables the derivation of typical capacitance of 20 to 55 pF/cm of span [6, 46, 84, 155, 156]. For the DBDs with 10 cm span used in the current work, this would result in a maximum capacitance of 550 pF. Given these estimations and the limitations of the amplifier, the voltage was chosen to range between 10 and 16 kV_{pp} for a frequency ranging from 0.5 to 2.0 kHz. Further test with a few actuators demonstrated the amplifier would trip at approximately 2.5 to 3.0 kHz at 16 kV_{pp}. During the experiments, it was frequently observed the peak-to-peak voltage reading could be effected by peaks in the voltage

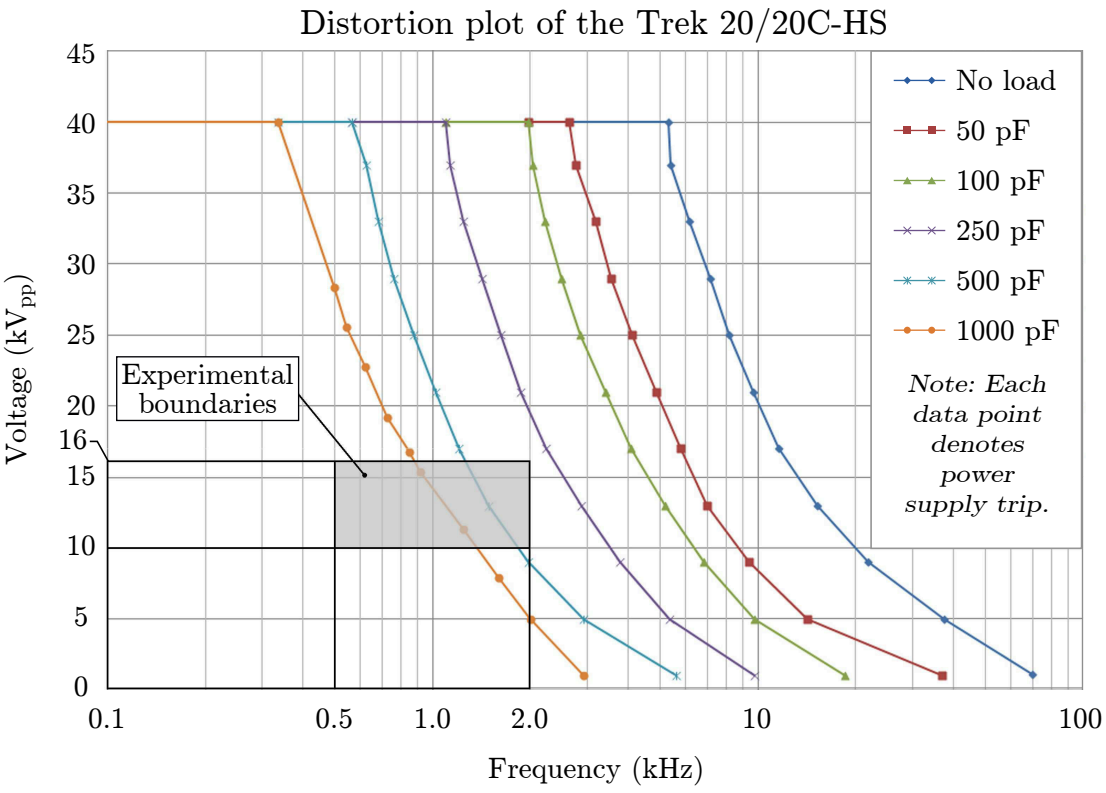

Figure 4.4: Distortion plot for the Trek 20/20C-HS (modified from [154]).

(possibly due to streamers in the plasma). Consequently, after all the runs had been tested, the voltage and frequency were numerically analysed to confirm their levels. The frequency was not found to be significantly different from the chosen levels. On the other hand, the actual voltage recorded during the experiments slightly differed from the theoretical level of 10 and 16 kV_{pp}. In order to increase the accuracy of the analysis, the levels where corrected, with a low level of 9.9 kV_{pp} and a high level of 15.7 kV_{pp}.

4.1.3 Control and Recording

The signals coming from the different pieces of equipment (current and voltage from the amplifier, frequency from the function generator, and force from the test rig) are acquired by a dSPACE DS1104 board, and are processed by a dSPACE Control Desk script. These data are sampled at a frequency of 25 kHz. As a result, 12.5 points can be processed for one AC period for a 2.0 kHz power input for the DBD, and 50 points can be processed for one AC period with a power supply input of 500 Hz. Due to the memory limitation of the equipment, the sampling frequency cannot be increased. Consequently, a lighter processing script has been written so that the electrical measurements can be recorded with more resolution. In this configuration, the board can be used with a sampling frequency of 40 kHz. Therefore, the electrical equipment is calibrated using the faster acquisition script at 40 kHz initially, and the standard script is activated for the thrust measurement at 25 kHz in a second time. If required, the DS1104 can be operated at a maximum sampling of 80 kHz. However, it depends on the number of stored variables, the complexity of the processing of the data, and the sampling time. Up to one million data points can be stored by the system. It was decided to record 5 s of data for each test. This represents 2.0×10^5 data points for the electrical measurements, and 1.25×10^5 for the force measurements.

The different levels of the nine design parameters presented in the present section are summarised in Table A.1. A DBD having these levels is expected not to generate more than 100 mN/m of electrode span (see Section 4.1.1). With this requirement and knowing the employed High-Voltage and acquisition apparatus, it is possible to present the design of the force measurement test rig.

4.2 Test Rig for Direct Thrust Measurement

This section presents the complete design of the created force acquisition test rig. It introduces the chosen design and apparatus of the test rig The installation of a DBD in the rig is presented, along with the different solutions that have been found, in order to cancel the mechanical sources of error. The calibration method is also detailed, and the error analysis of the measurements is realised.

4.2.1 Load Cell and Signal Conditioner

The force measurements are realised with a NovaTech F329 deci-Newton compression load cell, connected to a NovaTech SGA/D signal conditioner. The cell has the ability to read forces up to 0.1 N with a resolution of 4 μN (best) to 10 μN (recommended). When calibrated in isolation (refer to Appendix B), it was found that the output voltage from the system was approximately 9.5 V on average between the zero and maximum load (10 g or 0.0981 N), with a standard deviation of slightly less than 0.01 V. This standard deviation corresponds to a force smaller than 103 μN. In this situation, at least 107 points must be acquired in order to bring the standard error below 10 μN. The signal conditioner is connected to the dSPACE board for data acquisition. Thus, at 25 kHz sampling frequency, the 107 points are recorded within 4.3 ms. As explained previously, the sample size is 1.25×10^5 points (5 s at 25 kHz), leading to a two-tailed Student's t-value of 1.960 for the force measurements with a confidence level of 95%. With a standard error of 103 μN and 1.25×10^5 points per sample (5 s samples at 25 kHz sampling frequency), the standard error of the load cell is:

$$\sigma = \frac{105}{\sqrt{1.25 \times 10^5}} \approx 0.30\,\mu\text{N},$$

By multiplying the standard error by the t-value, the overall confidence interval of the load cell is ± 0.60 μN. The load cell mechanical stiffness is 1300 N/m, which is not negligible, and would represent a damping for real-time recordings. However, in these experiments no dynamics or time dependent behaviour were considered, and only the mean force exerted by the DBD is to be acquired. In addition, the SGA signal conditioner is set with an in-built low pass filter, that was enabled to damp the signal over 100 Hz. This reduces the load cell noise by approximately half, and more importantly, removes the electromagnetic noise induced by the HV amplifier and plasma actuator. The noise consists of a sine wave of constant amplitude having the same frequency as the high voltage supply.

The NovaTech F329 comes with a shielding for the load cell structure, but not for the wires that go to the signal conditioner. In order to provide electromagnetic shielding for the wires, they were wrapped in aluminium foil. PVC tape was stuck to the aluminium shield, so that it fits tight, and provide electric insulation. The signal conditioner is enclosed in a Faraday cage made of metallic mesh to ensure it is not impacted by electromagnetic interference either. The load cell and signal conditioner are shown in Figure 4.5, where the Faraday cage, shielded wire and shielded metal casing of the load cell are shown.

4.2.2 Force Amplification

The small force produced by the actuators needs to be amplified so that the load cell can measure it accurately. The higher the amplification, the smaller the actuators can be in span. It was estimated that the an actuator with the chosen span of the electrodes

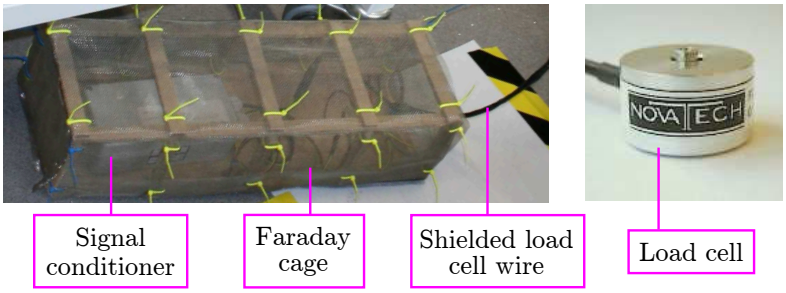

Figure 4.5: Electromagnetically shielded load cell and signal conditioner.

of 10 cm produces less than 100 mN/m. The rig was thus designed to measure up to 10 mN of force. A lever configuration was used, in a vertical arrangement as shown in Figure 4.6. The main disadvantage of the use of a lever configuration to amplify the force, lies in the requirement to reduce the friction in the mechanical linkage between the lever and its support, in order to obtain accurate results.

The load cell is not attached to the lever, in order to make the setting of different calibration masses at the bottom position and maintenance operations easier. The calibration mass at the bottom end of the lever is used to compensate the imbalance of the mass distribution of the lever above and below the hinge. Hence, it ensures

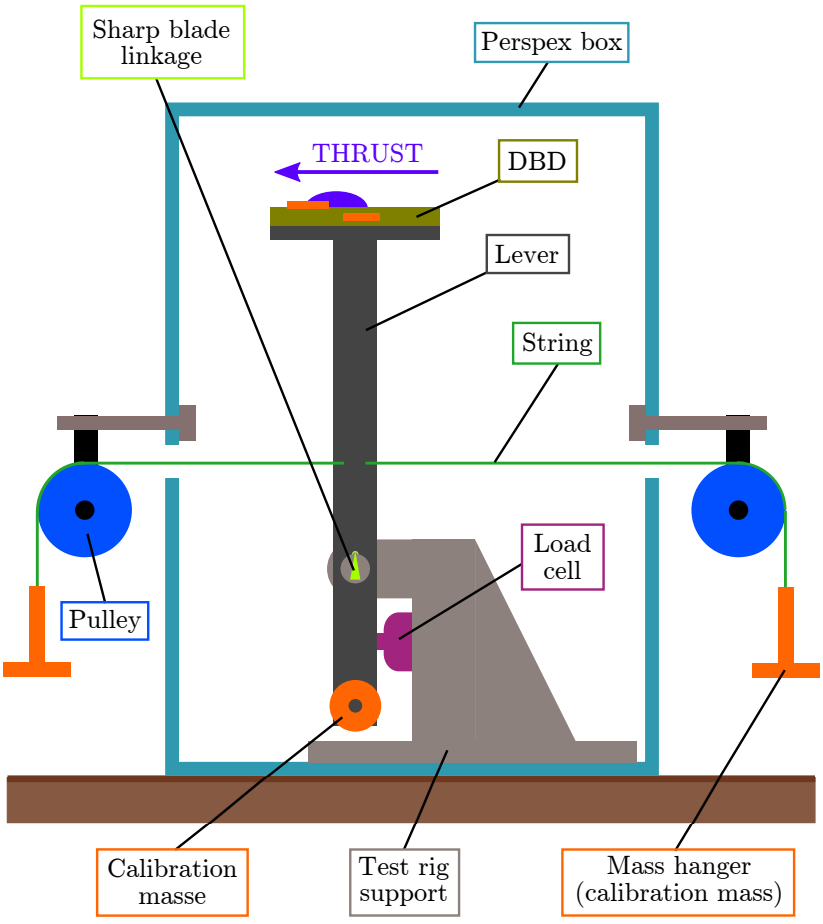

Figure 4.6: Schematics of the test rig.

the verticality of the lever, and this calibration sets initial load on the cell when the actuator is switched off. The fine tuning of the reference load is realised with the two mass hangers that protrude on both sides of the Perspex box. The calibration mass at the bottom of the lever can also be adjusted in order to compensate any variation in the mass of the actuator. The first design of the rig used plain bushings in the hinge, with a length of 32.5 mm between the hinge and the load cell pin, and 345 mm between the hinge and the platform. During the pre-calibration, it became clear that the bushings had too much static and dynamic friction, and were thus creating non-negligible non-linearity and hysteresis in the measurements. As a result, they were latter replaced by a sharp blade on which the lever is balanced. This mechanical linkage has theoretically no friction, but is also more fragile and more difficult to set up, due to the dimensions of the aluminium beam (38.1 mm width for 12.7 mm span and 1.6 mm thick walls). Yet, when placed and calibrated correctly, it proved a very efficient way to reduce friction. Due to this change, the actual hinge was shifted 4.5 mm up. A 0.5 mm-notch was realised in the top of the original hole in the beam. The blade is a standard heavy duty knife, that is cut in width to fit in the original holes of the test rig. Hence, the distances between the actuator and the hinge, and between the load cell and the hinge are respectively 340.5 mm and 37 mm. This leads to an amplification of 9.2 of the force ($\pm$ 0.1 due to inaccuracies in the mounting). Consequently, given the range of the load cell, a maximum force of $0.10/9.2 \approx 10.8$ mN can be applied by an actuator. Different annotated perspectives of the test rig are showed in Figure 4.7. Altogether, the confidence interval of the load cell (0.6 μN) can be multiplied by the amplification factor, and lead to an overall confidence interval of the test rig of less than 6 μN. The aluminium beam that was utilised as a lever was coated with one layer of Kapton tape and one layer of black PVC tape, for electrical insulation.

4.2.3 Installation of a DBD in the Test Rig

The DBDs are screwed to a 5 mm thick acrylic platform by four nylon machine screws. The platform can be changed, as it is itself screwed to a Delrin stand, inserted in the aluminium beam of the lever. As a result, any point of a DBD is at least separated by a dielectric layer of 10 mm from the aluminium core of the lever. Each electrode is soldered to a 0.050 mm diameter copper wire (0.063 mm outer diameter with the insulating coating made of a mix of polyesterimide and polyimide-imide). In order to connect the thin wires to the amplifier, they are soldered to small strips made of copper tape folded on themselves. The copper tape has a width of 5 mm and a copper thickness of 35 μm, with a 41 μm thick sheet of acrylic adhesive under the copper. The strips are thus 0.15 mm thick, which is enough to ensure a strong grip by the crocodile clips connected to the HV amplifier. The power cables are held in standard PVC pipes by blue foam corks and PVC tape. Thus, each crocodile clip lies mechanically unloaded, a few centimetres away from the DBD. Great care is taken with the grounded copper wire, so that it would not be placed too close to the exposed electrode and form a spark,

which can burn both the wire and copper track. Thus, this particular wire must be long enough not to contribute to the input force, but small enough not to electrically interfere with the DBD. An example of installation of a DBD is shown in Figure 4.8. The test rig is enclosed in a Perspex box, so that the DBD actuator is not effected by free-stream conditions.

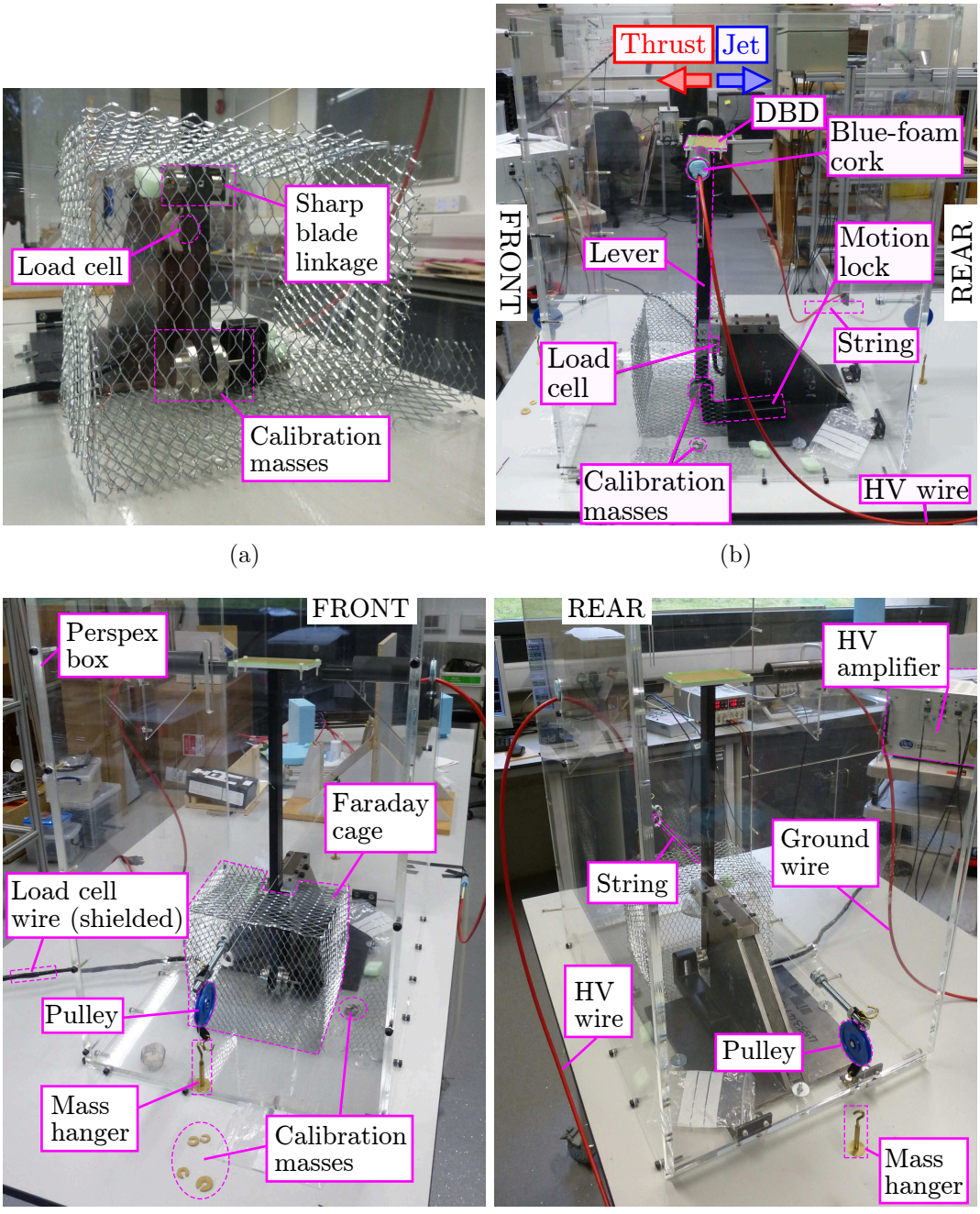

Figure 4.7: Force measurement test rig: load cell arrangement (a), and side (b), front (c) and back (d) of the test rig.

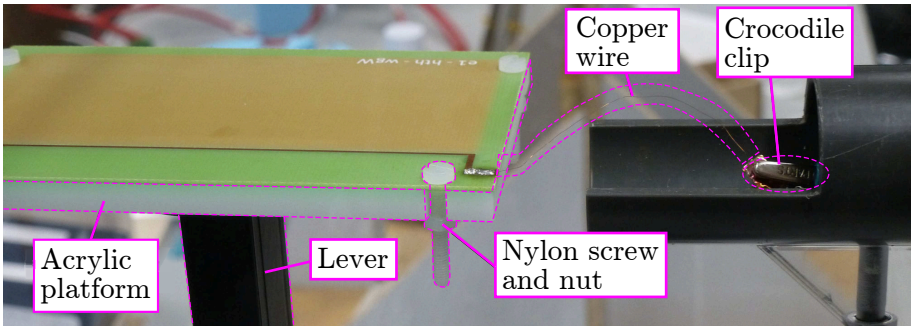

Figure 4.8: DBD mounted on the platform.

4.2.4 Electromagnetic Shielding

Recordings were performed with an unloaded load-cell, but with a DBD producing plasma. At a relatively low voltage setting (around 4 kV_{pp}, no plasma formation), it appeared that the load cell signal was sinusoidal and correlated with the applied voltage. As a result, the standard error jumped from 10^{-2} V to 10^{-1} V. Consequently, a better shielding was provided for the signal conditioner, and the load cell wire. With the same HV setting, the standard error was reduced to 2.5×10^{-2} V as a result of the Faraday cage built around the signal conditioner. After applying an aluminium foil shielding to the load cell wire, the standard error was decreased to approximately 3×10^{-2} V at 16 kV_{pp} and 2 kHz. The presence of a Faraday cage around the load cell did not impact on the electromagnetic noise of the signal. This is due to the in-built shielding of the device. However, using the signal conditioner second order low pass filter reduces the noise significantly, as it damps the high frequency sine wave. Thus, a lower noise level can be obtained. The different Faraday cages can be seen in Figure 4.7. The use of a 100 Hz filter decreases the noise in the measurement down to its original level (less than 10 μN), but also implies that only the average thrust can be measured. The Faraday cage around the load cell was latter removed.

4.2.5 Calibration Method

After fitting a DBD to the platform, the calibration mass located at the lower end of the lever is adjusted to ensure that the lever is vertical. The load in this configuration must not exceed 2 g, in order to avoid overloading the load cell during the calibration of the test rig. The zero is then set by using the two mass hangers at the front and rear of the Perspex box. The string connecting the hangers is attached to the lever 37 mm above the blade. Consequently, there should be no amplification of the force. Assuming an error of 1 mm, a possible amplification or reduction of 3% of the force is possible. It was determined (refer to Appendix C) that a more accurate calibration is obtained when using three points to find the load cell gain: 2, 5 and 8 g. Typically, two calibration sequences are performed before actuating the DBD, and one to two after. If the gain (in mN/V) differs greatly between the three to four sequences, the data series is cancelled and is started again from the beginning. If the gains calculated

through the sequences agree, their average is used for the derivation of the force. The reference voltage (at zero thrust) is recorded before and after actuation and is averaged. It must be noted the possibility to use a reference in a loaded state (usually 2 or 5 g). Pre-loading the load cell was found to improve the damping of the oscillations of the lever when igniting the plasma, resulting in a faster convergence of the load cell signal. The reference voltage and the gain obtained over the calibration sequences are used to derive the force. The calibration setup is presented in Figure 4.9. In order to assess the friction in the pulleys, small masses were placed on each of the hangers. The test rig was able to measure the force produced by a 5 mg mass (0.05 mN).

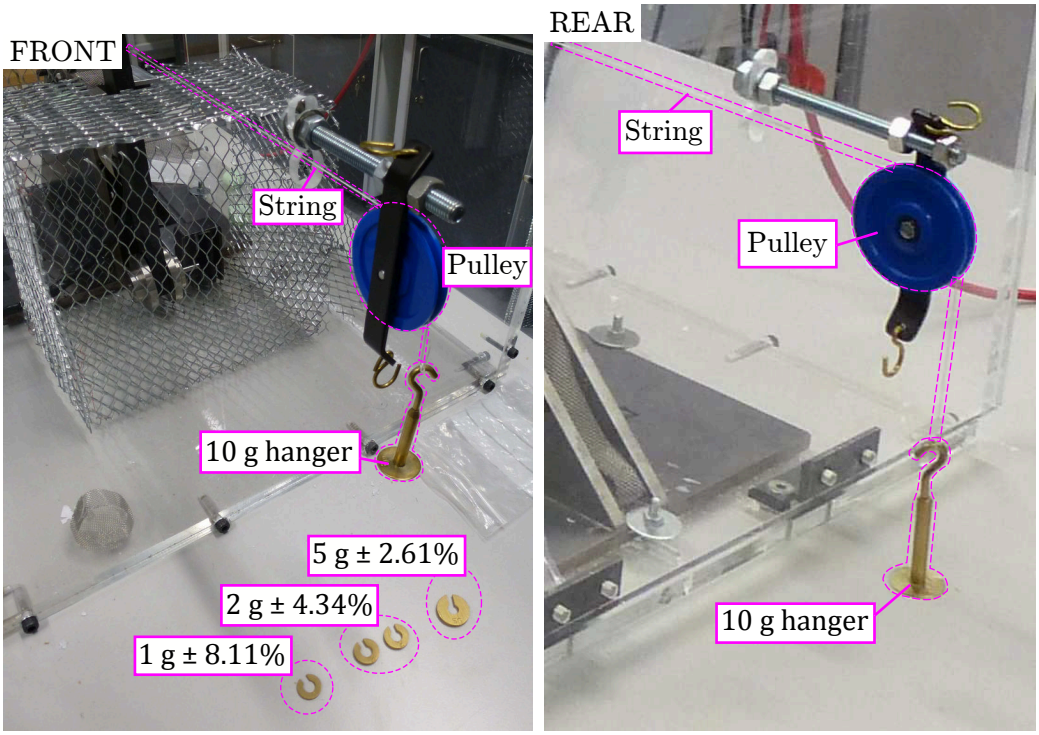

Figure 4.9: Calibration material for the thrust measurements.

4.2.6 Atmospheric Conditions

The atmospheric pressure and humidity impact the results [59, 73]. Consequently, the atmospheric conditions are recorded using a Traceable 6530 barometer. The room temperature can be measured between 0 and 55°C with an accuracy of ± 0.4°C. The relative humidity is obtained with an accuracy of ± 3% between 5% and 75%, and ± 5% from 75% to 95% (the percent represents here the standard unit of humidity, i.e. the percent of the saturation by water vapour). Finally, the barometric pressure is recorded between 500 and 1030 mbar with an accuracy of ± 4 mbar.

4.2.7 Error Analysis

The error for each set of data obtained with the force measurement test rig was already presented in Section 4.2.2. The confidence interval for the force averaged over 5 s

at a frequency of 25 kHz is ± 6 μN. For a result in thrust per unit of span of the electrodes, with a span of 10 cm as used in the study, this represents a confidence level of ± 60 μN/m.

The power is derived from voltage and current recorded at the monitors of the high-voltage amplifier with accuracies of ± 20 V and ± 0.2 $\mathrm{mA_{rms}}$ for full scales of 20 kV DC and 20 $\mathrm{mA_{rms}}$. Consequently, the standard error of the instantaneous power consumption ϖ (product of the voltage V by current I) can be derived:

$$\sigma_{\varpi} = \sqrt{(I \times \sigma_V)^2 + (V \times \sigma_I)^2} \ . \tag{4.1}$$

At full scale, Equation 4.1 results in an error of ± 4 W for a maximum of 400 W. The power consumption is calculated by integration of the instantaneous power over n periods, as shown in Equation 3.7. The integration is numerically performed through a standard trapezoidal rule. For a measurement run over n periods of the AC signal, with a signal frequency f_{ac} at a sampling frequency f_{s}, the power Π_{A} is given by:

$$\Pi_{\mathrm{A}} = \frac{f_{\mathrm{ac}}}{f_{\mathrm{s}}} \frac{1}{n} \sum_{k=1}^{m-1} \left(\frac{\varpi_{k+1} + \varpi_k}{2} \right) \ , \tag{4.2}$$

where ϖ_k is the instantaneous power consumption at observation k and m the total number of observations of the sample. The ratio of $f_{\mathrm{ac}} / (n \cdot f_{\mathrm{s}})$ gives the total number of points in the sample. Hence, Equation 4.2 results in:

$$\Pi_{\mathrm{A}} = \frac{1}{2\,m} (\varpi_1 + \varpi_m) + \frac{1}{m} \sum_{k=2}^{m-1} \varpi_k \ . \tag{4.3}$$

Since all the m observations have a standard error of $\sigma_{\varpi} = \pm 4$ W, the standard error of the consumed power Π_{A} is:

$$\begin{aligned} \sigma_{\Pi} &= \sigma_{\varpi} \cdot \sqrt{\sum_{k=1}^{m} \left(\frac{\partial \Pi_{\mathrm{A}}}{\partial \varpi_k} \right)^2} \ , \\ &= \sigma_{\varpi} \cdot \sqrt{2 \times \left(\frac{1}{2\,m} \right)^2 + (m-2) \times \left(\frac{1}{m} \right)^2} \ , \\ &= \sigma_{\varpi} \cdot \sqrt{\frac{1}{m} - \frac{3}{2\,m^2}} \ . \end{aligned} \tag{4.4}$$

Since the number of points is of the order of 10^5, the standard error of Equation 4.4 can be approximated to the standard error of the mean of the instantaneous power consumption over m observations:

$$\sigma_{\Pi} \approx \frac{\sigma_{\varpi}}{\sqrt{m}} \ . \tag{4.5}$$

With a 5 s recording sampled at a frequency of 40 kHz, the standard error for the average

power consumption is less than ±2.3 mW. With a t-value of 1.96, the confidence interval for the parameter is ±4.5 mW. For a more representative result, the power is typically provided as a consumption per unit of span of the electrode. The span in this study is $L = 10$ cm, leading to a confidence interval of ±45 mW/m.

The force efficiency η_A is defined as the ratio of the thrust over power, as shown in Equation 3.11. The standard error σ_η can be derived from the standard simplified error propagation formulae:

$$\begin{aligned}
\sigma_\eta &= \sqrt{\left(\frac{\partial \eta_\mathrm{A}}{\partial T_\mathrm{A}}\sigma_T\right)^2 + \left(\frac{\partial \eta_\mathrm{A}}{\partial P_\mathrm{A}}\sigma_P\right)^2}\ , \\
&= \sqrt{\left(\frac{\sigma_T}{P_\mathrm{A}}\right)^2 + \left(\frac{T_\mathrm{A}\cdot\sigma_P}{P_\mathrm{A}^2}\right)^2}\ , \\
\sigma_\eta &= \eta_\mathrm{A}\sqrt{\left(\frac{\sigma_T}{T_\mathrm{A}}\right)^2 + \left(\frac{\sigma_P}{P_\mathrm{A}}\right)^2}\ ,
\end{aligned} \tag{4.6}$$

where σ_T and σ_P are the previously derived standard errors for the thrust and power (respectively 60 μN/m and 45 mW/m). Replacing the thrust and power with their full scale values in Equation 4.6 would not be representative of the experiment. Equation 4.6 can be utilised to express the standard error for the force efficiency as a percentage of the value. By employing a maximum value of the thrust and minimum value of the power, that were achieved in the experiments, the maximum standard error can be given. Starting from Equation 4.6:

$$\frac{\sigma_\eta}{\eta_\mathrm{A}} = \sqrt{\left(\frac{\sigma_T}{T_\mathrm{A}}\right)^2 + \left(\frac{\sigma_P}{P_\mathrm{A}}\right)^2}\ . \tag{4.7}$$

In the experiments, the measured thrust reached a maximum of 5.77 mN/m on the second repeat of run number 13, and the measured power reached a minimum of 2.90 W on the second repeat of run number 29. Hence, a maximum of 6 mN/m and minimum of 2 W/m can be considered, leading to a standard error on the force efficiency of 2.5%. An upper bound can be found by utilising the maximum force efficiency captured with the set up. This maximum amounts to 174 μN/W on the second repeat of run 25, resulting in a maximum standard error of 4.34 μN/W. The standard errors for the thrust generation, power consumption and force efficiency for one data point obtained with the test rig are summarised in Table 4.1.

Parameter	T_A	P_A	η_A	
Standard	0.060	0.045	2.5	$\leq$ 4.34
error	mN/m	W/m	%	μN/W

Table 4.1: Confidence intervals of the thrust, power and force efficiency measurements.

The force measurement test rig has been found to provide accurate measurements

of small forces up to the maximum threshold of 10 mN (for a maximum thrust of 100 mN/m of a DBD). In its final design, the sensors and wires have been protected against the electromagnetic interference of the amplifier, and the sources of mechanical friction have been reduced so that they are insignificant compared to the measured forces. The test rig is able to capture a maximum force of 10.8 mN. In order to verify the measurements of the test rig, total pressure measurements have also been carried. The apparatus involved in this verification study are presented in the next section.

4.3 Total Pressure Measurement

4.3.1 Glass Capillary Pitot Tube

A capillary total probe was produced for precise flow measurements near the surface of DBDs. The tube is composed of three parts. A 3D printed tube was manufactured in PLA thermoplastic. A metal tube with an internal diameter of 1 mm, an outer diameter of 1.6 mm and a length of 50 mm is fitted to the upper end of the 3D printed part. A glass capillary tube with an internal diameter of 0.8 mm, an outer diameter of 1 mm and a length of approximately 15 mm is fitted at the bottom end of the 3D printed part. The resulting assembly is shown in Figure 4.10. The glass tube protrudes from its PLA support by approximately 10 mm. The support of the glass tube has a U-shape, and is sealed with super-glue and Kapton tape (35 μm thickness).

Figure 4.10: Capillary total pressure probe utilised in the study.

In order to assess the design, the capillary probe was compared to a Pitot static tube, using the anemometer described in Section 4.3.2. Both tubes were placed in the centre of the test section of an open return closed test section wind tunnel, with a test section of 343 mm $\times$ 249 mm. The wind tunnel is able to reach 10 m/s and the speed is set by a rotary switch dial (1 units on the dial approximatively correspond to 1 m/s). Data were acquired for each probe individually, with the total pressure obtained from the probe, and atmospheric pressure obtained at the reference pressure port of the anemometer. The anemometer was set to convert the measured dynamic pressure to a velocity assuming ISA conditions (air density 1.225 kg/m^3). The two data series

are compared in Figure 4.11 for equal wind tunnel speeds. The reference line in the figure shows the ideal situation of a perfect agreement between the capillary and Pitot tubes. The difference between the capillary and Pitot measurements is also displayed in Figure 4.11. The difference is given as a percent of the Pitot measurements. The results demonstrate the new capillary total pressure probe agrees with a standard Pitot probe within ± 2% of the data acquired with the Pitot probe. Overall, the capillary was judged able to provide proper measurements.

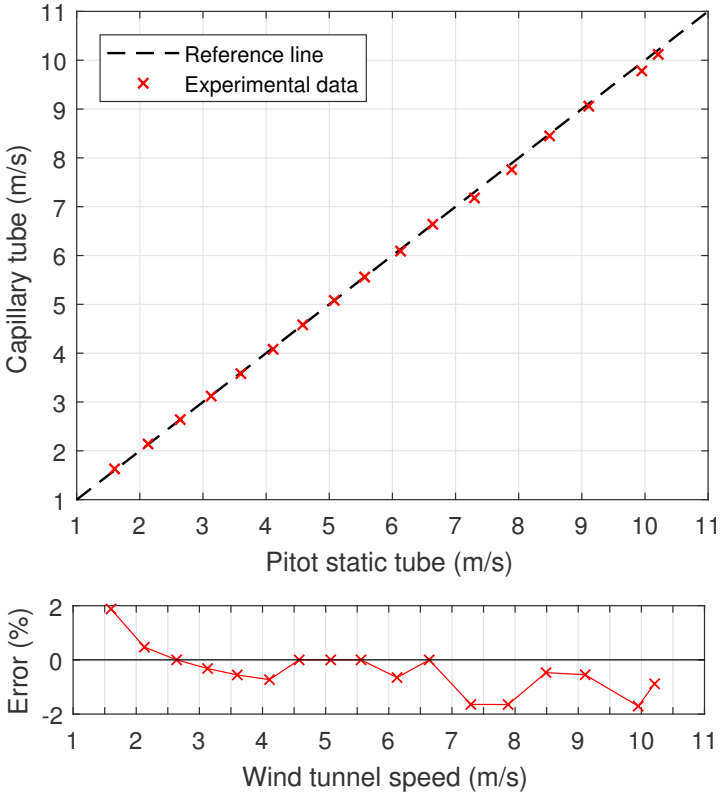

Figure 4.11: Validation of the capillary total probe: (top) capillary tube versus standard Pitot tube and (bottom) difference between the capillary and Pitot measurements.

4.3.2 Anemometer

The total pressure probe is connected to a Furness Control FCO332 differential pressure transmitter, as showed in Figure 4.13. The device can measure differential pressures up to 150 Pa with a resolution of 0.1 Pa and an accuracy of ±0.5% of the reading. The transmitter was connected to a computer through a standard RS232 serial port. An in-built filter can be activated, in order to damp the fluctuations over several seconds. The transmitter was set to average the data over 5 s for each data point. The anemometer can be set to provide velocity readings, for instance, the measurements performed in the verification of the capillary probe in Section 4.3.1. In the rest of the study, the anemometer was configured to provide with pressure measurements.

4.3.3 Traverse System

A two-dimensional traverse system can be used to move the probe in a vertical plane perpendicular to the plasma actuator (i.e. to the electrodes). The traverse consists of two EZ-Limo linear actuators. An EZA4E030MC controls the vertical motion (z-axis) with an accuracy of ± 0.02 mm at a maximum speed of 300 mm/s, and an EZS4E050MC drives the horizontal displacement (x-axis) with an accuracy of ± 0.02 mm at a maximum speed of 400 mm/s. A platform, similar to the one used for the force-measurement test rig, is screwed to a wooden support. The platform allows the placement of DBDs as for the thrust-measurement experiment. To suppress the bending of the wooden support, it is reinforced by a metal C-beam on its bottom side. For safety reasons, any conductive part is connected to the traverse frame, which is itself grounded. The capillary tube is screwed to a plastic and wood head that isolates it from the vertical actuator. The pressure transmitter is screwed to the frame of the traverse, and enclosed in a Faraday cage made of metallic mesh. Figure 4.12 shows the isolated traverse system, and the attachment points for the probe and actuator. Figure 4.13 shows the installation of a DBD actuator ready for testing and of the pressure transmitter. It can be remarked the plastic tubing linking the transmitter to the capillary probe is held against the vertical actuator so that it does not fall on the actuator. The tubing that connects the capillary probe to the anemometer was secured against the linear actuator, to avoid it from falling towards the DBD actuator beneath. The data points are acquired with a 3 s delay after the motion is performed by the actuators. Several wind off tests did not capture erroneous pressure readings during the displacement of either one of the two actuators. The atmospheric conditions are recorded with the equipment presented in subsection 4.2.6.

4.4 Coordinate System

The parametric study is performed on the previously described actuators. The DBDs measure 110 mm in span, for a width of 70 mm. The thickness can be 0.8 or 3.2 mm. The thickness of the dielectric is added to the length of the lever of the test rig to calculate a corrected amplification factor. As a result, the force is estimated at the surface of the dielectric layer, regardless of its thickness. For an actuator of thickness t in mm, the amplification factor acquired by the test rig is $(340.5 + t)/37$. A 0.8 mm thick dielectric results in a amplification of 9.22, and a 3.2 mm thick dielectric leads to a force amplification of 9.29. All the force data were corrected, in order to cancel the effect of the thickness of the dielectric on the measurement method.

As reported previously, the actuators are screwed to the top platform of the test rig with nylon bolts. The arrangement is displayed in Figure 4.14 along with its characteristic dimensions. The figure also shows the selected (x, y, z) coordinate system used in the study:

(x) Chord-wise coordinate. Direction: from the air electrode to the encapsulated elec-

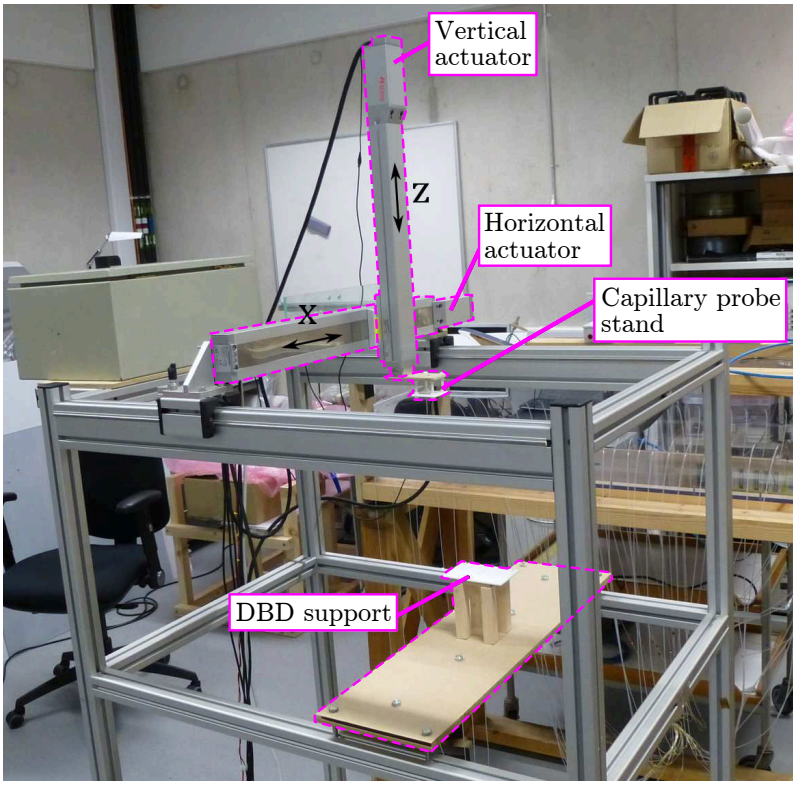

Figure 4.12: Traverse system for the aerodynamic study.

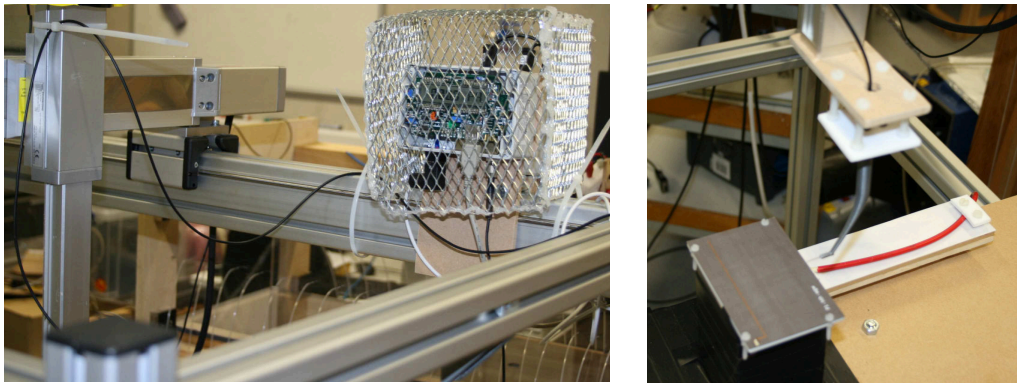

Figure 4.13: Pressure transmitter in its Faraday cage (left) and DBD installed in the traverse system (right).

trode, parallel to the wall.

(z) Wall normal coordinate. Direction: perpendicular to the wall, pointing upwards.

(y) Span-wise coordinate. Direction: parallel to the long edge of the exposed electrode, oriented so that (x, y, z) forms a right-handed system.

The wall jet induced by the plasma discharge follows the $+x$ direction. The $+x$ direction will thus be called the stream-wise direction, and contrariwise, the $-x$ direction will be named the upstream direction. The wall jet travels from the front to the rear of the actuator, as displayed in Figure 4.14.

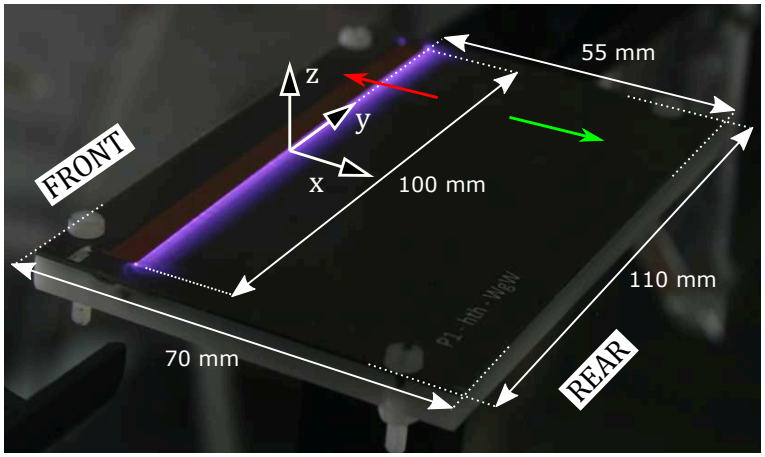

x	Chord-wise direction. → Stream-wise direction. → Upstream direction.
y	Span-wise directions.
z	Wall normal direction.

Figure 4.14: DBD actuator and its characteristic dimensions.

4.5 Mean Results and Accuracy of the Results

4.5.1 Accuracy of the Measurements

The accuracy of the measurements is discussed in Section 4.2.7. The parameters are summarised in Table 4.2 and the error of the output parameters are summarised in Table 4.3.

In **??**, the errors are given for single data points acquired with the described test rig, but also for means over various sets of data points. The means over the three data points correspond to means other the three tests of each run. The means over 24 observations represents the mean variables averaged over a quarter of the test matrix. This corresponds to the four means displayed on an interaction plot for instance. The means over 48 data points encompass half of the test matrix. They are employed in the calculation of the effects (see Equation 3.13), and appear on the main effect plots. Finally, the mean over 96 observations represents the grand average over the entire test matrix. As the grand average (average over the 96 data points) is utilised in several calculations, it is given for information purposes. The standard errors of the means are obtained through the standard propagation of uncertainty. For a mean value, the standard error is calculated by dividing the standard error of a single data point, by the square-root of the number of data points that are averaged. The confidence intervals are derived from the standard errors by multiplying by the corresponding two-tailed t-values for a confidence level of 95%. For degrees of freedom of 3, 24, 48 and 96,

	Variable name	Symbol	Unit
FACTORS	Exposed electrode width	w_1	mm
	Encapsulated electrode width	w_2	mm
	Gap between the electrodes	g	mm
	Exposed electrode height	h_1	μm
	Encapsulated electrode height	h_2	μm
	Dielectric thickness	t	mm
	Dielectric permittivity	ε_r	-
	Applied peak-to-peak voltage	V	kV_{pp}
	Signal frequency	f_{ac}	kHz
	Electrode span	L	0.10 m
RESPONSES	Generated thrust	T_A	mN/m
	Electric power	P_A	W/m
	Force efficiency	η_A	μN/W

Table 4.2: Summary of the parameters and their units.

these t-values are respectively 3.18, 2.06, 2.01 and 1.98. It can be noted that the table presents the error for the force efficiency through two values. The percentage of the force efficiency gives a better representation of the error, the second value is an upper bound relying of the maximum thrust, minimum power and maximum efficiency obtained through the entire experimental campaign. To finish, it can be remarked that a 99% confidence is reached at t-values of 5.84, 2.80, 2.68 and 2.63 for degrees of freedoms of 3, 24, 48 and 96.

4.5.2 Mean Results over the Repeats

The mean results are presented in Table 4.4. The presented values are the means over the repeats. For each run, this represents an average over three values. The standard deviations are also provided in the table, and can be compared to the errors reported in Table 4.3 for the mean over three data points. The standard deviation over the three tests of each run provides the repeatability of the measurements. The atmospheric conditions are presented in the same manner in Appendix D.

The cumulative probability of the standard deviations showed 70% of the runs fall within the confidence intervals regarding the thrust and efficiency. Regarding the power, more than 90% of the standard deviations stand out of the confidence interval. Since the chosen confidence level is 95%, either the rig is not as accurate as predicted, or the DBD actuators have greater variability in their performance. As a consequence, aerodynamic measurements were latter performed to verify the results obtained with

Parameter		T_A	P_A	η_A	
Single point	**Standard error**	0.060 mN/m	0.045 W/m	2.5 %	≤ 4.34 μN/W
Mean over 3 points	**Standard error**	0.035 mN/m	0.026 W/m	1.4 %	≤ 2.51 μN/W
	Confidence interval	0.110 mN/m	0.083 W/m	4.6 %	≤ 7.97 μN/W
Mean over 24 points	**Standard error**	0.012 mN/m	0.009 W/m	0.5 %	≤ 0.89 μN/W
	Confidence interval	0.025 mN/m	0.019 W/m	1.1 %	≤ 1.82 μN/W
Mean over 48 points	**Standard error**	0.009 mN/m	0.006 W/m	0.4 %	≤ 0.63 μN/W
	Confidence interval	0.017 mN/m	0.013 W/m	0.7 %	≤ 1.26 μN/W
Mean over 96 points	**Standard error**	0.006 mN/m	0.005 W/m	0.3 %	≤ 0.44 μN/W
	Confidence interval	0.012 mN/m	0.009 W/m	0.5 %	≤ 0.88 μN/W

Table 4.3: Accuracy of the measurements for single data points and for means over 3, 24, 48 and 96 data points.

the test rig (detailed in Chapter 8). Good agreement was found between the data obtained with the two measurement techniques. Therefore, the present study cannot conclude on the cause of this phenomenon. In conclusion, the thrust and force efficiency measurements have a good repeatability for each run, but the repeatability of the power measurements is greater than their expected inaccuracy due to experimental error.

4.6 Sources of Error during the Experiments

Throughout the experiments, several phenomena were observed and could represent additional sources of error.

4.6.1 Types of Plasma Discharges

Between different runs, several types of plasma discharge were evidenced. As an example, long exposure pictures are presented in Figure 4.15. From left to right, the discharges shown in the figure are the filamentary, streamer and glow discharges (refer to Section 2.4.1). The different types of discharge can have distinct behaviours (see Section 2.3.2). For instance, Thomas et al. [45] reported a scaling of the thrust with

Run	T_A	(mN/m)	P_A	(W/m)	η_A	(μN/m)
order	Mean	Dev.	Mean	Dev.	Mean	Dev.
1	4.98	± 0.24	70.0	± 0.7	71.1	± 2.7
2	0.01	± 0.02	3.3	± 0.1	3.3	± 5.8
3	0.49	± 0.01	8.7	± 0.1	56.7	± 1.9
4	0.02	± 0.02	3.3	± 0.1	6.1	± 5.7
5	0.13	± 0.02	3.4	± 0.0	38.2	± 6.7
6	2.96	± 0.14	71.9	± 1.2	41.1	± 1.3
7	0.07	± 0.06	24.6	± 0.1	3.0	± 2.6
8	0.06	± 0.10	3.4	± 0.3	17.7	± 30.7
9	0.44	± 0.01	9.5	± 0.3	46.6	± 0.9
10	0.08	± 0.02	25.4	± 0.5	3.3	± 0.6
11	0.76	± 0.16	65.7	± 0.8	11.5	± 2.3
12	0.76	± 0.11	9.6	± 0.3	78.6	± 9.2
13	5.44	± 0.47	99.9	± 8.3	54.6	± 3.6
14	1.30	± 0.05	11.1	± 1.1	117.7	± 13.6
15	0.07	± 0.04	25.5	± 0.3	2.7	± 1.4
16	0.47	± 0.01	63.8	± 0.2	7.4	± 0.1
17	0.77	± 0.10	34.2	± 3.0	22.3	± 2.2
18	1.49	± 0.05	14.7	± 0.2	101.6	± 2.2
19	0.34	± 0.12	4.1	± 0.1	81.7	± 25.8
20	1.17	± 0.02	10.5	± 0.1	110.6	± 2.1
21	1.32	± 0.03	29.1	± 0.6	45.5	± 1.3
22	0.32	± 0.05	5.1	± 0.1	63.6	± 11.5
23	0.20	± 0.02	3.5	± 0.1	59.0	± 5.0
24	5.16	± 0.20	84.6	± 4.9	61.1	± 1.4
25	1.56	± 0.14	9.8	± 0.1	159.3	± 12.4
26	0.06	± 0.05	25.8	± 0.1	2.4	± 1.8
27	0.59	± 0.01	66.6	± 0.1	8.9	± 0.2
28	3.64	± 0.63	69.8	± 1.6	52.1	± 8.1
29	0.02	± 0.04	3.0	± 0.1	7.8	± 11.6
30	2.28	± 0.22	18.9	± 0.3	120.6	± 10.0
31	0.58	± 0.82	25.3	± 0.4	23.1	± 32.7
32	0.03	± 0.03	25.8	± 0.2	1.2	± 1.1

Table 4.4: Mean and standard deviation of the results over the repeats (runs detailed in Table A.2).

two different power laws of voltage. The thrust increased with voltage to the power of 3.5, and reduces to 2.3 with a greater voltage, as the glow discharge transitioned towards filamentary discharge. As soon as the discharge has fully transitioned, the DBD saturates, and the thrust stagnates. These types of discharge do not represent an

additional source of error in the measurements. However, they add additional complications to the analysis of the results with a DOE. The DOE analysis relies on a standard linear regression over all the runs, when the different discharges can produce different scaling laws for the output parameters. Besides, if a transformation of the response is needed for the analysis of the result, the transformations are impacted by the various relationships of the output parameters with the design variables.

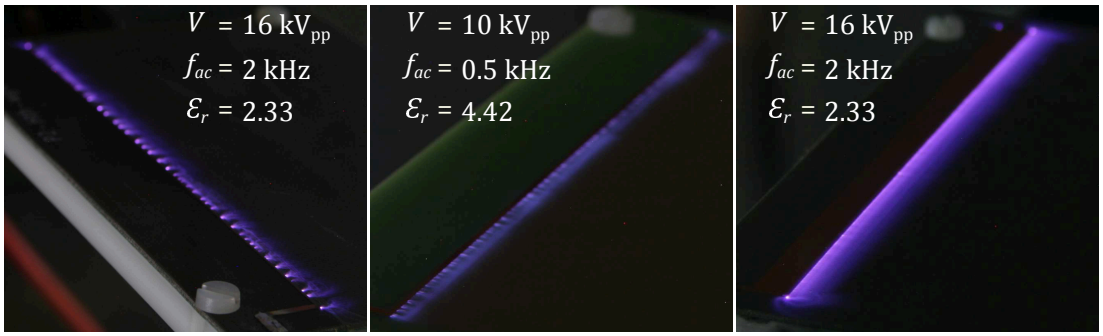

Figure 4.15: Long exposure pictures of three different discharges (filamentary on the left to glow on the right). From left to right, runs 21, 22 and 24.

4.6.2 Parasitic Plasma Generation

A parasitic plasma discharge was observed to take place around the high-voltage copper wire, particularly at higher voltage. The discharge is much weaker than the discharge of the DBDs, due to the lack of a well conducting ground electrode. A long exposure picture was modified in order to present the parasitic discharge in Figure 4.16. In Figure 4.16b, the brightness, contrast and colour saturation have been modified in the wire region to improve its visibility. Because the generated plasma is homogeneously spread around the wire over its entire length, and does not seem to be produced by the interaction between the wire and an external grounded part, it can be assumed it is symmetrical by rotation around the wire, and consequently does not generate thrust. The parasitic discharge is the result of the low insulation of the thin wire. The insulating layer being small (approximately 6.5 μm), it does not reduce the electric potential between the air and wire below the electric breakdown of the air. The main impact of the parasitic discharge is the possibility of an over-consumption of power due to the discharges.

4.6.3 Backward Plasma Discharge

During the experiments, it was regularly seen that the exposed electrode could ignite plasma on both the front and rear edges. This effect was particularly noticeable on the actuators having a narrow exposed electrode. This discharge is certainly produced by the curved electric field that links the front edges of the two electrodes. With a narrow air electrode, the distance between the two edges reduces, and thus, the electric field amplitude increases and can reach the breakdown of the air. This phenomenon

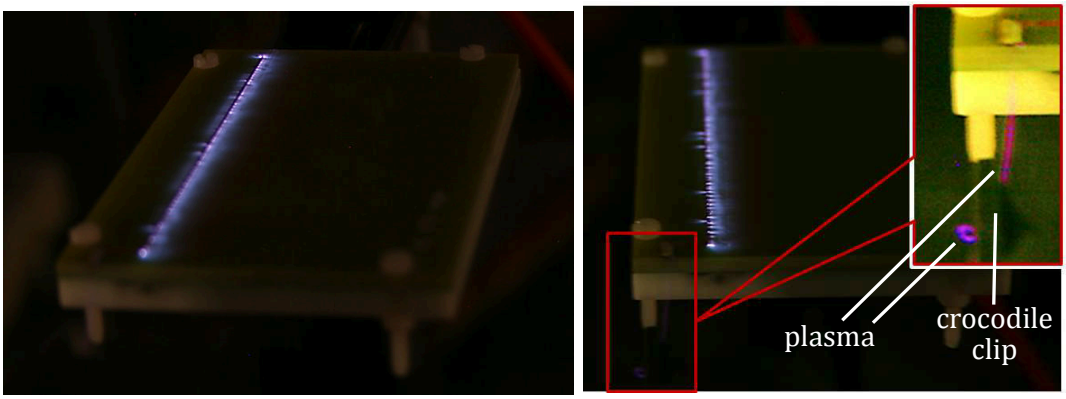

(a) (b)

Figure 4.16: Long exposure picture of run number 6 (15.7 kV_{pp}, 2.0 kHz) highlighting the plasma region (a) and the HV wire plasma generation (b).

is displayed in Figure 4.16a but also in Figure 4.17. In Figure 4.17, the two actuators are similar with an 0.8 mm thick PTFE layer, a 1 mm gap and 35 μm thick electrodes, and are both supplied with 16 kV_{pp} and 2 kHz, but with either wide exposed and encapsulated electrodes in Figure 4.17a (5 mm and 50 mm), or narrow electrodes in Figure 4.17b (0.5 mm and 10 mm). The second discharge blows in a counterflow direction, leading to a loss of thrust. As for the type of discharge, this phenomenon is expected to modify the behaviours of certain actuators, making it difficult for the DOE analysis to fully model the thrust generation. The dual streamer discharge appearing in Figure 4.16 proves how both the type of discharge and counter-streamwise discharges can also interact. In the rest of the thesis, if an electrode generates both the front and rear facing discharges, the discharge will be called dual, while it will be described as single, if only the rear facing discharge is produced.

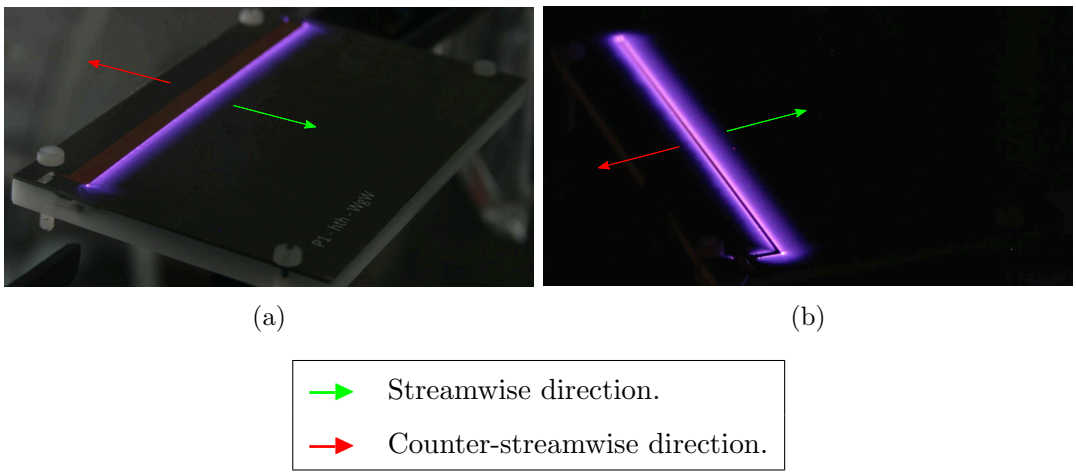

(a) (b)

Figure 4.17: Long exposure pictures of two similar DBDs, with a wide (left) or narrow (right) exposed electrode.

4.7 Known External Parameters and Potential Sources of Error

4.7.1 Glue Layer

As it was explained in Section 4.1.1, the DBD actuators that have two different electrode thickness consist of two PCBs bounded together with an epoxy glue (see Figure 4.14). The effect of the glue can be analysed separately to determine whether it affects the results. As for the DOE analysis, the change in the mean of the three output parameters caused by the glue can be focused on. The means are obtained over half of the tests, representing 48 data points. The results are given in Table 4.5, and also show the effects (the difference between the two means).

Glue:	**No**	**Yes**	Effect
T_A (mN/m)	1.16	1.18	0.02
P_A (W/m)	28.6	29.2	0.4
η_A (μN/W)	45.4	46.6	1.2

Table 4.5: Effect of the glue layer on the results.

The change in the means can be compared to the confidence intervals presented in Table 4.3 of 0.017 mN/m, 0.013 W/m and 1.26 μN/W. With effects similar to the errors, the glue does not seem to impact the thrust generation or force efficiency. The effect on the power consumption is three times higher than the inaccuracy. As mentioned previously (see Section 4.5.2), the error of the power recording system might be underestimated. Moreover, the power lost by Joule heating through the dielectric, due to the polarisation of the charges has been reported to scale linearly with the permittivity [2]. Hence, the altered dielectric layer might lead to a slight overconsumption of power for the PTFE based actuator. In the DOE analysis, since the effects are compared to the variance in the data rather than the error of the instrument, this effect is also negligible compared to the standard deviations presented in Table 4.4. In conclusion, the inhomogeneity of the dielectric does not affect the results significantly, and can be ignored from the DOE analysis.

4.7.2 Atmospheric Conditions

The mean atmospheric conditions for all the runs are provided in Appendix D. The pressure, temperature and humidity respectively fluctuates between nearly 985 and 1025 hPa, 19°C and 23°C, and 25% and 65% of relative humidity. If a thrust coefficient could be defined, in order to remove the dependency of the thrust on the atmospheric conditions, the scaling of the thrust produced by the actuator against the atmospheric variable is not certain. One way to verify the possible impacts of the atmospheric conditions on the thrust and power consists in visualising the distributions of the standard

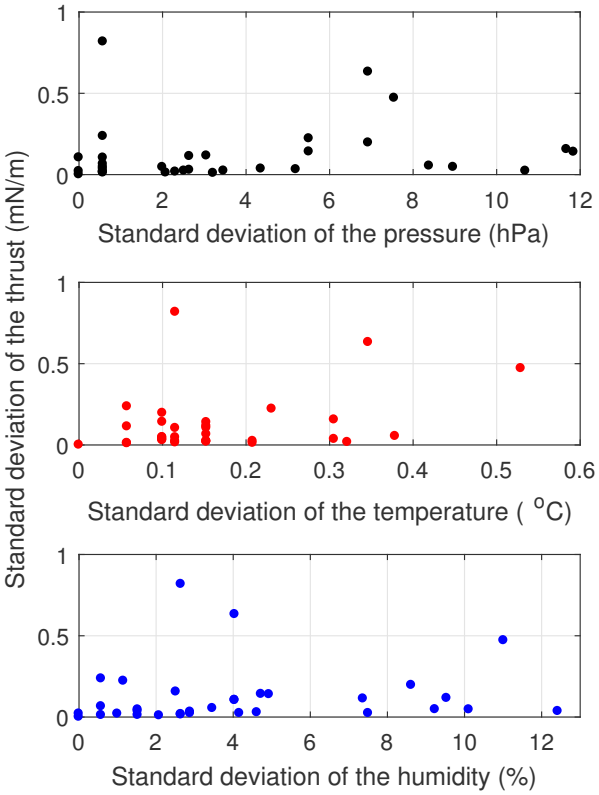

Figure 4.18: Standard deviations of the thrust generation against the standard deviations of the atmospheric conditions for all the runs.

deviations of the thrust or power measurements against the standard deviations of the atmospheric conditions for each of the runs. If the variations of the thrust or power were found to depend on the variations in the atmospheric parameters, it would indicate the atmospheric variables have a non negligible impact on the performance of the DBDs. The aforementioned distributions are displayed in Figure 4.18 for the thrust and Figure 4.19 for the power.

Both figures do not highlight any particular influence of the variations of the atmospheric pressure, room temperature or relative humidity on the thrust generation or power consumption. In addition, the presented deviations are, for most, smaller than the calculated confidence levels of 7.35 hPa, 0.73°C and 5.50 % (see Appendix D). As a consequence, the atmospheric conditions do not seem to greatly affect the performance of the actuators in this study.

In the next chapter, the results of the DOE analysis are presented for each of the three output parameters (thrust generation, power consumption and force efficiency). The different aspects of the DOE analysis are discussed in Section 3.3.

4.8 Summary

The present chapter has highlighted the nine different input parameters. Moreover, the design and accuracy of the created test rig has been presented. The confidence intervals

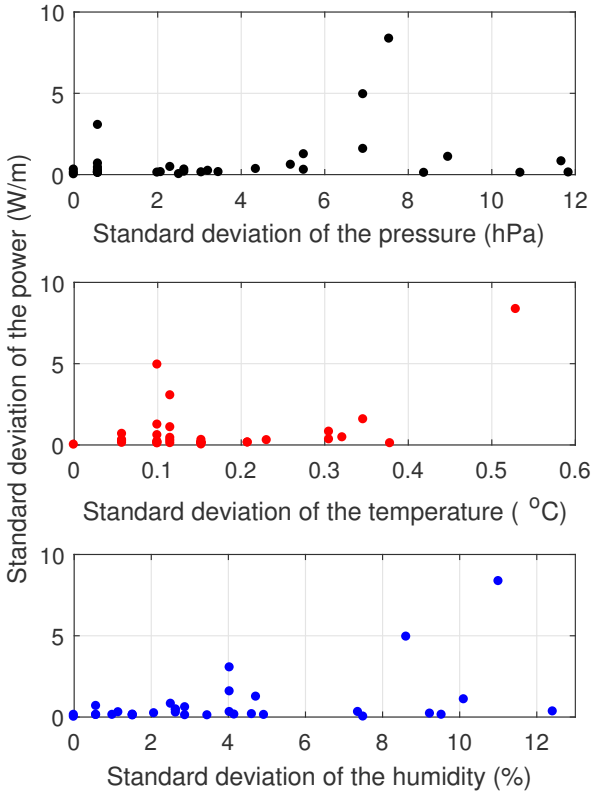

Figure 4.19: Standard deviations of the power consumption against the standard deviations of the atmospheric conditions for all the runs.

for the thrust generation, power consumption and force efficiency have been calculated for the different sizes of dataset utilised in the study. Furthermore, the repeatability of the measurements over the three tests for each run has been assessed and revealed the power consumption is measured with a repeatability slightly greater than the calculated accuracy, but much lower than the power measurements. Finally, some possible sources of error have been investigated, and the presence of glue for certain actuators and the variations of the atmospheric conditions have not been observed to impact the results significantly. Overall, the test rig is judged to provide proper results for the power consumption and thrust generation, with inaccuracies much lower than the typical measurements. In conclusion, the force measurement test rig can measure the thrust generation and power consumption accurately, and the external sources of error that have been found do not impact the results significantly. In the next three chapters, the DOE analyses of the thrust generation, power consumption and force efficiency are presented.

Chapter 5

Parametric Study for the Thrust Generation

The present chapter provides the analysis of the results for the thrust generation. Firstly, the mathematical validity of the analysis is discussed. Secondly, the significant effects are ranked and summarised. Explanations of the effects are given from known physical phenomena or from literature. Finally, the linear regression model derived from the DOE analysis is briefly presented. Its analysis is however treated in Chapter 8.

5.1 Validity of the Analysis

As discussed in Section 3.3.8, the DOE analysis relies on the assumption that the residuals of the linear regression are normally distributed. This assumption is validated by studying the square-root of the thrust generation. This mathematical correction does not impact the significance of the results, and it simply evidences that the significant effects increase in a non-linear trend. However, the linear regression models the square-root of the thrust generation. The residual plots for the thrust generation are presented in Figure 5.1 and are discussed below.

The histogram of the residuals (Figure 5.1a) does not exhibit a significant skewness. The normal probability plot (Figure 5.1b) shows the residuals are aligned, and thus follow a normal distribution with only a few outliers. The distributions of the residuals against the fitted values (Figure 5.1c) and against the observation orders (Figure 5.1d) do not follow any particular trend, and appear as random signals. Consequently, the DOE analysis of the square root of the thrust generation is mathematically valid.

5.2 Ranking of the Significant Parameters

5.2.1 Selection of the Significant Effects

In order to identify the significant parameters, the standardised effects of the factors and their interactions on the thrust generation are represented on the half-normal plot

in Figure 5.2. The distribution of the standardised effects is compared to two lines in the figure. The blue line represents a normal distribution having the same two-tailed t-value as the study (1.98 for 96 tests at a confidence level of 95%). If the effects were to follow this distribution, they would be insignificant. The dash line illustrates the best fitting of a normal distribution to the data. The more the standardised effects exceeds the predictions of the reference line, the more they influence the thrust generation.

In Figure 5.2, nineteen effects are significant, and form the model. Minitab calculates how much of the variance (square of the standard deviation) of the data can be imparted to each effect. This is done by dividing the sum-of-squares of a particular effect (see Equation 3.20) by the total sum-of-squares of the data. The more a design parameter contributes to the variance of the results, the more it affects the

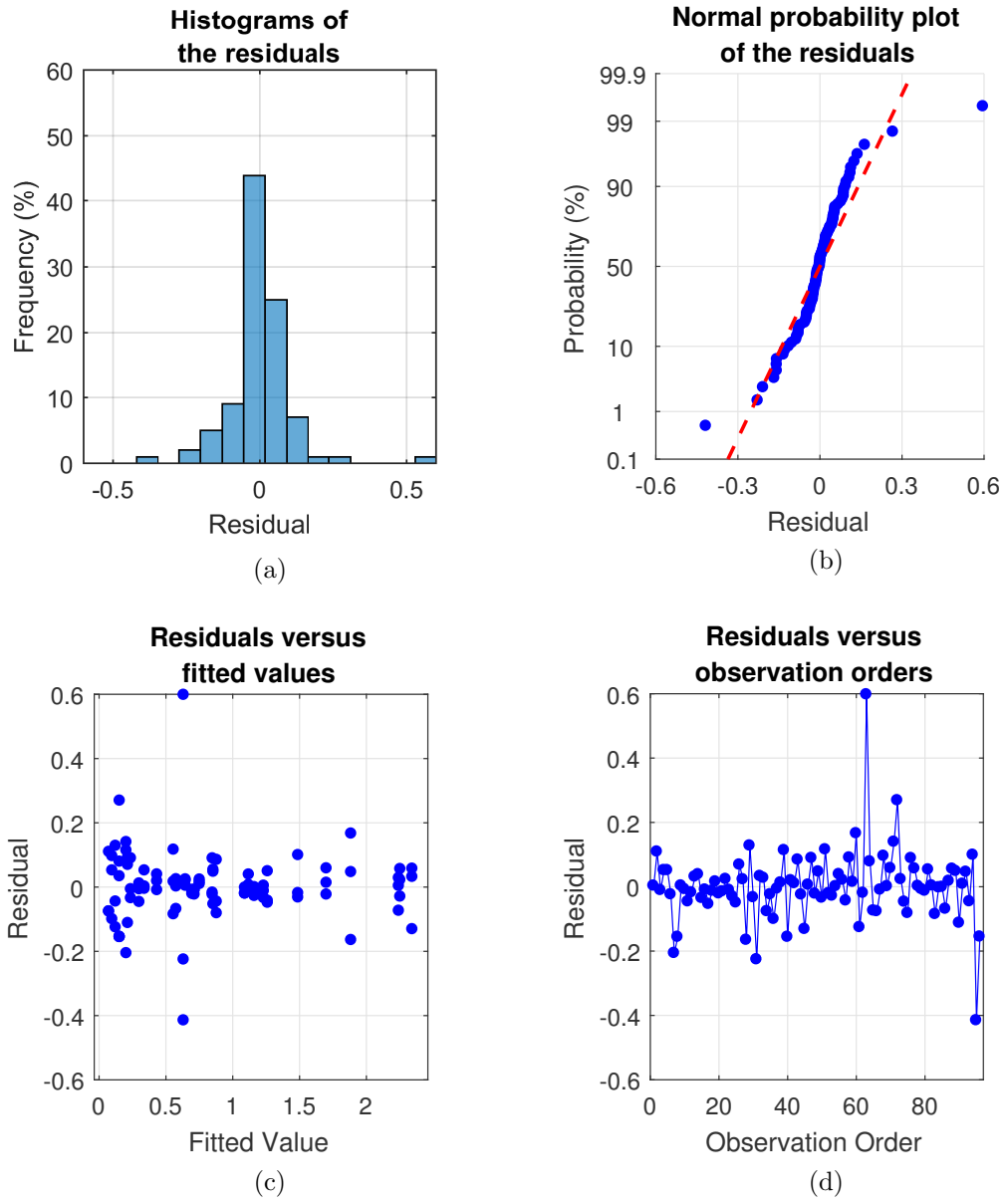

Figure 5.1: Residual plots of the analysis of the thrust generation.

output parameter. In total, the nineteen model terms are responsible for 97.39% of the total variance. The most significant effects are the voltage (V), inter-electrode gap (g), dielectric thickness (t) and frequency (f_{ac}), and they respectively contribute to 49.92%, 13.52%, 7.72% and 7.31% of the total variance (78.47% altogether). The other model terms only contribute to 3% or less each. The nineteen significant standardised effects are displayed in the Pareto chart in Figure 5.3. Since the standardised effects are absolute values, the bars are coloured by the signs of the effects. For instance, the effect of the voltage (V) is positive, meaning an increase in the supplied voltage results in an increase in the thrust generation. The Pareto chart shows that all the selected standardised effects are greater than the critical t-value of 1.98. It should be noted that most of the significant interaction effects are aliased. The mathematical aliases occur due to the design of the test matrix (see Section 3.3.2). The mathematical analysis is unable to determine whether an effect is caused by one parameter or its alias. In order

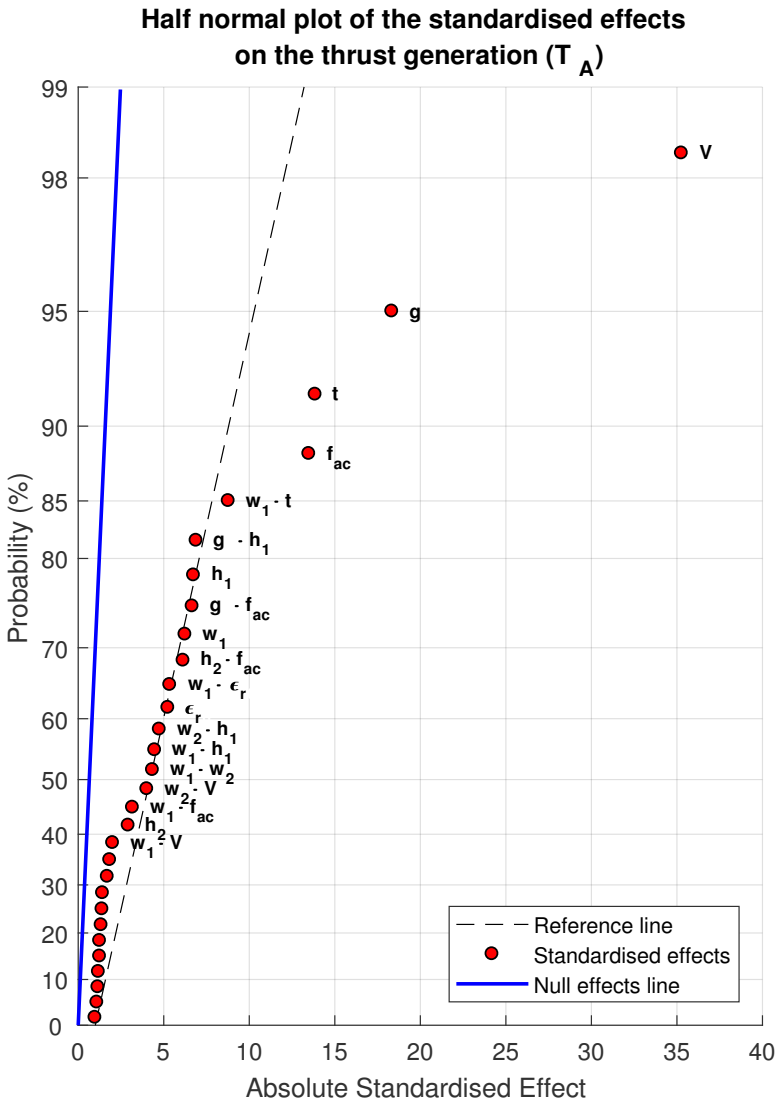

Figure 5.2: Half-normal plot of the standardised effects on the thrust generation.

to determine which of the aliased effect are factual, an analysis of the physical phenomena is required. Moreover, as previously reported, the t-value for a 99% confidence level is 2.63 for 96 tests. From the nineteen standardised effects appearing in Figure 5.3, eighteen are greater than this critical value. Consequently, most of the effects take place due to the changes in the design parameters. The effects and interactions are discussed in the next paragraphs.

5.2.2 Discussion of the Significant Effects

1 - Voltage

The first significant effect is the voltage. As explained previously, it contributes to 49.92% of the total variance of the thrust measurements. The effect is represented in the main effect plot in Figure 5.4.

The main effect plot displays the change in the mean value of the thrust generation,

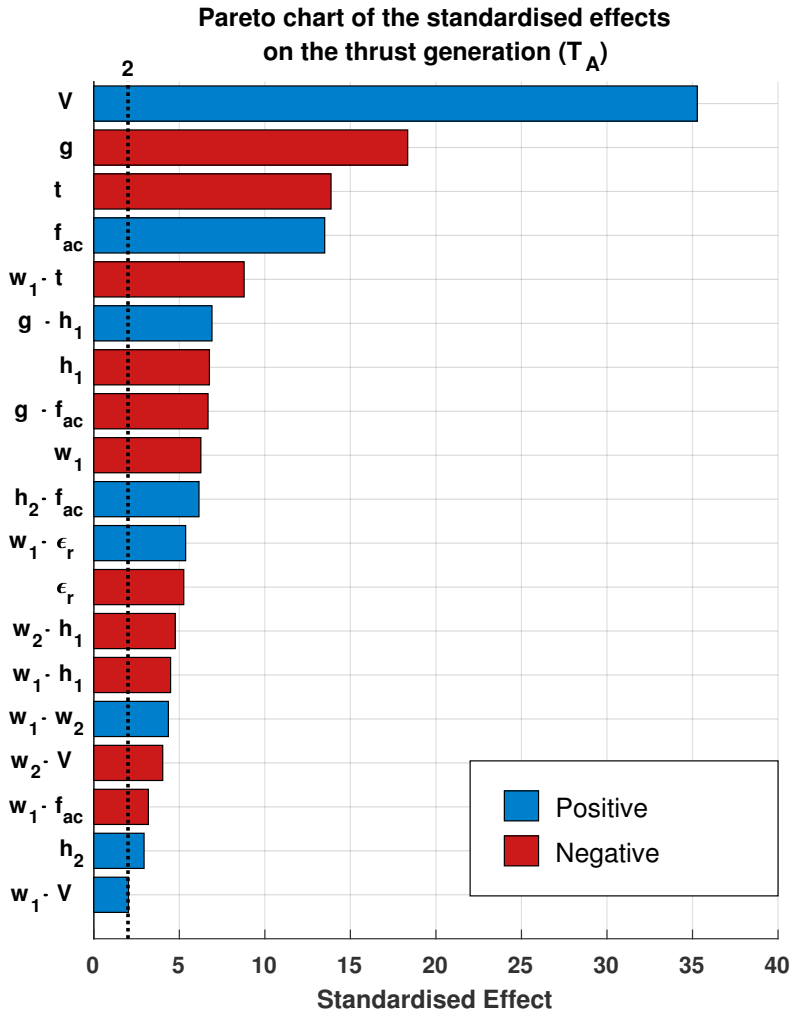

Figure 5.3: Pareto chart of the standardised effects on the thrust generation, coloured by sign of the effect.

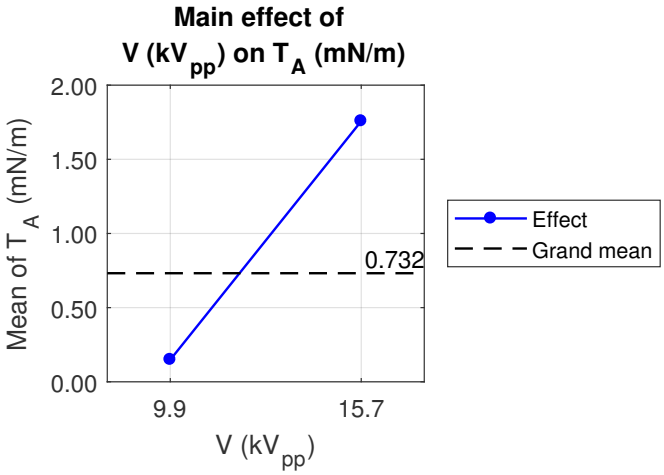

Figure 5.4: Main effect of the voltage on the thrust generation.

due to a change in the level of the voltage. The dash line represents the grand average of the thrust over all the ninety-six runs. It can be noted the mean of the thrust at 15.7 kV_{pp} has a greater separation from the grand average than the mean of the thrust at 9.9 kV_{pp}. This is a consequence of the transformation of the response. The transformed response (square-root of the thrust), although less useful, would present equal separations of each means from the grand average.

The main effect plot highlights an increase of the voltage from 9.9 to 15.7 kV_{pp} results in an increase of 1.61 mN/m on average. It must be remarked, that this value is a difference in the average of the thrust generated by all the runs at high voltage, minus the average of the thrust produced by all the runs at low voltage. As a consequence, this effect, as all the following ones, must not be taken as an absolute change in the output parameter (here thrust generation) that could be obtained with a particular DBD actuator when modifying the input parameter (here the voltage). As summarised in Section 3.1.1, the thrust was reported to depend on the voltage to the power of 2 to 3.5 [7, 45]. If the relationship cannot be verified with the DOE analysis, the effect of the voltage is positive and comes first in the ranking. The scaling of the thrust with the voltage is presented in Chapter 8. The voltage is linked to the amplitude of the electric field between the electrodes. A greater voltage results in a stronger electric field. Kriegseis et al. [77] estimated the drift velocity (v_d) of the charged particles by multiplying the electric field between the electrodes by the ion mobility (κ). The amplitude of the electric field (E) can be estimated by dividing the voltage (V) by the distance between the electrodes (l). Hence, the drift velocity can be approximated through the formula (see Equation 2.22):

$$v_d = \kappa E \approx \kappa \frac{V}{l} \ . \tag{5.1}$$

Consequently, and increase in the applied voltage increases the drift velocity of the charged particles. The collisions impart more kinetic energy to the neutral molecules,

which results in a higher momentum induction into the free-stream.

In addition, the plasma extent [1–3, 6, 8] increases with the voltage. Consequently, increasing the voltage applied to the DBD widens the plasma discharge, which increases the volume of charged particles that collide with the neutral air.

Therefore, an augmentation in the voltage both increase the number of charged particles in the plasma and the strength of the electric field that drives these particles. These phenomena explains the large positive effect of the voltage on the thrust generation.

2 - Inter-electrode gap

Before analysing the effect of the gap, it should be noted that Equation 5.1 is only an estimation, since it does not consider the difference of permittivity between the air and dielectric material. The dielectric layer has a higher permittivity than the surrounding air. From Coulomb's law, the force $\mathbf{F}$ acting on a particle of charge Q_1 separated by the distance r of a charge Q_2 has an amplitude of:

$$|\mathbf{F}| = \frac{1}{4\pi\varepsilon_r\varepsilon_0}\frac{Q_1 Q_2}{r^2} \ .$$

The electric field $\mathbf{E}$ is defined as $\mathbf{F} = Q_1\mathbf{E}$, and hence, its amplitude E is:

$$E = \frac{1}{4\pi\varepsilon_r\varepsilon_0}\frac{Q_2}{r^2} \ , \tag{5.2}$$

where ε_0 is the permittivity of the vacuum (8.854×10^{-12} F/m). Equation 5.2 highlights a higher separation or relative permittivity decreases the amplitude of the electric field. As a consequence, at a fixed voltage, the inter-electrode gap, dielectric thickness and dielectric permittivity are expected to all reduce the amplitude of the electric field (and hence, the drift velocity) at their high values. This conclusion is relevant for the analysis of the effects of the three parameters, because the voltage is constant for all the

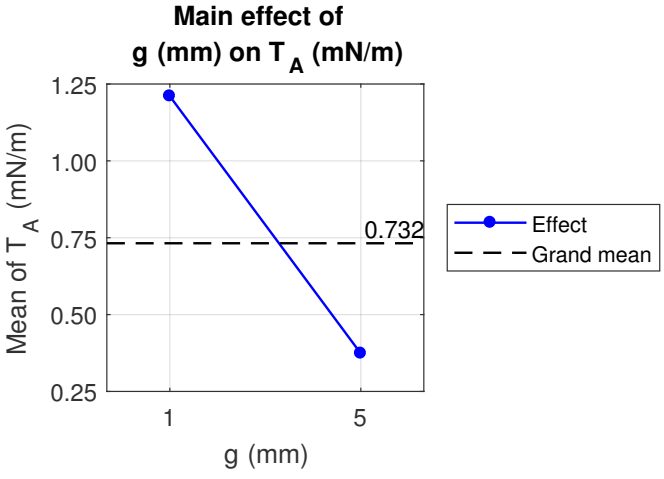

Figure 5.5: Main effect of the inter-electrode gap on the thrust generation.

effects that exclude the voltage. Specifically, the distance should have a greater impact on the results because the electric field decays as $1/r^2$ compared to $1/\varepsilon_r$. The stronger the electric field, the higher the drift velocity, and thus, the greater the momentum transfer. However, the previous equations are only applicable for point charges.

The inter-electrode gap is found to be the second most significant value in the study, and contributes to 13.52% of the variance of the results for the thrust generation. The main effect plot is given in Figure 5.5. An increase of 1 to 5 mm of the gap leads to a loss of 0.837 mN/m on average. A 5 mm gap was frequently observed to generate a weak discharge, due to the drop in the electric field, thus leading to a low induction of momentum in the free-stream falls as well.

3 - Thickness of the dielectric

The third significant effect is the dielectric thickness that contributes to 7.72% of the total variance of the data. The main effect plot is displayed in Figure 5.6.

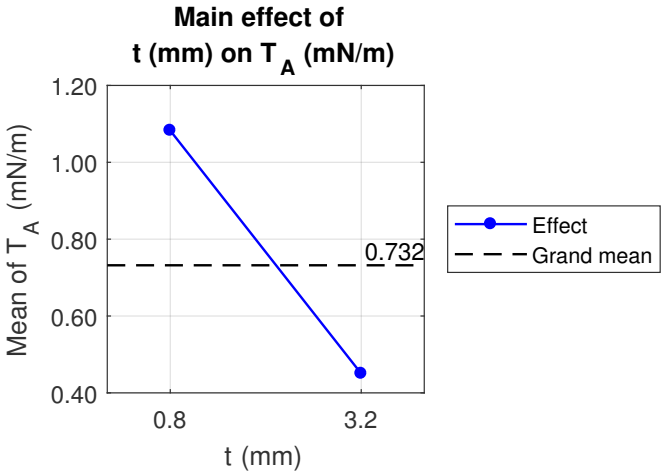

Figure 5.6: Main effect of the dielectric thickness on the thrust generation.

An increase of the thickness from 0.8 to 3.2 mm results in a drop of 0.632 mN/m on average. The effect is ranked third, but compared with the effect of the gap, the thickness presents a higher rate of loss per millimetre. This difference seems to be caused by the permittivity of the dielectric material being greater than the permittivity of the air. A possible explanation is that the overall electric field is weakened by the dielectric layer, because of the polarisation of the charges in the dielectric material. Consequently, the greater thickness adds more material of high permittivity between the electrodes, and leads to a greater loss ratio of the electric field. As a result, the drift velocity decreases further due to an increase of dielectric thickness, and thus the momentum induction into the free-stream declines as well.

4 - AC frequency

The fourth effect was found to be the frequency, and has a contribution of 7.31% in the variance of the measured thrust generation. The main effect plot of the frequency

is presented in Figure 5.7.

An increase of the AC frequency from 0.5 to 2.0 kHz, results in an increase of the thrust by 0.615 mN/m on average. The positive effect of the frequency on the thrust generation is a consequence of the higher collision frequency between the electrically driven charged particles, and the neutral gas. Over a constant time, more collisions occur with a greater AC frequency. With more numerous collisions between the charged and neutral species, the high frequency induces more momentum into the free-stream, thus increasing the thrust. It is important to point out several less significant interactions involving the frequency were found to influence the thrust generation, especially with the voltage.

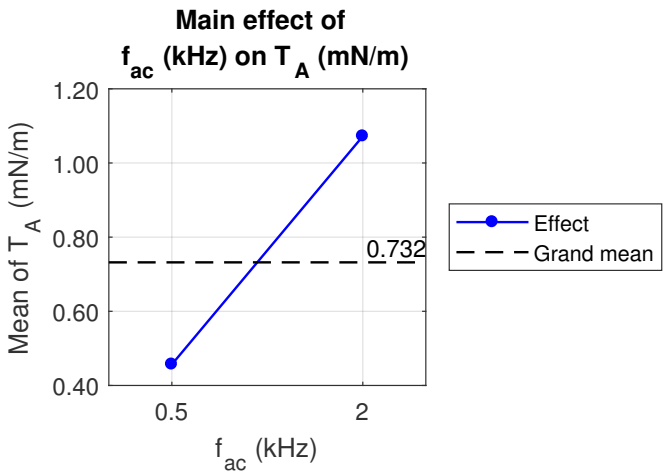

Figure 5.7: Main effect of the AC frequency on the thrust generation.

5 - Interaction between the exposed electrode width and the thickness of the dielectric

Most of the following effects have a smaller contributions to the variance of the results. The present interaction is responsible for 3.10% of the total variance. Moreover, four interactions are aliased, namely, the interactions between:

1. the width of the exposed electrode and the dielectric thickness,
2. the width of the encapsulated electrode and the dielectric permittivity,
3. the inter-electrode gap and the voltage,
4. the exposed electrode height and the frequency.

The four interactions are shown in Figure 5.8.

If these interactions cannot be isolated mathematically, two have a physical basis. Firstly, the interaction between the width of the exposed electrode and dielectric thickness shows a small effect of 0.141 mN/m of the width for a thin dielectric layer, that reduces to -0.538 mN/m for a thick layer. The ninth significant parameter is the width

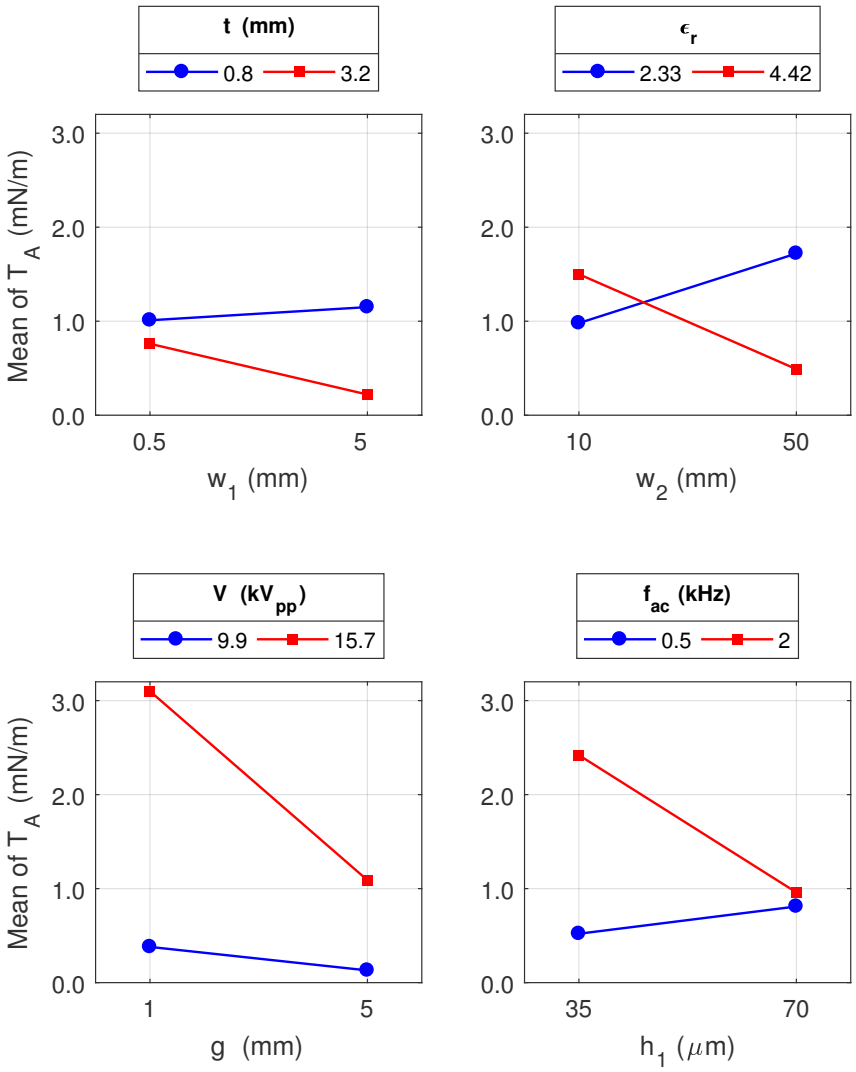

Figure 5.8: Interaction effect between the width of the exposed electrode and dielectric thickness on the thrust generation and its aliases.

of the exposed electrode, which has a negative effect. The positive effect of the width for a thin dielectric could indicate that the thin layer interacts with the discharge occurring on a wide air electrode. This could be by strengthening the transfer of charges on the front edge of the exposed electrode, that convect to the rear edge discharge. The higher charge density would enhance the momentum transfer.

However, the interaction between the gap and voltage seems to be the principal interaction of the four aliases. This interaction agrees with the finding of Thomas et al. [45], about the existence of a saturation of the thrust, involving the voltage, frequency, and dielectric permittivity and thickness. The saturation happens when the plasma discharge transitions from a glow to a filamentary regime. The authors observed the thrust increases with the voltage to the power of 3.5 for a lower voltage, and to the power

of 2.3 when approaching the saturation, and stagnates after saturation. The saturation voltage and thrust depend on the distance between the electrodes, the permittivity of the dielectric and the frequency of the signal. For a given material and geometry, the authors reported a reduction in the saturation voltage and saturation thrust for an increase in the frequency. For a given dielectric layer thickness and frequency, the authors highlighted the saturation thrust decreases with greater dielectric permittivity. For a given permittivity and frequency, the saturation thrust was found to increase with a thicker dielectric layer. Moreover, a thicker dielectric can sustain a higher voltage before reaching breakdown. However, the authors showed that, at a given voltage, a thicker dielectric reduces the thrust. Finally, the authors showed that, from saturation, an increase in the voltage results in a greater gain in the power consumption than the thrust generation, because of the filamentary discharge. Hence, the force efficiency can be expected to decrease drastically when supplied with a voltage greater than the saturation voltage.

In the present study, the saturation would involve the inter-electrode gap, the dielectric thickness and permittivity, the AC frequency and the voltage. In Figure 5.8, the negative effect of the interaction between the voltage and gap results in a drop of the mean thrust by 0.256 mN/m with a widening of the gap of 4 mm at a voltage of 9.9 kV_{pp}, that decreases to a drop of 2.006 mN/m with a widening gap of 4 mm at 15.7 kV_{pp}. This indicates that the obtainable thrust diminishes for a wide inter-electrode gap, particularly at high voltage. Several observations reveal a wide gap might lead to a low saturation voltage. For instance, two actuators having a long gap are displayed in Figure 5.9, where the brightness and contrast have been modified to highlight the filamentary discharges. This result tends to agree with the aforementioned saturation, with a lowering of the achievable thrust with a filamentary discharge. This interaction is more plausible, because several other interactions agree with an important saturation. Moreover, the interaction between the thickness and gap, although being insignificant, follows a similar trend with a loss of 0.374 mN/m with an increase of the gap of 4 mm, that reduces to a loss of 1.086 mN/m. The greater significance of the interaction of the voltage with the gap could be due to the greater significance of the gap over the dielectric thickness.

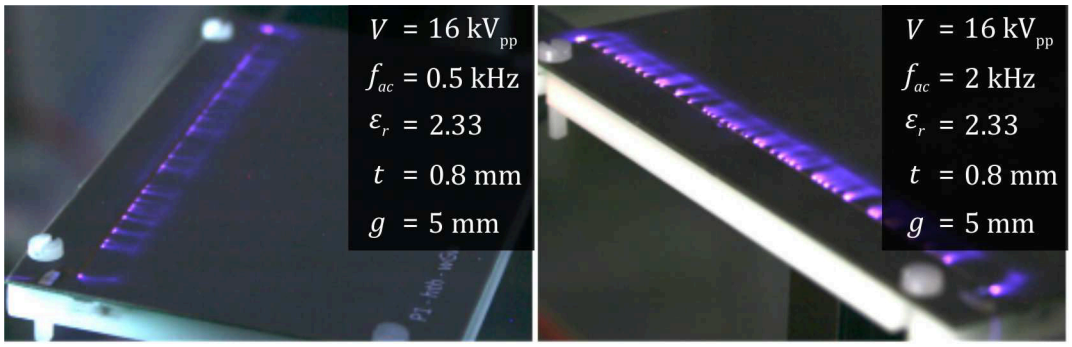

Figure 5.9: Long exposure pictures of runs 25 (left) and 28 (right), showing the formation of a filamentary discharge at high gap (modified brightness and contrast).

6 - Interaction between the inter-electrode gap and the height of the exposed electrode

The sixth most significant effect on the thrust is the interaction of the gap with the air electrode thickness. It is aliased with the interaction between the voltage and frequency. The interactions contribute to 1.92% of the variance of the results. The interaction plots are provided in Figure 5.10.

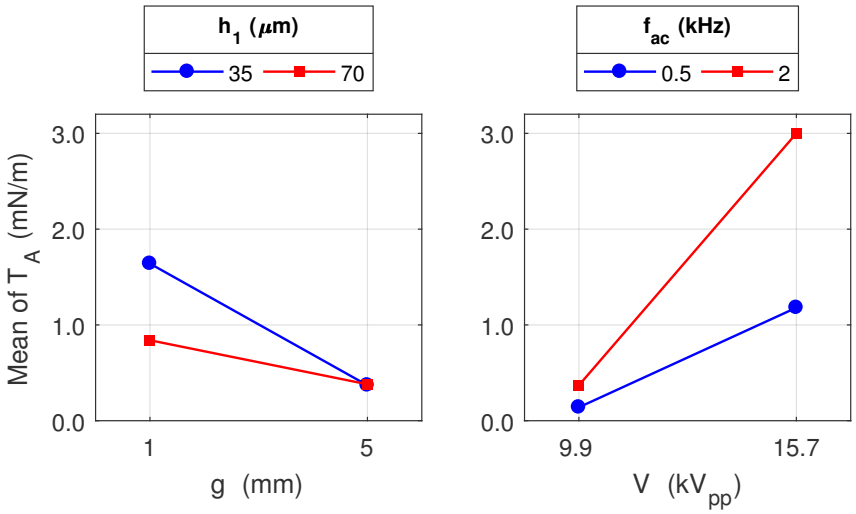

Figure 5.10: Interaction effect between the inter-electrode gap and height of the exposed electrode on the thrust generation and its alias.

The interactions between the height of the air electrode and inter-electrode gap suggests that, for a 1 mm gap, the 35 μm thick electrode increases the generated thrust by 0.802 mN/m on average. For a 5 mm gap, no significant difference exists between the thin or thick electrode. In Figure 5.3, the height of the exposed electrode h_1 is found to have a negative effect on the thrust generation. Hence, on average, a thin air electrode generates the greater thrust. The interaction does not contradict this finding. As discussed previously, a shorter gap increases the electric field between the electrodes. The interaction could suggest this increase of the electric field due to the short gap might be enhanced by the thinner electrode.

On the other hand, the aliased interaction between the voltage and frequency is larger. At 0.5 kHz, an increase of the voltage from 9.9 kV_{pp} to 15.7 kV_{pp} results in a gain of 1.046 mN/m, while it leads to an increase of 2.627 mN/m at 2.0 kHz. First, the saturation reported by Thomas et al. [45] does not seem to be significant for the frequency on average, because the higher frequency would decrease the saturation voltage, reducing the impact of the voltage on the thrust generation for a 2.0 kHz frequency. The greater the voltage, the more charges are transferred into the plasma and the stronger the electric field. The AC frequency is linked to the collision frequency between the charged and neutral particles in the plasma region. Consequently, it can be assumed the interaction could be the result of the collisions being more effective with

a greater number of charged particles, being forced by a stronger electric field, and colliding more often with the free gas. The more numerous ions and radicals colliding more frequently with the neutral molecules with a stronger force would transfer more momentum to the free-stream, and thus generate a higher thrust. The interaction is consistent with the reported trends, such as the Θ_A scaling parameter [7] ($\Theta_A = P_A/(f_{ac}^{1.5} \times V^{3.5})$), with a dependency of the maximum induced velocity with $f_{ac}^{1.5} \times V^{3.5}$. If the power laws cannot be verified through the DOE, the trend agrees with a positive interaction of the electric parameters.

7 - Height of the exposed electrode

The height of the exposed electrode is the seventh significant effect in Figure 5.3, with a contribution of 1.83% to the variance of the thrust measurement. Its effect is represented by the main effect plot in Figure 5.11.

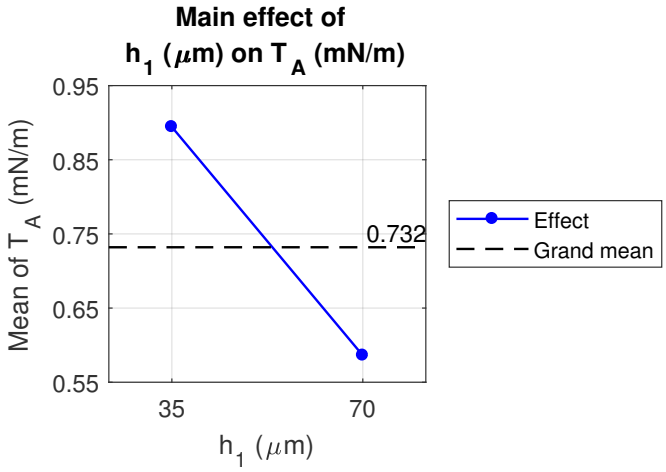

Figure 5.11: Main effect of the exposed electrode height on the thrust generation.

Previous works [66, 67] reported a wire electrode enhances the thrust generation compared to a plate electrode. A wire electrode of lower diameter revealed to further increase the thrust generation. Therefore, it can be expected a thin and narrow air electrode augments the thrust generation.

8 - Interaction between the inter-electrode gap and the AC frequency

The eighth influential parameter on the thrust generation is the interaction between the gap and the frequency, with a contribution of 1.79% of the variance of the results. It is aliased with the interaction between the height of the exposed electrode and the voltage. The interaction plots are given in Figure 5.12.

The interaction of the gap and frequency seems to agree with the previously mentioned saturation. The gap was already shown to decrease the thrust generation when widening. On average, it is unclear whether the longer gap reduces the thrust due to the saturation of the DBDs, or whether it simply reduces the electric field as seen in Equation 5.2. The work of Thomas et al. [45], showed the greater the distance between

the electrodes, the higher the saturation voltage, but the smaller the thrust at a particular voltage. Similarly, the authors observed a smaller frequency results in increased saturation voltage and thrust. If the previously detailed interaction between the voltage and frequency is trusted, the saturation was not found significant on average. Here, a 4 mm drop in the gap results in a loss of 0.420 mN/m at 0.5 kHz, but in a drop of 1.381 mN/m at 2.0 kHz. Only 25% of the runs present both a long inter-electrode gap and the high frequency. As a consequence, the AC frequency does not seem to lead to a lower saturation thrust on average, when isolated from the other parameters. However, the saturation seems to impact its interactions with the other design variables, that can influence the saturation thrust. For example, the saturation of the discharge with a long gap is evidenced in Figure 5.9. Moreover, the AC frequency is linked to the collision frequency of the charged particles with the neutral gas particle. With the weakening of the electric field due to a wide gap, the charge density and/or plasma extents in the x and z directions is constrained. The average momentum transfer from the charged particles depending on the products of the charge density and collision frequency, it decreases if either of the two variables are lowered. Since the momentum transfer also depends on the integral of the momentum of the charged species over the volume occupied by the plasma, the interaction could also result from the weakening of the electric field, rather than from the saturation of the thrust.

The aliased interaction between the voltage and thickness of the exposed electrode shows a negligible increase of 0.089 mN/m in the thrust generated by the actuator, with an increase of 35 μm of the exposed electrode height at 9.9 kV_{pp}, that becomes a major drop of 1.263 mN/m at 15.7 kV_{pp}. This result could back the already discussed interaction between the electrode thickness and gap. By increasing the voltage, the electric field strengthens, and could interact with the thinnest air electrode to enhance

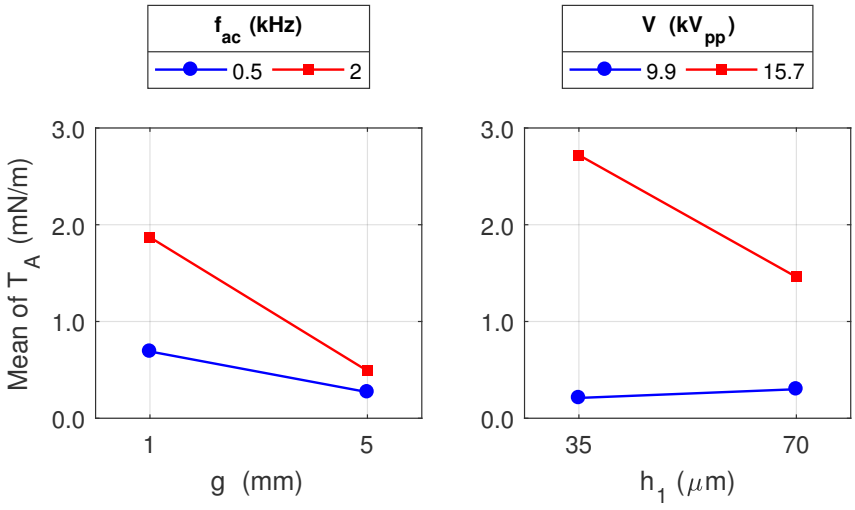

Figure 5.12: Interaction effect between the inter-electrode gap and AC frequency on the thrust generation and its alias.

the thrust generation. Therefore, it is difficult to fully conclude on the individual significance of either one of the interactions.

9 - Width of the exposed electrode

The ninth significant parameter in the Pareto (Figure 5.3) is the effect of the width of the exposed electrode, which is responsible for 1.57% of the variance of the thrust generation. The main effect plot of the width of the air electrode is displayed in Figure 5.13.

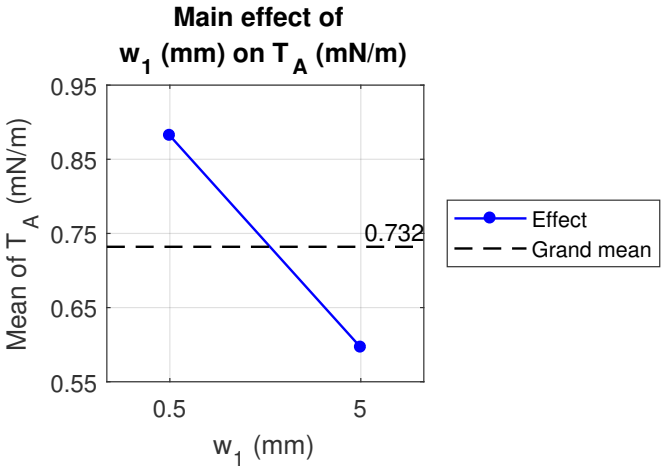

Figure 5.13: Main effect of the exposed electrode width on the thrust generation.

The decrease of the width from 5 to 0.5 mm brings the thrust to increase by 0.286 mN/m. This result agrees with other works [66, 67], that found a wire electrode of smaller diameter produces more thrust than a plate configuration.

10 - Interaction between the height of the encapsulated electrode and the AC frequency

The tenth most significant parameter is the interaction between the thickness of the buried electrode and frequency, and contributes to 1.52% of the total variance of the thrust generation results. The interaction is not aliased with other two-factor interactions, and its interaction plot is provided in Figure 5.14.

The thrust was observed to fall by 0.116 mN/m with a 35 μm increase in the height at 0.5 kHz, but to increase by 0.502 mN/m at 2.0 kHz. The phenomenon behind this result is unclear. The effect is believed to be caused by an aliased three-factor interaction (see Table 3.3), such as the interaction of the inter-electrode gap with the dielectric thickness and permittivity. Since these parameters are found to interact in several two-factor interactions, this seems more plausible.

11 - Interaction between the width of the exposed electrode and the dielectric permittivity

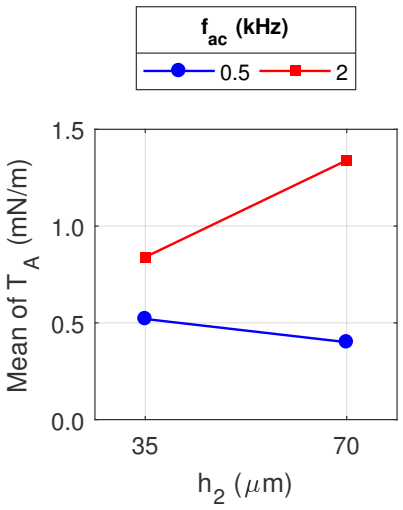

Figure 5.14: Interaction effect between the height of the encapsulated electrode and AC frequency on the thrust generation.

The eleventh significant effect on the thrust in Figure 5.3 is the interaction between the width of the air electrode and the relative permittivity of the dielectric material. It is aliased with the interaction between the width of the buried electrode and the thickness of the dielectric. The two aliased interaction are responsible for 1.16% of the variance of the results. The interaction plots are shown in Figure 5.15.

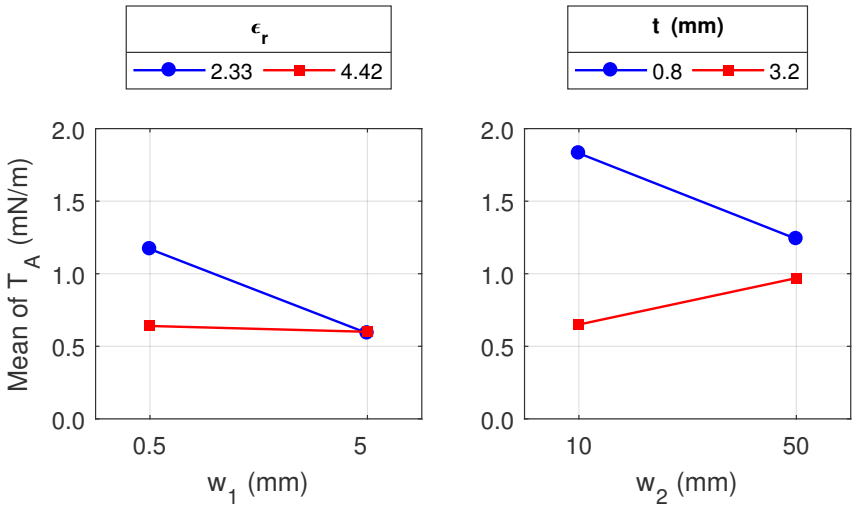

Figure 5.15: Interaction effect between the width of the exposed electrode and dielectric permittivity on the thrust generation and its alias.

If the dielectric permittivity does not seem important for a wide exposed electrode, for a narrow air electrode, lowering the permittivity from 4.42 to 2.33 leads to an average gain of 0.532 mN/m. If this interaction is actual, the width of the exposed electrode only matters for a low dielectric thickness. It should be noted that several actuators

were observed to generate plasma on both the front and rear edges of their air exposed electrodes (see Figures 4.15 and 4.17, and Section 4.6.3), particularly for narrow air electrodes. It is thus possible the lower permittivity helps to generate a stronger electric field, that can trigger discharges on both edges. A plausible explanation is that the discharge taking place at the front edge could transfer more radicals and charged particles to the rear-facing discharge. Hence, a low permittivity of the dielectric and narrow air electrode would produce more numerous charged species to transfer momentum to the free-stream. This hypothesis is unlikely. The width of the exposed electrode was already found to interact with the dielectric thickness (see Figure 5.8). But the two interactions show contradictory behaviours. Logically, the previous hypothesis would result in a higher thrust generation with a thin dielectric and a narrow air electrode, since the electric field would be stronger. A second more plausible explanation is the saturation of the discharge. At low permittivity, the dual discharge could spread the electric field and make the discharge more homogeneous. Hence, the single discharge generated by the wide electrode would saturate, and become filamentary, leading to a loss of thrust generation. Similarly in Figure 5.8, if the single discharge could saturate and transition to a filamentary discharge for a 3.2 mm thick dielectric. This phenomenon has however not been verified experimentally, and is only a hypothesis.

The aliased interaction involves the width of the encapsulated electrode and thickness of the dielectric. In Figure 5.15, for a 0.8 mm thick dielectric layer, the thrust drops by 0.589 mN/m for a widening of the buried electrode of 40 mm, yet, for a 3.2 mm thick layer, the thrust increases by 0.312 mN/m. No plausible physical explanation has been reached for this behaviour.

Without a proper accurate and repeatable light measurement technique, it is difficult to judge on the nature of the two interactions. It is also possible that both interactions have smaller negligible effects, that add due to the aliasing, making them mathematically significant.

12 - Permittivity of the dielectric

The twelfth most significant effect on the thrust generation belong to the permittivity of the dielectric, and contributes to 1.11% of the total variance of the results. The main effect plot of the permittivity is shown in Figure 5.16.

In the figure, the increase of the relative permittivity of the dielectric from 2.33 to 4.42 results in an average loss of 0.240 mN/m. As seen in Equation 5.2, an increase in the permittivity can be expected to reduce the amplitude of the electric field. Hence, it can reduce the strength of the plasma. This result also agrees with the observations of Thomas et al. [45], who found the lower permittivity allows to reach a higher saturation thrust. They add the plasma discharge transitions towards the filamentary regime with a smaller voltage as the permittivity becomes more important.

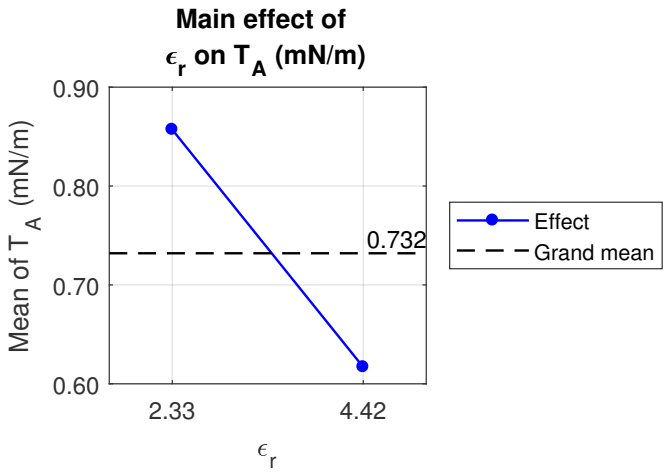

Figure 5.16: Main effect of the dielectric permittivity on the thrust generation.

13 - Interaction between the width of the encapsulated electrode and the height of the exposed electrode

The thirteenth most significant effect in Figure 5.3 is the interaction between the width of the buried electrode and the thickness of the air electrode. It is however aliased with the interaction between the frequency and the dielectric permittivity. The interactions are responsible for 0.91% of the variance of the results. The corresponding interaction plots are represented in Figure 5.17.

If a thin exposed electrode seems beneficial for both a narrow or wide encapsulated electrode, two different trends can be observed in the figure. For a 35 μm thick air electrode, a 40 mm widening of the encapsulated electrode produces a 0.189 mN/m increase of the thrust on average. On the contrary, for a 70 μm thick air electrode, the

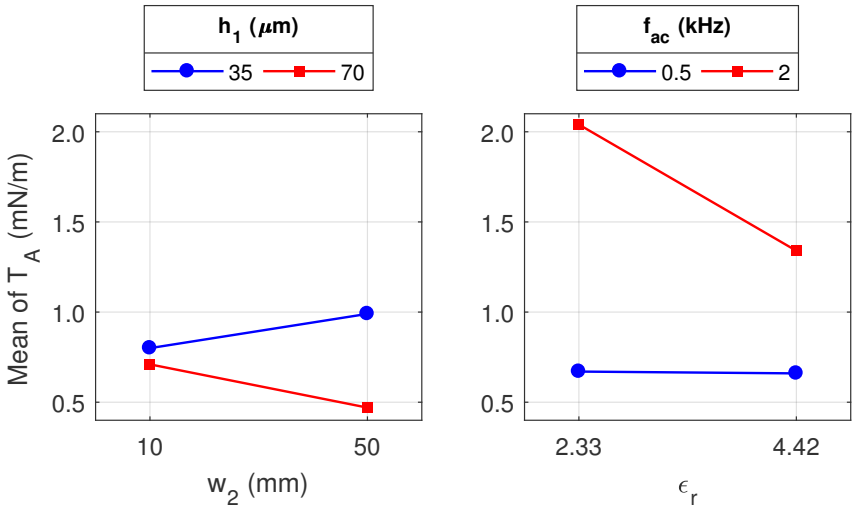

Figure 5.17: Interaction effect between the width of the encapsulated electrode and height of the exposed electrode on the thrust generation.

40 mm widening of the encapsulated electrode leads to a decrease of 0.235 mN/m on average. No plausible interpretation was reached for this interaction. It is believed to be caused by the aliased interaction.

On the other hand, the interaction between the dielectric permittivity and AC frequency does not show a significant effect of the permittivity at low frequency. At 2.0 kHz, the thrust generation drops by 0.697 mN/m on average, with an increase of the permittivity from 2.33 to 4.42. This results also agrees with the saturation presented by Thomas et al. [45]. In their results, they demonstrate the thrust saturates at a lower value for both a high frequency or high dielectric permittivity, leading to a lower obtainable thrust at high permittivity and frequency. At 0.5 kHz, the thrust only differs by 0.012 mN/m between the two levels of the permittivity. For an interaction, each point is an average over the quarter of the tests (24 observations). From Table 4.3, the confidence interval is ±0.025 mN/m. As a result, the 0.012 mN/m difference at 0.5 kHz can be ignored, as it is lower than the possible error. If the interaction was linked to the weakening of the electric field with a high permittivity of the dielectric (see Equation 5.2), it would be expected the low frequency would still slightly influence the thrust generation. As it is not the case, the saturation of the thrust seems more plausible, and only concerns the subset of runs that present a high frequency and high permittivity (twenty four runs). Since the effects are calculated by averaging the results for different subsets, the phenomenon does not suggest that all the twenty-four runs of the concerned subset are impacted by the saturation, but a sufficient number of the runs of this subset exhibit a loss of thrust, that is significant enough to influence the average of the subset.

14 - Interaction between the width and height of the exposed electrode

The fourteenth significant effect is the interaction between the height of width of the exposed electrode. It is aliased with the interaction between the thickness of the dielectric and the frequency. Overall, the interactions contribute to 0.81% of the variance of the thrust results together. The corresponding interaction plots are presented in Figure 5.18.

Both interactions seems equally likely. On the one hand, the interaction between the width and height of air electrode is showing that reducing either one of the two parameters leads to an increase in the thrust generation. As expressed previously, other studies [66, 67] showed a wire type air electrode produces more thrust than a rectangular electrode, and that the smaller the diameter, the greater the generated thrust. The interaction shows the same trend, with a narrower and thinner exposed electrode producing more thrust.

The second interaction shows a loss of 0.397 mN/m at 0.5 kHz for a thickening of the dielectric from 0.8 to 3.2 mm. On the other hand, the thrust drops by 1.062 mN/m for the same thickening of the dielectric layer at 2.0 kHz. Thomas et al. [45] proved the saturation thrust is decreased by a high frequency or thin dielectric. However,

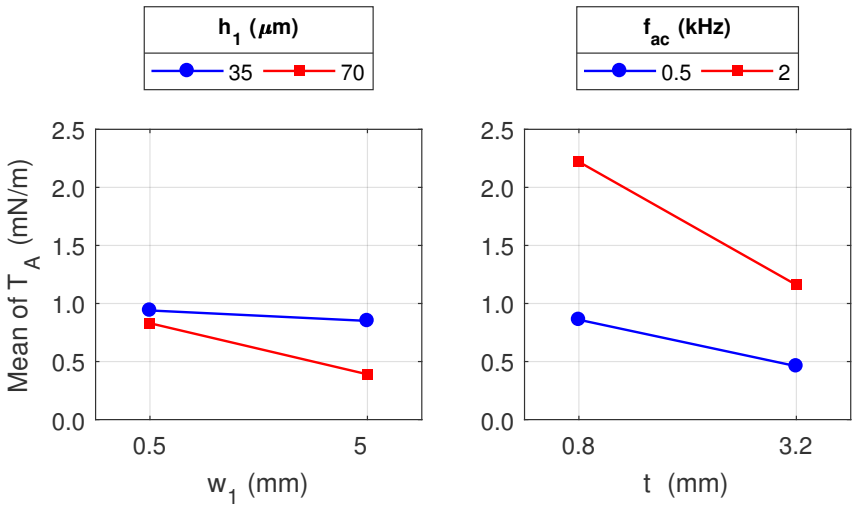

Figure 5.18: Interaction effect between the width and height of the exposed electrode on the thrust generation and its alias.

they also noted that the thin dielectric allows to reach a higher thrust at low voltage. Consequently, in the present case, the dielectric thickness seems to only leads to a drop in the amplitude of the electric field, resulting in a loss of thrust, whereas the frequency seems to lower the achievable thrust by saturating the actuator at its high value.

15 - Interaction between the widths of both electrodes

The fifteenth significant effect involves the interaction between the widths of both electrodes, and its aliased interaction between the dielectric layer thickness and relative permittivity. The interactions are responsible for 0.76% of the variance of the thrust data. They are presented in the interaction plots in Figure 5.19.

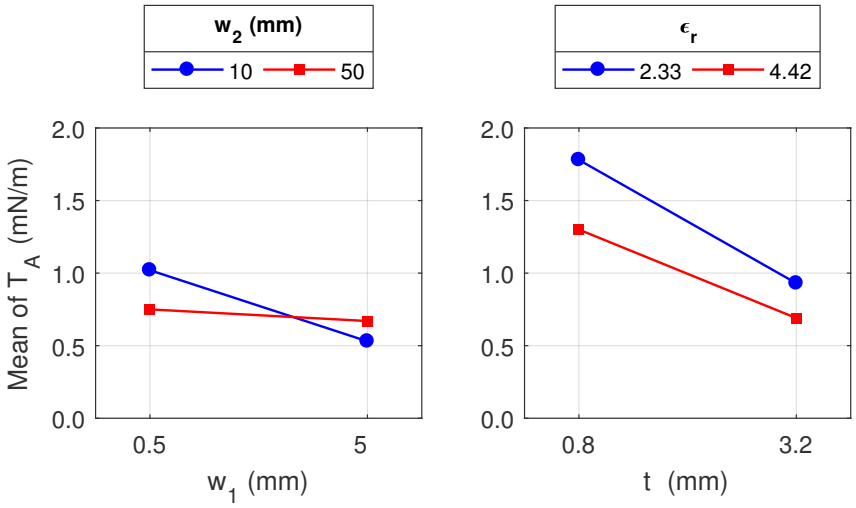

Figure 5.19: Interaction effect between the widths of the exposed and encapsulated electrodes on the thrust generation and its alias.

The interaction between the widths of the electrodes suggests the DBDs produce slightly more thrust if both electrodes are wide, or both are narrow. It is uncertain whether this interaction is accurate or a result of the aliasing. It is possible the single discharge occurring on a wide exposed electrode is constrained for certain runs, necessitating a wide encapsulated electrode.

Compared to the previous hypothetical interaction, the interaction between the thickness and permittivity of the dielectric agrees with the saturation discussed by Thomas et al. [45]. At a permittivity of 4.42, decreasing the dielectric thickness from 3.2 to 0.8 mm increases the thrust by 0.607 mN/m. This increases to a gain of 0.853 mN/m for a permittivity of 2.33. The saturation was shown to decrease the saturation thrust for greater permittivity of the dielectric material or lower thickness [45]. In addition, in Equation 5.2, the electric field depends on the inverse of the product of the distance from the electrode and permittivity of the material. It is believed the interaction is a combination of the two phenomena, with a weakening of the electric field with a greater thickness of the dielectric layer, and a lowering of the obtainable thrust through the saturation for a high dielectric permittivity.

16 - Interaction between the width of the encapsulated electrode and the voltage

The sixteenth significant effect in Figure 5.3 is the interaction between the voltage and the width of the encapsulated electrode. It is aliased with the interaction between the inter-electrode gap and the dielectric permittivity. The interactions contribute to 0.65% of the variance of the data.

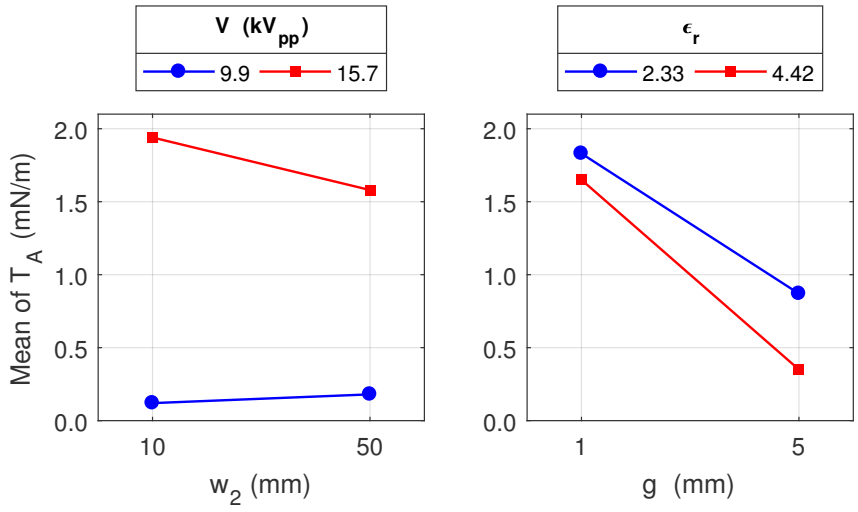

Figure 5.20: Interaction effect between the width of the encapsulated electrode and voltage on the thrust generation and its alias.

The interaction between the voltage and the width of the encapsulated electrode results from a drop of the thrust generation of 0.355 mN/m, with a widening of 40 mm of

the buried electrode at 15.7 kV_{pp}, becoming a slight increase of 0.062 mN/m at 9.9 kV_{pp}. It is believed that the effect of this interaction is caused by the aliased interaction. This conclusion is particularly motivated by the fact that this interaction tends to contradict the literature. It is more typical to see a narrow encapsulated electrode limiting the thrust generation at high voltage, because it constrains the plasma extent [45, 68–70]. The opposite phenomenon arises on the figure. Consequently, the aliased interaction is considered to produce this effect.

The interaction between the permittivity of the dielectric and inter-electrode gap also agrees with the saturation of the thrust [45]. For a 5 mm gap, the high permittivity lowers the achievable thrust, by reducing the amplitude of the electric field. The best configuration is a short gap and low permittivity. If the inter-electrode gap was not particularly focused on by Thomas et al. [45], the gap participates to the distance between the electrodes. The trend however slightly differs from the behaviour observed in the interaction of the dielectric thickness and permittivity (see Figure 5.19). As reported previously (see page 102), the long gap was found to trigger the saturation of the discharge. Hence, a longer gap can result in a greater decay of the thrust, especially when coupled to a higher permittivity of the dielectric.

17 - Interaction between the width of the exposed electrode and the AC frequency

The seventeenth significant parameter in Figure 5.3 involves the interactions between the width of the exposed electrode and the frequency on the one hand, and between the height of the exposed electrode and the dielectric thickness on the other hand. They contribute to 0.41% of the total variance of the results. The interactions are displayed in Figure 5.21.

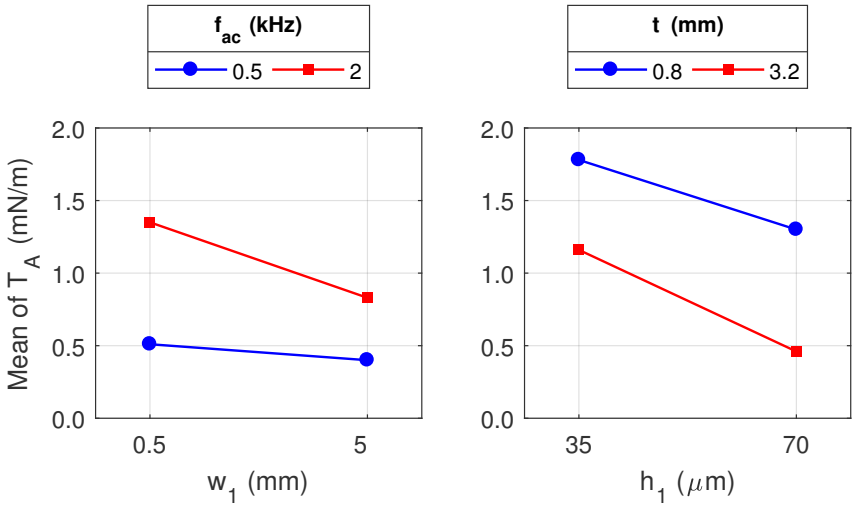

Figure 5.21: Interaction effect between the width of the exposed electrode and AC frequency on the thrust generation and its alias.

Both interactions are small. The thrust decreases by 0.111 mN/m for a widening of 4.5 mm of the air electrode at 0.5 kHz, against 0.522 mN/m at 2.0 kHz. Similarly, the thrust generation drops by 0.480 mN/m for a 35 μm thickening of the air electrode, for a 0.8 thick dielectric, against a fall of 0.694 mN/m for a 3.2 mm thick dielectric layer. It is unsure why these interactions occur. It is possible the high frequency interacts with the dual discharge generated by a narrow exposed electrode. The extra charges brought by the front discharge can collide more frequently with the neutral gaseous species. This could explain the slight increase in the thrust generation at high frequency on a narrow electrode. The assumption relies on the possibility that some charges generated on the front edge of the exposed electrode convects towards the rear of the actuators. The second interaction could be caused by the strengthening of the electric field induced by a thin dielectric or a thin exposed electrode. The aliasing between the interactions could also virtually increase their significance, by adding their contributions.

18 - Height of the encapsulated electrode

The eighteenth significant effect belongs to the thickness of the encapsulated electrode, which is responsible for 0.35% of the total variance of the results. Its main effect plot is shown in Figure 5.22.

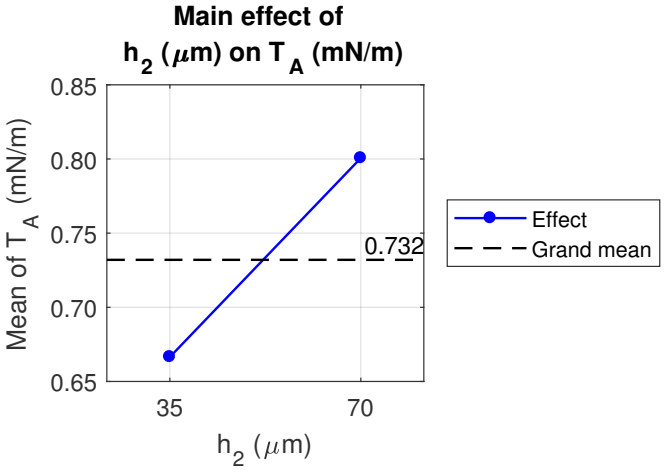

Figure 5.22: Main effect of the encapsulated electrode height on the thrust generation.

An increase of 35 μm of the height of the electrode leads to a gain of 0.134 mN/m on average. The effect could be the result of the spreading of the electric field close to the exposed electrode rear edge, due to the greater frontal wetted area of the encapsulated electrode. This explanation is hypothetical and cannot be verified in the present study.

19 - Interaction between the width of the exposed electrode and the voltage

The final significant effect on the thrust generation is the interaction of the width of the exposed electrode and voltage. It is aliased with the interaction between the gap and dielectric thickness. The interactions contributes to only 0.16% of the total variance of the result. Moreover, its standardised effect (2.03) is less than the critical

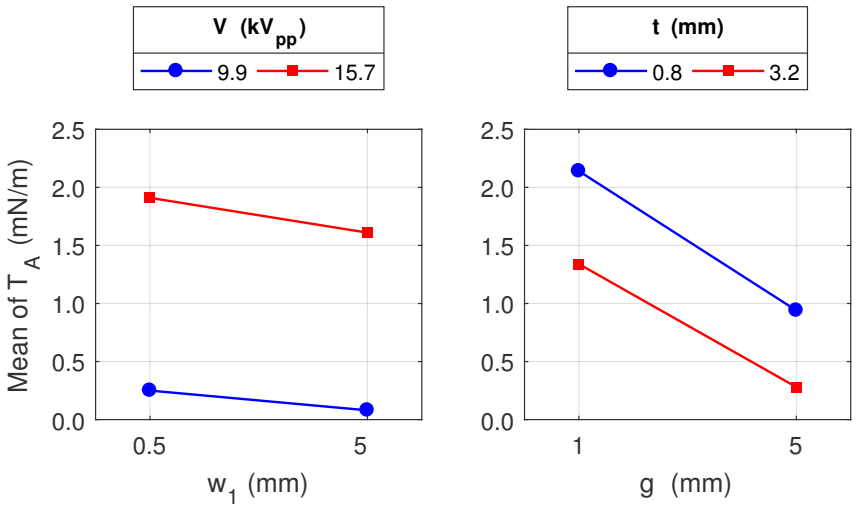

Figure 5.23: Interaction effect between the width of the exposed electrode and voltage on the thrust generation and its alias.

t-value of 2.63 for a 99% certainty. The interaction plots are provided in Figure 5.23, and show the interactions have negligible influence. The aliasing makes it more difficult to determine whether the effect is significant.

The thrust generation increases by 0.170 mN/m with a drop of 4.5 mm of the width of the air electrode at 9.9 kV_{pp}, but 0.299 mN/m at 15.7 kV_{pp}. The higher voltage provides more charges to exchange and a stronger electric field, and it could interact with the dual discharges for a narrow air electrode.

The aliased interaction comes from the 1.200 mN/m decrease in the thrust, with a widening of 4 mm of the gap for a 0.8 mm thick dielectric, lowering to a drop of 1.061 mN/m for a 3.2 mm thick dielectric. As previously, the interaction could also be explained by the weakening of the electric field caused by both interacting parameters.

5.3 Linear Regression Model

The DOE analysis performed by Minitab produces a linear regression model for the transformed response (square-root of the thrust here). The first limitation is the assumption that the transformed response depends linearly on all the factors and their interactions. Secondly, the model assesses the effect of the aliases through only one of the aliased effects. This selected alias is only chosen by name. If two interactions were found to be aliased, one involving w_1 (first variable in the study) and the second involving g (third variable in the study) for instance, the retained interaction will be the interaction of w_1. The model is hence expected to only provide approximate estimates of the thrust generation for different designs. The model can be expressed through the following equation:

$$\sqrt{T_\mathrm{A}} = X_\mathrm{d} \cdot M_T \cdot X_\mathrm{d}^T \ , \tag{5.3}$$

with X_d being the array of the input parameters:

$$X_\mathrm{d} = \begin{bmatrix} 1 & w_1 & w_2 & g & h_1 & h_2 & t & \varepsilon_r & V & f_\mathrm{ac} \end{bmatrix} . \tag{5.4}$$

In Equation 5.3, X_d^T is the transpose of X_d and M_T the ten by ten matrix of the model coefficients:

$$\begin{bmatrix} -10.4 & 0.03 & 1.818 & -17.94 & -0.014 & -1.357 & -9.19 & -19.68 & 15.91 & 19.54 \\ 0 & 0 & 0.1292 & -0.376 & -0.1521 & -0.0429 & -4.339 & 3.045 & 0.414 & -2.518 \\ 0 & 0 & 0 & -0.0618 & -0.0181 & 0.0044 & 0 & 0 & -0.0926 & -0.1211 \\ 0 & 0 & 0 & 0 & 0.2632 & 0.0421 & 0 & 0 & 0 & -5.937 \\ 0 & 0 & 0 & 0 & 0 & -0.0063 & 0 & 0 & 0 & 0 \\ 0 & 0 & 0 & 0 & 0 & 0 & 0.1089 & 0.0876 & 0.037 & 0.625 \\ 0 & 0 & 0 & 0 & 0 & 0 & 0 & 0 & 0 & 0 \\ 0 & 0 & 0 & 0 & 0 & 0 & 0 & 0 & 0 & 0 \\ 0 & 0 & 0 & 0 & 0 & 0 & 0 & 0 & 0 & 0 \\ 0 & 0 & 0 & 0 & 0 & 0 & 0 & 0 & 0 & 0 \end{bmatrix} \times 10^{-2} \tag{5.5}$$

Minitab calculates the fitness of the models through the R^2 and adjusted R^2 coefficients. They are here 97.39% and 96.19% respectively. Therefore, the model predicts the results of the tests matrix accurately, and does not include unnecessary input variables. The models for all three output parameters are further discussed in Chapter 8.

5.4 Summary

Of the nineteen significant effects discussed in the previous section, several agreed with phenomena reported in the literature. Many of the effects have a small impact on the results, with contribution of 1% or less to the total variance of the results. Besides, several aliased interaction could not be fully explained, and only hypotheses could be offered.

In total, the main effects were found to contribute to 83.40% of the variance, while the interactions cover 13.99% of the total variance of the data. Hence, the interactions between the design factors cannot be neglected when trying to maximise the thrust generated by an actuator. The first fifteen significant parameters are responsible for 94.95% of the variance, and the first ten contribute to 90.20% of the variance.

The results show that the factors of primary importance are the voltage, the inter-electrode gap, the dielectric thickness, the frequency and the exposed electrode width and height. The higher voltage and frequency were found to produce more thrust. If the inter-electrode gap and dielectric thickness were observed to simply decrease the thrust through their ability to weaken the electric field in the plasma. The results evidenced that the saturation of the thrust, reported by Thomas et al. [45], influences the effects of the gap, dielectric thickness and permittivity, and AC frequency. The present study suggests a long inter-electrode gap lowers the saturation voltage. The maximum obtainable thrust increases with a low permittivity of the dielectric, a thinner dielectric layer, a short inter-electrode gap and a smaller AC frequency. This conclusion is however limited to the case where the voltage is kept constant. The voltage being the

most important parameter, increasing the dielectric thickness and/or permittivity can enable the use of a higher voltage, which can further improve the thrust generation. Since the effect of the frequency is higher than the effects of the saturation, a high frequency was yet found to produce more thrust on average. A thin and narrow exposed electrode was observed to increase the thrust generation, agreeing with the conclusion of Debien et al. [66] and Hoskinson et al. [67], that a wire air electrode generates a greater thrust than a plate rectangular electrode.

Chapter 6

Parametric Study for the Power Consumption

This chapter details the analysis of the results for the power consumption. Firstly, the validity of the mathematical analysis is performed, through the study of the residuals. Secondly, the effects of the nine design parameters on the power consumption are calculated and ranked based on their significance. The effects are discussed, and the explanations are provided to describe the underlying physical phenomena. Finally, the model computed through the DOE analysis is provided.

6.1 Validity of the Analysis

First, it must be reminded that the DOE analysis is mathematically valid if the residuals of the linear regression model of the output variable are normally distributed (see Section 3.3.8). The power consumption must be analysed through its natural logarithm in order to verify this assumption. It must be noted the transformation does not impact the results. In the case of a natural logarithm, the transformation indicates that a few significant effects are much greater than the others. The residual plots for the power consumption are presented in Figure 6.1.

The histogram of the residuals (Figure 6.1a) does not exhibit a significant skewness. The normal probability plot (Figure 6.1b) shows the residuals are aligned, and thus follow a normal distribution with only a few outliers. The distributions of the residuals against the fitted values (Figure 6.1c) and against the observation orders (Figure 6.1d) do not follow any particular trend, and appear as random signals. Consequently, the DOE analysis of the power consumption is mathematically valid.

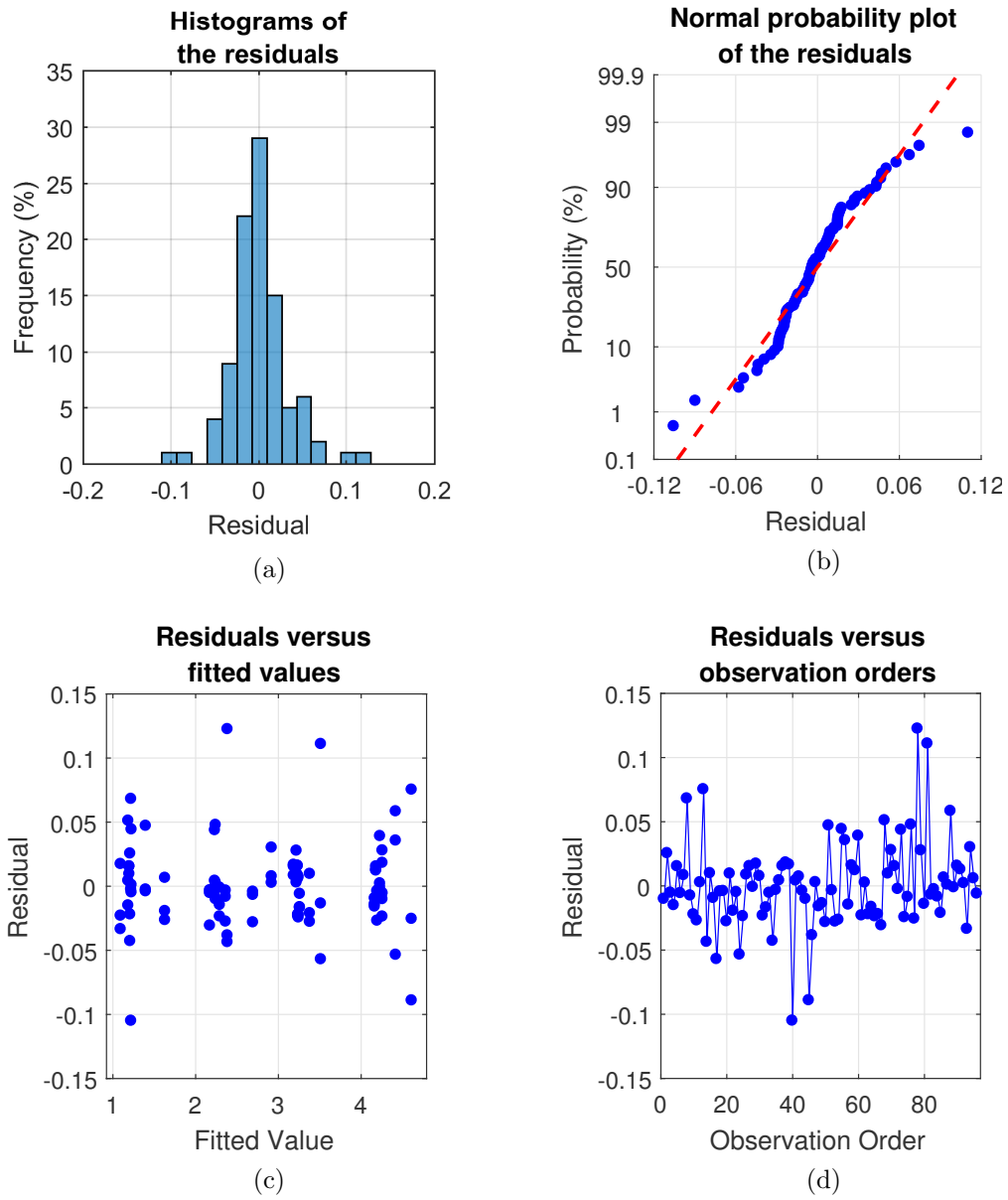

Figure 6.1: Residual plots of the analysis of the power consumption.

6.2 Ranking of the Significant Parameters

6.2.1 Selection of the Significant Effects

In order to identify the significant parameters, the standardised main effects of the factors and the standardised interaction effects on the power consumption are represented on the half-normal plot in Figure 6.2. The distribution of the standardised effects is compared to two lines in the figure. The solid blue line represents a normal distribution having the same two-tailed t-value as the study (1.98 for 96 tests at a confidence level of 95%). If the effects were to follow this distribution, they would be insignificant. The dash line illustrates the best fitting of a normal distribution to the data. The standardised effect whose amplitude exceeds the predictions of this distribution have

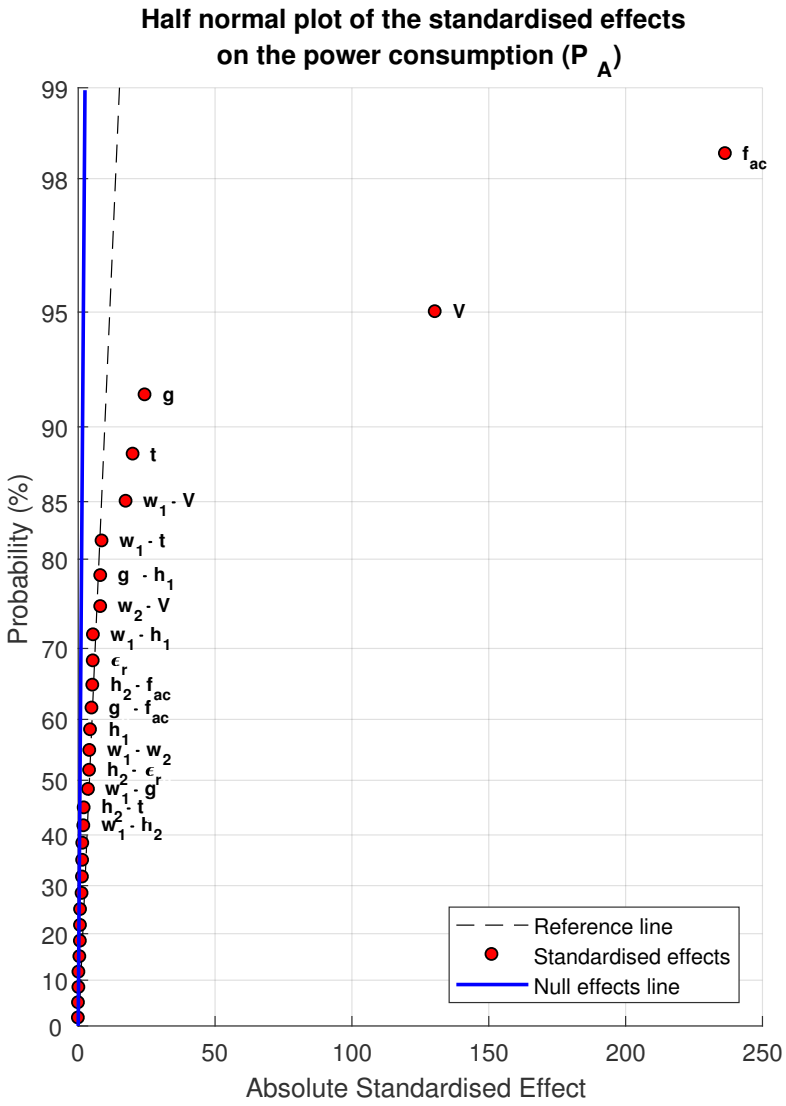

Figure 6.2: Half-normal plot of the standardised effects on the power consumption.

the greater influence on the power consumption.

In Figure 6.2, eighteen effects are significant, and form the model. Minitab calculates how much of the variance (square of the standard deviation) of the data can be imparted to each effect. The more a design parameter contributes to the variance of the results, the more it affects the output parameter. In total, the eighteen model terms are responsible for 99.91% of the total variance. The most significant effects are the frequency (f_{ac}), the voltage (V), the inter-electrode gap (g) and the dielectric thickness (t), and they respectively contribute to 74.78%, 22.78%, 0.81% and 0.54% of the total variance respectively (98.91% altogether). The other model terms only contribute to less than a percent each. The eighteen significant standardised effects are displayed in the Pareto chart in Figure 6.3. Since the standardised effects are absolute values, the bars are coloured by the signs of the effects. For instance, the effect of the voltage (V) is positive, meaning an increase in the supplied voltage results in an increase in the

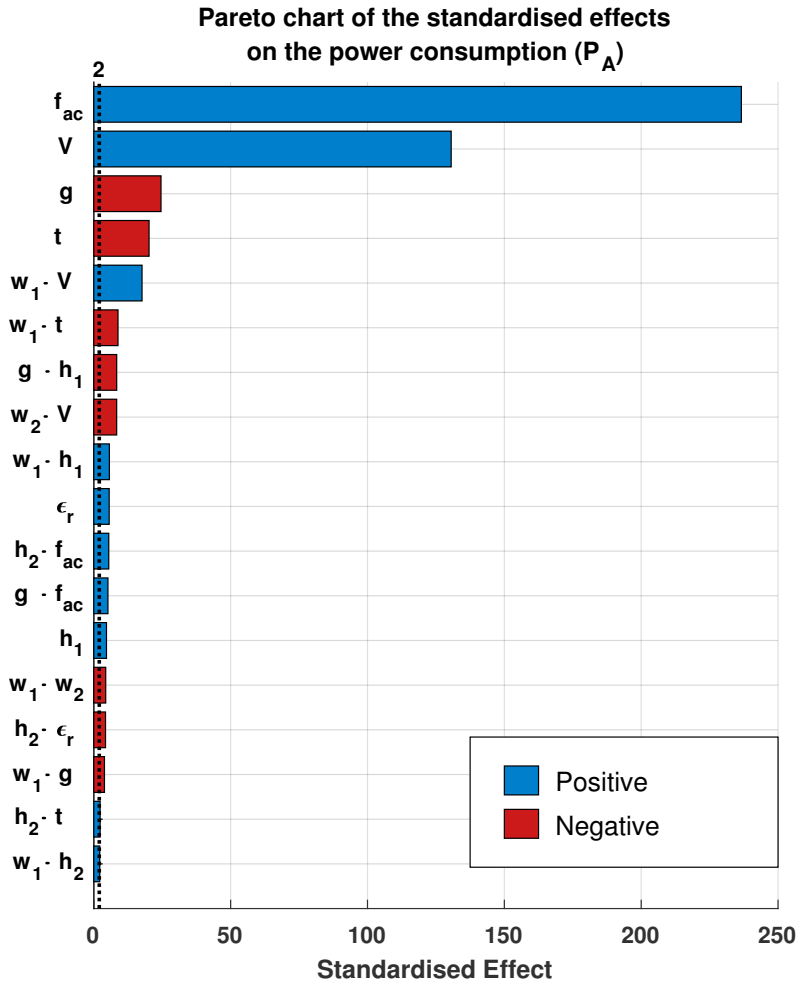

Figure 6.3: Pareto chart of the standardised effects on the power consumption, coloured by sign of the effect.

consumed electrical power. The Pareto chart shows that all the selected standardised effects are greater than the critical t-value of 1.98. It should be noted that most of the significant interaction effects are aliased. As a consequence, the mathematical analysis of the DOE cannot determine if these effects are caused by one specific interaction or its aliases. In order to find which of the interaction(s) generates the effect, the physical basis of all the aliased interactions must be analysed. Moreover, as previously reported, the t-value for a 99% confidence level is 2.63 for 96 tests. From the eighteen standardised effects appearing in Figure 6.3, sixteen are greater than this critical value. Consequently, most of the effects discussed in the following section take place because of the changes of the design variables. The effects and interactions are discussed in the next paragraphs.

6.2.2 Discussion of the Significant Effects

1 - AC frequency

In Figure 6.3, the AC frequency is the first significant factor, and is responsible for

77.78% of the variance of the data. The main effect plot of the frequency on the power consumption is displayed in Figure 6.4.

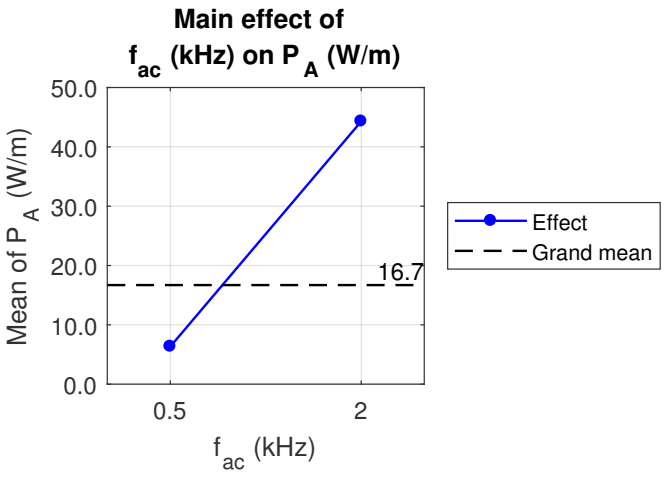

Figure 6.4: Main effect of the AC frequency on the power consumption.

In the main effect plot, the increase of the frequency from 0.5 to 2.0 kHz increases the power consumption by 37.96 W/m. First, it can be reminded that, by definition, the power consumption depends at least linearly on the frequency (see Equation 3.7). The positive effect of the frequency is unsurprising based on previous studies [7, 45, 59, 69]. In the scaling proposed by Kriegseis et al. [7], the power depends of the frequency to the power of 1.5 and of the voltage to the power of 3.5. Here, the higher dependency on the frequency could be explained by the saturation of the actuator. In their study, Thomas et al. [45] evidenced a saturation at high frequency, where the plasma discharge transitions from a uniform glow discharge, to a heterogeneous filamentary discharge. The filamentary discharge is more power consuming but does not generate more thrust than the glow discharge. Besides, as it is expressed by Corke et al. [2], the power lost through Joule heating in the dielectric layer due to the polarisation of the charges, is expected to scale linearly with the frequency. Hence, the high value of the frequency in the current study adds the power lost through the discharge (which can be increased when the discharge is filamentary), to the power lost in the dielectric. Several effects evidenced the existence of a saturation in the analysis of the thrust, backing the possibility of a more numerous saturated actuators in the subset of runs at the frequency of 2.0 kHz.

2 - Voltage

The voltage is the second significant effect on the power consumption in Figure 6.3. It is responsible for 22.78% of the total variance of the power data. The main effect plot of the voltage is presented in Figure 6.5.

On average, increasing the voltage from 9.9 to 15.7 kV_{pp} leads to a gain of 18.9 W/m. First, it must be noted, that the instantaneous electric power consumption depends on the product of the voltage and current. Moreover, for a pure resistive load, the

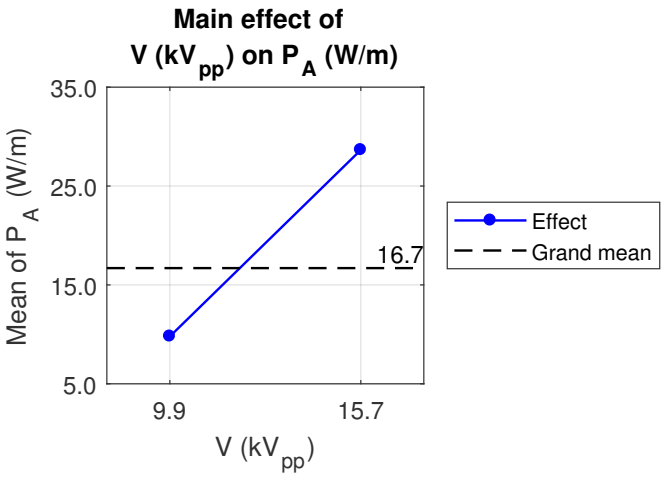

Figure 6.5: Main effect of the voltage on the power consumption.

instantaneous power consumption depends on the square of the voltage. Finally, the positive effect of the voltage on the power agrees with other studies [45, 59, 66, 69]. The increase in the consumed electrical power with an increase in the voltage can thus be expected, due to the partial electrically resistive properties of the discharge.

3 - Inter-electrode gap

The third significant effect in Figure 6.3 involves the inter-electrode gap, with a contribution to the variance of the power measurements of 0.81%. The main effect plot is showed Figure 6.6.

As explained for the thrust generation on page 100, the 5 mm gap was typically observed to generate weak discharges among the runs. The discharge was either almost invisible or composed of isolated streamers. Hence, less electric current is passing through the plasma on average for a wide gap. As a consequence, the power lost through Joule heating decreases in the plasma. The main effect plot shows a loss of 3.39 W/m for a widening of the gap from 1 to 5 mm. The weakening of the plasma discharge by a growth of the gap was also reported to decrease the thrust generation.

4 - Thickness of the dielectric

The thickness of the dielectric layer is the fourth most significant effect in Figure 6.3. It is responsible for 0.54% of the variance of the results. Figure 6.7 provides its main effect plot.

As for the inter-electrode gap, an increase in the dielectric thickness leads to a weakening of the electric field, and therefore, of the plasma discharge. Since most of the power consumption is lost through the plasma discharge, the power drops if the dielectric layer thickens. In the main effect plot, the 2.4 mm increase in the thickness of the dielectric results in a decrease of 2.78 W/m on average.

It can be remarked the decrease of the thrust induced by a widening of the gap was found to be 0.837 mN/m against 0.632 mN/m for a thickening of the dielectric. The

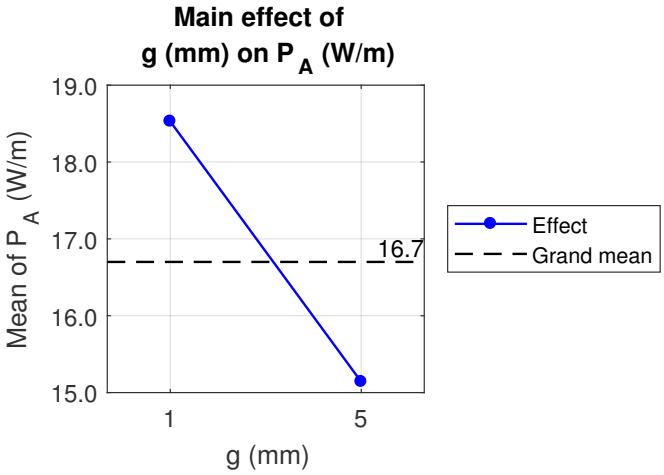

Figure 6.6: Main effect of the inter-electrode gap on the power consumption.

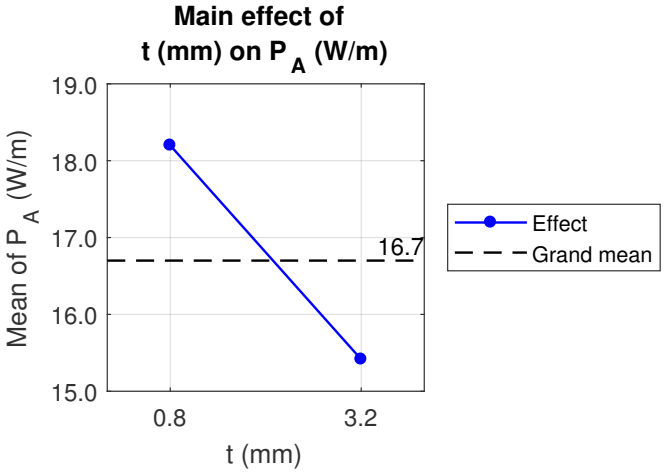

Figure 6.7: Main effect of the dielectric thickness on the power consumption.

ratio of the effects in 1.32. For the power consumption, this ratio is $3.39/2.78 = 1.22$. Consequently, either the gap impacts the thrust generation slightly more than the power consumption, or the dielectric thickness influences the power more than the thrust. Since the losses through the dielectric due to the polarisation of the charges are expected to scale with the opposite of the thickness (see [2]), the second assumption seems more probable.

5 - Interaction between the width of the exposed electrode and the voltage

The fifth significant effect on the power is the interaction between the width of the exposed electrode and the voltage. It is aliased with the interaction between the inter-electrode gap and the thickness of the dielectric layer. The two interactions contribute to 0.42% of the variance of the power measurements. The interaction plots are showed in Figure 6.8.

The interaction between the width of the exposed electrode and the voltage shows that increasing the width of the air electrode at 9.9 kV_{pp} results in a negligible loss

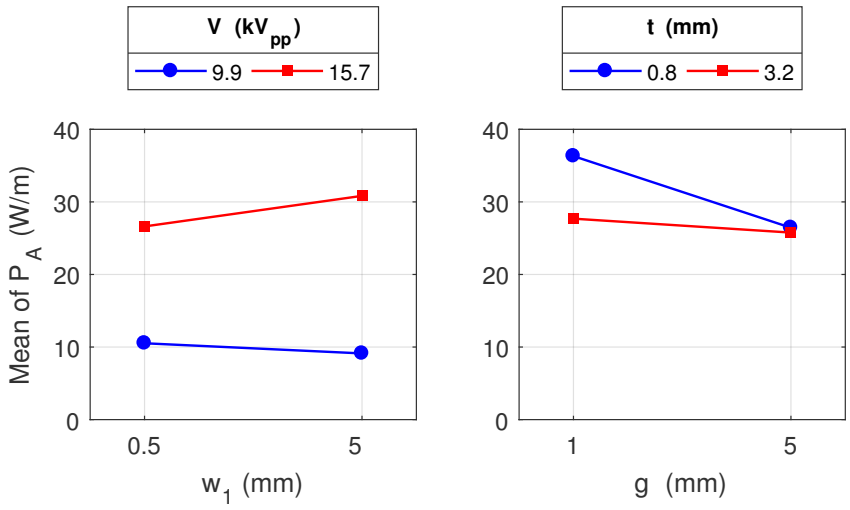

Figure 6.8: Interaction effect between the width of the exposed electrode and voltage on the power consumption and its alias.

of 1.40 W/m. However, at 15.7 kV_{pp}, the increase of 4.5 mm in the width leads to a gain of 4.20 W/m. These results suggest the dual discharge occurring on a narrow electrode is slightly more power consuming than the single discharge produced by the wide exposed electrode at a voltage of 9.9 kV_{pp}. On the other hand, at 15.7 kV_{pp}, the higher consumption observed with the wide electrode indicates that the single discharge might have transitioned to a more power consuming discharge such as the filamentary discharge. In this scenario, the dual discharge happening on the narrow exposed electrode spreads and weaken the electric field, and thus keeps the discharge to a less power consuming state (such as the glow discharge). Because these explanations are speculative, this effect is believed to be caused by the aliased interaction, that has a stronger physical basis.

The aliased interaction shows there is little difference in the power consumption for a long gap, with only a slight decrease of 0.67 W/m with the thickening of the dielectric. However, for a short gap of 1 mm, the reduction of the dielectric thickness from 3.2 mm to 0.8 mm results in an increase of the power of 8.62 W/m. The inter-electrode gap and dielectric thickness were previously observed to reduce the power consumption at their high value. These effects were imparted to the weakening of the electric field induced by a greater distance between the electrodes. With an electric field of lower amplitude, the plasma discharge weakens as well, with smaller spatial extents and possibly a smaller charge density. Consequently, less electrical power is lost through electrically resistive effects in the plasma. If this interaction seems more probable, it is difficult to absolutely conclude without a proper visual study.

6 - Interaction between the width of the exposed electrode and the dielectric thickness

The sixth most significant effect on the power in Figure 6.3 involves the interaction between the width of the exposed electrode and the dielectric thickness. It is aliased with the interactions between the width of the encapsulated electrode and the dielectric permittivity, between the inter-electrode gap and the voltage, and between the height of the air electrode and the frequency. The four interactions contributes to 0.10% of the variance of the results. The four corresponding interaction plots are displayed in Figure 6.9.

In the figure, the interaction of the air electrode width with the thickness of the dielectric transpires through a gain of 1.35 W/m with a widening of 4.5 mm of the exposed electrode at a dielectric thickness of 0.8 mm, that becomes a decay of 1.10 W/m for the same widening for a 3.2 mm thick dielectric layer. The thin dielectric increases

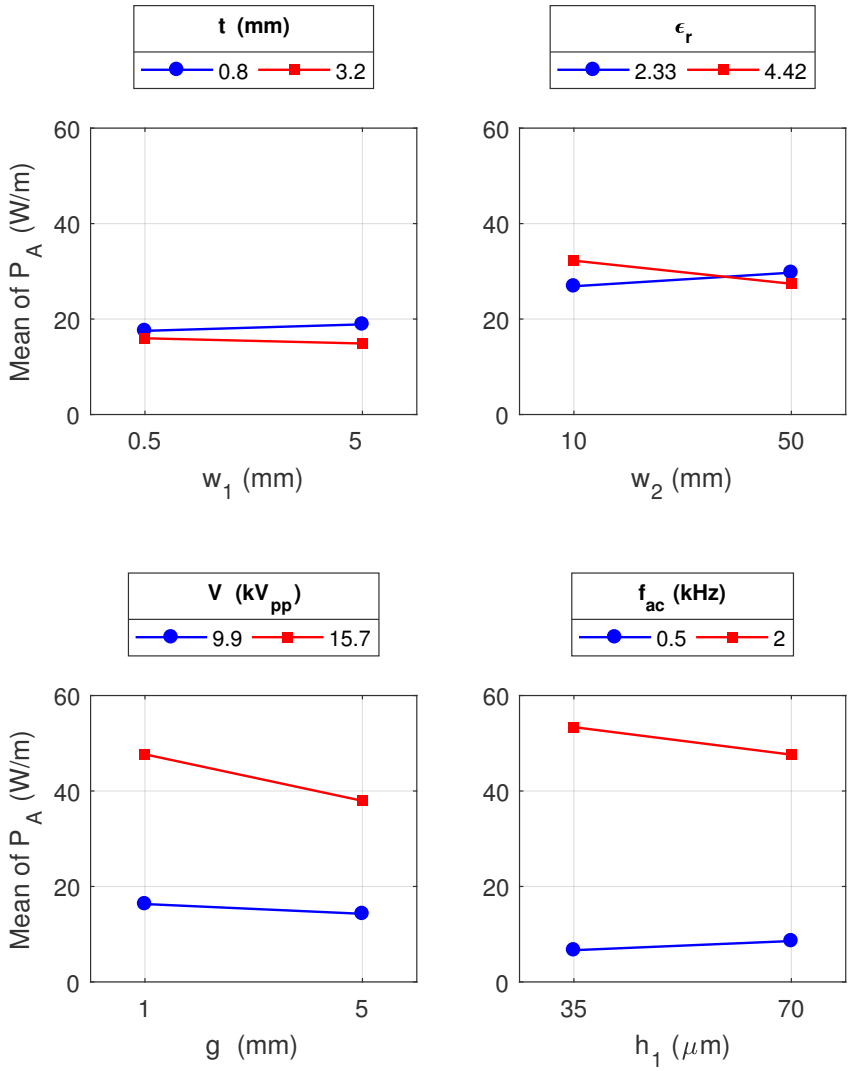

Figure 6.9: Interaction effect between the width of the exposed electrode and dielectric thickness on the power consumption and its aliases.

the amplitude of the electric field in the air. In this condition, the single discharge occurring on the wide exposed electrode could become slightly stronger, with a greater charge density and/or a larger volume. Hence, more power could be lost in the plasma due to its electrically resistive behaviour. However, the loss of power with the thick dielectric is difficult to explain. No physical explanation has been found to justify the second aliased interaction between the width of the encapsulated electrode and the dielectric permittivity.

The interaction of the gap with the voltage seems more plausible. At 9.9 kV_{pp}, on average, the power decreases by 2.06 W/m with an increase of 4 mm of the gap. At 15.7 kV_{pp}, the same widening of the gap results in a loss of 9.74 W/m. The short electric gap was already observed to grow the power consumption. By strengthening the electric field in the plasma, a short gap allows a greater voltage to extend the plasma and/or increase the number of charges exchanged through the plasma, especially if the discharge transitions to a filamentary discharge. As a result, an increase in the gap can have a greater effect at high voltage.

The final aliased interaction of the height of the exposed electrode with the AC frequency is also difficult to interpret. The interaction plot indicates a loss of 5.76 W/m at 2.0 kHz for a 35 μm thickening of the electrode, against a gain of 1.92 W/m at 0.5 kHz. No proper explanation was found to justify this behaviour.

Of the four interactions, only the interaction between the gap and the voltage seems to have some physical ground. Due to the aliasing, some interactions can be disturbed, due to the addition of their effects with the effects of their aliased interactions.

7 - Interaction between the inter-electrode gap and the height of the exposed electrode

The seventh significant effect on the consumed power is the interaction between the gap and height of the exposed electrode. It is responsible for 0.09% of the variance of the data. This effect has one alias with the interaction between the voltage and the frequency. The interaction plots are presented in Figure 6.10.

The interaction plot shows a minor effect of the interaction between the gap and exposed electrode height. However, the interaction between the electric input parameters indicates an increase of 7.96 W/m with the 5.8 kV_{pp} growth of the voltage at 0.5 kHz, against an increase of 47.06 W/m for the same growth in the voltage at 2.0 kHz. A similar effect was observed for the thrust generation (see page 105). The higher electric field associated to the higher voltage is responsible for an increase in the volume of the discharge and/or increase in the charge density in the plasma. The higher frequency results in a greater collision frequency of the neutral particles with the neutral gas particles. The collision with the neutral gas means viscous losses occurs in the plasma. As a consequence, the high levels of the frequency and voltage results in a greater momentum injection to the flow, but also in a stronger plasma, and greater loss of power through viscous and resistive interferences in the process.

8 - Interaction between the width of the encapsulated electrode and the voltage

The eighth most significant effect in Figure 6.3 is the interaction between the width of the buried electrode and the voltage. It is aliased with the interaction between the inter-electrode gap and the permittivity of the dielectric. The two aliased interactions share 0.09% of the total variance of the results. The corresponding interaction plots are given in Figure 6.11.

The interactions appear to be small in the figures. In the interaction between the width of the encapsulated electrode and the voltage, at 9.9 kV_{pp}, the power increases

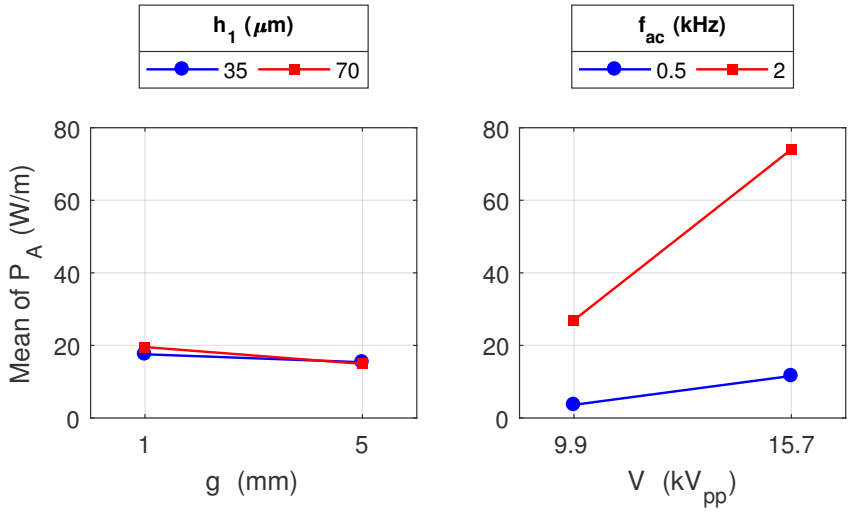

Figure 6.10: Interaction effect between the inter-electrode gap and height of the exposed electrode on the power consumption and its alias.

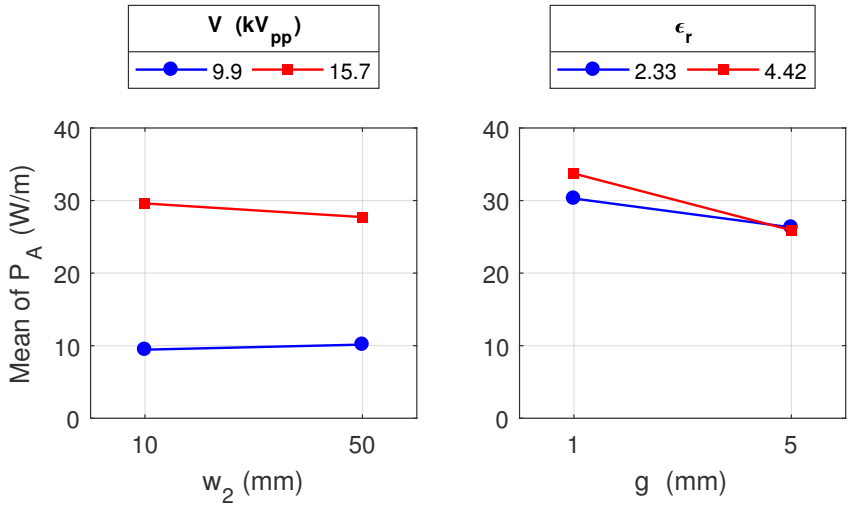

Figure 6.11: Interaction effect between the width of the encapsulated electrode and voltage on the power consumption and its alias.

by 0.70 W/m with a 40 mm widening of the electrode. At 15.7 kV_{pp}, the same growth in the width of the electrode results in a drop of 1.88 W/m. No proper physical explanations have been found to explain this effect.

The interaction between the gap and dielectric permittivity shows the increase of 4 mm in the gap leads to decreases of 3.99 W/m for the low permittivity and 7.81 W/m for the high permittivity. Moreover, for a 5 mm wide gap, the power consumption is only 0.39 W/m higher with a low dielectric permittivity. The inter-electrode gap and dielectric permittivity both reduce the amplitude of the electric field at their high values. Hence, their high levels are expected to weaken the discharge by reducing the charge density and/or the volume of the discharge, and consequently, reduce the loss of power in the plasma due to its electrically resistive behaviour. However, the small interaction between the parameters for a 5 mm wide gap is counter-intuitive if only this phenomenon takes place. As it has been previously mentioned, Corke et al. [2] explained the power lost in the dielectric layer due to the polarisation of the charges can be expected to linearly scale with the permittivity of the dielectric. For a 5 mm gap, it is possible the loss of power through the dielectric has a non-negligible contribution to the total power consumption. Moreover, the high gap and high permittivity were previously associated with a possible saturation of the actuators. The saturation does not seem to play a major role in the power consumption. It is not fully certain this phenomenon is physical or due to the aliasing of the interactions.

9 - Interaction between the width and the height of the exposed electrode

From this point forward, the effects contribute to much less than a tenth of a percent to the variance of the data. Therefore, even if the effects are present, they have a minor impact on the power consumption. The ninth significant effect in the Pareto chart (Figure 6.3) involves the width and height of the exposed electrode. It is aliased with the interaction between the thickness of the dielectric and the frequency. The interactions are responsible for 0.04% of the variance of the power measurements together. The interaction plots are given in Figure 6.12.

The first interaction between the height and width of the air electrode shows a small decrease of 0.74 W/m with a 4.5 mm widening of the gap for a 35 μm thick electrode, against a small gain of 0.83 W/m for a 70 μm thick electrode. For a narrow electrode, the lower height results in an increase of 0.15 W/m of the consumed power. The same interaction was observed to enhance the thrust generation for a thin and narrow air exposed electrode (see page 112). On the contrary, the results here suggest the higher loss of power is reached for a thick and wide electrode. It is uncertain whether this behaviour comes from the increase of the wetted area of the electrode, or from the aliasing of the interaction.

The aliased interaction involves the thickness of the dielectric and the frequency of the electrical signal. At 0.5 kHz, the thickening of the dielectric of 2.4 mm leads to a lowering of the power consumption by 1.98 W/m, whereas it results in a 7.31 W/m

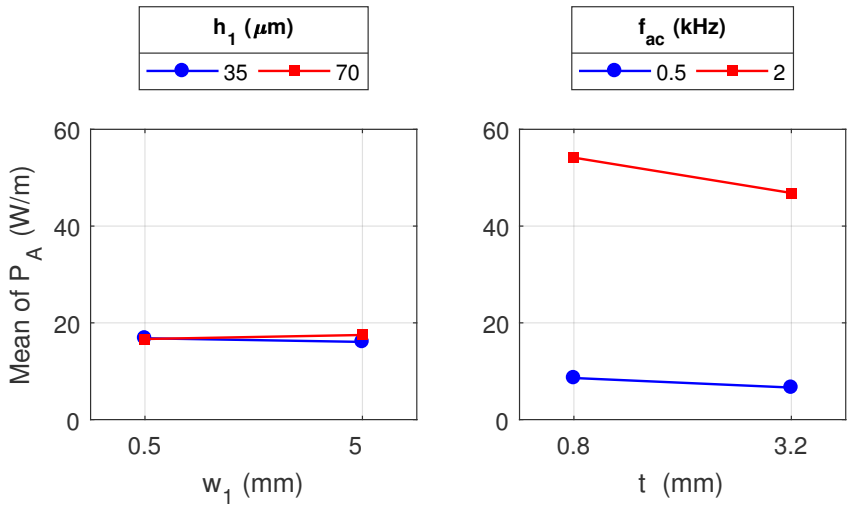

Figure 6.12: Interaction effect between the width and height of the exposed electrode on the power consumption and its alias.

reduction at 2.0 kHz. This interaction seems more likely. The thin dielectric layer is expected to strengthen the electric field, with a greater density of the charged species and/or higher volume of the discharge. As explained previously, the higher the frequency, the more frequent the collisions between the charged and neutral particles. Consequently, if the charged particles are more numerous or the discharge as a greater wetted area, increasing the frequency can lead to a greater transfer of the momentum from the electrically driven charged species on average. This could explain the greater power losses, due to the transfer of kinetic energy to the gas in the electrically resistive plasma at high frequency for a thin dielectric layer. For a thick dielectric, it can firstly be remarked the high frequency was previously linked to the saturation of the actuator. It does not seem the power consumed by the filamentary discharge is further increased by the type of discharge. Hence, the loss of power at a frequency of 2.0 kHz is certainly caused by the weakening of the discharge produced by the thick dielectric.

10 - Dielectric permittivity

The tenth significant effect on the power consumption is the main effect of the dielectric permittivity, that contributes to 0.04% of the variance of the results. The main effect plot is shown in Figure 6.13.

In the figure, an increase of the permittivity from 2.33 to 4.42 leads to a gain of 0.78 W/m. This minor increase of the power consumption could be the result of the increase of the power lost through Joule due to the polarisation of the charges in the dielectric layer, since it is expected to scale linearly with the permittivity [2].

11 - Interaction between the height of the encapsulated electrode and the AC frequency

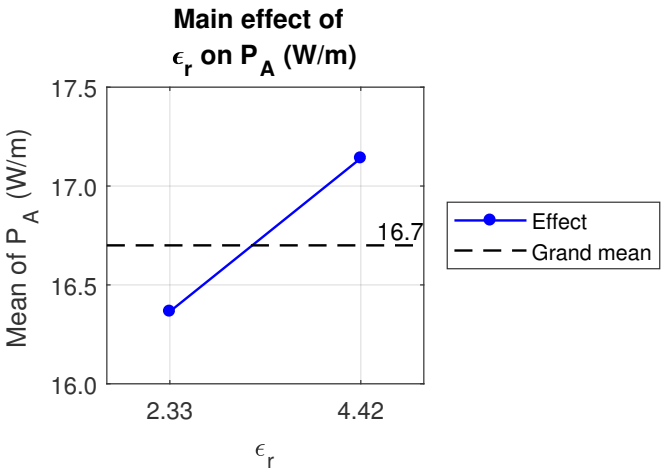

Figure 6.13: Main effect of the dielectric permittivity on the power consumption.

The eleventh significant effect in Figure 6.3 involves the interaction of the height of the buried electrode with the frequency. It contributes to 0.04% of the variance of the results. The corresponding interaction plot is provided in Figure 6.14.

The power drops by 0.23 W/m with a thickening of 35 μm of the encapsulated electrode at a frequency of 0.5 kHz, but increases by 2.35 W/m at 2.0 kHz. This behaviour, even if not as pronounced, follows the effect of the interaction on the thrust (see page 108). The physical reason behind this phenomenon is unclear. It is thought to be caused by the aliasing with a three-factor interaction such as the interaction between the gap, the dielectric thickness and its permittivity (see Table 3.3). This assumption is supported by the fact that several interactions involving these three parameters have been reported in the analysis of the results.

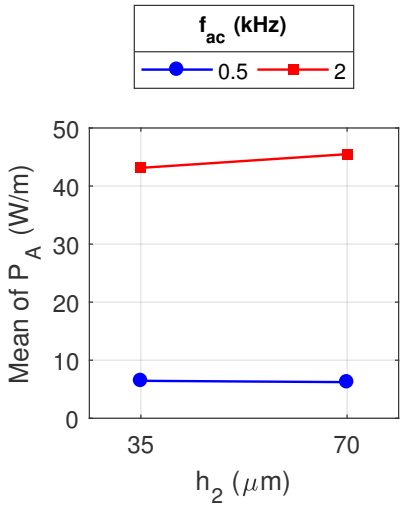

Figure 6.14: Interaction effect between the height of the encapsulated electrode and AC frequency on the power consumption.

12 - Interaction between the inter-electrode gap and the AC frequency

The twelfth most significant effect on the power is the interaction between the inter-electrode gap and the frequency. It is aliased with the interaction between the height of the exposed electrode and the voltage. The two interactions are responsible for 0.04% of the variance of the data. The corresponding interaction plots are displayed in Figure 6.15.

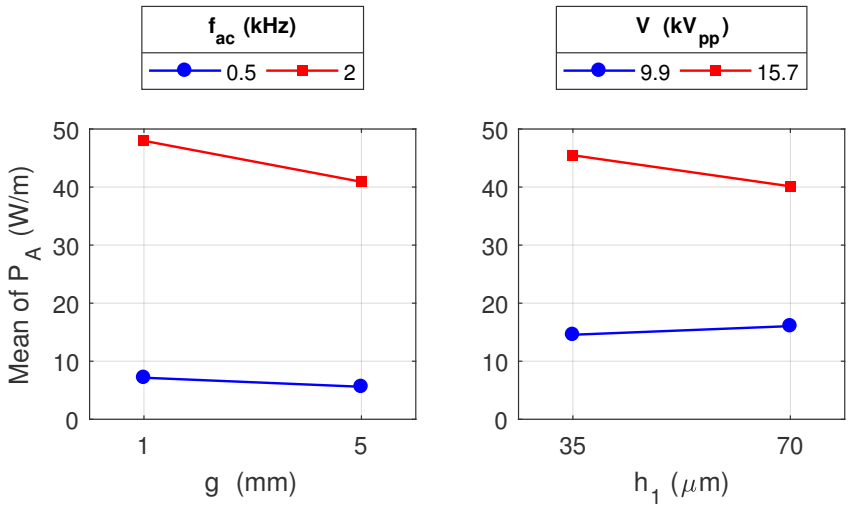

Figure 6.15: Interaction effect between the inter-electrode gap and AC frequency on the power consumption and its alias.

In the first interaction between the gap and frequency, for a widening of the gap of 4 mm, the power decreases by 1.55 W/m at 0.5 kHz, while it lowers by 7.07 W/m at 2.0 kHz. This behaviour agrees with the previously reported effect of the interaction between the dielectric thickness and frequency (see page Figure 6.2.2). Both interactions indicate an increase in the power consumption with a short distance between the electrodes at high frequency. This phenomenon is thought to be the result of the plasma discharge gaining in volume and/or charge density because of to the short separation of the electrodes. As a consequence, this greater amount of charged particles collides more frequently with the neutral gas. Therefore, more power is required to sustain the plasma discharge.

Concerning the second interaction of the voltage with the height of the air electrode, the thickening of 35 μm of the electrode results in an increase of 1.50 W/m at a voltage of 9.9 kV_{pp}, whereas it results in a decrease of 5.36 W/m at 15.7 kV_{pp}. For a narrow air electrode, a dual discharge was typically observed, on both the front and rear edges of the electrode at high voltage. It could explain the increase in the power consumption. However, it does not explain the increase in the power for a low voltage and thick electrode. This interaction is assumed to be caused by the alias.

13 - Exposed electrode height

The thirteenth most significant effect in Figure 6.3 is the main effect of the height of the exposed electrode. It contributes to 0.03% of the total variance of the results. The corresponding main effect plot is shown in Figure 6.16.

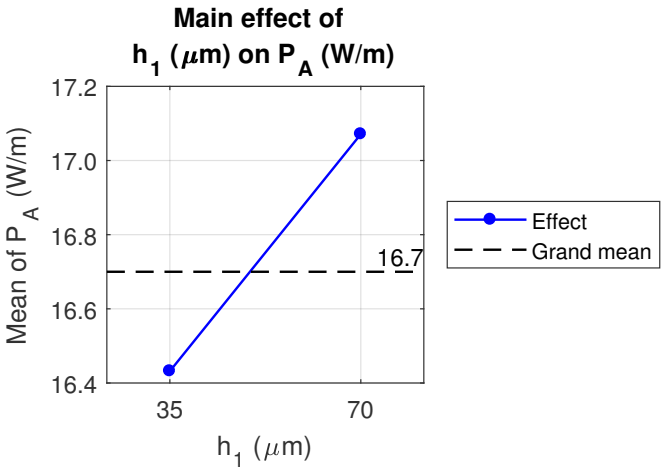

Figure 6.16: Main effect of the exposed electrode height on the power consumption.

In the figure, the power consumption increases by 0.64 W/m when the height of the exposed electrode increases from 35 to 70 μm. The thin electrode was previously observed to improve the thrust generation. It is unknown whether this small effect is produced by an aliased three-factor interaction (see Table 3.3) or is the result of the greater wetted area of the electrode. It is possible the thick electrode releases more charges to the air than the thin electrode, due to its larger exposed surface, leading to a greater loss of power through resistive effects in the plasma. This is however very hypothetical.

14 - Interaction between the widths of both electrodes

The fourteenth most significant effect on the power consumption is the interaction between the widths of the two electrodes. It is aliased with the interaction of the thickness of the dielectric layer with its permittivity. The interactions share 0.03% of the variance of the data. The interaction plots are provided in Figure 6.17.

In the first interaction, for a 10 mm wide encapsulated electrode, a growth of 4.5 mm in the width of the air electrode results in a 0.67 W/m increase of the power consumption. On the other hand, the same increase in the width of the exposed electrode leads to a loss of 0.57 W/m for a 50 mm wide buried electrode. No physical justification has been found to explain these trends.

For the aliased interaction, the power consumption reduces by 3.60 W/m at a permittivity of 2.33, and by 5.69 W/m at a permittivity of 4.42, with a thickening of the dielectric of 2.4 mm. This interaction shows the same behaviour than the interaction between the inter-electrode gap and dielectric permittivity presented on page 131. In both interactions, the shorter distance between the electrodes leads to a greater power consumption when the permittivity of the dielectric is high, although the permittivity

hardly makes a difference in the consumed power for a large gap or thick dielectric. It is hypothesised that two distinct phenomena are responsible for these results. For a thick dielectric or large gap, an increase in the permittivity further decreases the amplitude of the electric field (as suggested by Equation 5.2). Thus, the discharge is further weakened when all the variables are at their high levels. On the opposite, for a short gap or thin dielectric, the electric field being stronger, the greater permittivity could lead to the transition of the discharge from the glow type to the filamentary type. This phenomenon was observed by Thomas et al. [45], and its consequence is a saturation of the thrust, with a greater power consumption. The glow discharge has a more homogeneous distribution of the charge density. For the filamentary discharge, a greater portion of the charges is sent towards the dielectric through localised strong filaments. The authors concluded that a greater permittivity of the dielectric layer enhanced the saturation. For instance, a filamentary discharges is shown in Figure 5.9. The figure highlights the filamentary discharge was also observed to occur at low permittivity on a thin dielectric and with a long gap. An accurate, repeatable and systematic photographic investigation was not conducted in the current study. Therefore, most of the runs supplied with a 9.9 kV_{pp} signal were not photographed, due to the low visibility of the plasma with the employed camera in the used facility. Consequently, it is uncertain whether the filamentary discharges concerned the majority of the runs having a 0.8 mm thick dielectric with a permittivity of 2.33. As a result, the present assumption was not verified.

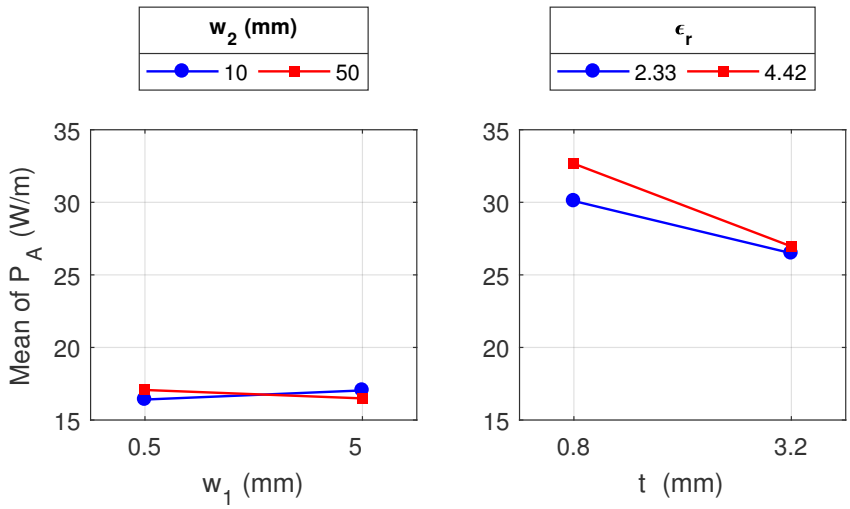

Figure 6.17: Interaction effect between the widths of the exposed and encapsulated electrodes on the power consumption and its alias.

15 - Interaction between the height of the encapsulated electrode and the dielectric permittivity

The fifteenth most significant effect in Figure 6.3 is the interaction between the

thickness of the buried electrode and the permittivity of the dielectric, with a contribution of 0.02% to the variance of the results. The corresponding interaction plot is displayed in Figure 6.18.

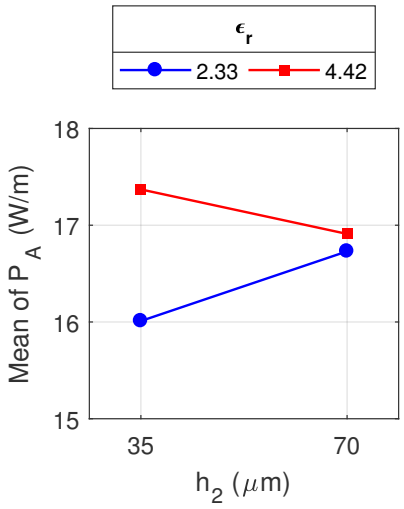

Figure 6.18: Interaction effect between the height of the encapsulated electrode and dielectric permittivity on the power consumption.

In the figure, it can be seen that the power increases by 0.71 W/m with a 35 μm thickening of the encapsulated electrode for a dielectric of low permittivity, but drops by 0.46 W/m for a dielectric of high permittivity. No proper physical explanations has been reached for this interaction. It should be noted the repeatability of the power measurements was found to be greater than the expected error of the material in Table 4.4. The given effects are of the order of the variations of the data between each of the three experimental tests for each run. It is possible this effect has been generated by the slightly greater than anticipated error of the measurements. Besides, the interaction is aliased with several three-factor interactions which involves parameters that were already observed to interact (see Table 3.3). The interactions concern the height and width of the air electrode, the inter-electrode gap, the dielectric thickness, the frequency and the voltage.

16 - Interaction between the width of the exposed electrode and the inter-electrode gap

The sixteenth significant factor on the power consumption belongs to the interaction of the width of the air electrode with the inter-electrode gap. It is aliased with the interaction between the dielectric thickness and the voltage. The two interactions are responsible for 0.02% of the variance of the data. The interaction plots are presented in Figure 6.19.

The interaction between the width of the air electrode and the gap results from an increase of 0.62 W/m with a widening of the electrodes for a gap of 1 mm, that changes

to a drop of 0.46 W/m for a gap of 5 mm. These effects are negligible, and could be the result of the previously mentioned greater inaccuracy of the power measurements. Moreover, a physical ground has not been found to explain this behaviour. This effect is believed to be the result if the alias.

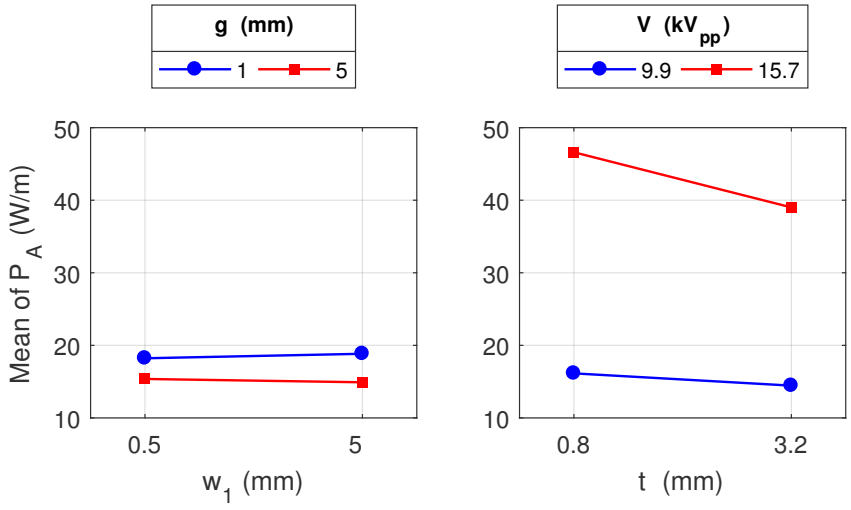

Figure 6.19: Interaction effect between the width of the exposed electrode and inter-electrode gap on the power consumption and its alias.

For the aliased interaction, the figure shows a drop of 1.69 W/m with the thickening of the dielectric layer at 9.9 kV_{pp}, versus a loss of 7.60 W/m with the same thickening at 15.7 kV_{pp}. The higher consumption for a 0.8 mm thick dielectric at 15.7 kV_{pp} is thought to be caused by the increased stronger electric field produced by the thin dielectric, interacting with the increase in the electric field imparted to the greater voltage. It is possible the increase of the power is enhanced by the transition of the discharge to the filamentary type, as shown in Figure 5.9.

17 - Interaction between the height of the encapsulated electrode and the thickness of the dielectric

The seventeenth significant effect in Figure 6.3 belongs to the interaction between the dielectric thickness with the height of the buried electrode, and contributes to 0.01% of the total variance of the results. The interaction plot is presented in Figure 6.20. It should be noted this effect is 95% certain, but its standardised effect is lower than the critical t-value for 99% confidence.

The figure highlights a small drop of 0.20 W/m with the thickening of the encapsulated electrode for a thin dielectric layer, against a small increase of 0.42 W/m for a thick dielectric. It is unknown why these effects occur. Given the values, and compared to the typical standard deviations captured in Table 4.4, it is possible these changes are due to errors. Moreover, this effect is aliased with several three-factor interactions which contain variables that are involved in two-factor interactions. In particular, the

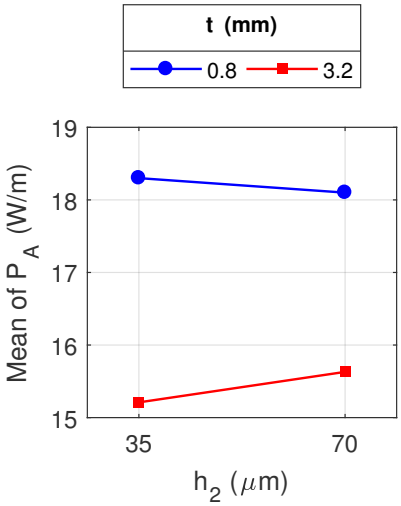

Figure 6.20: Interaction effect between the height of the encapsulated electrode and dielectric thickness on the power consumption.

three-factor interactions implicate the gap, the permittivity, the frequency, the voltage and the height of the air electrode (see Table 3.3).

18 - Interaction between the width of the exposed electrode and the height of the encapsulated electrode

The final significant effect in Figure 6.3 is the interaction of the height of the width of the exposed electrode with the height of the encapsulated electrode. It is responsible for 0.01% of the variance of the results. The interaction plot is shown in Figure 6.21. The effect is also only 95% certain.

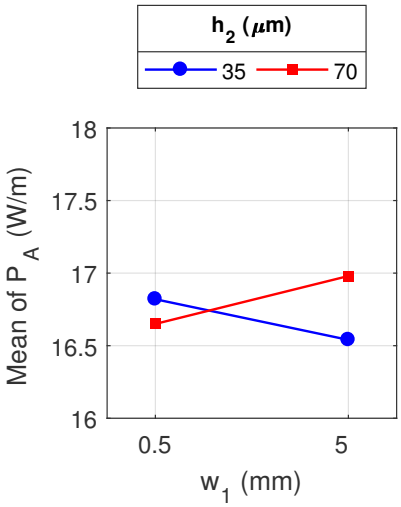

Figure 6.21: Interaction effect between the width of the exposed electrode and height of the encapsulated electrode on the power consumption.

In the figure, the interaction transpires through the slight drop of 0.27 W/m with the widening of the air electrode for thin electrode, that augments to an increase of 0.33 W/m for a thick buried electrode. As for the previous interaction, it is unclear why this behaviour occurs. Moreover, the effects are of the order of the standard deviations of the power for each run. As the previous effect, it is aliased with a three-factor interaction which involves the dielectric permittivity, the voltage and the frequency (see Table 3.3). Since the three factors were found to interfere through two-factor interactions, this seems possible the negligible effect is caused by the alias.

6.3 Linear Regression Model

The DOE analysis performed by Minitab produces a linear regression model for the transformed response (natural logarithm of the power). The first limitation is the assumption that the transformed response depends linearly on all the factors and their interactions. Secondly, the model assesses the effect of the aliases through only one of the aliased effects. This selected alias is only chosen by name. If two interactions were found to be aliased, one involving w_1 and the second involving g for instance, the retained interaction will be the interaction of w_1 since it is the first parameter of the study while g is the third. The model is hence expected to only provide approximate estimates of the power consumption for different designs. The model can be expressed through the following equation:

$$\ln\left(P_{\mathrm{A}}\right) = X_{\mathrm{d}} \cdot M_P \cdot X_{\mathrm{d}}^T \ , \tag{6.1}$$

with X_{d} being the array of the input parameters:

$$X_{\mathrm{d}} = \left[\begin{array}{cccccccccc} 1 & w_1 & w_2 & g & h_1 & h_2 & t & \varepsilon_r & V & f_{\mathrm{ac}} \end{array} \right] \ . \tag{6.2}$$

In Equation 6.1, X_{d}^T is the transpose of X_{d} and M_P the ten by ten matrix of the model coefficients:

$$\left[\begin{array}{cccccccccc} -1082 & -145.4 & 9.84 & -12.8 & 3.935 & 1.2 & -56 & 64.1 & 172.26 & 1172.1 \\ 0 & 0 & -0.399 & -3.56 & 0.595 & 0.228 & -13.48 & 3.16 & 11.109 & -0.59 \\ 0 & 0 & 0 & -0.159 & -0.011 & 0.005 & 0 & 0 & -0.592 & -0.203 \\ 0 & 0 & 0 & 0 & -0.983 & 0.206 & 0 & 0 & 0 & 14.16 \\ 0 & 0 & 0 & 0 & 0 & -0.023 & 0 & 0 & 0 & 0 \\ 0 & 0 & 0 & 0 & 0 & 0 & 0.455 & -0.965 & -0.075 & 1.713 \\ 0 & 0 & 0 & 0 & 0 & 0 & 0 & 0 & 0 & 0 \\ 0 & 0 & 0 & 0 & 0 & 0 & 0 & 0 & 0 & 0 \\ 0 & 0 & 0 & 0 & 0 & 0 & 0 & 0 & 0 & 0 \\ 0 & 0 & 0 & 0 & 0 & 0 & 0 & 0 & 0 & 0 \end{array} \right] \times 10^{-3} \tag{6.3}$$

Minitab calculates the fitness of the models through the R^2 and adjusted R^2 coefficients. There are here 99.91% and 99.87% respectively. Therefore, the model predicts the results of the tests matrix accurately, and does not include unnecessary input variables. The models for all three output parameters are further discussed in Chapter 8.

6.4 Summary

Of the eighteen significant effects discussed in the previous section, several agreed with phenomena reported in the literature. Many of the effects have a small impact of the results, with contribution of 1% or less to the total variance on the data. Besides, several aliased interaction could not be fully concluded on, and could only be explained through hypotheses, with the possibility there are due to the observed higher inaccuracy of the power measurements.

In total, the main effects were found to contribute to 98.98% of the variance, while the interactions only cover 0.93% of the total variance of the data. Hence, the interactions between the design factors can be neglected when trying to minimise the power consumed by an actuator. The first four significant parameters are responsible for 98.91% of the variance. They are by order of importance: the AC frequency, the voltage, the inter-electrode gap and the dielectric thickness.

The higher voltage and frequency were found to consume a greater electrical power. This agrees with other observations [7, 45, 59, 69]. Finally, the gap and thickness of the dielectric were seen to decrease the consumed power. It is thought to be due to the weakening of the electric field caused by the longer distance between the electrodes, that causes a weakening of the discharge. Through this effect, the volume of the plasma discharge and/or its charge density diminishes, and consequently the momentum injection and power consumption reduce.

Minimising the power is not fully practicable in reality, if a lower bound is not defined, or if another target (such as a target thrust) is not drawn. Indeed, a simple mathematical minimisation of the power without other(s) condition(s), the power can mathematically be lowered to zero, but then, the DBD is switched off. The force efficiency is a more useful parameter to assess, in order to determine which of the significant parameters have a stronger effect on the thrust generation or power consumption. Besides, the saturation [45] of the actuator was found to have a significant impact on the thrust generation, but did not seem to result in a significant increase in the power consumption. If the saturation phenomenon is important, it is expected to increase the consumed power per unit thrust, and hence, decrease the force efficiency. The next section focuses on the DOE analysis of the force efficiency.

Chapter 7

Parametric Study for the Force Efficiency

The current chapter presents the DOE analysis of the force efficiency. First, the response transformation and residuals are detailed, in order to highlight the mathematical validity of the analysis. Secondly, a ranking of the significant effects of the nine design parameters is presented, and the physical phenomena that explain these effects are discussed. Finally, the model of the force efficiency that is calculated through a linear regression of the results is presented.

7.1 Validity of the Analysis

The analysis of the force efficiency is performed on the square-root of the results, in order for the residuals of the linear regression to follow the normal distribution assumption (see Section 3.3.8). As for the thrust analysis (see Chapter 5), this transformation suggests the that the increase in the significant effects is non-linear. The residual plots for the force efficiency are presented in Figure 7.1.

The histogram of the residuals (Figure 7.1a) exhibits a slight negative skewness, with more numerous negative residuals. The normal probability plot (Figure 7.1b) shows the residuals between 0.025 and -0.025 follow a linear trend. However, numerous outliers can be identified, especially on the negative side. Consequently, the transformation is not completely sufficient. Since the thrust was analysed through its square-root and the power through its logarithm, it is not surprising the thrust over power ratio requires a complex transformation to fully respect the normal distribution assumption. The distributions of the residuals against the fitted values (Figure 7.1c) and against the observation orders (Figure 7.1d) do not follow any particular trend, and appear as random signals. Nevertheless, the residuals versus fitted values plot (Figure 7.1c) highlights a slightly greater spreading of the residuals at the low fitted values, resulting in a higher inaccuracy of the model at the low values of the force efficiency. In the previous analyses, the thrust was modelled through its square root, while the power was investigated through its natural logarithm. Therefore, the ratio of the two quantities

possesses a more complex behaviour than a simple square-root. Using a Box-Cox transformation in Minitab did not change the transformation. In conclusion, the DOE analysis must be considered with caution, as it might not be able to model the smallest values of the force efficiency correctly. However, the R^2 coefficient of the model is 91.67%, meaning most of the observed effects are accurate.

7.2 Ranking of the Significant Parameters

7.2.1 Selection of the Significant Effects

In order to identify the significant parameters, the standardised effects of the factors and their interactions on the force efficiency are represented on the half-normal plot in

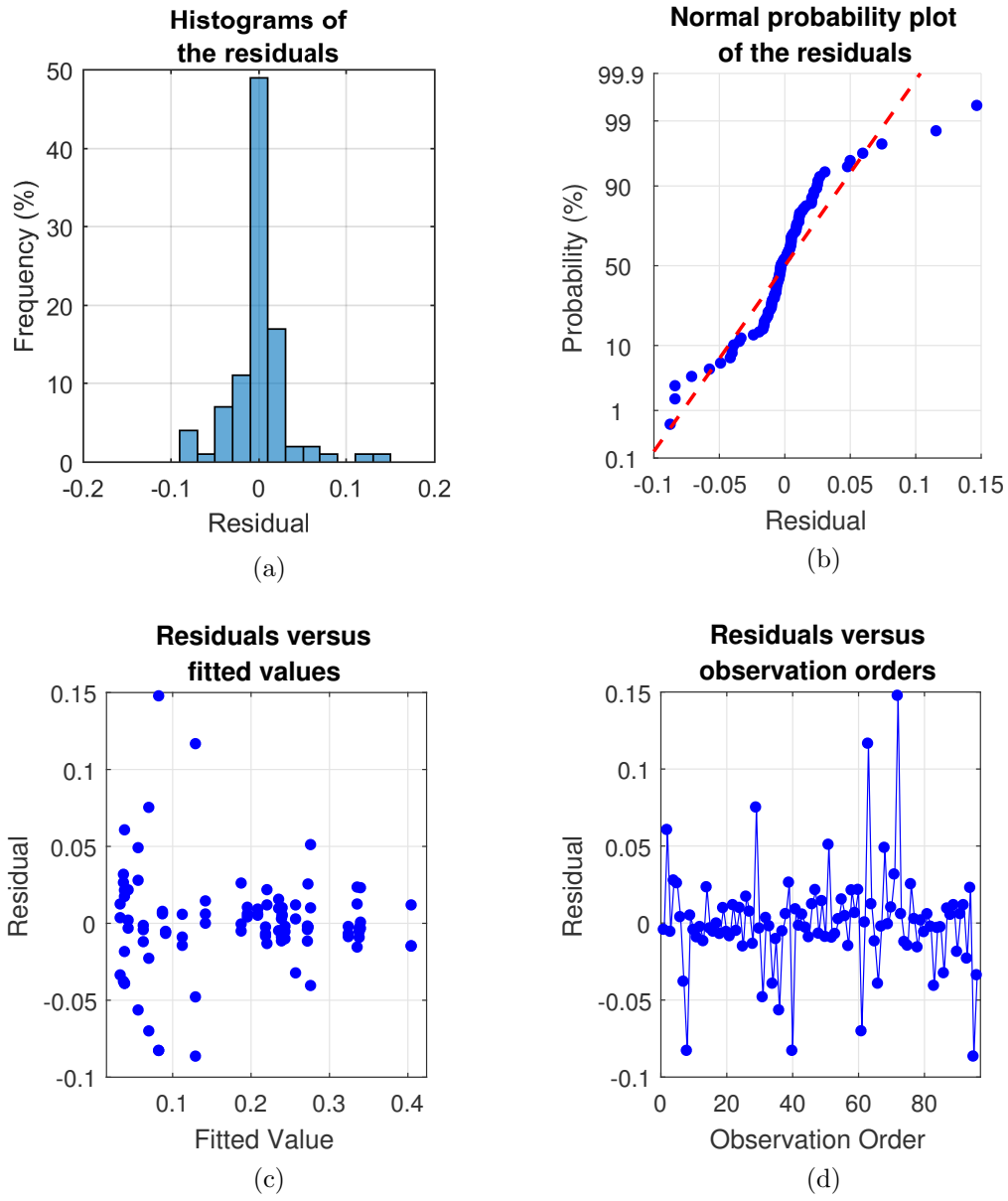

Figure 7.1: Residual plots of the analysis of the force efficiency.

Figure 7.2. The distribution of the standardised effects is compared to two lines in the figure. The solid blue line represents a normal distribution having the same two-tailed t-value as the study (1.98 for 96 tests at a confidence level of 95%). If the effects were to follow this distribution, they would be insignificant. The dash line illustrates the best fitting of a normal distribution to the data. The absolute standardised effects of the most influential parameters exceeds the predictions of this distribution.

In Figure 7.2, fifteen effects are significant, and form the model. Minitab calculates how much of the variance (square of the standard deviation) of the data can be imparted to each effect. The more a design parameter contributes to the variance of the results, the more it affects the output parameter. In total, the fifteen model terms are responsible for 91.67% of the total variance. The most significant effects are the voltage (V), the frequency (f_{ac}), the inter-electrode gap (g), the dielectric thickness (t) and the width of the exposed electrode (w_1), and they respectively contribute to

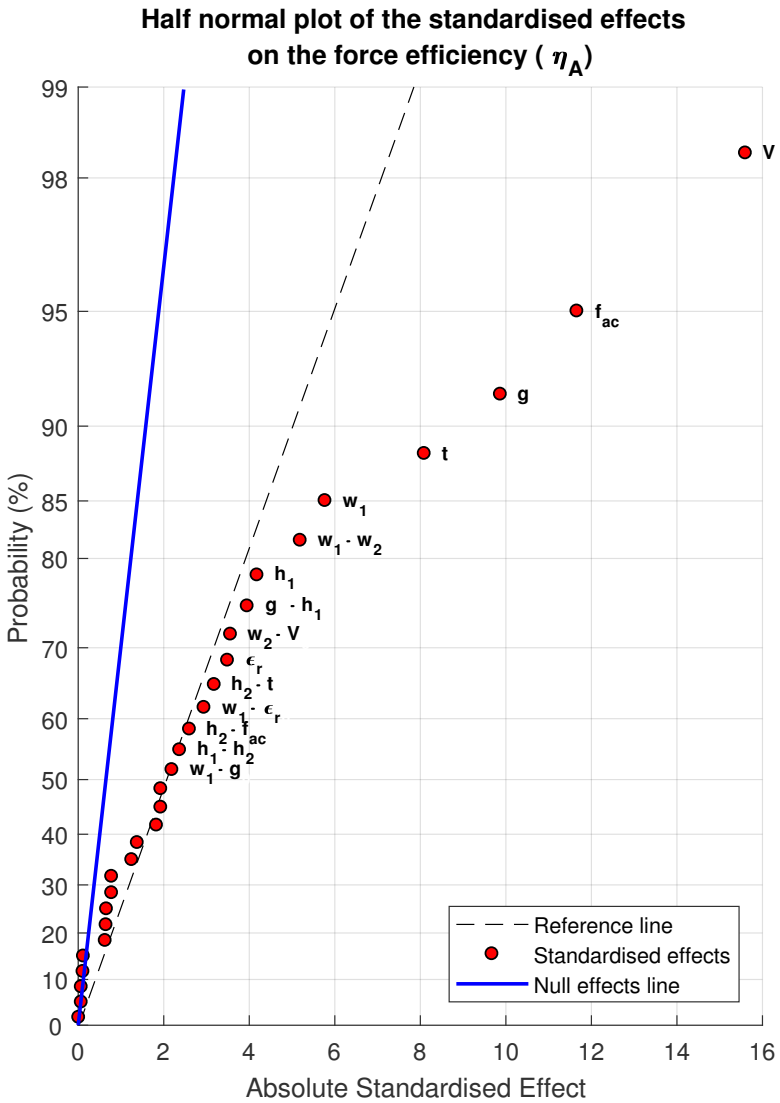

Figure 7.2: Half-normal plot of the standardised effect on the force efficiency.

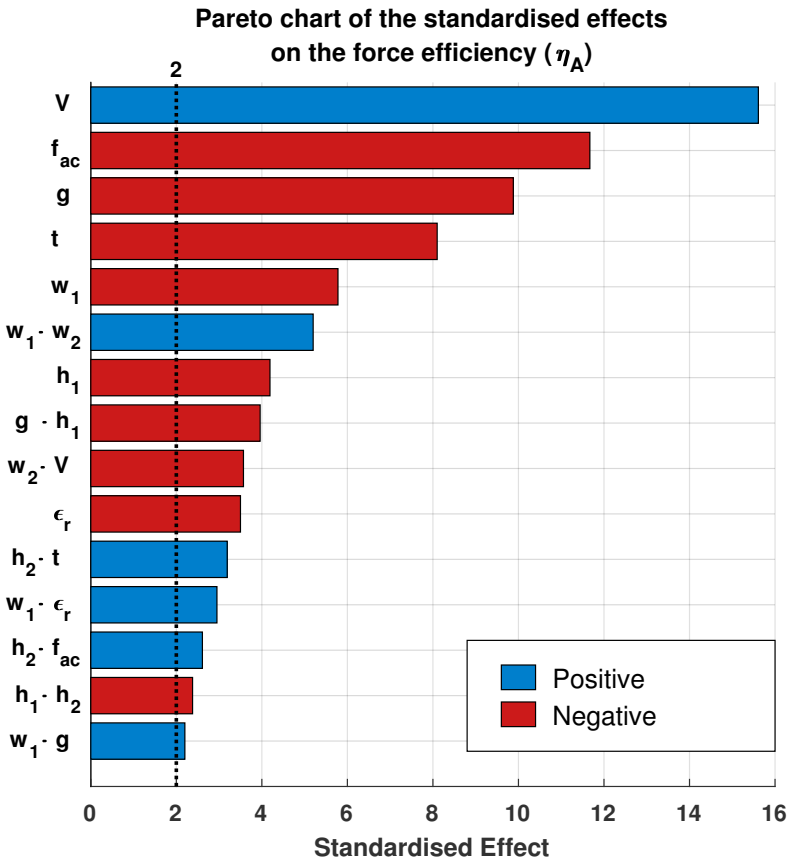

Figure 7.3: Pareto chart of the standardised effects on the force efficiency, coloured by sign of the effect.

31.25%, 17.46%, 12.52%, 8.42% and 4.28% of the total variance resctively (73.93% altogether). The fifteen significant standardised effects are displayed in the Pareto chart in Figure 7.3. In the figure, since the standardised effects are absolute values, the bars are coloured by the signs of the effects. For instance, the effect of the voltage (V) is positive, meaning an increase in the supplied voltage leads to an increase in the force efficiency. The Pareto chart shows that all the selected standardised effects are greater than the critical t-value of 1.98. It should be noted that most of the significant interaction effects are aliased. The mathematical analysis of the DOE cannot determine which of the aliased interactions cause the effect. Therefore, the physical basis of each of the aliased interactions must be analysed in order to draw a conclusion. Moreover, as previously reported, the t-value for a 99% confidence level is 2.63 for 96 tests. From the fifteen standardised effects appearing in Figure 7.3, twelve are greater than this critical value. Consequently, most of the effects place due to the changes in the design parameters.

7.2.2 Discussion of the Significant Effects

1 - Voltage

In Figure 7.3, the most significant effect belong to the voltage, which is responsible

for 31.25% of the variance of the data. The main effect plot is represented in Figure 7.4.

In Figure 7.4, the increase of 5.8 kV_{pp} results in a gain of 46.2 μN/W. It can be remarked the voltage was found to have positive effects on both the thrust generation and the power consumption. This positive effect on the force efficiency demonstrates the voltage impacts the thrust generation in a larger extent than the power consumption. It must be noted that this conclusion is true for the ranges used in the study. For instance, with different designs and/or supplied electric signal, the saturation [45] could lead to greater gain/loss in thrust with a still increasing power. The significance of this conclusion could be enhanced by knowing the saturation voltages and frequencies of the different runs. It would however require a new study, in which the two electric parameters would be investigated over more values for every single run.

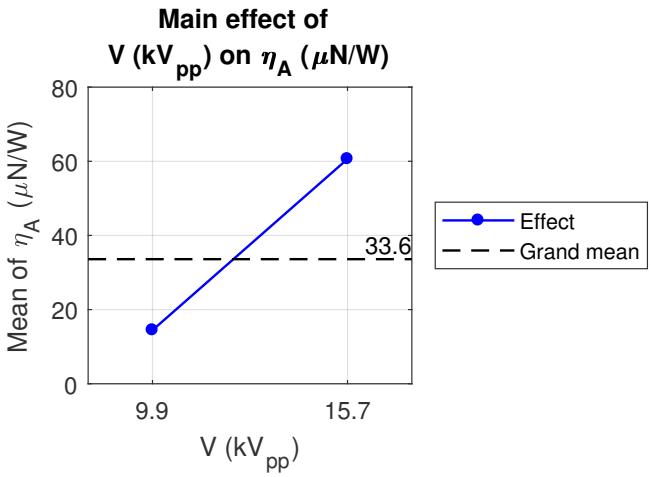

Figure 7.4: Main effect of the voltage on the force efficiency.

2 - AC frequency

The second most significant effect on the force efficiency belongs to the frequency of the applied sine wave signal, with a contribution of 17.46% to the total variance of the results. Its main effect plot is displayed in Figure 7.5.

The effect is here negative, with a loss of 34.5 μN/W for an increase of 1.5 kHz of the frequency. As the frequency was observed to have positive effects on both the thrust generation and power consumption, this results implies that the frequency has a stronger effect on the power. Several effect evidenced the saturation phenomenon described by Thomas et al. [45] must have occurred throughout the experimental campaign. The authors showed that the higher the frequency, the lower the saturation thrust of the actuator. After saturation, the thrust was found to stagnate. Far from reaching the saturation voltage, the thrust was found to scale as the voltage to the power of 3.5. When approaching the saturation, the thrust was observed to scale as the voltage to the power of 2.3. Simultaneously, the authors conducted some power measurements that proved the power did not seem to be affected, and kept increasing. As a result, a great loss of force efficiency can be expected as soon as the actuator approaches or

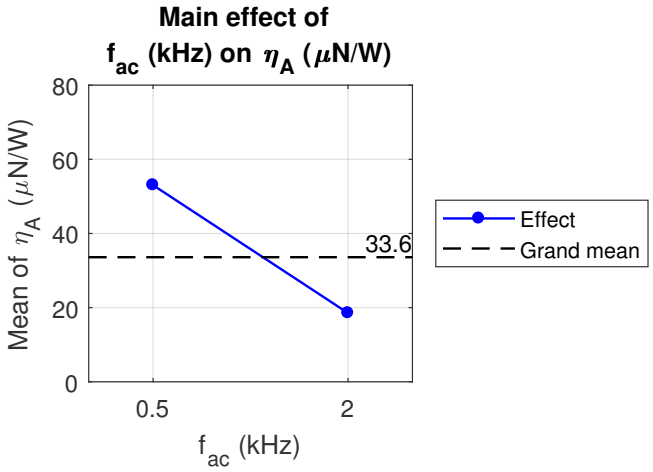

Figure 7.5: Main effect of the AC frequency on the force efficiency.

reaches its saturation. The consequence in the present analysis is the negative effect of the frequency. The saturation of the discharge was reached or approached by several runs (especially at high voltage, as shown in Figure 5.9), leading to a general loss of thrust over power ratio at high frequency. In Figure 5.9, it can be seen the filamentary discharge was also captured for run 25 with at 0.5 kHz. This is certainly a result of the interaction of the voltage with the frequency (see page 151).

3 - Inter-electrode gap

In Figure 7.3, the third most significant parameter is the gap between the electrodes. It is responsible for 12.52% of the total variance of the data. The corresponding main effect plot is shown in Figure 7.6.

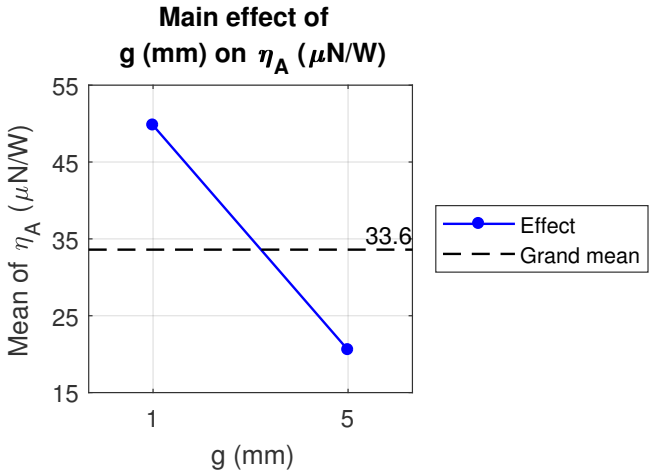

Figure 7.6: Main effect of the inter-electrode gap on the force efficiency.

In the figure, the widening of the inter-electrode gap from 1 to 5 mm results in a loss of 29.2 μN/W. The gap was already seen to have negative effects on the thrust and power. The result demonstrates a larger gap leads to a greater loss of thrust than loss

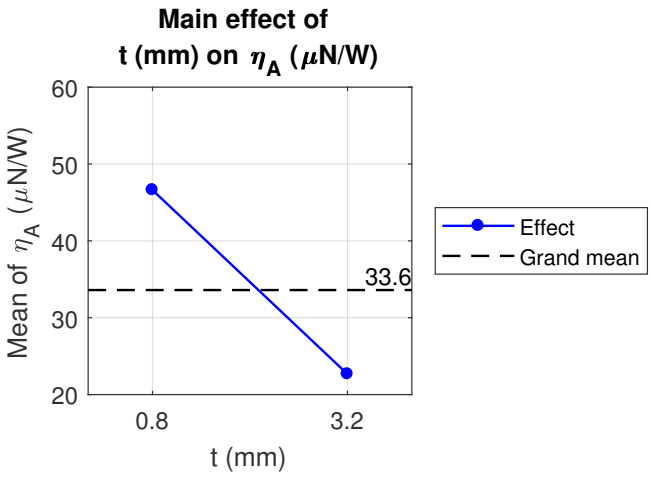

Figure 7.7: Main effect of the dielectric thickness on the force efficiency.

of power. This result is thought to be the outcome of the decrease in the amplitude of the electric field induced by a greater distance between the electrodes.

4 - Thickness of the dielectric

The fourth most significant effect in Figure 7.3 is the thickness of the dielectric layer, which contributes to 8.42% of the variance of the data. Figure 7.7 presents the main effect plot of the dielectric thickness.

It can be seen in the figure, that a thickening of the dielectric layer from 0.8 to 3.2 mm leads to a drop of 24.0 μN/W. As for the inter-electrode gap, the thickness of the dielectric was observed to have negative effects on the thrust generation and power consumption. As a result, the overall decrease in the force efficiency with the increase in the thickness indicates a greater loss of thrust induced by the thick layer. The efficiency is found to drop by 10 μN/W/mm of dielectric thickness against 7.3 μN/W/mm of inter-electrode gap. The greater rate of loss caused by the dielectric thickness is certainly a consequence of the higher permittivity of the dielectric medium over the air.

5 - Width of the exposed electrode

The fifth significant effect on the force efficiency belongs to the width of the exposed electrode. Its participation to the total variance of the results amounts to 4.28%. The main effect plot of the parameter is represented in Figure 7.8.

In the figure, the increase of the width from 0.5 to 5 mm induces a decrease of the force efficiency of 17.1 μN/W. The parameter was found to have a negative effect on the thrust generation, but was not significant for the power consumption. Hence, it is unsurprising the width of the air electrode has a negative effect on the force efficiency. The result demonstrates a narrow electrode reaches a greater efficiency. This concurs with the observations of Enloe et al. [8]. They captured an almost linear relationship between the generated thrust and consumed power. In their study, wire electrodes were employed, and the lower the diameter, the greater the thrust gained per unit of power,

and consequently, the higher the thrust over power ratio.

6 - Interaction between the widths of the two electrodes

In Figure 7.3, the sixth most significant effect belongs to the interaction between the widths of both electrodes. It is aliased with the interaction between the dielectric thickness and permittivity. The two interactions share 3.46% of the total variance of the results. The interaction plots are displayed in Figure 7.9.

The first interaction between the widths of the two electrodes shows a negligible effect for a wide encapsulated, with a slight loss of 1.8 μN/W with the widening of the exposed electrode. For interactions, the confidence interval for each point is 1.82 μN/W (see Table 4.3), hence this difference could be caused by measurement errors. For a narrow exposed electrode, the increase of the width of the air electrode results in a decrease of 31.6 μN/W. No proper interpretation has been determined to explain this behaviour. It is believed to be caused by the aliased interaction.

In the interaction of the thickness of the dielectric layer with its permittivity, the force efficiency lowers by 36.1 μN/W with the thickening of the dielectric of 2.4 mm at a permittivity of 2.33, whereas the force efficiency drops by 8.8 μN/W with the same thickening at the permittivity of 4.42. For a 3.2 mm thick dielectric, the increase of the dielectric permittivity results in an increase of 1.7 μN/W, which is lower than the confidence interval of 1.82 μN/W. To sum up, the thickness of the dielectric has a negative effect on average, yet, a high permittivity leads to an even greater loss of efficiency for a thin dielectric layer. This behaviour could be explained by the saturation phenomenon described by Thomas et al. [45]. The thick dielectric results in a weakening of the electric field over the dielectric layer, since it can store more of the electric field through the polarisation of the medium. Thus, the plasma discharges over the thick dielectric can be relatively weak, so that the change in the permittivity does not affect them significantly on average. Moreover, a thicker dielectric makes the saturation thrust and voltage higher [45]. The stronger discharge occurring over thin

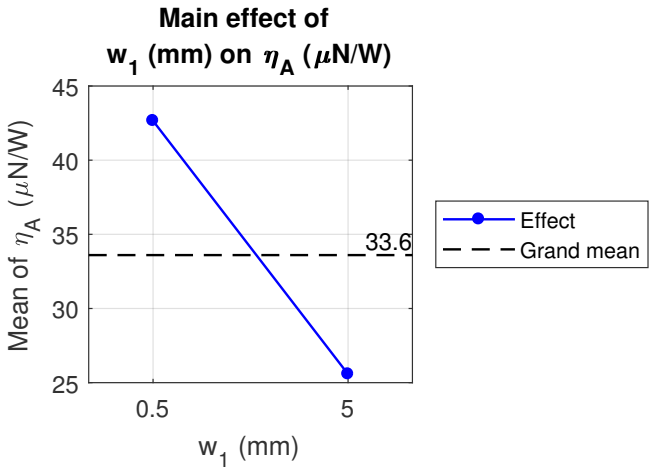

Figure 7.8: Main effect of the exposed electrode width on the force efficiency.

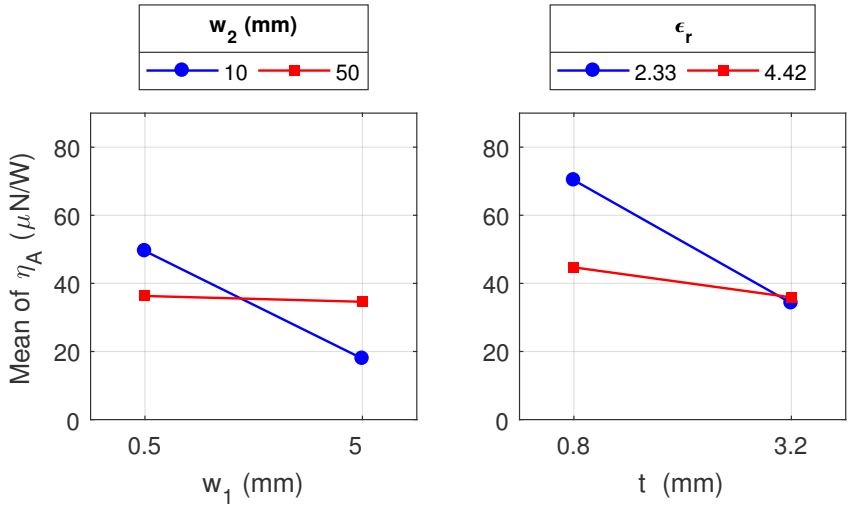

Figure 7.9: Interaction effect between the widths of the exposed and encapsulated electrodes on the power consumption and its alias.

dielectric layers can hence be more sensitive to the saturation. However, an increase in the dielectric constant decreases the saturation thrust of the actuator [45]. Even if the saturation point is not reached, the thrust induction lowers as the saturation is approached [45]. Simultaneously, it was observed the increase in the dielectric permittivity brings a greater power consumption on average (see page 133). Consequently, the higher permittivity of the dielectric reduces the obtainable thrust due to the saturation of the discharge, and increases the power consumption. The overall effect is a great loss of efficiency with a thin dielectric when the permittivity of the material increases.

7 - Height of the exposed electrode

The seventh most significant effect in Figure 7.3 is caused by the height of the exposed electrode. It provides 2.24% of the total variance of the results. The corresponding main effect plot is presented in Figure 7.10.

On average, the height of the air electrode is seen to reduce the efficiency by 12.4 μN/W when it grows from 35 to 70 μm. As it has been discussed for the width of the exposed electrode on page 149, a wire electrode of thin diameter can be expected to give a better efficiency [8]. The current study agrees with this trend by showing a narrow and thin exposed electrode produces a higher thrust and reaches a greater force efficiency on average.

8 - Interaction between the inter-electrode gap and the height of the exposed electrode

The eighth most significant effect in Figure 7.11 belongs to the interaction of the inter-electrode gap with the exposed electrode height. It is aliased with the interaction between the voltage and the AC frequency. The two interactions share 2.01% of the

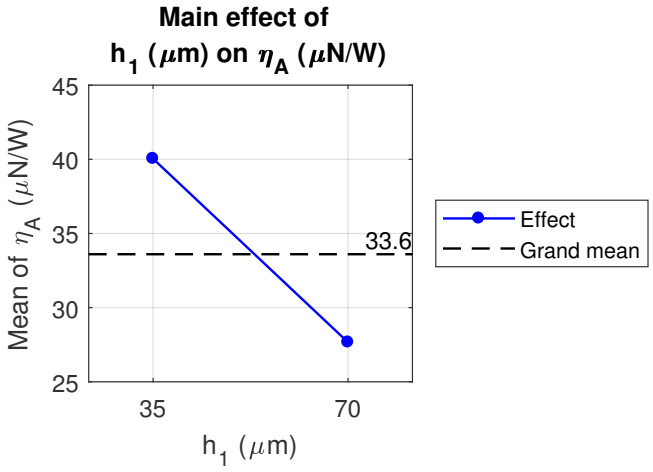

Figure 7.10: Main effect of the exposed electrode height on the force efficiency.

variance of the data. The interaction plots are presented in Figure 7.11.

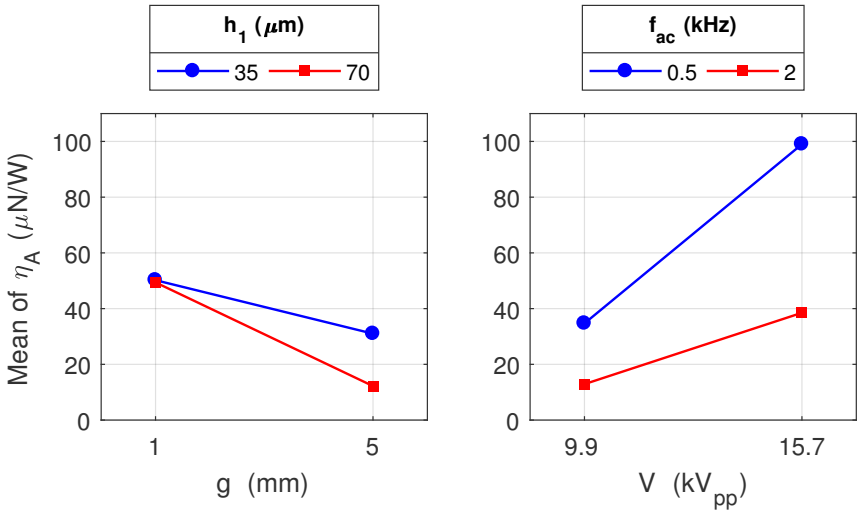

Figure 7.11: Interaction effect between the inter-electrode gap and the height of the exposed electrode on the power consumption and its alias.

The first interaction plot between the gap and the air electrode thickness shows a negligible effect of the height of the electrode on the force efficiency for a short gap of 1 mm, with only a 0.8 μN/W difference (lower than the confidence interval of 1.82 μN/W presented in Table 4.3). For a 35 μm thick electrode, the widening of the gap of 4 mm decreases the force efficiency by 19.1 μN/W. For a 70 μm thick electrode, the same widening of the inter-electrode gap lowers the efficiency by 37.2 μN/W. Both the height of the exposed electrode and gap between the electrodes were observed to increase the efficiency at their low values. The interaction suggests the loss of force efficiency with the increase of the gap is partly damped at the lower value of the height. It is possible the effect is caused by the increases of the electric field induced by either a small gap or thin electrode. However, it is unknown whether this effect is factual or

the result of the aliasing.

The second interaction involves the voltage and frequency of the supplied electrical signal. The efficiency is found to increase by 64.3 μN/W with a 5.8 kV_{pp} increase in the voltage at a frequency of 0.5 kHz, but to only grow by 25.5 μN/W with the 5.8 kV_{pp} increase in the voltage at 2.0 kHz. The interaction between the electrical parameters was already observed to impact the thrust (page 105) and power (page 130). In both cases, the voltage had positive effects the thrust and power, with an even greater gain with a high frequency. The frequency having a negative effect on the force efficiency, it was concluded it has a greater impact on the power consumption. As a result, the interaction here reverted with the higher efficiency obtained at the high voltage and low frequency. This phenomenon seems to be caused by the saturation of the actuator, since the saturation voltage reduces with a greater frequency. That could explain the greater difference observed at 15.7 kV_{pp}, since when saturated, the higher the voltage, the greater the power increases when the thrust stagnates.

9 - Interaction between the width of the encapsulated electrode and the voltage

The ninth significant effect in Figure 7.3 is the interaction between the width of the buried electrode and the voltage. It is aliased with the interaction of the inter-electrode gap with the dielectric permittivity. The two interactions are responsible for 1.64% of the overall variance of the results. The interaction plots are displayed in Figure 7.12.

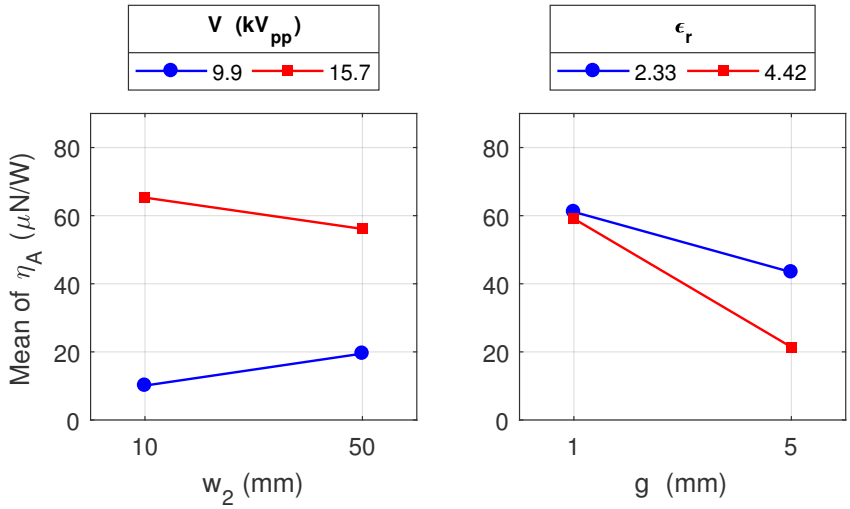

Figure 7.12: Interaction effect between the width of the encapsulated electrode and voltage on the power consumption and its alias.

For the interaction between the width of the encapsulated electrode and the voltage, the force efficiency grows by 9.4 μN/W with the widening of the encapsulated electrode from 10 to 50 mm at 9.9 kV_{pp}. At 15.7 kV_{pp}, the same increase in the width of the buried electrode decreases the efficiency by 9.2 μN/W. This effect is thought to be

generated by the aliased interactions.

In the aliased interaction, the widening of the inter-electrode gap from 1 to 5 mm results in a loss of 17.7 μN/W for a dielectric permittivity of 2.33, and 37.7 μN/W for a permittivity of 4.42. The gap was found to have negative effect on the force efficiency, with a drop of efficiency for a wider gap. The interaction plot shows a negligible difference of 2.0 μN/Wfor a 1 mm gap due to the change in the permittivity. With the confidence interval of 1.82 μN/W, this difference could be the result of the error of the measurements. However, for a 5 mm gap, the efficiency lowers at high permittivity. The effect of the interaction on the force efficiency is similar to its effect on the thrust generation (see page 114), but not to its effect on the power consumption (see page 131). This demonstrates the loss of thrust caused by the interaction is more significant than the loss of power generated by the interaction. The present study suggests the wider gap can enhance the saturation (see Figure 5.9). This overall loss of thrust with a long gap could be due to both a lower saturation voltage due to the long gap or decrease in the amplitude of the electric field with a longer distance between the electrodes.

10 - Permittivity of the dielectric

The tenth most significant effect on the force efficiency is the permittivity of the dielectric. It contributes to 1.57% of the total variance of the data. The main effect plot is shown in Figure 7.13.

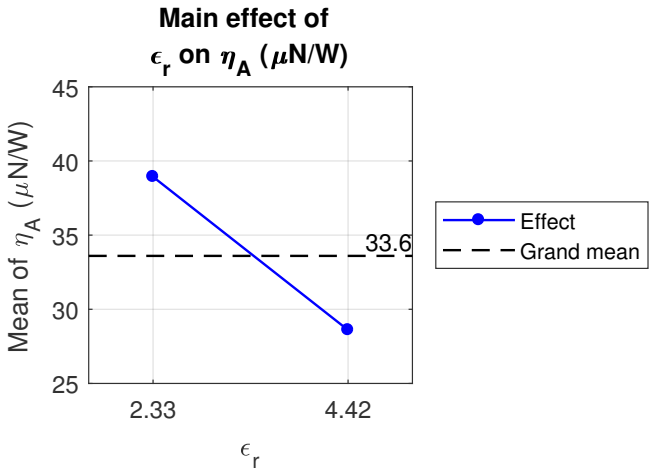

Figure 7.13: Main effect of the dielectric permittivity on the force efficiency.

In the figure, the growth of the dielectric permittivity from 2.33 to 4.42 decreases the force efficiency by 10.3 μN/W. The increase in the permittivity was observed to increase the power consumption (page 133) and reduce the thrust generation (page 110). Thus, it is unsurprising the overall effect on the ratio of the thrust over power is negative. This effect can be imparted to the weakening of the electric field and the decrease of the saturation thrust with a material of high permittivity [45].

11 - Interaction between the height of the encapsulated electrode and the thickness of the dielectric

The eleventh most significant effect in Figure 7.3 belongs to the interaction between the height of the buried electrode and the dielectric thickness. It has a participation of 1.30% to the variance of the data. The corresponding interaction plot is presented in Figure 7.14.

In the figure, the force efficiency decreases by 8.4 μN/W with the thickening of the buried electrode of 35 μm for a 0.8 mm thick dielectric layer, but increases by 9.7 μN/W for the same increase in the height of the electrode for a 3.2 mm thick dielectric. Overall, the thin dielectric always leads to a greater force efficiency. It is unknown whether this effect is factual or caused by an aliased three-factor interaction (see Table 3.3) such as the interaction of the inter-electrode gap, dielectric permittivity and AC frequency. The aforementioned three-factor interaction contains variables that were already observed to impact the results and to interact in other two-factor interactions.

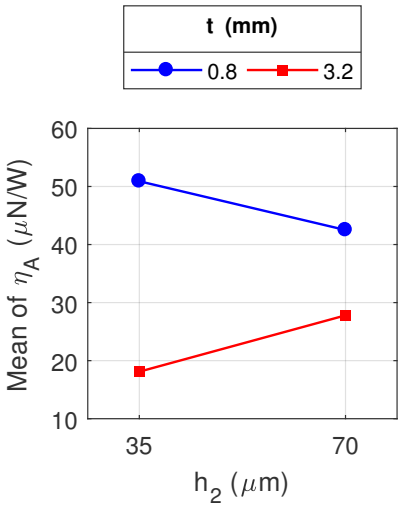

Figure 7.14: Interaction effect between the height of the encapsulated electrode and dielectric thickness on the power consumption.

12 - Interaction between the width of the exposed electrode and the permittivity of the dielectric

The twelfth most significant parameter in Figure 7.3 is the interaction between the width of the air electrode and the permittivity of the dielectric. It is aliased with the interaction between the width of the encapsulated electrode and the thickness of the dielectric layer. The two interactions share 1.12% of the results. The corresponding interaction plots are displayed in Figure 7.15.

In the first interaction, the force efficiency drops by 27.8 μN/W with the increase of the width of the exposed electrode of 4.5 mm at a dielectric permittivity of 2.33. At the permittivity of 4.42, the same widening of the air electrode results in a loss of 7.7 μN/W.

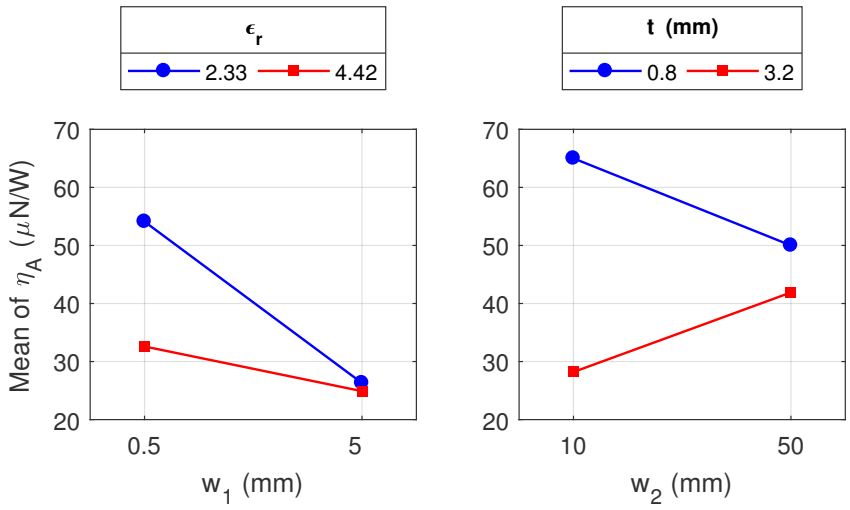

Figure 7.15: Interaction effect between the width of the exposed electrode and dielectric permittivity on the power consumption and its alias.

For a wide electrode, the increase of the permittivity induces a decrease of 1.4 μN/W, which is of the order of the confidence interval of 1.82 μN/W. This interaction was not found significant for the power consumption, however it was observed to be significant for the thrust generation (see page 108). The effect of the interaction on the force efficiency is similar to its effect on the thrust generation. Consequently, the significance of the interaction on the force efficiency results from its potential to alter the generated thrust.

The same conclusion can be reached with the aliased interaction. The same effect can be observed on the thrust and force efficiency. With a growth of the width of the encapsulated of 40 mm, the force efficiency decreases by 15.0 μN/W for a 0.8 mm thick dielectric, and increases by 13.7 μN/W. It is believed the effect of this interaction is due to its alias.

13 - Interaction between the height of the encapsulated electrode and the AC frequency

The thirteenth most significant effect on the force efficiency belongs to the interaction of the height of the encapsulated electrode with the AC frequency. It contributes to 0.87% of the total variance of the results. The interaction plot is shown in Figure 7.16. It should be noted the following effects (ranks 13, 14 and 15) are significant at a confidence level of 95%, but insignificant with a confidence level of 99%.

The interaction plot shows a drop of 6.7 μN/W with an increase of the height of the electrode of 35 μm at 0.5 kHz, whereas a gain of 7.5 μN/W can be observed with the same thickening of the buried electrode at 2.0 kHz. It is unsure why this effect is significant. It is believed to be a cause of the aliasing of the present two factor interaction with the more sensible three-factor interaction between the inter-electrode

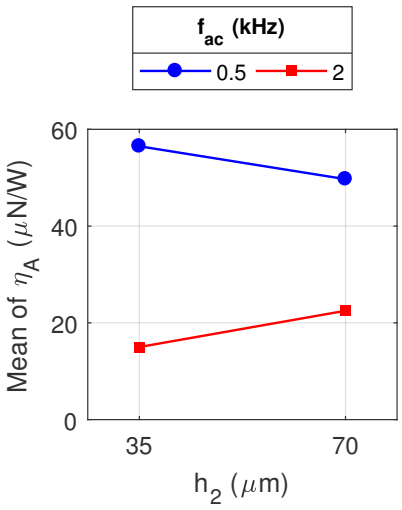

Figure 7.16: Interaction effect between the height of the encapsulated electrode and AC frequency on the power consumption.

gap, the dielectric thickness and the dielectric permittivity. The aforementioned three-factor interaction has a better agreement with the previously described saturation of the DBDs, that has been detailed in other two-factor interactions.

14 - Interaction between the heights of the two electrodes

The fourteenth most significant interaction in Figure 7.3 is the interaction between the heights of the two electrodes. The interaction is responsible for 0.73% of the variance of the data. The corresponding interaction plot is presented in Figure 7.17.

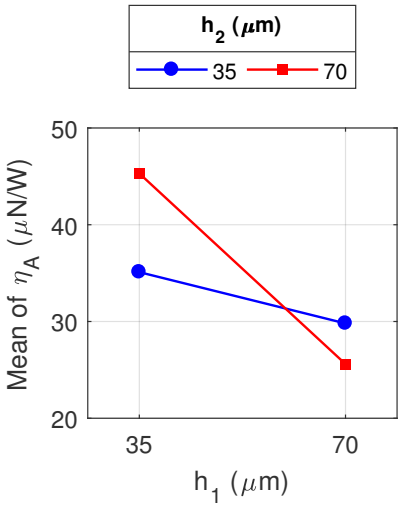

Figure 7.17: Interaction effect between the heights of the exposed and encapsulated electrodes on the power consumption.

The figure indicates the thickening of the exposed electrode of 35 μm induces a loss of 5.2 μN/W for a 35 μm thick encapsulated electrode, whereas the same increase in the height of the air electrode leads to a reduction of 19.8 μN/W for a 70 μm thick encapsulated electrode. However, the interaction is believed to be caused by a three-factor interaction, such as the interaction between the width of the exposed electrode, inter-electrode gap and dielectric permittivity. These two interactions contain parameters that were found to interact in other two-factor interactions.

15 - Interaction between the width of the exposed electrode and the inter-electrode gap

The final significant effect in Figure 7.3 is the interaction of the air electrode width with the inter-electrode gap. It is aliased with the interaction between the voltage and the dielectric thickness. The interactions share 0.62% of the total variance of the measurements. The corresponding interaction plots are presented in Figure 7.18.

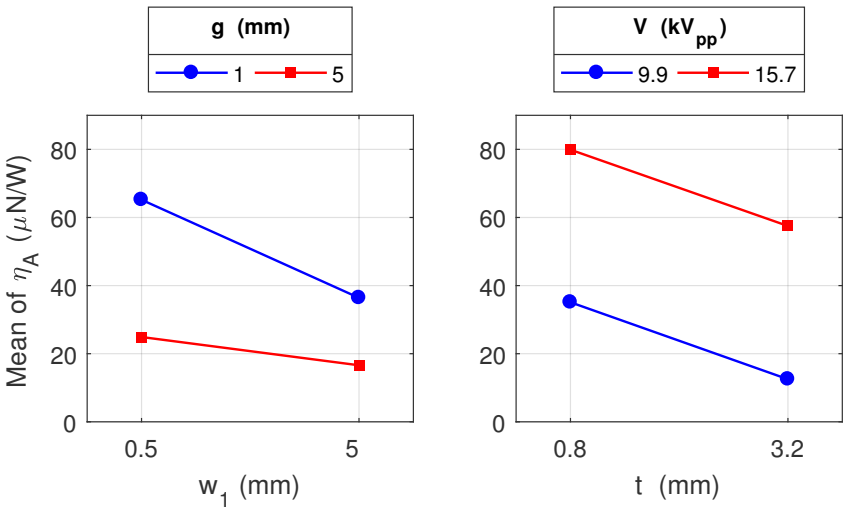

Figure 7.18: Interaction effect between the width of the exposed electrode and inter-electrode gap on the power consumption and its alias.

The first interaction between the width of the air electrode and the inter-electrode gap suggests the short gap of 1 mm provides the better efficiency for any width of the electrode. But lowering the width of the exposed electrode from 5 to 0.5 mm is seen to increase the force efficiency by 28.7 μN/W for a gap of 1 mm and by 8.3 μN/W for a 5 mm long gap. The interaction was found to have a negative effect on the power consumption, but did not seem to impact the thrust generation. The effect is positive on the force efficiency, leading to the conclusion it mostly affects the power consumption. This interaction could arise from the strengthening of the electric field with both a narrow air electrode and short gap, and from the saturation of the DBDs for a long gap.

The aliased interaction involves the voltage and dielectric thickness. A high voltage

results in a higher efficiency in general. At 9.9 kV_{pp}, the thickening of the dielectric layer of 2.4 mm reduces the force efficiency by 22.4 μN/W, and the same growth in the dielectric thickness decreases the efficiency by 22.6 μN/W at 15.7 kV_{pp}. This effect is hence negligible. It is unknown whether the effect is caused by either one of the aliased interactions, given the low amplitude of the effect on the power and force efficiency.

7.3 Linear Regression Model

The DOE analysis performed by Minitab produces a linear regression model for the transformed response (square-root of the force efficiency). The first limitation is the assumption the transformed response depends linearly on all the factors and their interactions. Secondly, the model assesses the effect of the aliases through only one of the aliased effects. This selected alias is only chosen by name. If two interactions were found to be aliased, one involving w_1 (first variable in the study) and the second involving g (third variable in the study) for instance, the retained interaction will be the interaction of w_1. The model is hence expected to only provide approximate estimates of the force efficiency for different designs. The model can be expressed through the following equation:

$$\sqrt{\eta_{\mathrm{A}}} = X_{\mathrm{d}} \cdot M_{\eta} \cdot X_{\mathrm{d}}^{T} \ , \tag{7.1}$$

with X_{d} being the array of the input parameters:

$$X_{\mathrm{d}} = \left[\begin{array}{cccccccccc} 1 & w_1 & w_2 & g & h_1 & h_2 & t & \varepsilon_r & V & f_{\mathrm{ac}} \end{array} \right] \ . \tag{7.2}$$

In Equation 7.1, X_{d}^{T} is the transpose of X_{d} and M_{η} the ten by ten matrix of the model coefficients:

$$\left[\begin{array}{cccccccccc} 3420 & -1515 & 117.9 & 319 & 83.9 & -6.7 & -1868 & -1377 & 1031 & -2996 \\ 0 & 0 & 14.74 & 62.3 & 0.41 & 0.39 & -3.8 & 160.3 & -1.5 & 1.7 \\ 0 & 0 & 0 & -2.10 & -0.669 & 0.2355 & 0 & 0 & -7.86 & -16.51 \\ 0 & 0 & 0 & 0 & 14.44 & -7.06 & 0 & 0 & 0 & 57.0 \\ 0 & 0 & 0 & 0 & 0 & -0.993 & 0 & 0 & 0 & 0 \\ 0 & 0 & 0 & 0 & 0 & 0 & 19.38 & 9.71 & -1.99 & 25.34 \\ 0 & 0 & 0 & 0 & 0 & 0 & 0 & 0 & 0 & 0 \\ 0 & 0 & 0 & 0 & 0 & 0 & 0 & 0 & 0 & 0 \\ 0 & 0 & 0 & 0 & 0 & 0 & 0 & 0 & 0 & 0 \\ 0 & 0 & 0 & 0 & 0 & 0 & 0 & 0 & 0 & 0 \end{array} \right] \times 10^{-3} \tag{7.3}$$

Minitab calculates the fitness of the models through the R^2 and adjusted R^2 coefficients. There are here 91.67% and 87.82% respectively. Therefore, the model predicts the results of the tests matrix with fair accuracy, and does not include unnecessary input variables. The models for all three output parameters are further discussed in Chapter 8.

7.4 Summary

Of the fifteen significant effects discussed in the previous section, several agreed with phenomena reported in the literature. Several effects have a small impact of the results, with contribution of 1% or less to the total variance of the data. The force efficiency being the ratio of the thrust over the power, the effects that influence the parameter indicate whether they have a greater significance for the thrust generation or power consumption.

In total, the main effects were found to contribute to 78.02% of the variance, while the two-factor interactions cover 13.65% of the total variance of the data. Hence, the interactions between the design factors cannot be neglected when trying to maximise the force efficiency of a DBD. Compared with the analyses of the thrust generation and power consumption, the effects have a more linear increase (see Figure 7.3 compared to Figures 5.3 and 6.3). The ten most significant effects are responsible for 84.85% of the variance of the force efficiency results, whereas the ten most significant effects on the thrust were observed to participate to 90.20% of the variance of the thrust measurements, and the four most significant effects on the power shared 98.91% of the variance of the power data. This result is mostly caused by the lower significances of the effects of the voltage and frequency, in comparison to the others. If the two electrical parameters were seen to dominate in the analyses of the thrust generation and power consumption, the ratio of the two quantities must lower their influences on the results. The most significant effects are the voltage, the frequency, the two components of the distance between the electrodes, the geometry of the exposed electrode, and the dielectric permittivity.

The higher the voltage and the lower the frequency, the higher the force efficiency. This demonstrates that the voltage mostly impacts the thrust generation, while the frequency primarily affects the power consumption. The inter-electrode gap and the thickness and permittivity of the dielectric layer were seen to decrease the force efficiency at their high values. Several interactions involving these three parameters, and the fact that the frequency has a negative effect suggest that the saturation of the actuators presented by Thomas et al. [45] certainly occurred throughout the test campaign. The thin and narrow exposed electrode was found to increase the force efficiency, showing its stronger effect on the thrust generation. This agrees with the findings of Enloe et al. [8], who observed a greater thrust over power ratio for a wire electrode as its diameter reduces.

Chapter 8

Aerodynamic Measurements and Modelling of the Flow-Control Performance of the DBD

This chapter presents evaluations of the models of the three output parameters (see Sections 5.3, 6.3 and 7.3), and the aerodynamic measurements carried out to measure the flow induced by the actuators. Firstly, the design of the two selected DBD actuators is given. Secondly, the methodology of the aerodynamic test campaign is presented, along with an error analysis, and a discussion of the results. Thirdly, the models reported in the previous three chapters are compared to the experimental data obtained in the present experiments. The thrust derived from the aerodynamic measurements is also compared to the thrust obtained with the dedicated test rig. Finally, the results are used to verify the scaling of the thrust generation and power consumption against the voltage and frequency, and the findings are compared to the observations realised by other studies.

8.1 Design of the Actuators

In the last three chapters, several linear regression models were created from the DOE analysis. These models of the thrust generation, power consumption and force efficiency need to be assessed, in order to determine their abilities to predict the performances of DBDs for flow control. Two actuators were employed to perform the analysis. The actuator named DBD-1 corresponds to run 24 of the DOE test matrix. DBD-2 is an additional actuator, that is predicted to exhibit greater force efficiency, using the model derived in the DOE. The two actuators are shown in Figure 4.17. The design parameters are presented in Table 8.1. As previously, the span of the electrodes L is 10 cm.

	w_1	h_1	g	t	ε_r	w_2	h_2
DBD-1	5	35	1	0.8	2.33	50	35
DBD-2	0.5	35	1	0.8	2.33	10	35
Units	(mm)	(μm)	(mm)	(mm)	(-)	(mm)	(μm)

Table 8.1: Designs of the DBDs used to assess the models.

8.2 Aerodynamic Study

8.2.1 Experimental Method

The aerodynamic study is performed with the apparatus presented in Section 4.3 in quiescent conditions. The test rig is composed of a traverse system and a pressure acquisition system. The traverse utilises two linear actuators; one in the horizontal direction and one in the vertical direction.

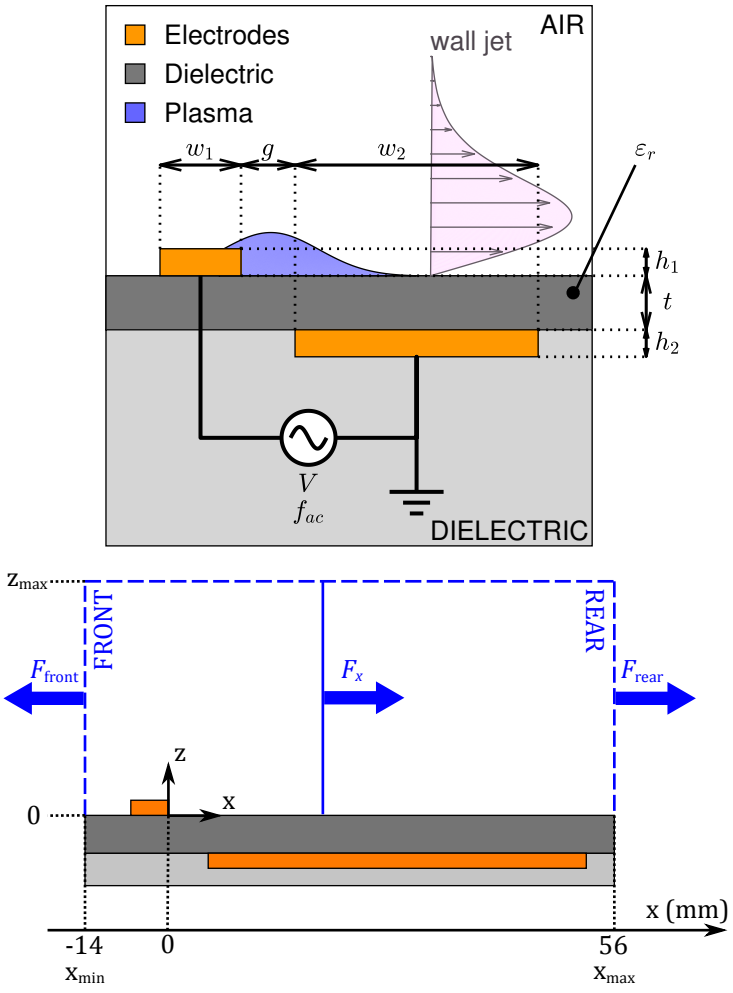

Figure 8.1: Schematic of the DBD configuration (top) and its associated coordinate system and control volume (bottom).

To capture the wall jets, it has been assumed the flow is predominantly two-dimensional, as displayed in Figure 8.1. The three-dimensional coordinate system is represented in Figure 4.14, and the two-dimensional coordinate system appears on Figure 8.1. In the study, the x-direction is parallel to the wall and oriented from the exposed electrode to the buried electrode. The y-direction is the span-wise direction, which is parallel to the long edges of the electrodes. The z-direction is the wall normal direction oriented upwards from the surface of the DBDs. The flow is assumed to predominantly follow the x and z coordinates. As a result, the measurements are performed in the (x,z) plane located in the centre of the span of the electrodes. The origin ($x = z = 0$) has been chosen at the exposed surface of the dielectric layer, on the rear edge of the air electrode. Hence, the actuators extend from -14 to +56 mm.

The traverse system can travel in both the x and z-directions. The capillary Pitot tube can measure the x-component of the total pressure. Therefore, it is assumed the wall jet mostly travel parallel to the wall. The room conditions are measured with the same equipment as during the DOE test campaign. The stagnation pressure p in Pa recorded by the pressure recording system is transformed into a velocity u in m/s via the formula:

$$u = \sqrt{\frac{2\,p}{\rho_0}}\ , \tag{8.1}$$

where ρ_0 is the air density, and can be derived from the atmospheric conditions using Equation 3.1. It is possible to turn the DBD support, so that the velocity is obtained in the $+x$ or $-x$ directions. The velocities recorded at negative x-locations are negative ($-x$-direction), and the velocities recorded at positive x-locations are positive ($+x$-direction). The method does not allow to capture the z-component of the velocity.

With the simplifications that the flow is two-dimensional and only has an x-component, the thrust per unit span T_A can be derived over a control volume through:

$$T_\mathrm{A} = \left(\int_0^{z_\mathrm{max}} \rho_0 u^2 \mathrm{d}z\right)_{x_\mathrm{max}} - \left(\int_0^{z_\mathrm{max}} \rho_0 u^2 \mathrm{d}z\right)_{x_\mathrm{min}}\ , \tag{8.2}$$

where x_min and x_max are the extents of the control volume in the $-x$ and $+x$ directions, and z_max is the height of the control volume (see Figure 8.1). This model is oversimplified and deriving the data from PIV measurements with more complex equations would produce more accurate results [47]. This experimental set-up was chosen, due to its ease of installation and to the shorter time required to perform the measurements. Moreover, with the design of the force measurement test rig, only the x-component of the thrust is measured. In the following sections, the aerodynamic data obtained with the capillary tube were judged to be sufficient for the verification of the force measured with the thrust measurement test rig.

8.2.2 Uncertainty of the Measurements

The error analysis of the aerodynamic measurements is performed in Appendix E. The uncertainty of the different parameters is summarised in the present section.

First, the atmospheric conditions are obtained with the equipment that was used for the DOE study, and that is described in Section 4.3. The errors of the temperature (T_0), humidity (H_0), pressure (p_0) and density (ρ_0) are respectively 0.4°C, 3%, 4 hPa and 5.0×10^{-3} kg/m^3. The complete experimental setup (capillary probe, tubing and anemometer) was found to be less than 2% accurate. The maximum velocity of 4 m/s that was acquired during the experiments was approximately 4 m/s. Therefore, the velocity (u) as an accuracy of less than 0.08 m/s. The errors of the force per unit span (F_x) generated by the plasma at the location x (see Figure 8.1) has an error of 0.17 mN/m. The thrust per unit span (T_A) derived from the forces exerted at the rear and the front of the actuator is 0.25 mN/m. It can be noted this error is greater than the error of the thrust measured with the force measurement test rig (0.060 mN/m). Finally, the mass flow rate ($\mathring{m}$) that goes through a boundary of the control volume has an accuracy of 2.1%, which is less than 0.051 g/s in the present experiment.

8.2.3 Visualisation of DBD-2 at Different Voltages and Frequencies

The setup of the aerodynamic study made it possible to install a camera, in order to obtain long exposure pictures of DBD-2 at different voltages and frequencies, and visualised from the same location. Long exposure pictures of DBD-2 are presented in Figure 8.2. In the figure, the camera has the same exposure and sensitivity settings for all the pictures. A picture was taken every two kilovolts and every five hundred hertz between the boundaries of the DOE: 10 to 16 $\mathrm{kV_{pp}}$, and 0.5 to 2.0 kHz.

Although it is difficult to draw conclusions from the light intensity or the patterns observed in the discharge without more information about the light sensor of the apparatus, it is however possible to analyse and compare the brightness and extents of the discharges. In Figure 8.2, it appears that the greater the frequency, the brighter the discharge. It also seems the visible plasma has a larger extent with the greater frequency. Since the plasma can be expected to emit ultra-violet light as well [14–18], it is difficult to determine whether the plasma only extends as far as it is visible on the pictures, because of the inability of the camera to capture UV light. The effect of the frequency seems limited in Figure 8.2. The increase in the brightness with an increase in frequency is caused by the more numerous charged particles, that travel in the plasma during the constant exposure time with a greater AC frequency. The main impact on the plasma extent comes from the applied voltage. With the greater voltage, both the brightness and extent increase. The voltage dictates how many charges travel in the electrical circuit. As long as the power limit of the high-voltage amplifier is not reached, it will provide enough current so that the requested voltage is achieved. Through the electrically resistive plasma, the current increases with the voltage. Hence, the higher the voltage, the more numerous the charged particles, and consequently, the brighter the plasma. The electric field can be expected to increase in strength with a greater voltage (see Coulomb's law in Equation 5.2). However, it reduces in amplitude as it moves away from the electrodes. For the plasma to ignite, the electric field needs to

Figure 8.2: Long exposure pictures of DBD-2 at the tested voltages and frequencies.

exceed the breakdown value for the air. With a higher voltage, a greater distance from the electrodes has to be exceeded before the electric field falls below the breakdown

value of the air. Therefore, an increase in the voltage leads to a growth in the plasma extent.

8.2.4 Wall Jet Profiles

Due to the resolution and possible error (0.08 m/s), low velocities (less than 0.1 m/s) cannot be recorded by the pressure acquisition system with a good enough accuracy. As explained previously, the maximum measured velocity is less than 4 m/s. The lower thrust was obtained with smaller velocities. Hence, certain data points could not be measured, since the maximum velocity of the wall jet was of the order of the resolution of the measurement system. In the end, the wall jets were assessed at 12 kV_{pp} from 1.5 to 2.0 kHz, at 14 kV_{pp} from 1.0 to 2.0 kHz and at 16 kV_{pp} from 0.5 to 2.0 kHz. All these points were acquired with DBD-2. However, DBD-1 broke-down and was thus only tested at 16 kV_{pp} and 0.5 kHz. Therefore, the next sections focus on DBD-2. For the sake of clarity, only the results obtained at 12 kV_{pp} and 2.0 kHz, 16 kV_{pp} and 2.0 kHz, and 16 kV_{pp} and 0.5 kHz are presented in the next sections. The full set of results can be found in Appendix F. The three selected cases are representative of the full set of data, and give the effects of both the frequency and of the voltage on the wall jet. In the $+x$ direction, the wall jet was measured every 5 mm between 0 and 15 mm, every 10 mm between 15 and 45 mm, and at 56 mm. For the analysis of the backward facing discharges, the DBD stand was simply turned around, allowing the wall jet to be captured at -5, -10 and -14 mm. The wall jets developing over DBD-2 are presented in Figures 8.3 (12 kV_{pp}, 2.0 kHz), 8.4 (16 kV_{pp}, 2.0 kHz) and 8.5 (16 kV_{pp}, 0.5 kHz).

The three figures carry the raw data and fitted Glauert laminar wall jets (see [42]). In the Glauert laminar wall jet, the velocity (u) is obtained by solving the differential equation:

$$f''' + ff'' + 2f'^2 = 0 \ , \tag{8.3}$$

where $f(\eta)$ is a function with the boundary conditions $f(0) = f'(0) = f'(\infty) = 0$. η is defined as:

$$\eta = \left(\frac{135\ F}{32\ \nu_0^3\ x^5} \right)^{1/4} z \ , \tag{8.4}$$

where ν_0 is the kinematic viscosity, x and z are respectively the chord-wise location on and height over the flat plate over which the wall jet travels, and F is a constant given by:

$$F = \int_0^\infty xu \left(\int_z^\infty u^2 \mathrm{d}y \right) \mathrm{d}y \ . \tag{8.5}$$

The velocity u can then be calculated:

$$u = \left(\frac{15\ F}{2\ \nu_0\ x^3} \right)^{1/2} f'(\eta) \ . \tag{8.6}$$

In agreement of Murphy et al. [41], the wall jet generated by the plasma follows a Glauert laminar wall jet profile. For 16 kV_{pp} and 0.5 kHz, it can be seen the resolution

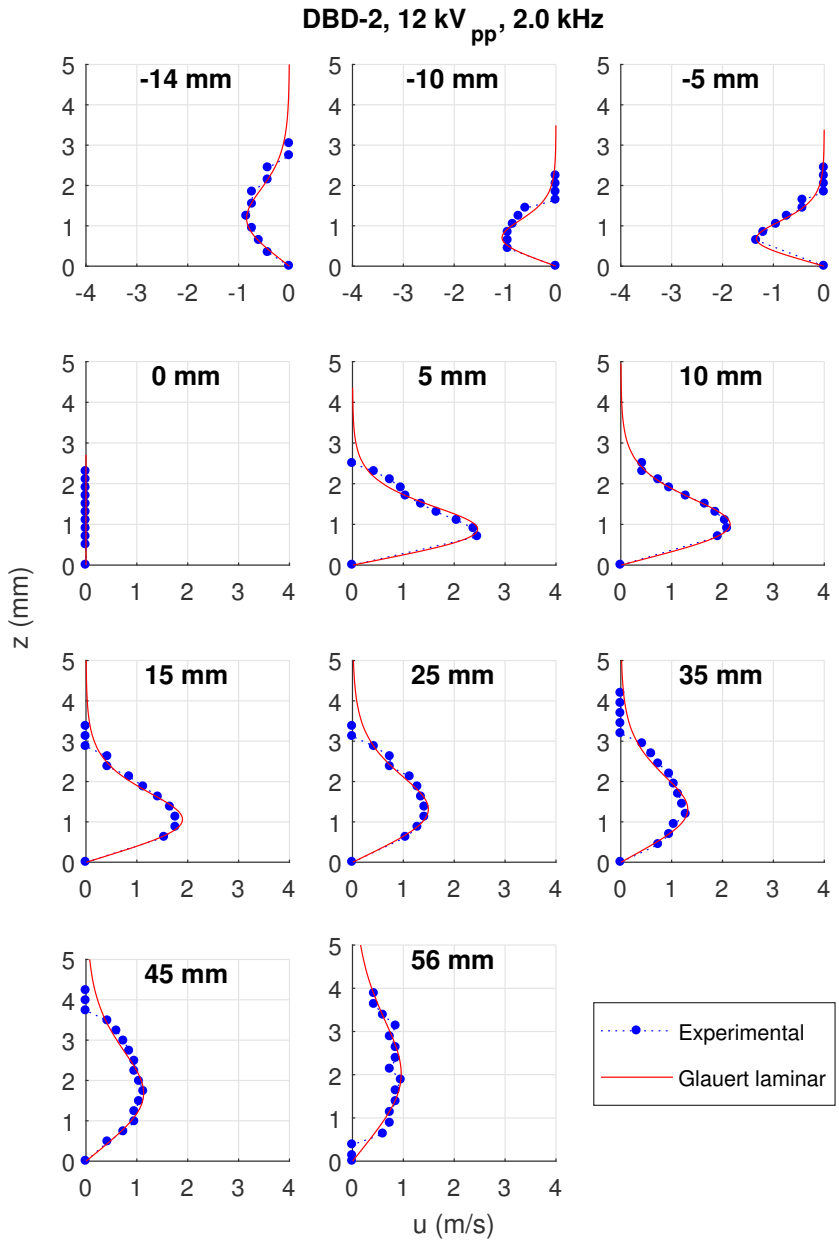

Figure 8.3: Wall jet profiles for DBD-2 at 12 kV_{pp} and 2.0 kHz at different x locations.

of the system was reached at the x locations where the maximum induced velocity is less or equal to 1 m/s (-14, -10, -5, 45 and 56 mm). As a result, the velocity distribution of these particular profiles only takes discreet values.

From the different profiles, it can be seen the wall jet is thinner and stronger close to the electrode. An increase in the voltage or frequency seems to increase the maximum velocity. Besides, with the narrow exposed electrode, two wall jets form in opposite directions. Since only the x component of the velocity was measured, a vertical flow downwards towards the actuator must occur near the air electrode to conserve the mass flow rate through the boundaries.

For a wall jet, it is common to analyse two parameters, namely, the maximum induced velocity u_{max}, and the maximum of the two heights where the induced velocity

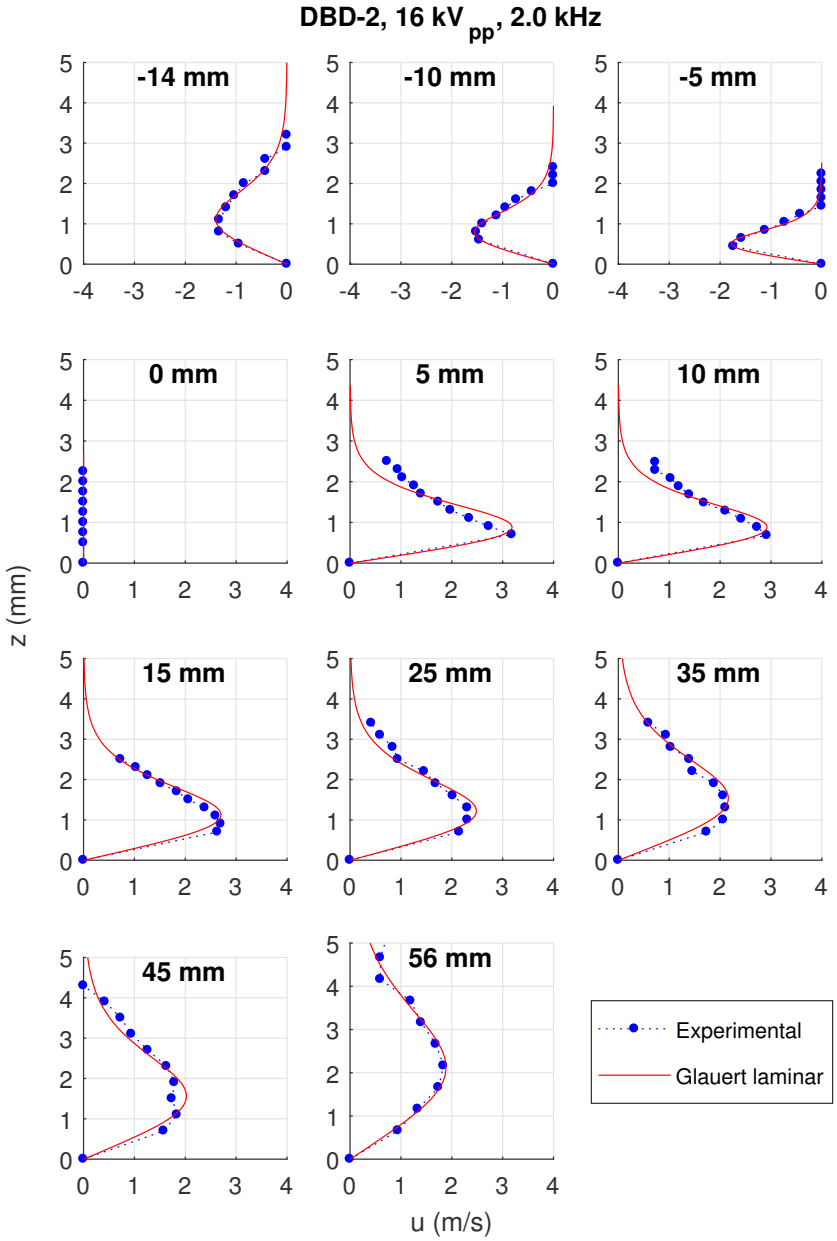

Figure 8.4: Wall jet profiles for DBD-2 at 16 kV_{pp} and 2.0 kHz at different x locations.

amounts to half of its maximum value $z_{1/2}$. The evolution of these parameters are analysed in the next section.

8.2.5 Maximum Velocity and Wall Jet Thickness

The evolutions of the maximum induced velocity u_{max} and the wall jet thickness $z_{1/2}$ with the x position for DBD-2 are presented in Figures 8.6 (12 kV_{pp}, 2.0 kHz), 8.7 (16 kV_{pp}, 2.0 kHz) and 8.8 (16 kV_{pp}, 0.5 kHz). The experimental data are also presented for both sides of the exposed electrode. Best fit lines have been added on the rear side ($+x$ direction), with a linear fit for the thickness ($z_{1/2} = a \cdot x + b$), and a power law fit for the induced velocity ($u_{max} = a \cdot x^b + c$).

The comparison of Figures 8.6 and 8.7 provides the effect of the voltage on the wall

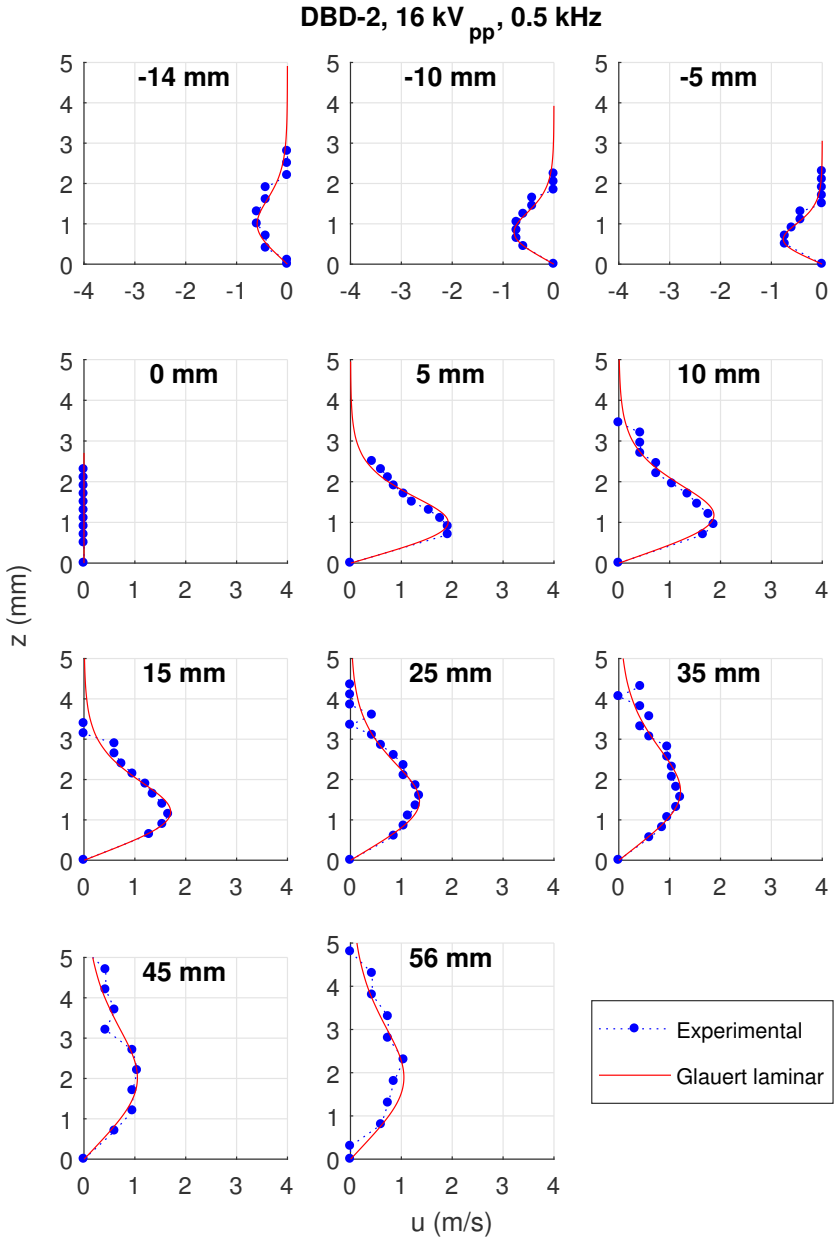

Figure 8.5: Wall jet profiles for DBD-2 at 16 kV_{pp} and 0.5 kHz at different x locations.

jet at 2.0 kHz. The thickness of the jet hardly differs between the two test conditions, with a increase from approximately 1.5 mm at the edge of the air electrode ($x = 0$ mm) to nearly 4.0 mm at the rear end of the actuator ($x = 56$ mm). The backward facing wall jet also shows little difference between the two voltages. On the other hand, the maximum induced velocity is greatly affected. At 12 kV_{pp}, the wall jet decreases from 2.5 m/s at the rear edge of the electrode, to 1.0 m/s at the rear end of the DBD. At 16 kV_{pp}, the shift of the wall jet from the electrode to the rear end of the actuator results in a decrease from 3.2 m/s to 1.8 m/s. The maximum velocity of the backward facing wall jet also increases with the increase of the voltage.

The same conclusion can be reached regarding the frequency. By comparing Figures 8.7 and 8.8, the effect of the frequency on the wall jet behaviour can be visualised

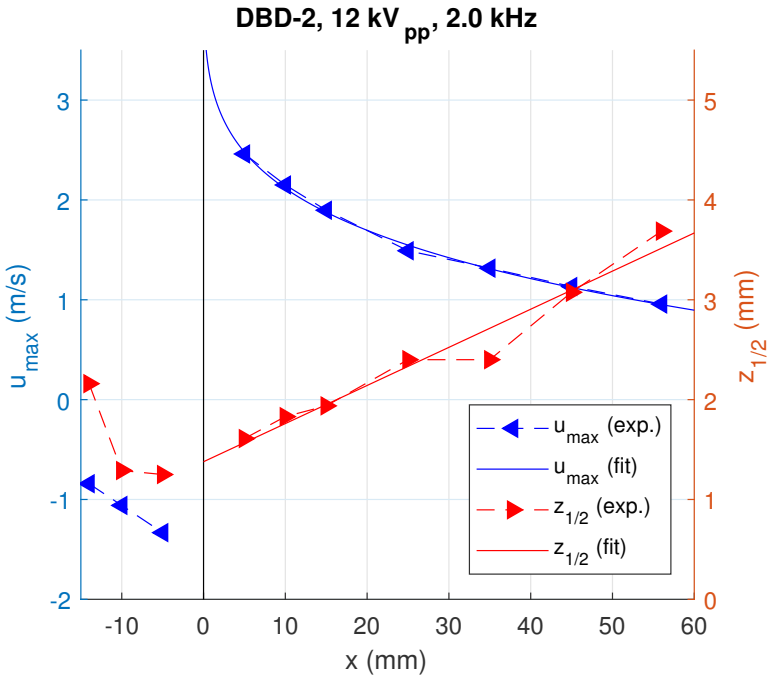

Figure 8.6: Evolution of the maximum velocity and of the thickness of the wall jet for DBD-2 at 12 kV_{pp} and 2.0 kHz.

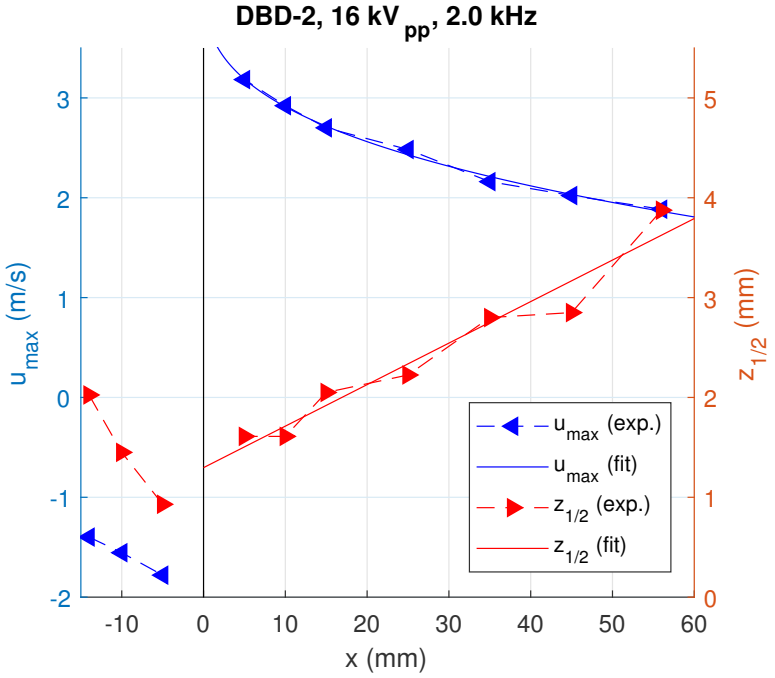

Figure 8.7: Evolution of the maximum velocity and of the thickness of the wall jet for DBD-2 at 16 kV_{pp} and 2.0 kHz.

at 16 kV_{pp}. The increase in the frequency does not seem to have a significant effect on the thickness of the wall jet. At the frequency of 0.5 kHz, the maximum velocity drops from nearly 2.0 m/s to 1.0 m/s between the exposed electrode (0 mm) and rear of the actuator (56 mm). At 2.0 kHz, this decrease is from 3.2 to 1.9 m/s. Thus, an increase

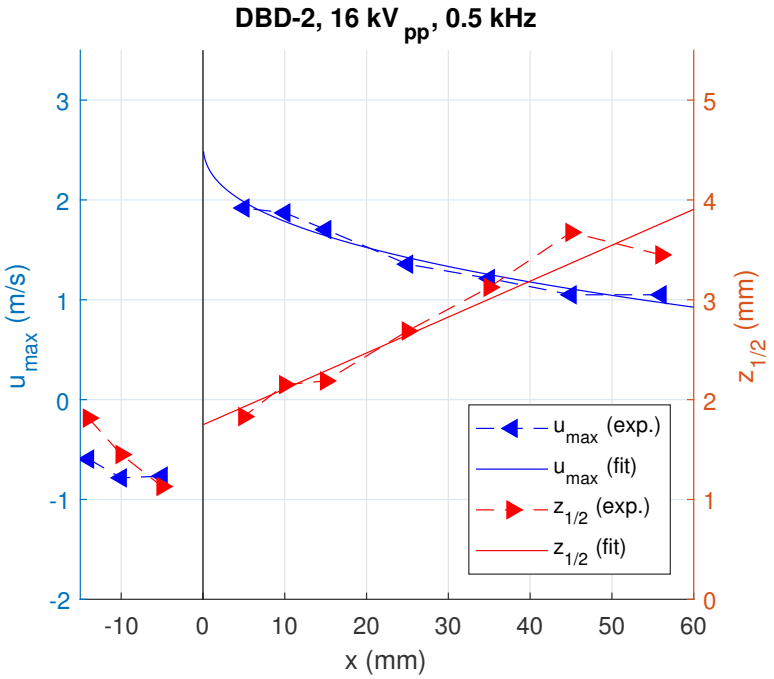

Figure 8.8: Evolution of the maximum velocity and of the thickness of the wall jet for DBD-2 at 16 kV_{pp} and 0.5 kHz.

of the frequency yields a greater maximum induced velocity.

As the thickness of the wall jet seems not to be influenced by the electrical parameters, the higher the maximum induced velocity, the greater the momentum injection into the flow, and consequently, the higher the thrust of the actuator. Therefore, DBD-2 is expected to produce a higher thrust at 12 kV_{pp} and 2.0 kHz, than at 16 kV_{pp} and 0.5 kHz. The interaction of the voltage and frequency on the thrust (see page 105) has indicated a greater growth rate of the thrust with the voltage at high frequency. By using the linear fit of the DOE in Figure 5.10, the average thrust of all the DOE runs is predicted to be approximately 1.4 mN/m at 12 kV_{pp} and 2.0 kHz, against 1.2 mN/m at 16 kV_{pp} and 0.5 kHz. Hence, this finding is in good agreement with the DOE analysis, and a mid-range velocity and high frequency can produce a greater thrust than a high voltage and low frequency. This phenomenon is certainly caused by the saturation of the discharge. Thomas et al. [45] evidenced the saturation value of thrust decreases at high frequency. Moreover, an increase in the voltage increases the number of charged particles in the plasma, while an increase in the frequency increases the kinetic energy of the charges. As a consequence, increasing the number of charges in the plasma is more important than increasing the velocity of the charged species in order to obtain a higher thrust generation.

8.2.6 Mass Flow Rate and Thrust

The present section focuses on the evolution of the mass flow rate at the surface of DBD-2. The mass flow rate is calculated using Equation E.13. The results are displayed in

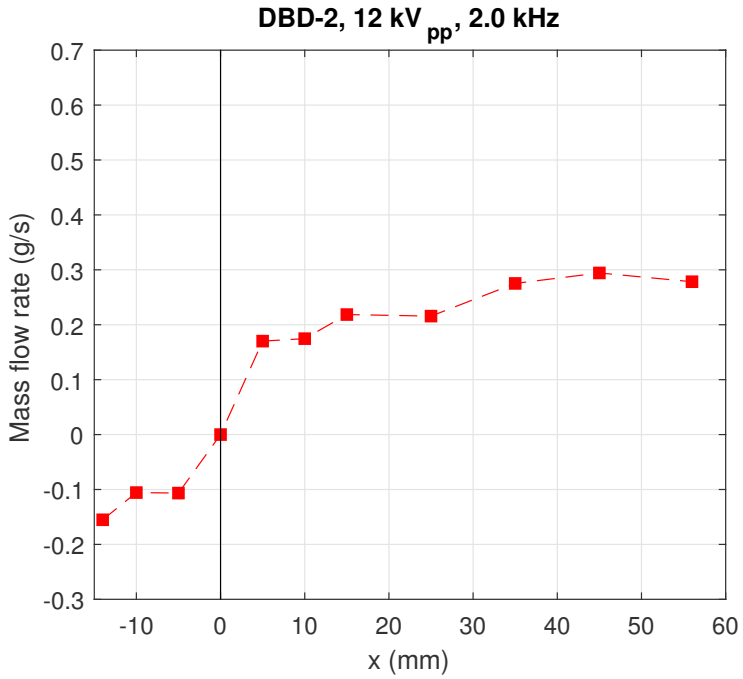

Figure 8.9: Evolution of the mass flow rate of the wall jet for DBD-2 at 12 kV_{pp} and 2.0 kHz.

Figures 8.9 (12 kV_{pp}, 2.0 kHz), 8.10 (16 kV_{pp}, 2.0 kHz) and 8.11 (16 kV_{pp}, 0.5 kHz).

By comparing Figure 8.9 to Figure 8.10, the effect of the voltage on the mass flow rate can be assessed. The increase in the voltage increases the mass flow rate at all x locations in the figures. At the front end of the actuator (-14 mm), the mass flow

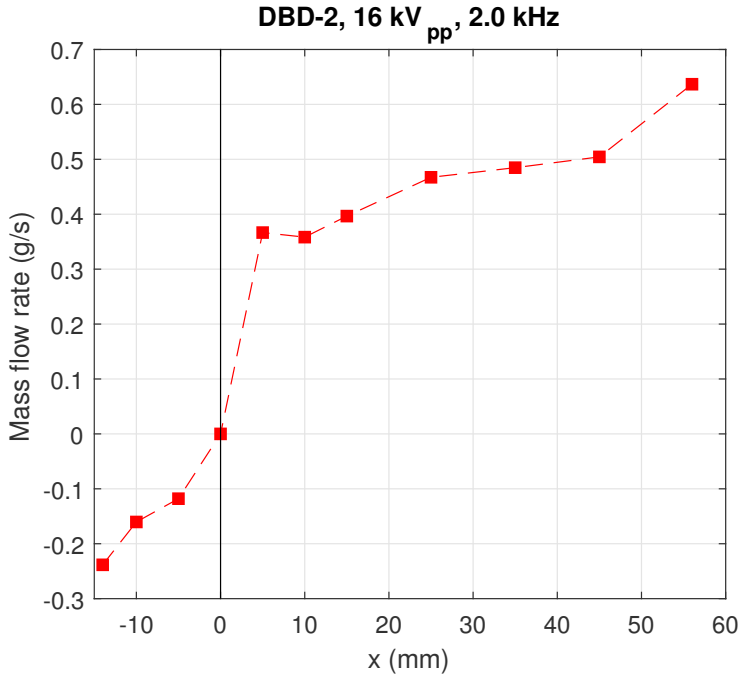

Figure 8.10: Evolution of the mass flow rate of the wall jet for DBD-2 at 16 kV_{pp} and 2.0 kHz.

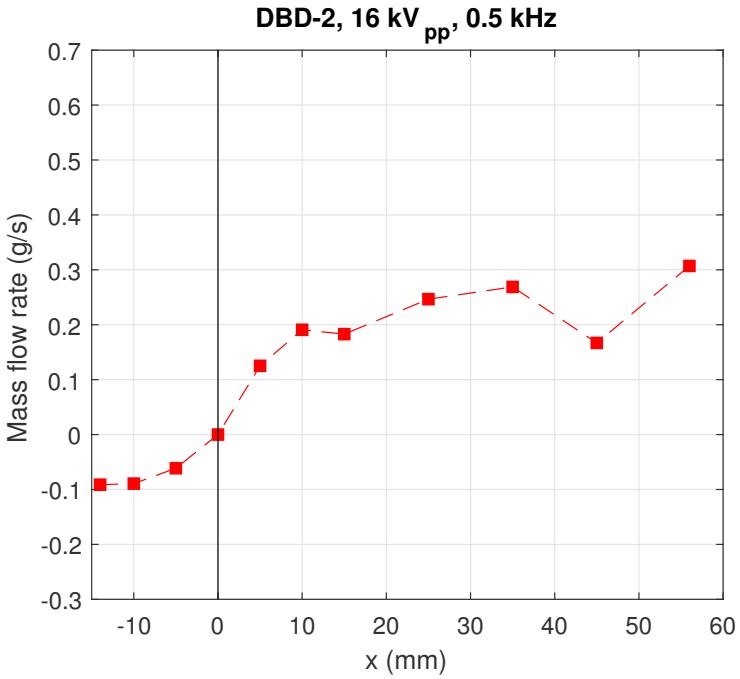

Figure 8.11: Evolution of the mass flow rate of the wall jet for DBD-2 at 16 kV_{pp} and 0.5 kHz.

rate increases by 0.1 g/s in the $-x$ direction with the increase in the voltage, while it grows by nearly 0.32 g/s in the $+x$ direction at the rear end of the DBD (56 mm). Hence, the increase of 4 kV_{pp} results in an increase of 0.27 g/s of the mass flow rate convected through the control volume. The fact that the flow is negative at -14 mm and positive at +56 mm, and that the mass flow rate increases with x for all tests conditions demonstrate that a vertical inflow must bring some mass inside the control volume. In addition, for $x \geq 35$ mm, the mass flow rate could virtually be increased, because the resolution of the equipment is met at these locations.

Figures 8.10 and 8.11 allow to determine the effect of the frequency on the mass flow rate. At 0.5 kHz, the backward facing flow is responsible for a mass flow rate of 0.1 g/s leaving the control volume in the $-x$ direction at the front end of the actuator (-14 mm), and the forward facing wall jet induces a loss of approximately 0.3 g/s through the boundary at the rear end of the DBD (56 mm). At 2.0 kHz, nearly 0.23 g/s are lost at the front of the actuator, while 0.63 g/s cross the rear limit of the DBD. Consequently, the mass flow rate is increased as the frequency increases. As for the voltage, the mass flow rate grows more significantly at the rear of the actuator than at its front, leading to an overall greater momentum induction at higher frequency.

8.2.7 Force per Unit Span

The force per unit span at location x, F_x, is obtained by integrating Equation E.3 over the full height of the wall jet at this location. The evolution of the induced force per unit span is presented for DBD-2 in Figures 8.12 (12 kV_{pp}, 2.0 kHz), 8.13 (16 kV_{pp},

2.0 kHz) and 8.14 (16 kV_{pp}, 0.5 kHz). The figures show four data series: the estimates from the raw total pressure measurement, the estimates from the fitted Glauert laminar wall jets, a power fitting of the form ($F_x = a \cdot x^b + c$) to the Glauert estimation, and the constant value obtained with the force measurement test rig. The force lost due to the presence of the backward facing wall jet is also showed in the $-x$ direction. On the three figures, it can be seen that the thrust decreases by approximately 2 mN/m between the locations 0 and 56 mm. If the viscous losses can partly explain this reduction of the force per unit span, it must be reminded that a vertical jet is expected to bring some air towards the wall. As a result, Equation 8.2 is incomplete, and would require the contribution of the cross flow on the top boundary of the control volume to be computed for more accurate results. Nevertheless, the vertical component of the velocity was not recorded, and the simplified derivation of the thrust tend to agree with the data obtained with the thrust measurement test rig.

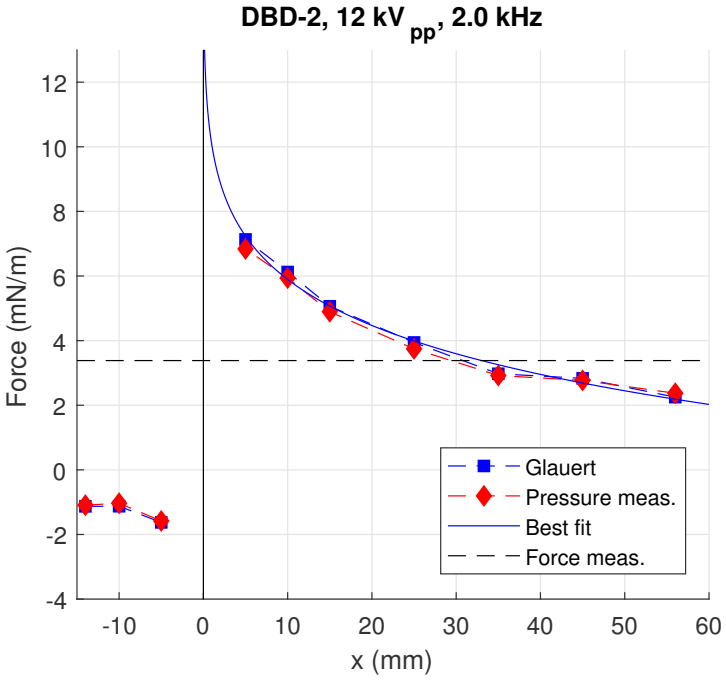

Figure 8.12: Evolution of the force per unit span of the wall jet for DBD-2 at 12 kV_{pp} and 2.0 kHz.

The effect of the voltage can be analysed through Figures 8.12 and 8.13. As for the velocity and mass flow rate, the greater voltage is found to increase the force generation, both in the $+x$ and $-x$ directions. The same conclusion can be reached regarding the frequency. Figures 8.14 and 8.13 reveal the force induction is increased in both x directions at high frequency. However, the growth of 1.5 kHz of the frequency results in an increase from 6 to 7 mN/m in the forward facing discharge, but of only 2 mN/m in the $-x$ direction. Similarly, the increase of 4 kV_{pp} leads to a raise of 5 to 7 mN/m of the force induction in the $+x$ direction, against a growth of 1 mN/m in the backward facing jet. As a consequence, although the backward facing discharge strengthens at high voltage and/or frequency, the thrust is still expected to increase with a growth in

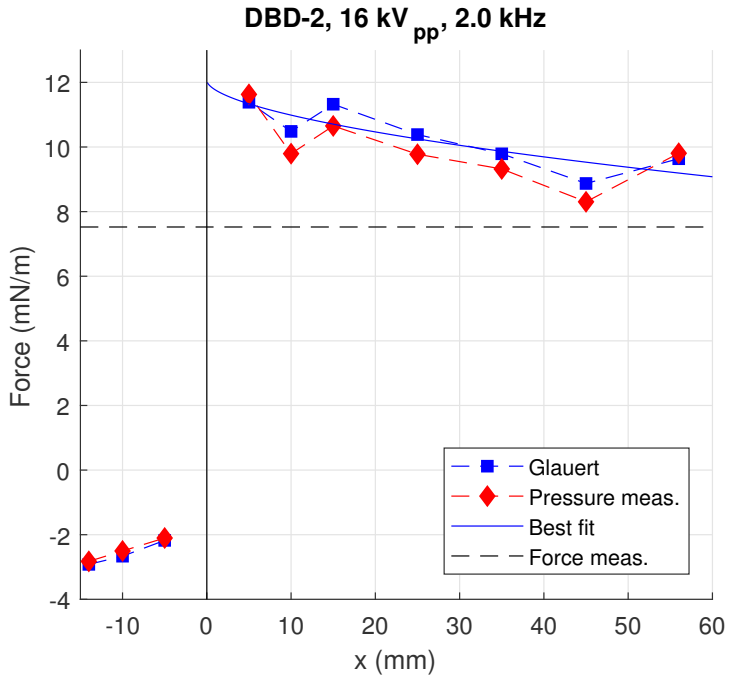

Figure 8.13: Evolution of the force per unit span of the wall jet for DBD-2 at 16 kV_{pp} and 2.0 kHz.

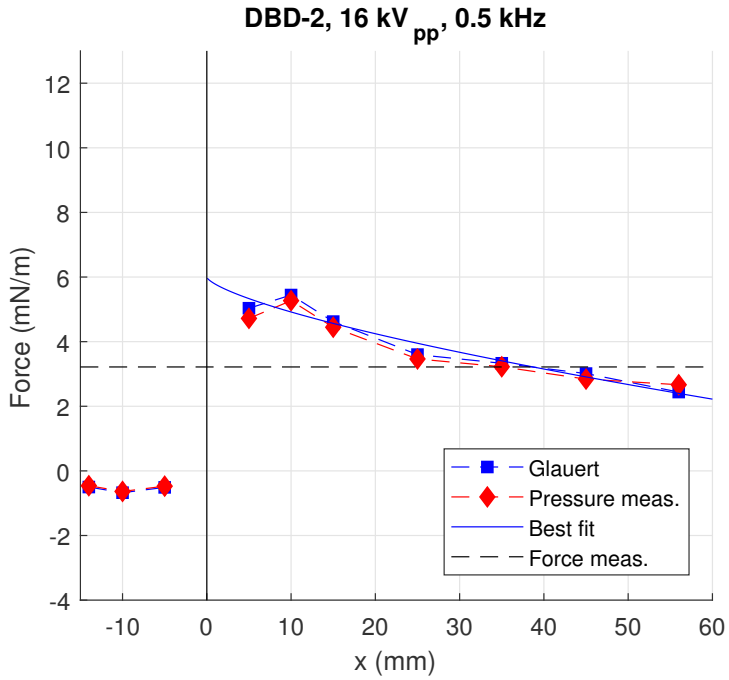

Figure 8.14: Evolution of the force per unit span of the wall jet for DBD-2 at 16 kV_{pp} and 0.5 kHz.

any of the two electrical parameters.

The thrust is derived from the force distribution. The main limitations lie in the neglect of the vertical component of the velocity, and that the profiles close to the rear end of the DBD were frequently found to reach the resolution of the equipment. After processing the results, it came clear that, on average, the thrust had to be derived from

the subtraction of the forces at +25 mm and -14 mm so that the experimental data obtained with the force measurement test rig are approached. This phenomenon can especially be observed for DBD-1 which was not determined to generate a backward facing discharge (see Figure F.40). Using the maximum x extent (-14 and +56 mm) brings a lower generated thrust. This result is believed to be caused by the aforementioned neglect of the vertical component of the velocity or increased error due to the resolution of the recording system for the farther profiles. The loss of momentum due to the skin friction and neglect of the z component of the velocity could result in an overestimated loss for the long dielectric surface of the actuator. The thrust results are presented in the next section, in order to compare to the DOE models, and to the direct force measurements data.

8.3 Evaluation of the Models

The aforementioned DBDs (DBD-1 and DBD-2) were evaluated with the force measurement test rig previously described. Thrust and power measurements have been carried out every kilovolt between 10 and 16 kV_{pp}, and every 0.5 kHz between 0.5 and 2.0 kHz. Therefore, twenty eight data points are captured for each DBD. For DBD-2, the results of the thrust can also be compared to the total pressure measurements discussed in the previous section. The three DOE models (see Equations 5.3, 6.1 and 7.1) are compared in the following sections. It should be noted that DBD-1 was part of the DOE study, with a voltage of 16 kV_{pp} and a frequency of 2.0 kHz, while DBD-2 was not.

8.3.1 Power Consumption

The results for the power consumption are displayed in Figure 8.15 for the two actuators. In the case of DBD-1, the measured power is higher than the model data for all the test points, even at the point 16 kV_{pp}, 2.0 kHz. At this particular data point, DBD-1 was found to consume 84.6 ± 4.9 W/m (see Table 4.4). If the model predicts this measurement well, the aerodynamic experimental datum exceeds the value by 10 W/m. In the next section, this increase of the power can also be linked to an increase of the thrust compared to the original measurements. It is unclear why this actuator was more effective in the additional study. If the force measurement test rig was responsible for the greater thrust measurement, the power consumption would not be impacted. DBD-1 latter broke down during the second acquisition of total pressure data. It is hypothesised the greater thrust could be due to the ageing of the actuator. This hypothesis is further discussed in Section 8.3.3. The root-mean-square of the errors (see Equation 3.30) is 9.6 W/m for the full sample.

In the case of DBD-2, the experimental data also reveal an underestimation of the consumed power by the model, with a maximum undervaluation of nearly 30 W/m at 16 kV_{pp} and 1.5 kHz. The main differences can be found at high voltage and high frequency, with an underestimation of nearly 20 W/m for a voltage greater than 15 kV_{pp}

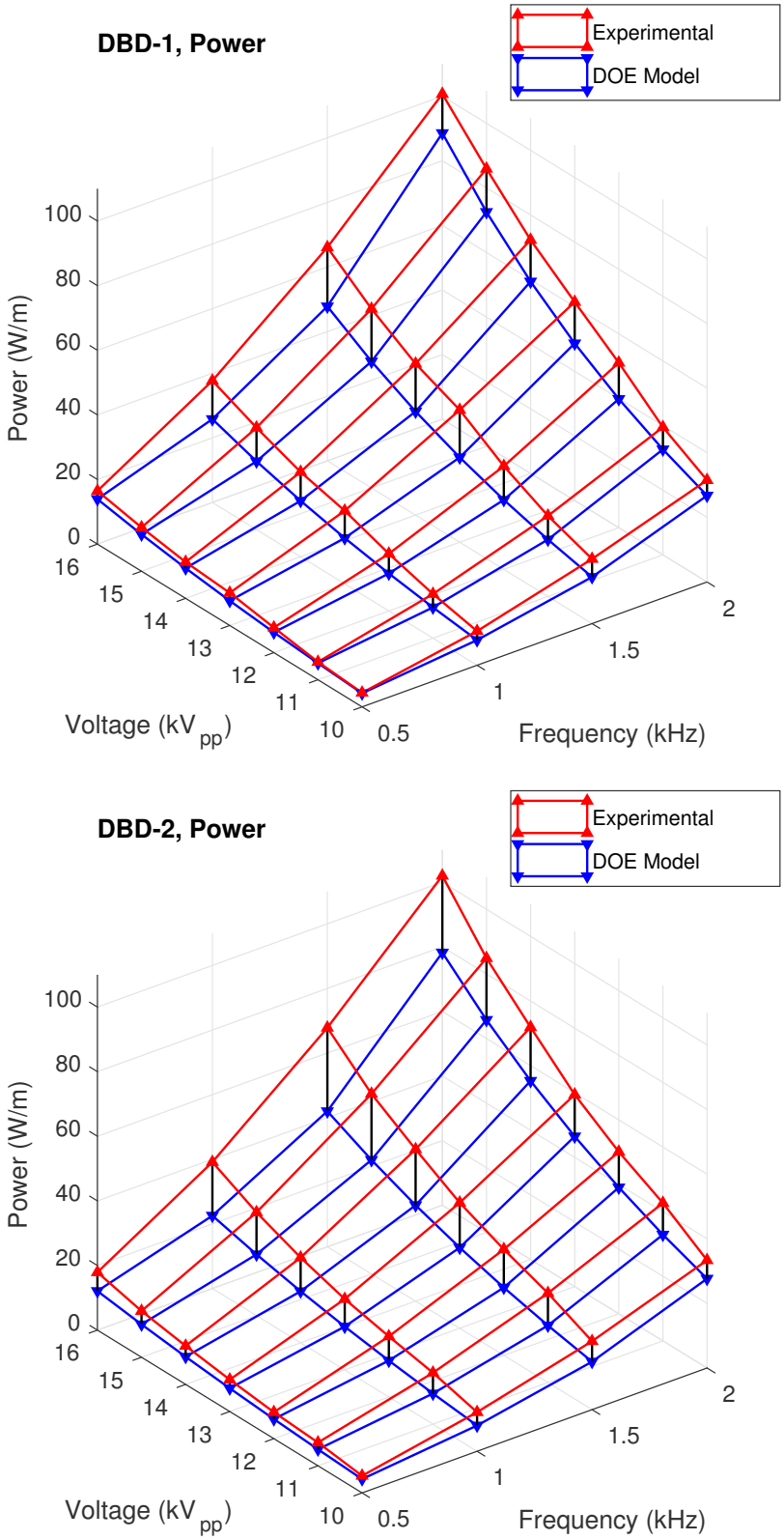

Figure 8.15: Comparison of the DOE model and experimental data for the power consumption for DBDs 1 (top) and 2 (bottom).

and a frequency higher than 1.5 kHz. The root-mean-square of the errors for the entire sample is 12.4 W/m.

8.3.2 Force Efficiency

The data obtained for the force efficiency are presented in Figure 8.16 for DBD-1 and DBD-2. It is important to highlight that, for the sake of visualisation, the figures have rotated voltage and frequency axes compared to Figure 8.15. The force efficiency of the two actuators show very distinct behaviours compared to the DOE model.

For DBD-1, the force efficiency measurements follow the model predictions at 2.0 kHz for all voltages, and at 16 kV_{pp} for all frequencies. As the voltage and frequency lower, the model overestimates the experimental results, with a peak over-prediction of nearly 45 μN/W at 0.5 kHz and 10 kV_{pp}. This phenomenon shows the model of the force efficiency fails to capture the more complex dependency with the electrical parameters. However, the model is able to predict the greater efficiency with a low frequency of 0.5 kHz and a high voltage of 16 kV_{pp}, as predicted by the DOE analysis. The root mean square of the errors for the full sample is 25.5 μN/W.

In the case of DBD-2, the force efficiency follows a convex trend with the voltage, with a peak of efficiency at all frequencies at 13 to 14 kV_{pp}. On the other hand, the force efficiency depends monotonously on the frequency, with either an approximately constant value against the frequency at low voltage ($\leq$ 11 kV_{pp}) or a decrease for an increase in the frequency at higher voltage ($>$ 11 kV_{pp}). With its convex behaviour, the force efficiency of DBD-2 reaches its maximum at 14 kV_{pp} and 0.5 kHz. The photographic study (see Figure 8.2) does not exhibit any remarkable difference in the discharge type. Since not all the data points at 0.5 kHz were obtained with the total pressure measurements, it is difficult to judge whether the loss of efficiency at high voltage is due to the partial transition of the discharge and the subsequent saturation of the actuator, or to the strengthening of the backward facing discharge. The analysis of the force per unit span (refer to Section 8.2.7) has proved a greater voltage leads to a stronger backward discharge, with a higher force in the $-x$ direction. This strengthening of the backward facing discharge could thus result in both a loss of thrust generation and an increase in the power consumption, and overall, a fall in the force efficiency. The interaction of the saturation and the strengthening of the backward facing discharge is also a possibility to explain the loss of efficiency at high voltage. For the entire sample of data, the root-mean-square of the errors is 35.9 μN/W.

8.3.3 Thrust Generation

The results for the thrust generation are displayed in Figure 8.17 for DBD-1 and DBD-2, with the same axes orientation as in Figure 8.15 (for the power consumption). Two sets of data are compared to the experimental results in the figure. Firstly, the DOE model of the thrust generation (given by Equation 5.3) is provided. Secondly, the data obtained with the DOE models of the power consumption (Equation 6.1) and force efficiency (Equation 7.1) are multiplied, and provide a second model of the thrust generation. The first model for T_A is simply referred to as the thrust model in the following paragraphs, while the second model for $T_A = \eta_A \times P_A$ is referred to as the

combined DOE models. For DBD-2, the figure presents another data set; the total

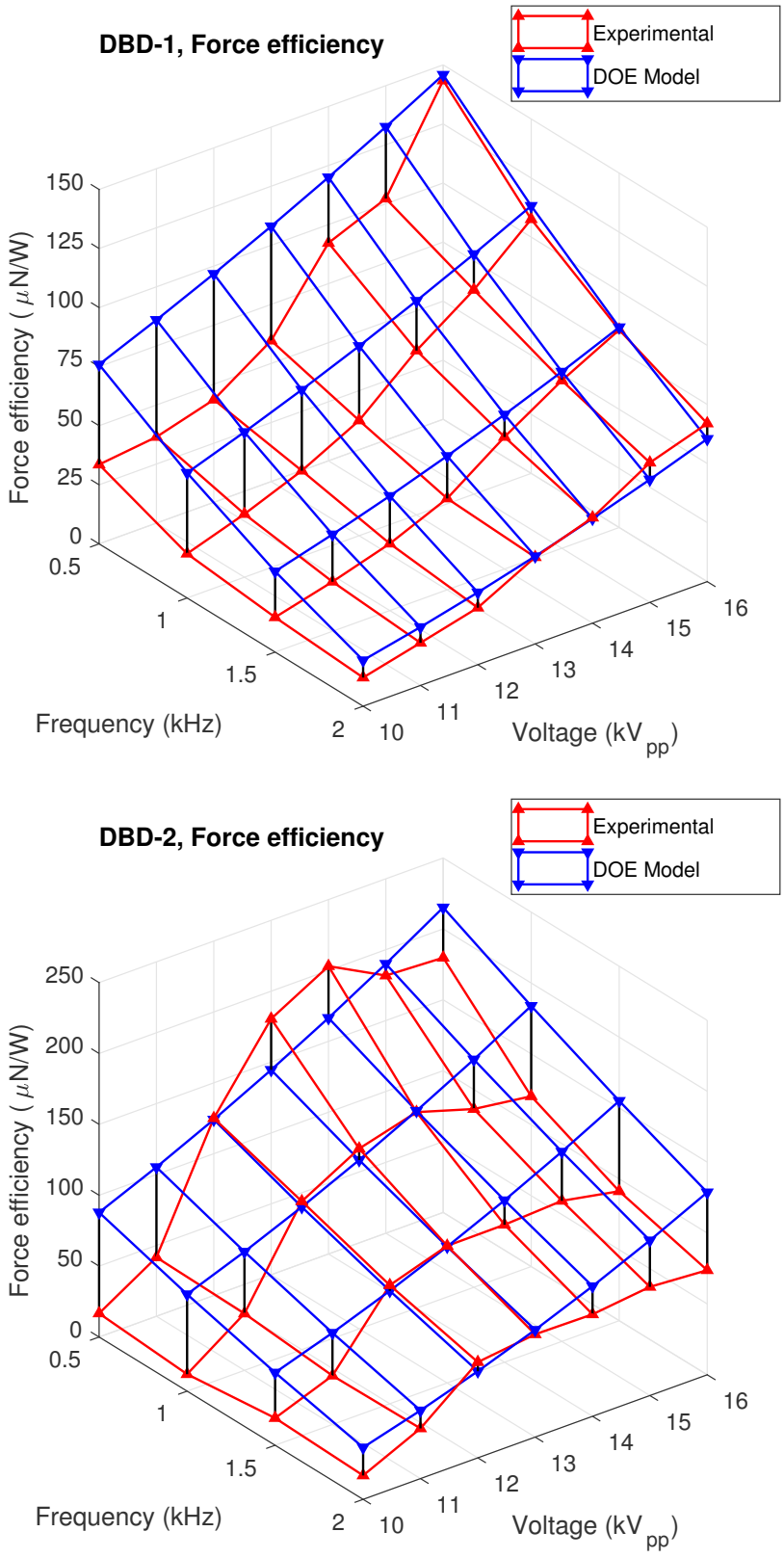

Figure 8.16: Comparison of the DOE model and experimental data for the force efficiency for DBDs 1 (top) and 2 (bottom).

pressure measurements. The thrust derived of the total pressure measurements is the difference of the force per unit span, between the x locations -14 and 25 mm.

For DBD-1, it can be seen that the experimentally recorded thrust at point 16 kV_{pp} and 2.0 kHz is approximately 1.5 mN/m higher than the predictions of the models. The DOE model of the thrust generation predicts the data of the DOE study with good accuracy, with a prediction of 5.08 mN/m at 15.7 kV_{pp} and 2.0 kHz, and an original measurement of 5.16±0.20 mN/m (see Table 4.4). It must be remarked DBD-1 broke down after the first total pressure measurement. With its repeated usage at high voltage (DOE study, parametric sweep over the voltage and frequency, and first data point of the aerodynamic measurement), the dielectric is likely to have aged faster under the high electric field. It is hypothesised the PTFE material degrades over time in the plasma, and hence, loses its ability to store the electric field in the material through the polarisation of the charges. With the lowering of the permittivity, the increased electric field in the air could lead to an increase of the thrust. This hypothesis could not be verified, due to the lack of material to recreate a similar actuator. The second possibility lies in a higher inaccuracy of the force measurement test rig. This hypothesis can be verified with DBD-2, as the actuator was studied with both the force measurement test rig, and the total pressure measurements. The figure reveals the combined models of the power times force efficiency provide a better estimation of the thrust, with a close fitting of the data at low frequency and low voltage. The main visible discrepancy consists of the high voltage and high frequency corner ($\geq$ 14 kV_{pp}, $\geq$ 1.0 kHz), where the experimental data is underestimated by up to 1.5 mN/m by the combined models. The root mean square of the errors of the DOE model of the thrust compared to the experimental data is 1.51 mN/m, against 0.60 mN/m for the errors of the combined models of the power and force efficiency. This result shows the product of the models of the power by force efficiency has a lower inaccuracy than the model of the thrust. It is not fully understood why this phenomenon arises. It is assumed the dividing the thrust by the power attenuates the non-linear scaling of the thrust with the voltage and frequency caused by the transition of the plasma discharge, and saturation of the actuator. As a consequence, the DOE analysis of the data and the fitting of a linear regression could be more accurate due to the lower non-linearity of the force efficiency against the voltage and frequency. On the other hand, the power consumption only depends on a few design variables, and predominantly on the frequency and voltage. Consequently, the product of the two models could result in better predictions.

For DBD-2, the two experimental methods are compared. In general, the direct thrust measurements agree with each other. Most of the data obtained through direct thrust measurements and total pressure measurements diverge by less than the uncertainty of the data (0.25 mN/m from the total pressure measurement test rig, and 0.060 mN/m for the force measurement test rig). Only the thrust acquired at 1.0 kHz and 16 kV_{pp} shows a significant difference between the two measurement techniques, with a discrepancy of nearly 1 mN/m. The aerodynamic measurements were obtained by increasing the frequency at each voltage, by starting from the low voltage

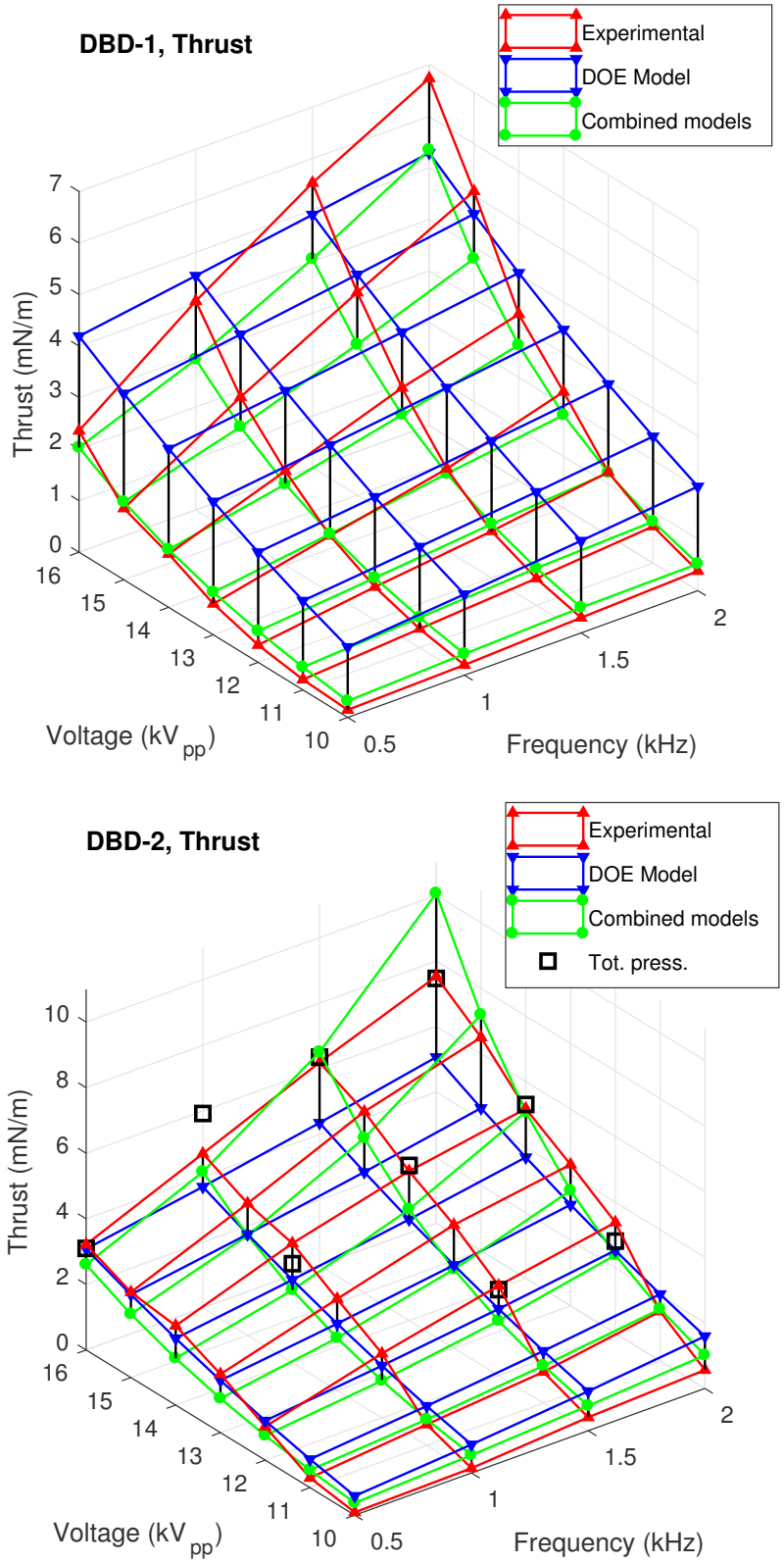

Figure 8.17: Comparison of the DOE model and experimental data for the thrust generation for DBDs 1 (top) and 2 (bottom). DOE Model: model of the thrust obtained with the DOE. Combined models: product of the models of the force efficiency and power consumption obtained with the DOE.

(eg. 12 kV_{pp}: 1.5 then 2.0 kHz, then 14 kV_{pp}: 1.0 then 1.5 then 2.0 kHz, and so forth). The actuator used at 1.0 kHz and 16 kV_{pp} broke down and was replaced by a second one. The first actuator served for both the direct thrust measurements and the first points obtained with the total pressure measurement system. The possible link between the higher thrust and the time for which the DBD was utilised was not considered before the end of the test campaign, and thus, this particular data point was not repeated. It is hence difficult to determine whether the observed discrepancy is due to error (due to the acquisition system or an unexpected wind near the test rig), or to the ageing of the actuator under the electric field. Regarding the models, as for DBD-1, the DOE model of the thrust is unable to predict the experimental results accurately. On the other hand, the combined models of the power multiplied by the force efficiency provides better estimations of the experimental measurements, certainly due to the aforementioned phenomenon. The main discrepancy can be observed at 16 kV_{pp} and 2.0 kHz, with an over-prediction of approximately 2 mN/m. The root-mean-square of the differences of the thrust between the two experimental techniques is 0.51 mN/m. Regarding the models, the errors of the DOE model of the thrust compared to the experimental data have a root-mean-square of 1.10 mN/m, against 0.89 mN/m for the combined models of the power and the force efficiency.

8.3.4 Summary

Regarding the power consumption and force efficiency, the DOE models have limited abilities to predict the experimental observations. For the thrust generation, the combined models of the power multiplied by the force efficiency provide better estimations of the experimental data than the model of the thrust. Moreover, the two experimental techniques tend to agree on the results. The limited abilities of the DOE models to predict the results demonstrate the dependency of the output variables needs more complex scaling than offered by the DOE analysis. In order to determine the scaling laws of the thrust and power against the voltage and frequency, and compare them to the findings reported in the literature, the previously presented results were analysed using curve fitting tools. The result are discussed in the next section.

8.4 Scaling Laws against the Voltage and Frequency

Although they provide approximate estimates, the DOE models cannot accurately predict the performance of DBDs for flow control. The restriction of the DOE models to simple mathematical functions, and the assumption the scaling of the output variable with the design parameters is homogeneous (i.e. that the output parameter has the same scaling laws for all the parameters) makes it difficult to capture the complex behaviour of DBD actuators. In the present study, most of the design parameters are hard-to-change, meaning they can only take a few discreet values. Consequently, a complete sweep of all the parameters cannot be carried out but for two variables that

can be precisely adjusted, i.e. the voltage and frequency of the input AC signal. Using the previously shown results, it is possible to scale the thrust and power of DBD-1 and DBD-2 with the two electric parameters. This work is performed in the next sections.

8.4.1 Power Consumption

If the behaviour of the thrust generation depends on a very complex set of equations (see Section 2.1.3), it is possible to simplify the electrical model of the DBD actuator (see Figure 2.3), in order to estimate the relationship between the consumed power and the two electric variables.

8.4.1.1 Analytical Solution for a Resistor-Capacitor Model

The complex modelling presented in Figure 2.3 can be simplified by assuming that the different time-varying resistors and capacitors can be approximated as constants over a long enough time period (tens of AC periods for these actuators). The resulting electrical network is shown in Figure 8.18.

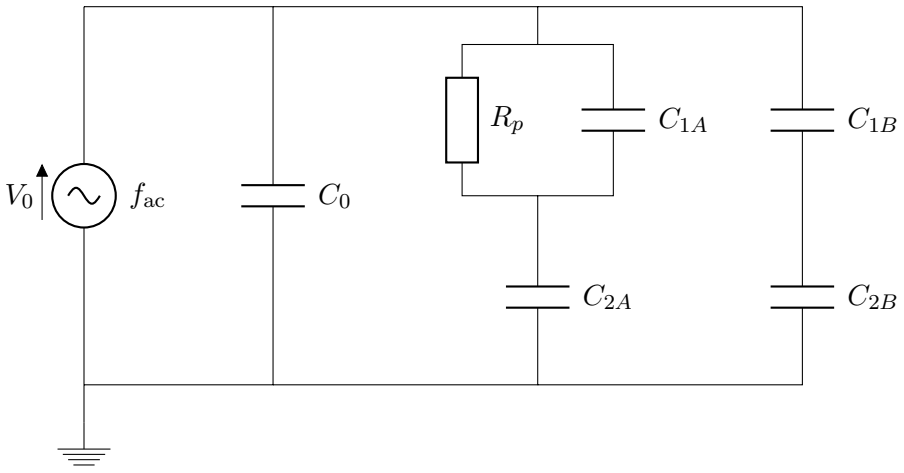

Figure 8.18: Electrical network for the resistor-capacitor model of the DBD.

By expressing the different electrical components by their complex impedance, the complete electrical network can be reduced to a standard resistor-capacitor model. For instance, in Figure 8.18, the resistance of the plasma R_p has an impedance $Z_p = R_p$, the capacitances of the plasma C_{1A} and C_{2A} have impedances $Z_{1A} = -j/(\omega\, C_{1A})$ and $Z_{2A} = -j/(\omega\, C_{2A})$, where ω is the angular AC frequency $2\pi f_{ac}$ and j is the complex number ($j^2 = -1$). The inverse of the equivalent impedance of a parallel combination (eg. R_p and C_{1A}) is obtained by adding the inverses of the impedances of each component:

$$\frac{1}{Z_{eq}} = \frac{1}{Z_p} + \frac{1}{Z_{1A}} \ .$$

The equivalent impedance of a series combination (eg. C_{1B} and C_{2B}) is obtained by

adding the impedances of each component:

$$Z_B = Z_{1B} + Z_{2B} \ .$$

Equivalent impedances can be combined in the same way, for example, with Z_{eq} and Z_{2A}:

$$Z_A = Z_{eq} + Z_{2A} \ .$$

As a consequence, the electrical network can be simplified to a standard resistor capacitor model, as presented in Figure 8.19. The full derivation of R and C will not be discussed, since there are uncertainties associated with the original model (Figure 2.3). However, this particular model provides a straightforward derivation of the consumed electrical power.

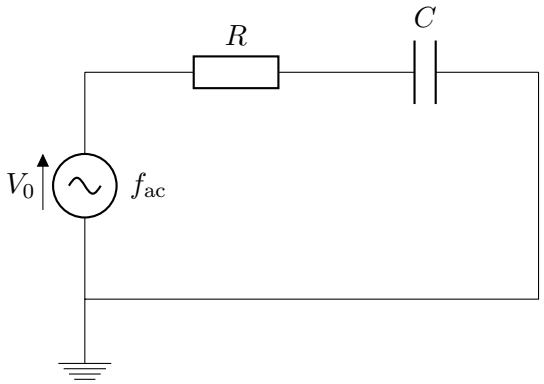

Figure 8.19: Electrical network for the resistor-capacitor model of the DBD.

First, the complex value of the voltage V^* can be defined as:

$$V^* = V_0 \cdot (\cos(\omega\, t) + j \cdot \sin(\omega\, t)) \ , \tag{8.7}$$

$$V^* = V_0 \cdot e^{j\omega t} \ , \tag{8.8}$$

where $\omega = 2\pi f_{\mathrm{ac}}$ is the angular frequency and t is the time. The impedance Z of the series combination of the resistor and capacitor is:

$$Z = R - \frac{j}{\omega\, C} \ . \tag{8.9}$$

With the voltage and impedance, the current I^* can be expressed as:

$$I^* = \frac{V^*}{Z} \ ,$$

$$I^* = V_0 \cdot \frac{(\omega\, C)^2}{1 + (\omega\, R\, C)^2} \cdot \left(R \cdot e^{j\omega t} + \frac{1}{\omega\, C} \cdot e^{j\left(\omega t + \frac{\pi}{2}\right)} \right) \ . \tag{8.10}$$

The real parts of the voltage V and current I can be multiplied to give the electric

power ϖ:

$$\begin{aligned}
\varpi &= V \cdot I \ , \\
\varpi &= V_0^2 \cdot \frac{(\omega\, C)^2}{1 + (\omega\, R\, C)^2} \cdot \left(R \cdot \cos^2(\omega\, t) + \frac{1}{\omega\, C} \cdot \cos(\omega\, t + \pi/2) \cdot \cos(\omega\, t) \right) \ , \\
\varpi &= \frac{V_0^2}{2} \cdot \frac{(\omega\, C)^2}{1 + (\omega\, R\, C)^2} \cdot \left(R \cdot (1 + \cos(2\,\omega\, t)) + \frac{1}{\omega\, C} \cdot (\omega\, t + \pi/2) \right) \ . \qquad (8.11)
\end{aligned}$$

The power consumed by the actuator over one AC period Π_A can be derived from Equation 8.11 by integration:

$$\begin{aligned}
\Pi_\mathrm{A} &= f_\mathrm{ac} \cdot \int_0^{1/f_\mathrm{ac}} \varpi \, \mathrm{d}t \ , \\
\Pi_\mathrm{A} &= \frac{V_0^2}{2} \cdot \frac{(\omega\, R\, C)^2}{1 + (\omega\, R\, C)^2} \ . \qquad (8.12)
\end{aligned}$$

It is common to define the time constant $\tau = RC$, leading to:

$$\Pi_\mathrm{A} = \frac{V_0^2}{2} \cdot \frac{(\omega\, \tau)^2}{1 + (\omega\, \tau)^2} \ . \qquad (8.13)$$

Throughout the study, the power was typically found to be of the order of 10 W. Moreover, the amplitude of the voltage varied around 10^4 V and the angular AC frequency around 10^4 rad/s. Hence, it can estimated from Equation 8.13 that $(\omega\, \tau)^2$ is of the order of 10^{-7} and τ^2 is of the order of 10^{-15} s. Using a Taylor series, it is possible to simplify Equation 8.13 with $(\omega\, \tau) \ll 1$:

$$\begin{aligned}
\Pi_\mathrm{A} &= \frac{V_0^2}{2} \cdot \left((\omega\, \tau)^2 + O\left((\omega\, \tau)^4 \right) \right) \ , \\
\Pi_\mathrm{A} &\approx \frac{(\omega\, \tau\, V_0)^2}{2} \ . \qquad (8.14)
\end{aligned}$$

From Equation 8.14, it can be estimated that the consumed power should depend approximately on the power of 2 on the voltage and frequency of the AC signal.

8.4.1.2 Measured Scaling Law: Standard Power Laws

Through the literature, the most typical curve fitting that is applied to the data are power laws. For instance, Kriegseis et al. [7] reported a scaling of the power consumption with the frequency to the power of 1.5 and voltage to the power of 3.5. However, the dependency has also been observed to be closer to a quadratic relationship [45]. Thus the first function fitted to the data is a combination of the frequency to the power of b and voltage to the power of c:

$$P_\mathrm{A} = a \cdot f_\mathrm{ac}^b \cdot V^c + d \ . \qquad (8.15)$$

Equation 8.15 was fitted to the power measurements provided in Figure 8.15 using Matlab curve fitting tool. The resulting coefficients are presented in Table 8.2.

DBD	a	b	c	d
1	0.03146	1.467	2.541	1.098
2	0.02854	1.480	2.568	2.499

Table 8.2: Coefficients of the power laws for the power consumption for DBD-1 and DBD-2 (with $P_A = a \cdot f_{ac}^{b} \cdot V^{c} + d$).

It can be seen that, for both DBDs, the power consumption depends on the frequency to a power of almost 1.5, as reported by Kriegseis et al. [7]. On the other hand, the power is found to scale with the voltage to a power of approximately 2.5, which tends to have better agreement with the results of Thomas et al. [45]. It is not fully surprising, since the saturation phenomenon discussed by the authors seems to have been met in the present study. With the given coefficients, Matlab calculates the fitting statistics (as presented in Section 3.3.8) which provide with the goodness of the fitting function. These results are given in Table 8.3.

DBD	$SS_{\text{residuals}}$	R^2	$\bar{R}^2$	$RMSE$
1	28.87	0.9983	0.9981	1.097
2	34.98	0.9979	0.9977	1.207

Table 8.3: Goodness of fitting of the power laws for the power consumption for DBD-1 and DBD-2.

It is clear the two fitting functions predict the experimental data accurately, with fitted R-squared ($\bar{R}^2$) of almost 1 for both actuators. Moreover, for both actuators, the fitting functions are similar and could be approximated to:

$$P_A = 0.03 \cdot f_{ac}^{1.47} \cdot V^{2.55} + P_0 \ . \tag{8.16}$$

Using this fitting function for both actuators results in the statistics represented in Table 8.4.

DBD	P_0	$SS_{\text{residuals}}$	R^2	$\bar{R}^2$	$RMSE$
1	1.864	36.55	0.9979	0.9979	1.164
2	2.528	35.91	0.9979	0.9979	1.153

Table 8.4: Common fitting for the power consumption for DBD-1 and DBD-2 (see Equation 8.16).

The relationship presented in Equation 8.16 slightly differs from the resistor-capacitor model ($P_A \propto f_{ac}^2 \times V^2$). In both cases, the differences between the analytical and experimental power laws is approximately 0.5. This result is certainly caused by the

dependency of the resistance and capacitance of the actuator on the time. The slightly higher dependency on the voltage suggests that more resistive effects occur in the plasma, while the lower dependency on the frequency suggests fewer capacitive effects occur in the plasma. The greater resistance could be caused by the loss of energy of the charged particles that is produced by the collisions with the neutral gas. Also, charges could escape the plasma, because they are radical species that do not carry a charge (like ozone) and are thus less sensitive to the electric field. These radicals could be convected away from the plasma before they have time to recombine in stable species. Consequently, charged species could be lost and not stored at the surface of the dielectric, resulting in a decrease of the capacitance of the plasma.

8.4.1.3 Measured Scaling Law: Modified Power Laws

More sophisticated functions have been assessed, by allowing the power laws to vary with the electric variables:

$$P_{\mathrm{A}} = a \cdot f_{\mathrm{ac}}^{b(V)} \cdot V^{c(f_{\mathrm{ac}})} + d \ , \tag{8.17}$$

with:

$$\begin{cases} b(V) &= b_0 + b_1 \cdot V \ , \\ c(f_{\mathrm{ac}}) &= c_0 + c_1 \cdot f_{\mathrm{ac}} \ . \end{cases}$$

In order for Matlab to determine the proper fitting functions using Equation 8.17, the coefficient b_0 and c_0 needs to be provided. Based on Equation 8.16, the coefficients were respectively chosen as 1.47 and 2.55. Consequently, the coefficients of Equation 8.17 can be derived by Matlab, and are given in Table 8.5.

DBD	a	b_0	b_1	c_0	c_1	d
1	0.02423	1.47	-0.02849	2.55	0.1009	0.3017
2	0.02481	1.47	-0.02357	2.55	0.08391	1.627

Table 8.5: Coefficients of the modified power laws for the power consumption for DBD-1 and DBD-2 (see Equation 8.17).

With the ranges of the frequency and voltage of the study, the power b has the following ranges:

$$\begin{aligned} 1.014 \leq \ & b \ \leq 1.185 \quad \text{for DBD-1} \\ 1.093 \leq \ & b \ \leq 1.234 \quad \text{for DBD-2} \end{aligned}$$

Similarly, the ranges of the power c are:

$$\begin{aligned} 2.600 \leq \ & c \ \leq 2.752 \quad \text{for DBD-1} \\ 2.592 \leq \ & c \ \leq 2.718 \quad \text{for DBD-2} \end{aligned}$$

Employing the provided fitting functions for the power consumption give the statistics presented in Table 8.6.

DBD	$SS_{\text{residuals}}$	R^2	$\bar{R}^2$	$RMSE$
1	10.83	0.9994	0.9993	0.6718
2	23.67	0.9986	0.9984	0.9932

Table 8.6: Goodness of fitting of the modified power laws for the power consumption for DBD-1 and DBD-2.

Even if the modified models slightly improve the fitting with higher coefficients of determination R^2, the difference is negligible between Equations 8.17 and 8.16.

8.4.2 Thrust Generation

8.4.2.1 Measured Scaling Law: Standard Power Laws

As for the power consumption, the first fitting function that had been assessed is a combination of power laws of the voltage and frequency:

$$T_{\text{A}} = a \cdot f_{\text{ac}}^{b} \cdot V^{c} + d \ . \tag{8.18}$$

Equation 8.18 was fitted to the thrust measurements provided in Figure 8.17 using Matlab curve fitting tool. The resulting coefficients are presented in Table 8.7.

DBD	a	b	c	d
1	1.245×10^{-6}	0.7669	5.420	-0.1815
2	0.03746	0.3366	1.948	-2.997

Table 8.7: Coefficients of the power laws for the thrust generation for DBD-1 and DBD-2 (with $T_{\text{A}} = a \cdot f_{\text{ac}}^{b} \cdot V^{c} + d$).

In contrast to the power consumption, the fitting functions of the thrust generation for the two actuators diverge. For DBD-1, the powers of the relationship between the thrust and the electrical variables are more than twice the values drawn for DBD-2. It is possible the already mentioned ageing of DBD-1 has resulted in an over-prediction of the thrust at high voltage and frequency. It is also possible the dual discharge generated by DBD-2 damps the increase of the thrust with the voltage and frequency, and leads to a lower increase of the thrust with the electrical parameters. The statistics of the fittings of Equation 8.18 to the thrust generated by DBD-1 and DBD-2 is provided in Table 8.8.

DBD	$SS_{\text{residuals}}$	R^2	$\bar{R}^2$	$RMSE$
1	0.2329	0.9973	0.9970	0.09850
2	3.555	0.9701	0.9664	0.3849

Table 8.8: Goodness of fitting of the power laws for the thrust generation for DBD-1 and DBD-2.

The results indicate the given scaling laws fit the experimental data well, with R-squared coefficients of nearly 1. However, for DBD-2, it can be seen the root-mean-square of the errors is 0.3849 mN/m, which is non negligible compared with the typically recorded values of the thrust (up to 8 mN/m). The maximum errors occur at low voltage (10 to 11 kV_{pp}) and especially at high frequencies ($\geq$ 1.5 kHz). Because of this discrepancy of the fitting with the voltage and frequency, it was decided to modify the power laws, so that they can adjust to the voltage and frequency.

8.4.2.2 Measured Scaling Law: Modified Power Laws

As for the power consumption, the simple scaling laws of the thrust with the voltage and frequency were modified, so that the powers of Equation 8.18 can be modified with different voltages and frequencies:

$$T_A = a \cdot f_{ac}^{b(V)} \cdot V^{c(f_{ac})} + d \ , \tag{8.19}$$

with:

$$\begin{cases} b(V) &= b_0 + b_1 \cdot V \ , \\ c(f_{ac}) &= c_0 + c_1 \cdot f_{ac} \ . \end{cases}$$

Matlab requires the coefficients b_0 and c_0 to be constants for the other coefficients to be computed. b_0 was chosen to be 3/4 for DBD-1, and 1/3 for DBD-2, whereas c_0 is set to 5.45 and 2.00 based on Table 8.7. The resulting coefficients are presented in Table 8.9.

DBD	a	b_0	b_1	c_0	c_1	d
1	1.140 $\times 10^{-6}$	0.75	9.320 $\times 10^{-4}$	5.45	9.779 $\times 10^{-4}$	-0.1722
2	0.03022	0.33	-7.048 $\times 10^{-4}$	2.00	0.01243	-2.773

Table 8.9: Coefficients of the modified power laws for the thrust generation for DBD-1 and DBD-2 (see Equation 8.19).

With the ranges of the voltage and frequency utilised in the study, the powers b and c have the following bounds:

$$\begin{aligned} 0.7593 \leq \ & b \ \leq 0.7649 \quad \text{for DBD-1} \ , \\ 0.3230 \leq \ & b \ \leq 0.3387 \quad \text{for DBD-2} \ , \end{aligned}$$

$$\begin{aligned} 5.451 \leq \ & c \ \leq 5.452 \quad \text{for DBD-1} \ , \\ 2.006 \leq \ & c \ \leq 2.025 \quad \text{for DBD-2} \ . \end{aligned}$$

Moreover, the statistics of the fitting of the modified models to the experimental data is given in Table 8.10.

The models produce negligibly better coefficients of determination, with values at least equal to the previous fitting. However, the effect on the root-mean-square of the

DBD	$SS_{\text{residuals}}$	R^2	$\bar{R}^2$	$RMSE$
1	0.2351	0.9973	0.9970	0.09898
2	3.485	0.9707	0.9670	0.3811

Table 8.10: Goodness of fitting of the modified power laws for the thrust generation for DBD-1 and DBD-2.

errors is limited. Because of the lack of evidence to back a particular scaling it seems unnecessary to further analyse the fitting of the thrust measurements. Most noticeably, the present study did not capture the linear scaling between the thrust generation and power consumption reported by other authors [59], with different scaling of the variables with the voltage and frequency. A valid explanation was not found to justify this disagreement.

8.4.3 Summary

The scaling of the power consumption revealed that it behaves as the frequency to the power of 1.47 and as the voltage to the power of 2.55. The scaling was determined to fit the data, with coefficients of determination of 99.8% for both actuators (DBD-1 and DBD-2). The dependencies of the power on the frequency and voltage agree with reports from the literature. Moreover, the relationship of the power consumption with the voltage further evidences the employed actuators, under the selected voltages and frequencies, approach the saturation of the actuator. Finally, the fitting function is close to the behaviour that could be expected from a standard resistor-capacitor network, but demonstrates the reliance of the electrical behaviour of the actuator on the voltage and frequency.

The scaling of the thrust generated by the actuators does not have a common scaling against the electric parameters in the study. The larger growth rate of the thrust produced by DBD-1 over DBD-2 could be explained by the deterioration of the dielectric layer of DBD-1 throughout the test campaign, and to the creation of a backward facing flow by DBD-2.

In general, allowing the scaling of the voltage to depend on the frequency, or on the frequency to depend on the voltage does not improve the fitting of the scaling laws to the experimental data.

Chapter 9

Conclusions

9.1 Design of a Test Rig for the Measurement of the Thrust Produced by DBDs

The first objective of the study was to produce a suitable test rig for the measurement of the small force created by DBD actuators. A test rig has been designed, using a lever configuration, in order to amplify the thrust generated by 100 mm wide DBDs. After calibration, the accuracy of the test rig was calculated to be 6 μN (60 μN/m of electrode span) and 4.5 mW (45 mW/m of electrode span) with the used acquisition system. Later pressure measurements, although limited due to the higher inaccuracy of the pressure recording system and low resolution of the probe compared to the measured airflows, have shown good agreement with the thrust captured by the dedicated force measurement test rig. In the present study, deriving the thrust generation from the total pressure measurements of the horizontal component of the velocity led to an underestimation of the thrust. Good agreement between the direct force measurements and total pressure measurements was reached when the capillary probe was located 25 mm downstream of the edge of the exposed electrode.

9.2 Parametric Study and Ranking of the Effects of the Design Parameters of the DBD

The parametric investigation has been performed through a design of experiment using a fractional factorial design. The study provides a ranking of the effects of the nine design parameters on the thrust generation, power consumption and force efficiency. The resolution of the selected DOE design provides the significance of the effects of single parameters and their interactions on the three output variables, which are the thrust generation, the power consumption and the force efficiency. The important effects highlighted several physical phenomena, some of which were reported in the literature. The study did not highlight any new interaction between the parameters that were not already observed in the literature. However, the present work provides a

ranking of these effects. The study also proves that the saturation of the actuator that was presented by Thomas et al. [45] is also triggered by a large inter-electrode gap.

9.2.1 Thrust Generation

Regarding the thrust generated by the DBD actuator, it has been observed to be influenced mainly by seven parameters. First, a higher voltage causes a higher gain in thrust, since an increase in the voltage increases the amplitude of the electric field that drives the charged species in the plasma region, and provides more charged particles to the plasma. Secondly, the distance between the electrodes (both the inter-electrode gap and the dielectric layer thickness) reduces the achievable thrust. Two physical phenomena explain this decrease in thrust. The larger distance results in a weakening of the electric field, which is the primary effect in the study. In addition, the interactions of the two variables with the permittivity of the dielectric and with the voltage and frequency of the sine wave signal, demonstrate that some of the actuators used in this study approached their saturation thrust. This saturation lowers the obtainable thrust for a thick dielectric at high frequency and/or voltage. The present study provided evidence that the high inter-electrode gap is also linked to the saturation of the DBD. The fourth parameter is the AC frequency that improves the thrust generation at its high value, due to the increase collision frequency between the charged and neutral particles. As a result, a greater thrust is generated with a high voltage and low frequency. The fifth and sixth most significant parameters are the thickness and width of the air exposed electrode. A thin and narrow air exposed electrode leads to a greater thrust generation, because it increases the electric field in the near electrode region. Finally, the permittivity of the dielectric layer has a lower effect of its own on the thrust generation, but in its interactions with the inter-electrode gap, dielectric thickness, voltage and frequency, the higher permittivity is shown to reduce the obtainable thrust due to causing the saturation of the actuator.

9.2.2 Power Consumption

For the power consumption, four design parameters have been shown to mainly impact the results. First the AC frequency increases the consumed power at its high value. The great significance of the frequency in the present work indicates that the aforementioned saturation phenomenon (that is enhanced by the high frequency of the driving signal) cannot be ignored when optimising the DBD actuator. Secondly, the voltage has a positive effect on the power, with a greater consumption at high voltage. This effect is not surprising, because of the partial electrically resistive behaviour of the plasma. The third and fourth most significant parameters are the inter-electrode gap and dielectric thickness. In their case, a longer distance between the two electrodes results in a decrease in the power consumption. These parameters were also found to decrease the thrust generated by the actuator. If the saturation of the actuator was the predominant effect, the thrust would stagnate. Consequently, on average in the DOE study, the two

parameters decrease the electric field at their high values.

9.2.3 Force Efficiency

The force efficiency (i.e. thrust over power ratio) is more useful than the raw power consumption to determine the flow control performances of DBD actuators, because its analysis demonstrates which of the design parameters have a greater impact on the thrust generation, and which primarily influence the power consumption. For the voltage, seven parameters are mainly responsible for most of the variance of the results, either directly or through their interactions. First, the greater voltage leads to a higher force efficiency, showing its effect is on the thrust generation rather than on the power consumption. Secondly, the frequency has a negative effect on the force efficiency, with a loss of efficiency at high frequencies. This demonstrates the higher impact of the frequency on the power consumption. This phenomenon agrees with the saturation of the thrust at high frequency, reducing the thrust a DBD can produce, while increasing the power consumption. The third and fourth effect are the inter-electrode gap and dielectric thickness. For both parameters, a large distance between the electrodes leads to a loss of efficiency, demonstrating the two variables predominantly influence the thrust generation. This result also indicates the average effect of the gap and dielectric thickness on the discharge is a weakening of the electric field, due to the decrease of the electric field, that is produced by the larger distance between the electrodes. The fifth most influential parameter on the force efficiency is the width of the exposed electrode. The narrow electrode was observed to create plasma on both its edges throughout the test campaign. Therefore, the result shows the gain in the thrust generation that is imparted to a narrow air electrode exceeds the gain in the power consumption, that is caused by the dual discharge. The sixth most significant parameter is the permittivity of the dielectric. However, its significance is mainly the result of its interactions. This phenomenon is a consequence of the saturation of the actuator, that makes the maximum achievable thrust lower at high permittivity for a thick dielectric or long inter-electrode gap. Finally, the seventh most significant effect is the thickness of the air exposed electrode. A thin electrode results in a higher force efficiency, proving it mainly increases the thrust by strengthening the electric field in the vicinity of the electrode.

9.3 Guidelines to Achieve the Best Flow-Control Performance of a DBD

The ranking of the effects performed in this study allows a DBD configuration to be optimised for flow control.

In general, four physical phenomena have been found to effect the three output parameters of the study, namely, the thrust produced by the DBD per unit span, the power consumed by the DBD per unit span, and the force over power ratio. First

the voltage controls the amount of charged species that are transferred to the plasma. A greater voltage results in both a higher thrust and a higher power consumption. Nevertheless, it mainly impacts the thrust, and needs to be maximised for better flow control performance. The AC frequency drives the collision frequency of the charged and neutral species in the plasma. A high frequency increases the thrust generation and the power consumption. However, it mainly influences the power consumption. This phenomenon is caused by the saturation of the plasma discharge from a glow regime to a filamentary regime. Thus, the frequency interacts with the distance between the electrodes and the permittivity of the dielectric. Thus the saturation of the thrust at high frequency cannot be neglected from the optimisation of the DBD for flow control. But a high frequency also improves the thrust generation. The distance between the electrodes (dielectric thickness and inter-electrode gap) effects the amplitude of the electric field. The main effect of the two parameters was observed to be the weakening of the electric field with a large distance. A high separation of the electrodes decreases both the thrust generation and power consumption. Its predominant effect is the loss of thrust, and consequently, a short separation of the electrodes should be preferred. Moreover, a secondary effect of these parameters is the saturation of the thrust, and they must be minimised for more efficient actuators. Finally, the geometry of the air-exposed electrode also alters the electric field. A thin and narrow exposed electrode generates a higher thrust and consumes more power. However, it mainly impacts the thrust. For a narrow exposed electrode, a dual discharge was observed on both edges of the electrode. Aerodynamic measurements proved the dual discharge is responsible for emergence of two opposing wall jets. If the parasitic wall jet reduces the force efficiency, the study proves a narrow electrode still generates more thrust and force efficiency for a wide air electrode.

As a result, the following guidelines for the optimisation of a DBD for flow control are concluded by the study:

1. The permittivity of the employed dielectric material must first be chosen. The material has a maximum voltage at which it can be operated before reaching its electric breakdown. If a dielectric material of low permittivity can be preferred to maximise the thrust, such a material typically also has a low breakdown voltage. Since the voltage is the most important parameter for the force efficiency, a material of high permittivity that has a high electric breakdown can be chosen.

2. With such a material, the thickness of the dielectric and the length of the inter-electrode gap must be kept to a minimum in order to improve the thrust generation of the DBD. The small distance between the electrodes increases the electric field, and allows a higher voltage and higher frequency of the AC signal before reaching the saturation of the DBD. However, it should be kept in mind that a thick dielectric can withstand a greater voltage before reaching breakdown. Consequently, if a high voltage can be reached by the power supply, the dielectric layer should be thick enough to reach this high voltage.

3. A thin and narrow exposed electrode should be preferred if the main focus is thrust generation. If the force efficiency is a concern, a wide electrode cancels the parasitic plasma discharge that occurs on the front edge of the air electrode, and thus, increases the force efficiency.

4. The geometry of the encapsulated electrode is not important. The width of the electrode should however be large enough not to constrain the plasma extent. The 10 mm width was not observed to constrain the plasma in the present study.

5. The highest possible voltage should be supplied to this DBD. First, the frequency needs to be set at a minimum. The voltage can then be increased. If the plasma discharge is seen to transition from an homogeneous discharge to a filamentary discharge, the saturation of the actuator is approached. Consequently, the voltage must not be further increased.

6. If the maximum achievable voltage is constrained by the power supply or the breakdown voltage of the dielectric, and if this voltage does not trigger the saturation of the DBD, this maximum voltage should be applied. At this fix voltage, if the oblective is a greater thrust generation, the frequency can be increased, until reaching the saturation of the actuator, with the transition from a glow plasma discharge to a filamentary plasma discharge. If the main focus is the force efficiency of the DBD, the frequency can be kept at a low setting.

7. In order to reduce the ageing of the dielectric material beneath the plasma region, the study recommends using a voltage and a frequency that are slightly lower than their values at the saturation of the DBD.

Such a method is expected to provide the highest thrust generation or force efficiency, depending on the requirements of the application.

9.4 Modelling of the Flow Control Performance of the DBD

The design of experiment method enables linear regression models to be calculated, that can estimate the thrust generation, power consumption and force efficiency of particular designs of DBDs. Two actuators were tested over a more numerous sets of voltages and frequencies with the ranges used in the DOE. The limitation of the DBDs and power supply used in the study prevented the assessment of the DBDs outside of the boundaries employed in the study. The first actuator was part of the DOE study. The results demonstrated this particular actuator generated a greater thrust during this test campaign. After its breakdown, it has been hypothesised the ageing of the employed PTFE dielectric material, due to the long exposure to plasma over the duration of the experiments, could result in a loss of permittivity over time. As a result, the actuator would generate more thrust thanks to the lower dielectric

permittivity, until the aged material would reach its breakdown. The hypothesis has not been verified in the present study. However, the measurements performed on the second actuator did not capture a significant difference between the thrust recorded with the test rig, and the thrust derived from the total pressure measurements. The study demonstrates that the linear regression models that are derived by the DOE can estimate the power consumption and force efficiency with accuracies of approximatively 9 to 12 W/m, and 25 to 35 μN/W respectively. More interestingly, the DOE model of the thrust performed worse than the product of the models of the power and force efficiency to predict the thrust generation. The product of the models of the force efficiency and power consumption could predict the experimental results with an error of less than 0.9 mN/m. The models could be improved by including more complex mathematical laws. For instance, the present study agrees with a dependency of the power on the AC frequency to the power of 1.5, and on the peak-to-peak voltage to the power of 2.5 to 2.6. These trends are in agreement with the literature. Nevertheless, the thrust generation has not been observed to follow a unique scaling against the electrical parameters for the two DBDs used in the experiment. The thrust depends on the frequency to the power of 0.77 and on the voltage to the power of 5.4 for the first tested actuator, and on the frequency to the power of 0.34 and on the voltage to the power of 1.9 for the second tested DBD. This trend comes from the different types of discharges that are generated by the two actuators. For instance, the second DBD created plasma discharges on both edges of the air electrode.

In general, the linear regression models of the power consumption and force efficiency, that are found in the present study, could be used in preliminary studies. Their estimation of these two parameters derives approximate values of the two variables. Moreover, the product of the two models results in good estimations of the thrust generation. The design that is derived from the models, can then be used by following the guidelines of Section 9.3.

9.5 Recommendations for Future Work

While the work performed in the present study provided useful results about the effects of the design parameters of the DBD actuator on its flow control performance, it could be improved by adding more runs to the Design of Experiments. Particularly centre points (i.e. with all design parameters at the centre of the ranges of this study) could allow the modelling of the non-linear relationships between the input and output variables. In the present study, these centre points were not possible, because several design parameters were constrained by the available materials. These centre points would certainly require a different parametric study, that focuses on the few important parameters that have been highlighted in the present work. For instance, a suitable numerical model could be employed using the same analytical method. The parametric study would be easier, since the design parameters could be set to any value. However, the new study could restrict the number of variables to the seven important paramet-

ers determined in the present study: the AC voltage, the AC frequency, the dielectric thickness, the inter-electrode gap, the dielectric permittivity, the air electrode thickness and the air electrode width. With more numerous data points, it would be easier to draw conclusions about the non-linear scaling of the thrust and power with these variables.

Moreover, a quantitative analysis of the light emission could to be realised. The results of this study could verify several assumptions made in this work. Such a study would also need to analyse the ageing of the DBD, and its possible effect(s) on the discharge. This new study could also be restricted to the important parameters evidenced in the present work.

This study also demonstrated the empirical modelling of the flow control performance of the DBD by using a simple two-level DOE is insufficient for an accurate derivation of the flow control performance of a DBD. The accuracy of the models could be improved by using centre points in the DOE designs, or by performing a response surface method on the subset of significant design parameters that are evidenced by the present study.

References

[1] C. L. Enloe, T. E. McLaughlin, R. D. Van Dyken, K. D. Kachner, E. J. Jumper, and T. C. Corke. Mechanisms and responses of a single dielectric barrier plasma actuator: Plasma morphology. *AIAA Journal*, 42(3):589–594, 2004.

[2] T. C. Corke, C. L. Enloe, and S. P. Wilkinson. Dielectric barrier discharge plasma actuators for flow control. *Annual Review of Fluid Mechanics*, 42(1):505–529, 2010.

[3] T. C. Corke, M. L. Post, and D. M. Orlov. SDBD plasma enhanced aerodynamics: concepts, optimization and applications. *Progress in Aerospace Sciences*, 43(7-8):193–217, 2007.

[4] J. R. Roth. Aerodynamic flow acceleration using paraelectric and peristaltic electrohydrodynamic effects of a one atmosphere uniform glow discharge plasma. *Physics of Plasmas*, 10(5):2117, 2003.

[5] J. Pons, E. Moreau, and G. Touchard. Asymmetric surface dielectric barrier discharge in air at atmospheric pressure: electrical properties and induced airflow characteristics. *Journal of Physics D: Applied Physics*, 38(19):3635–3642, 2005.

[6] J. Kriegseis, S. Grundmann, and C. Tropea. Power consumption, discharge capacitance and light emission as measures for thrust production of dielectric barrier discharge plasma actuators. *Journal of Applied Physics*, 110(1):013305, 2011.

[7] J. Kriegseis, B. Möller, S. Grundmann, and C. Tropea. Capacitance and power consumption quantification of dielectric barrier discharge (DBD) plasma actuators. *Journal of Electrostatics*, 69(4):302–312, 2011.

[8] C. L. Enloe, T. E. McLaughlin, R. D. Van Dyken, K. D. Kachner, E. J. Jumper, T. C. Corke, M. Post, and O. Haddad. Mechanisms and responses of a single dielectric barrier plasma actuator: Geometric effects. *AIAA Journal*, 42(3):595–604, 2004.

[9] D. M. Orlov. *Modelling and Simulation of Single Dielectric Barrier Discharge Plasma Actuators*. Thesis, 2006. University of Notre Dame.

[10] D. F. Opaits, M. N. Shneider, R. B. Miles, A. V. Likhanskii, and S. O. Macheret. Surface charge in dielectric barrier discharge plasma actuators. *Physics of Plasmas*, 15(7):073505, 2008.

[11] C. L. Enloe, G. I. Font, T. E. McLaughlin, and D. M. Orlov. Surface potential and longitudinal electric field measurements in the aerodynamic plasma actuator. *AIAA Journal*, 46(11):2730–2740, 2008.

[12] S. Pavon, J. L. Dorier, C. Hollenstein, P. Ott, and P. Leyland. Effects of high-speed airflows on a surface dielectric barrier discharge. *Journal of Physics D: Applied Physics*, 40(6):1733–1741, 2007.

[13] R. Tirumala, N. Benard, E. Moreau, M. Fenot, G. Lalizel, and E. Dorignac. Temperature characterization of dielectric barrier discharge actuators: influence of electrical and geometric parameters. *Journal of Physics D: Applied Physics*, 47(25):255203, 2014.

[14] B. Sanders, B. DeBlauw, G. Elliott, C. Dutton, and N. Glumac. Temporally and spatially resolved spectroscopic measurements of plasma-actuator thermal properties. *AIAA Journal*, 52(8):1–5, 2014.

[15] K. Shimizu, Y. Mizuno, M. Blajan, and H. Yoneda. Characteristics of an atmospheric nonthermal microplasma actuator. *IEEE Transactions on Industry Applications*, 53(2):1452–1458, 2017.

[16] S. A. Shcherbanev, A. Yu Khomenko, S. A. Stepanyan, N. A. Popov, and S. M. Starikovskaia. Optical emission spectrum of filamentary nanosecond surface dielectric barrier discharge. *Plasma Sources Science and Technology*, 26(2):02LT01, 2016.

[17] W. W. Wang, F. Liu, X. Wang, H. Y. Han, Y. B. Huang, and R. Q. Liang. Optical and electrical characteristics of air dielectric barrier discharges in mode transition at atmospheric pressure. *Plasma Sources Science and Technology*, 24(2):025001, 2015.

[18] K. Shimizu, Y. Mizuno, and M. Blajan. Basic study on force induction using dielectric barrier microplasma array. *Japanese Journal of Applied Physics*, 54(1):01AA07, 2015.

[19] B. Eliasson, M. Hirth, and U. Kogelschatz. Ozone synthesis from oxygen in dielectric barrier discharges. *Journal of Physics D: Applied Physics*, 20(11):1421, 1987.

[20] B. Eliasson, U. Kogelschatz, and P. Baessler. Dissociation of o 2 in n 2 /o 2 mixtures. *Journal of Physics B: Atomic and Molecular Physics*, 17(22):L797, 1984.

[21] J. D. Skalny, J. Orszagh, N. J. Mason, J. A. Rees, Y. Aranda-Gonzalvo, and T. D. Whitmore. Mass spectrometric study of negative ions extracted from point to plane negative corona discharge in ambient air at atmospheric pressure. *International Journal of Mass Spectrometry*, 272(1):12–21, 2008.

[22] M. M. Shahin. Massspectrometric studies of corona discharges in air at atmospheric pressures. *The Journal of Chemical Physics*, 45(7):2600–2605, 1966.

[23] A. Castellanos. *Electrohydrodynamics*. CISM International Centre for Mechanical Sciences. Springer Vienna, 1998.

[24] A. Castellanos. Coulomb-driven convection in electrohydrodynamics. *IEEE Transactions on Electrical Insulation*, 26(6):1201–1215, 1991.

[25] A. Kourmatzis and J. S. Shrimpton. Electrohydrodynamics and charge injection atomizers: A review of the governing equations and turbulence. *Atomization and Sprays*, 19(11):1045–1063, 2009.

[26] A. Kourmatzis and J. S. Shrimpton. Turbulent three-dimensional dielectric electrohydrodynamic convection between two plates. *Journal of Fluid Mechanics*, 696:228–262, 2012.

[27] J. P. Boeuf, Y. Lagmich, and L. C. Pitchford. Contribution of positive and negative ions to the electrohydrodynamic force in a dielectric barrier discharge plasma actuator operating in air. *Journal of Applied Physics*, 106(2):023115, 2009.

[28] B. Jayaraman and W. Shyy. Modeling of dielectric barrier discharge-induced fluid dynamics and heat transfer. *Progress in Aerospace Sciences*, 44(3):139–191, 2008.

[29] S. Yamamoto and K. Fukagata. Numerical simulation of a plasma actuator based on ion transport. *Journal of Applied Physics*, 113(24):243302, 2013.

[30] J. Y. Yu, F. Chen, H. P. Liu, and Y. P. Song. Numerical study of fluid dynamics and heat transfer induced by plasma discharges. *Plasma Science and Technology*, 17(1):41–49, 2015.

[31] J. Reece Roth, Daniel M. Sherman, and Stephen P. Wilkinson. Electrohydrodynamic flow control with a glow-discharge surface plasma. *AIAA Journal*, 38(7):1166–1172, 2000.

[32] W. Shyy, B. Jayaraman, and A. Andersson. Modeling of glow discharge-induced fluid dynamics. *Journal of Applied Physics*, 92(11):6434–6443, 2002.

[33] J. G. Zheng, Z. J. Zhao, J. Li, Y. D. Cui, and B. C. Khoo. Numerical simulation of nanosecond pulsed dielectric barrier discharge actuator in a quiescent flow. *Physics of Fluids*, 26(3):036102, 2014.

[34] J. P. Boeuf and L. C. Pitchford. Electrohydrodynamic force and aerodynamic flow acceleration in surface dielectric barrier discharge. *Journal of Applied Physics*, 97(10):103307, 2005.

[35] J. P. Boeuf, Y. Lagmich, T. Unfer, T. Callegari, and L. C. Pitchford. Electrohydrodynamic force in dielectric barrier discharge plasma actuators. *Journal of Physics D-Applied Physics*, 40(3):652–662, 2007.

[36] Y. Lagmich, T. Callegari, L. C. Pitchford, and J. P. Boeuf. Model description of surface dielectric barrier discharges for flow control. *Journal of Physics D-Applied Physics*, 41(9):095205, 2008.

[37] T. Unfer and J. P. Boeuf. Modelling of a nanosecond surface discharge actuator. *Journal of Physics D-Applied Physics*, 42(19):194017, 2009.

[38] T. Unfer and J. P. Boeuf. Modeling and comparison of sinusoidal and nanosecond pulsed surface dielectric barrier discharges for flow control. *Plasma Physics and Controlled Fusion*, 52(12):124019, 2010.

[39] D. Caruana. Plasmas for aerodynamic control. *Plasma Physics and Controlled Fusion*, 52(12):124045, 2010.

[40] J.-J. Wang, K.-S. Choi, L.-H. Feng, T. N. Jukes, and R. D. Whalley. Recent developments in DBD plasma flow control. *Progress in Aerospace Sciences*, 62:52–78, 2013.

[41] J. P. Murphy, J. Kriegseis, and P. Lavoie. Scaling of maximum velocity, body force, and power consumption of dielectric barrier discharge plasma actuators via particle image velocimetry. *Journal of Applied Physics*, 113(24):243301, 2013.

[42] M. B. Glauert. The wall jet. *Journal of Fluid Mechanics*, 1(06):625, 2006.

[43] R. D. Whalley and K.-S. Choi. The starting vortex in quiescent air induced by dielectric-barrier-discharge plasma. *Journal of Fluid Mechanics*, 703:192–203, 2012.

[44] X. Che, W. Nie, T. Shao, X. Tian, Z. Hou, H. He, P. Zhou, S. Zhou, and C. Yang. Study of flow fields induced by surface dielectric barrier discharge actuator in low-pressure air. *Physics of Plasmas*, 21(4):043508, 2014.

[45] F. O. Thomas, T. C. Corke, M. Iqbal, A. Kozlov, and D. Schatzman. Optimization of dielectric barrier discharge plasma actuators for active aerodynamic flow control. *AIAA Journal*, 47(9):2169–2178, 2009.

[46] J. Pons, E. Moreau, L. Léger, M. Forte, and G. Touchard. *Study of dielectric barrier discharges at atmospheric pressure for airflow control applications*. WEHD 2004, 2004.

[47] J. Kriegseis, C. Schwarz, C. Tropea, and S. Grundmann. Velocity-information-based force-term estimation of dielectric-barrier discharge plasma actuators. *Journal of Physics D: Applied Physics*, 46(5):055202, 2013.

[48] G. I. Font, C. L. Enloe, and T. E. McLaughlin. Plasma volumetric effects on the force production of a plasma actuator. *AIAA Journal*, 48(9):1869–1874, 2010.

[49] N. Benard, A. Debien, and E. Moreau. Time-dependent volume force produced by a non-thermal plasma actuator from experimental velocity field. *Journal of Physics D: Applied Physics*, 46(24):245201, 2013.

[50] C. L. Enloe, M. G. McHarg, and G. I. Font. *Plasma-induced force and self-induced drag in the dielectric barrier discharge aerodynamic plasma actuator*. AIAA Paper 2009-1622, 2009.

[51] C. L. Enloe, M. G. McHarg, and T. E. McLaughlin. Time-correlated force production measurements of the dielectric barrier discharge plasma aerodynamic actuator. *Journal of Applied Physics*, 103(7):073302, 2008.

[52] N. Benard and E. Moreau. Electrical and mechanical characteristics of surface ac dielectric barrier discharge plasma actuators applied to airflow control. *Experiments in Fluids*, 55(11), 2014.

[53] M. Kotsonis. Diagnostics for characterisation of plasma actuators. *Measurement Science and Technology*, 26(9):092001, 2015.

[54] J. Kriegseis, A. Duchmann, C. Tropea, and S. Grundmann. On the classification of dielectric barrier discharge plasma actuators: A comprehensive performance evaluation study. *Journal of Applied Physics*, 114(5):053301, 2013.

[55] W.-L. Wang, J. Li, H.-M. Song, D. Jin, M. Jia, and Y. Wu. Thermal and induced flow characteristics of radio frequency surface dielectric barrier discharge plasma actuation at atmospheric pressure. *Chinese Physics B*, 26(1):015205, 2017.

[56] R. Pereira, D. Ragni, and M. Kotsonis. Effect of external flow velocity on momentum transfer of dielectric barrier discharge plasma actuators. *Journal of Applied Physics*, 116(10):103301, 2014.

[57] R. Durscher and S. Roy. Evaluation of thrust measurement techniques for dielectric barrier discharge actuators. *Experiments in Fluids*, 53(4):1165–1176, 2012.

[58] A. R. Hoskinson, N. Hershkowitz, and D. E. Ashpis. Force measurements of single and double barrier DBD plasma actuators in quiescent air. *Journal of Physics D: Applied Physics*, 41(24):245209, 2008.

[59] T. Abe, Y. Takizawa, S. Sato, and N. Kimura. Experimental study for momentum transfer in a dielectric barrier discharge plasma actuator. *AIAA Journal*, 46(9):2248–2256, 2008.

[60] J. Claus, P.-Å. Krogstad, and I. P. Castro. Some measurements of surface drag in urban-type boundary layers at various wind angles. *Boundary-Layer Meteorology*, 145(3):407–422, 2012.

[61] H. J. Yan, L. Yang, X. H. Qi, and C. S. Ren. Effect of a direct current bias on the electrohydrodynamic performance of a surface dielectric barrier discharge actuator for airflow control. *Journal of Applied Physics*, 117(6):063302, 2015.

[62] N. Benard, J. Jolibois, M. Forte, G. Touchard, and E. Moreau. Control of an axisymmetric subsonic air jet by plasma actuator. *Experiments in Fluids*, 43(4):603–616, 2007.

[63] N. Benard, P. Noté, M. Caron, and E. Moreau. Highly time-resolved investigation of the electric wind caused by surface dbd at various ac frequencies. *Journal of Electrostatics*, 88:41–48, 2017.

[64] C. Porter, J. W. Baughn, T. McLaughlin, C. L. Enloe, and G. I. Font. Plasma actuator force measurements. *AIAA Journal*, 45(7):1562–1570, 2007.

[65] T. Abe, Y. Takizawa, and S. Syunichi. *A Parametric Experimental Study for Momentum Transfer by Plasma Actuator*. AIAA Paper 2007-187, 2007.

[66] A. Debien, N. Benard, and E. Moreau. Streamer inhibition for improving force and electric wind produced by DBD actuators. *Journal of Physics D: Applied Physics*, 45(21):215201, 2012.

[67] A. R. Hoskinson, N. Hershkowitz, and D. E. Ashpis. *Comparisons of Force Measurement Methods for DBD Plasma Actuators in Quiescent Air*. AIAA Paper 2009-485, Orlando, Florida, 2009.

[68] N. Benard, J. Jolibois, G. Touchard, and E. Moreau. *A Directional Plasma-Jet Device Generated by a Double DBD Actuators - An Active Vortex Generated for Aerodynamic Flow Control*. AIAA Paper 2008-3763, 2008.

[69] M. Forte, J. Jolibois, J. Pons, E. Moreau, G. Touchard, and M. Cazalens. Optimization of a dielectric barrier discharge actuator by stationary and non-stationary measurements of the induced flow velocity: application to airflow control. *Experiments in Fluids*, 43(6):917–928, 2007.

[70] M. Forte, J. Jolibois, E. Moreau, G. Touchard, and M. Cazalens. *Optimization of a Dielectric Barrier Discharge Actuator by Stationary and Non-stationary Measurements of the Induced Flow Velocity - Application to Airflow Control*. AIAA Paper 2006-2863, 2006.

[71] J. Jolibois and E. Moreau. Enhancement of the electromechanical performances of a single dielectric barrier discharge actuator. *IEEE Transactions on Dielectrics and Electrical Insulation*, 16(3):758–767, 2009.

[72] N. Benard, N. Balcon, and E. Moreau. *Electric Wind Produced by a Single Dielectric Barrier Discharge Actuator Operating in Atmospheric Flight Conditions - Pressure Outcome*. AIAA Paper 2008-3792, 2008.

[73] N. Benard, N. Balcon, and E. Moreau. *Electric Wind Produced by a Surface Dielectric Barrier Discharge Operating Over a Wide Range of Relative Humidity*. AIAA Paper 2009-488, 2009.

[74] N. Balcon, N. Benard, Y. Lagmich, J. P. Boeuf, G. Touchard, and E. Moreau. Positive and negative sawtooth signals applied to a dbd plasma actuator influence on the electric wind. *Journal of Electrostatics*, 67(2-3):140–145, 2009.

[75] Z. Falkenstein and J. J. Coogan. Microdischarge behaviour in the silent discharge of nitrogenoxygen and waterair mixtures. *Journal of Physics D: Applied Physics*, 30(5):817825, 1997.

[76] J. Kriegseis, K. Barckmann, J. Frey, C. Tropea, and S. Grundmann. Competition between pressure effects and airflow influence for the performance of plasma actuators. *Physics of Plasmas*, 21(5):053511, 2014.

[77] J. Kriegseis, S. Grundmann, and C. Tropea. Airflow influence on the discharge performance of dielectric barrier discharge plasma actuators. *Physics of Plasmas*, 19(7):073509, 2012.

[78] K. Asano, T. Ajima, and Y. Higashiyama. The measurement of ion mobility by using an axisymmetric ion-flow anemometer. In *Industry Applications Conference, 1995. Thirtieth IAS Annual Meeting, IAS '95., Conference Record of the 1995 IEEE*, volume 2, pages 1206–1210 vol.2.

[79] D. Nelson, M. Benhenni, O. Eichwald, and M. Yousfi. Ion swarm data for electrical discharge modeling in air and flue gas mixtures. *Journal of Applied Physics*, 94(1):96–103, 2003.

[80] E. Moreau, L. Léger, and G. Touchard. Effect of a dc surface-corona discharge on a flat plate boundary layer for air flow velocity up to 25m/s. *Journal of Electrostatics*, 64(3-4):215–225, 2006.

[81] A. Soldati and S. Banerjee. Turbulence modification by large-scale organized electrohydrodynamic flows. *Physics of Fluids*, 10(7):1742, 1998.

[82] E. Moreau. Airflow control by non-thermal plasma actuators. *Journal of Physics D: Applied Physics*, 40(3):605–636, 2007.

[83] E. Moreau, C. Louste, G. Artana, M. Forte, and G. Touchard. Contribution of plasma control technology for aerodynamic applications. *Plasma Processes and Polymers*, 3(9):697–707, 2006.

[84] J. Pons, E. Moreau, and G. Touchard. *Surface DC Corona Discharges and AC Barrier Discharges in Ambient Air at Atmospheric Pressure: Measurement of the Induced Ionic Wind Velocity.* GD 2004, 2004.

[85] A. Labergue, L. Léger, E. Moreau, and G. Touchard. Effect of a plasma actuator on an airflow along an inclined wall: P.I.V. and wall pressure measurements. *Journal of Electrostatics*, 63(6-10):961–967, 2005.

[86] A. Labergue, L. Léger, E. Moreau, G. Touchard, and J.-P. Bonnet. *Contrôle du Décollement et du Recollement d'un Ecoulement d'Air le Long d'un Plan Incliné à l'Aide d'une Décharge Couronne Pulsée.* Toulouse, France, 2002.

[87] E. Moreau, R. Sosa, and G. Artana. Electric wind produced by surface plasma actuators: a new dielectric barrier discharge based on a three-electrode geometry. *Journal of Physics D: Applied Physics*, 41(11):115204, 2008.

[88] A. Berendt, J. Podliński, and J. Mizeraczyk. Comparison of airflow patterns produced by DBD actuators with smooth or saw-like discharge electrode. *Journal of Physics: Conference Series*, 301:012018, 2011.

[89] N. Benard, A. Mizuno, and E. Moreau. A large-scale multiple dielectric barrier discharge actuator based on an innovative three-electrode design. *Journal of Physics D: Applied Physics*, 42(23):235204, 2009.

[90] R. Erfani, T. Erfani, S. V. Utyuzhnikov, and K. Kontis. Optimisation of multiple encapsulated electrode plasma actuator. *Aerospace Science and Technology*, 26(1):120–127, 2013.

[91] C. Hale, R. Erfani, and K. Kontis. *Plasma Actuators with Multiple Encapsulated Electrodes to Influence the Induced Velocity.* AIAA Paper 2010-1223, 2010.

[92] C. Hale, R. Erfani, and K. Kontis. *Multiple Encapsulated Electrode Plasma Actuators to Influence the Induced Velocity: Further Configurations.* AIAA Paper 2010-5106, 2010.

[93] C. Hale, R. Erfani, and K. Kontis. *Optimization of Induced Velocity for Plasma Actuator with Multiple Encapsulated Electrodes using Response Surface Methodology.* AIAA Paper 2011-1206, 2011.

[94] P. F. Zhang, C. F. Dai, A. B. Liu, and J. J. Wang. The effect of actuation frequency on the plasma synthetic jet. *Science China Technological Sciences*, 54(11):2945–2950, 2011.

[95] G. Neretti, A. Cristofolini, and C. A. Borghi. Experimental investigation on a vectorized aerodynamic dielectric barrier discharge plasma actuator array. *Journal of Applied Physics*, 115(16):163304, 2014.

[96] X. Luo. *Plasma Based Jet Actuators for Flow Control.* Thesis, 2012. University of Southampton.

[97] D. Caruana, F. Rogier, G. Dufour, and C. Gleyzes. The plasma synthetic jet actuator, physsics, modeling and flow control application on separation. *AerospaceLab Journal*, 6(10), 2013.

[98] A. Belinger, P. Hardy, P. Barricau, J. P. Cambronne, and D. Caruana. Influence of the energy dissipation rate in the discharge of a plasma synthetic jet actuator. *Journal of Physics D: Applied Physics*, 44(36):365201, 2011.

[99] L. Wang, Z.-X. Xia, Z.-B. Luo, and J. Chen. Three-electrode plasma synthetic jet actuator for high-speed flow control. *AIAA Journal*, 52(4):879–882, 2014.

[100] N. Benard, N. Zouzou, A. Claverie, J. Sotton, and E. Moreau. Optical visualization and electrical characterization of fast-rising pulsed dielectric barrier discharge for airflow control applications. *Journal of Applied Physics*, 111(3):033303, 2012.

[101] Z. Zhao, J.-M. Li, J. Zheng, Y. D. Cui, and B. C. Khoo. Study of shock and induced flow dynamics by nanosecond dielectric-barrier-discharge plasma actuators. *AIAA Journal*, 53(5):1–13, 2014.

[102] K. D. Bayoda, N. Benard, and E. Moreau. Elongating the area of plasma/fluid interaction of surface nanosecond pulsed discharges. *Journal of Electrostatics*, 74:79–84, 2015.

[103] T. N. Jukes and K.-S. Choi. Dielectric-barrier-discharge vortex generators: characterisation and optimisation for flow separation control. *Experiments in Fluids*, 52(2):329–345, 2011.

[104] M. Riherd and S. Roy. Serpentine geometry plasma actuators for flow control. *Journal of Applied Physics*, 114(8):083303, 2013.

[105] C.-C. Wang, R. Durscher, and S. Roy. Three-dimensional effects of curved plasma actuators in quiescent air. *Journal of Applied Physics*, 109(8):083305, 2011.

[106] R. J. Durscher and S. Roy. Three-dimensional flow measurements induced from serpentine plasma actuators in quiescent air. *Journal of Physics D: Applied Physics*, 45(3):035202, 2012.

[107] C. W. Wong, L. Wang, Z. Wu, C. Li, M. M. Alam, and Y. Zhou. *Control of Separated Flow on a NACA 0015 Airfoil using Three-Dimensional Plasma Actuator.* AIAA Paper 2014-2665, 2014.

[108] I. Moralev, S. Boytsov, P. Kazansky, and V. Bityurin. Gas-dynamic disturbances created by surface dielectric barrier discharge in the constricted mode. *Experiments in Fluids*, 55(5), 2014.

[109] R. Durscher and S. Roy. *Novel Multi-Barrier Plasma Actuators for Increased Thrust.* AIAA Paper 2010-965, Orlando, Florida, 2010.

[110] A. Kurz, S. Grundmann, C. Tropea, M. Forte, A. Seraudie, O. Vermeersch, D. Arnal, N. Goldin, and R. King. Boundary layer transition control using DBD plasma actuators. *AerospaceLab Journal*, 6(2), 2013.

[111] R. D. Whalley and K.-S. Choi. Turbulent boundary-layer control with plasma spanwise travelling waves. *Experiments in Fluids*, 55(8), 2014.

[112] M. Zadeh, V. Rohani, F. Cauneau, F. Fabry, and L. Fulcheri. Toward the design of multi asymmetric surface dielectric barrier discharge (asdbd) actuators. *Plasma Science and Technology*, 17(1):56–63, 2015.

[113] J. Kriegseis, B. Simon, and S. Grundmann. Towards in-flight applications? a review on dielectric barrier discharge-based boundary-layer control. *Applied Mechanics Reviews*, 68(2):020802, 2016.

[114] M. Riherd and S. Roy. Stabilization of boundary layer streaks by plasma actuators. *Journal of Physics D: Applied Physics*, 47(12):125203, 2014.

[115] D. P. Rizzetta and M. R. Visbal. Plasma-based flow control for delay of excrescence-generated transition. *AIAA Journal*, 53(6):1–13, 2015.

[116] N. Benard, J. Jolibois, and E. Moreau. Lift and drag performances of an axisymmetric airfoil controlled by plasma actuator. *Journal of Electrostatics*, 67(2-3):133–139, 2009.

[117] N. Benard, P. Braud, J. Jolibois, and E. Moreau. *Airflow Reattachment Along a NACA 0015 Airfoil by Surfaces Dielectric Barrier Discharge Actuator - Time Resolved Particle Image Velocimetry Investigation.* AIAA Paper 2008-4202, 2008.

[118] N. Benard, P. Braud, J. Jolibois, and E. Moreau. *Contrôle par actionneur plasma de la séparation au bord dattaque dun profil NACA 0015 en incidence : Analyse spatiotemporelle par PIV rapide.* Futuroscope, Poitiers, France, 2008.

[119] J. Little, M. Nishihara, I. Adamovich, and M. Samimy. High-lift airfoil trailing edge separation control using a single dielectric barrier discharge plasma actuator. *Experiments in Fluids*, 48(3):521–537, 2009.

[120] J. Little, M. Nishihara, I. Adamovich, and M. Samimy. *Separation Control from the Flap of a High-Lift Airfoil Using DBD Plasma Actuators.* Aerospace Sciences Meetings. AIAA Paper 2009-145, 2009. doi:10.2514/6.2009-145.

[121] J. Little and M. Samimy. High-lift airfoil separation with dielectric barrier discharge plasma actuation. *AIAA Journal*, 48(12):2884–2898, 2010.

[122] C. He, T. C. Corke, and M. P. Patel. Plasma flaps and slats: An application of weakly ionized plasma actuators. *Journal of Aircraft*, 46(3):864–873, 2009.

[123] M. Sato, K. Asada, T. Nonomura, H. Aono, A. Yakeno, and K. Fujii. *Effective Mechanisms for Turbulent-separation Control by DBD Plasma Actuator around NACA0015 at Reynolds Number 1,600,000.* AIAA Paper 2014-2663, 2014.

[124] X. Zhang, Y. Huang, W. B. Wang, X. N. Wang, and H. X. Li. Unmanned air vehicle flow separation control using dielectric barrier discharge plasma at high wind speed. *Science China Physics, Mechanics & Astronomy*, 57(6):1160–1168, 2014.

[125] D. P. Rizzetta and M. R. Visbal. Numerical investigation of plasma-based control for low-reynolds-number airfoil flows. *AIAA Journal*, 49(2):411–425, 2011.

[126] S. Bhattacharya and J. W. Gregory. Effect of three-dimensional plasma actuation on the wake of a circular cylinder. *AIAA Journal*, 53(4):958–967, 2015.

[127] P. Sujar-Garrido, N. Benard, E. Moreau, and J. P. Bonnet. Dielectric barrier discharge plasma actuator to control turbulent flow downstream of a backward-facing step. *Experiments in Fluids*, 56(70), 2015.

[128] G.-Y. Zhao, Y.-H. Li, H. Liang, M.-H. Han, and W.-Z. Hua. Control of vortex on a non-slender delta wing by a nanosecond pulse surface dielectric barrier discharge. *Experiments in Fluids*, 56(1), 2014.

[129] L.-H. Feng, K.-S. Choi, and J.-J. Wang. Flow control over an airfoil using virtual gurney flaps. *Journal of Fluid Mechanics*, 767:595–626, 2015.

[130] K. Yugulis, S. Hansford, J. W. Gregory, and M. Samimy. Control of high subsonic cavity flow using plasma actuators. *AIAA Journal*, 52(7):1542–1554, 2014.

[131] V. Kopiev, I. V. Belyaev, V. A. Kopiev, and M. Zaitsev. *Plasma Actuator for Cylinder Noise Mitigation*. AIAA Paper 2016-2890, 2016.

[132] S. Chappell. *Active Control with Dielectric Barrier Discharge Actuators Applied to High-Lift Devices*. Thesis, 2013.

[133] S. Chappell, Z. Cai, X. Zhang, and D. Angland. *Slat Noise Feedback Control with a Dielectric Barrier Discharge Plasma Actuator*. AIAA Paper 2012-2806, 2012.

[134] A. Inasawa, C. Ninomiya, and M. Asai. Suppression of tonal trailing-edge noise from an airfoil using a plasma actuator. *AIAA Journal*, 51(7):1695–1702, 2013.

[135] J. Kriegseis, D. Schröter, S. Grundmann, and C. Tropea. Online-characterization of dielectric barrier discharge plasma actuators for optimized efficiency of aerodynamical flow control applications. *Journal of Physics: Conference Series*, 301:012020, 2011.

[136] R. E. Hanson, K. M. Bade, B. A. Belson, P. Lavoie, A. M. Naguib, and C. W. Rowley. Feedback control of slowly-varying transient growth by an array of plasma actuators. *Physics of Fluids*, 26(2):024102, 2014.

[137] R. Dadfar, O. Semeraro, A. Hanifi, and D. S. Henningson. Output feedback control of blasius flow with leading edge using plasma actuator. *AIAA Journal*, 51(9):2192–2207, 2013.

[138] N. Benard, E. Moreau, J. Griffin, and L. N. Cattafesta III. Slope seeking for autonomous lift improvement by plasma surface discharge. *Experiments in Fluids*, 48(5):791–808, 2009.

[139] J. Dandois and P.-Y. Pamart. Narx modeling and extremum-seeking control of a separation. *AerospaceLab Journal*, 6(6), 2013.

[140] L. Francioso, C. De Pascali, E. Pescini, M. G. De Giorgi, and P. Siciliano. Modeling, fabrication and plasma actuator coupling of flexible pressure sensors for flow separation detection and control in aeronautical applications. *Journal of Physics D-Applied Physics*, 49(23):235201, 2016.

[141] E. Pescini, F. Marra, M. G. De Giorgi, L. Francioso, and A. Ficarella. Investigation of the boundary layer characteristics for assessing the dbd plasma actuator control of the separated flow at low reynolds numbers. *Experimental Thermal and Fluid Science*, 81:482–498, 2017.

[142] F. Ternoy, J. Dandois, F. David, and M. Pruvost. Overview of ONERA actuators for active flow control. *AerospaceLab Journal*, 6(3), 2013.

[143] M. Amitay and A. Glezer. Role of actuation frequency in controlled flow reattachment over a stalled airfoil. *AIAA Journal*, 40(2):209–216, 2002.

[144] V. Brunet, J. Dandois, and C. Verbeke. Recent ONERA flow control research on high-lift configurations. *AerospaceLab Journal*, 6(5), 2013.

[145] V. Ciobaca and J. Wild. An overview of recent DLR contributions on active flow-separation control studies for high-lift configurations. *AerospaceLab Journal*, 6(12), 2013.

[146] A. Seifert, A. Darabi, and I. Wyganski. Delay of airfoil stall by periodic excitation. *Journal of Aircraft*, 33(4):691–698, 1996.

[147] T. Naveh, A. Seifert, A. Tumin, and I. Wygnanski. Sweep effect on parameters governing control of separation by periodic excitation. *Journal of Aircraft*, 35(3):510–512, 1998.

[148] A. Seifert and L. G. Pack. *Oscillatory Excitation of Unsteady Compressible Flows over Airfoils at Flight Reynolds Numbers*. AIAA Paper 99-0925, 1999.

[149] D. Greenblatt and I. J. Wygnanski. The control of flow separation by periodic excitation. *Progress in Aerospace Sciences*, 36(7):487–545, 2000.

[150] J. R. Barlow, W. H. Jr. Rae, and A. Pope. *Low-Speed Wind Tunnel Testing*. John Wiley and Sons, Inc, 3rd edition, 1999.

[151] M.J. Anderson and P.J. Whitcomb. *DOE Simplified : Practical Tools for Effective Experimentation*. CRC Press, 2nd edition, 2007.

[152] D. R. Williams. Moon fact sheet. NASA Goddard Space Flight Center, https://nssdc.gsfc.nasa.gov/planetary/factsheet/moonfact.html, last updated: 03/07/2017.

[153] G. E. P. Box and D. R. Cox. An analysis of transformations. *Journal of the Royal Statistical Society. Series B (Methodological)*, 26(2):211–252, 1964.

[154] *Trek Model 20/20C-HS Data Sheet*. http://www.trekinc.com/pdf/20-20C-HSSales.pdf, last accessed: 09/09/2015.

[155] A. Duchmann, S. Grundmann, and C. Tropea. Delay of natural transition with dielectric barrier discharges. *Experiments in Fluids*, 54(3), 2013.

[156] F. Rodrigues, J. Pascoa, and M. Trancossi. Heat generation mechanisms of dbd plasma actuators. *Experimental Thermal and Fluid Science*, 90:55–65, 2018.

Appendices

Appendix A

Test Matrix

Parameter	Symbol	Unit	Low	High
Width of the exposed electrode	w_1	(mm)	0.5	5
Width of the encapsulated electrode	w_2	(mm)	10	50
Height of the exposed electrode	h_1	(μm)	35	70
Height of the encapsulated electrode	h_2	(μm)	35	70
Thickness of the dielectric	t	(mm)	0.8	3.2
Relative permittivity of the dielectric	ε_r		2.33 (PTFE)	4.42 (epoxy)
Inter-electrode gap	g	(mm)	1	5
Peak-to-peak voltage of the electric signal	V	($\mathrm{kV_{pp}}$)	9.9	15.7
Frequency of the electric signal	f_{ac}	(kHz)	0.5	2.0

Table A.1: Low and high values of the nine factors.

In order to be easily differentiable, each DBD has a unique name based on its geometry. The latter is printed on the air-exposed dielectric layer (silk-screen of the PCB). As shown in Figure 4.2, the DBD name takes the following form: e1-hTh-wgw. The first two characters indicate the used dielectric material ("e": epoxy, "P": PTFE), and whether it is a plain (1) or glued (2) design. The next three characters describe the thickness of the different layers (respectively h_1, t, h_2). The final three characters stand for the width of the electrodes, and the gap between them (respectively w_1, g, w_2). Upper cases represent the higher values of the corresponding parameters, and lower cases correspond to lower values of the corresponding parameters. For example, Run No. 6 and 27 (left and right in Figure 4.2), and Run No. 21 have the codes:

Run 6:	e	1	-	h	T	h	-	w	g	w
	ε_r	one		h_1	t	h_2		w_1	g	w_2
	epoxy	plain		35	3.2	35		0.5	1	10
	4.42	PCB		μm	mm	μm		mm	mm	mm

Run 27:	e	1	-	H	T	H	-	W	G	W
	ε_r	one		h_1	t	h_2		w_1	g	w_2
	epoxy	plain		70	3.2	70		5	5	50
	4.42	PCB		μm	mm	μm		mm	mm	mm

Run 21:	P	2	-	H	t	h	-	w	g	w
	ε_r	two		h_1	t	h_2		w_1	g	w_2
	PTFE	glued		70	0.8	35		0.5	1	10
	2.33	PCBs		μm	mm	μm		mm	mm	mm

Table A.2: Test Matrix. (**G**: glued DBD

Run. No.	**Std. No.**	$\mathbf{w_1}$ (mm)	$\mathbf{w_2}$ (mm)	**g** (mm)	$\mathbf{h_1}$ (μm)	$\mathbf{h_2}$ (μm)	**t** (mm)	$\boldsymbol{\varepsilon_r}$	**V** (kV)	**f** (kHz)
1	19**G**	0.5	50	1	35	70	3.2	2.33	15.7	2.0
2	30	5	10	5	70	70	0.8	4.42	9.9	0.5
3	8	5	50	5	35	35	3.2	4.42	15.7	0.5
4	13**G**	0.5	10	5	70	35	3.2	4.42	9.9	0.5
5	16**G**	5	50	5	70	35	0.8	2.33	9.9	0.5
6	1	0.5	10	1	35	35	3.2	4.42	15.7	2.0
7	6	5	10	5	35	35	0.8	4.42	9.9	2.0
8	31	0.5	50	5	70	70	3.2	2.33	9.9	0.5
9	22**G**	5	10	5	35	70	3.2	2.33	15.7	0.5
10	21**G**	0.5	10	5	35	70	3.2	4.42	9.9	2.0
11	15**G**	0.5	50	5	70	35	0.8	4.42	15.7	2.0
12	23**G**	0.5	50	5	35	70	0.8	4.42	15.7	0.5
13	18**G**	5	10	1	35	70	0.8	4.42	15.7	2.0
14	11**G**	0.5	50	1	70	35	3.2	2.33	15.7	0.5
15	7	0.5	50	5	35	35	3.2	2.33	9.9	2.0
16	14**G**	5	10	5	70	35	3.2	2.33	15.7	2.0
17	27	0.5	50	1	70	70	0.8	4.42	9.9	2.0
18	28	5	50	1	70	70	0.8	2.33	15.7	0.5
19	17**G**	0.5	10	1	35	70	0.8	2.33	9.9	0.5
20	25	0.5	10	1	70	70	3.2	4.42	15.7	0.5
21	9**G**	0.5	10	1	70	35	0.8	2.33	9.9	2.0
22	3	0.5	50	1	35	35	0.8	4.42	9.9	0.5
23	20**G**	5	50	1	35	70	3.2	4.42	9.9	0.5
24	4	5	50	1	35	35	0.8	2.33	15.7	2.0
25	5	0.5	10	5	35	35	0.8	2.33	15.7	0.5
26	26	5	10	1	70	70	3.2	2.33	9.9	2.0
27	32	5	50	5	70	70	3.2	4.42	15.7	2.0
28	29	0.5	10	5	70	70	0.8	2.33	15.7	2.0
29	2	5	10	1	35	35	3.2	2.33	9.9	0.5
30	10**G**	5	10	1	70	35	0.8	4.42	15.7	0.5
31	24**G**	5	50	5	35	70	0.8	2.33	9.9	2.0
32	12**G**	5	50	1	70	35	3.2	4.42	9.9	2.0

The runs presented in Table A.2 are repeated three times. Consequently, runs number 33 to 64, and 65 to 96 are obtained by repeating the given table.

Appendix B

Isolated Load Cell Calibration

The load cell was screwed vertically to a fix rigid support. Several sampling times and sampling frequencies were assessed. It was found that the results did not greatly differ after a warming up time of 15 to 30 minutes of the load cell, and waiting a few seconds (less than 5) for the load cell signal to converge. The signals over a million points were then recorded for inputs of 0 and 10 g, which respectively represent forces of 0 and 98.1 mN. The 10 g calibration weight was centred, yet, it became clear that the location of the mass on the load cell pin was critical in order to obtain repeatable values. The mass is a F1 OIML standard calibration mass, having an uncertainty of ± 0.20 mg.

Figure B.1 and Table B.1 show the histogram and statistical results for measurements realised at a sampling frequency of 25 kHz. It was noticed that the probability distribution was not normal. A best fit for the measurements was found empirically using MATLAB. The fit consists in the superposition of three Gaussian curves. One curve is centred on the mean of the signal, and the other two curves are symmetrically distributed around the mean and segregated from it by one standard deviation. This fit is given in Equation B.1, where μ and σ respectively represents the mean and standard deviation of the data. This model results in a flatter distribution. The coefficients a, b and c are computed by the program. The $150 \cdot \sigma$ weighting in the last exponent was found empirically, but an analytic justification has presently not been drawn.

$$p(x) = a \cdot \left\{ e^{-b\left(\frac{x-\mu-\sigma}{\sigma}\right)^2} + e^{-b\left(\frac{x-\mu+\sigma}{\sigma}\right)^2} \right\} + c \cdot \left\{ e^{-150\,\sigma\left(\frac{x-\mu}{\sigma}\right)^2} \right\} \quad . \tag{B.1}$$

The coefficients showed in Table B.1 generate curves in percent of the total number of points. It can be noted that the area under a curve described by Equation B.1 is given by Equation B.2:

$$A = 2a\sigma\sqrt{\frac{\pi}{b}} + c\sqrt{\frac{\sigma\pi}{150}} \quad . \tag{B.2}$$

Looking at the lesser than 3 kurtosis and small negative skewness in Table B.1, it can be concluded that the measured distribution is more platykurtic (i.e. slightly closer to a uniform distribution) than a normal distribution, with a slightly longer left tail. 99%

of the data are met within three standard deviations from the mean, and 95% of the data are comprised in a two standard deviation interval around the mean.

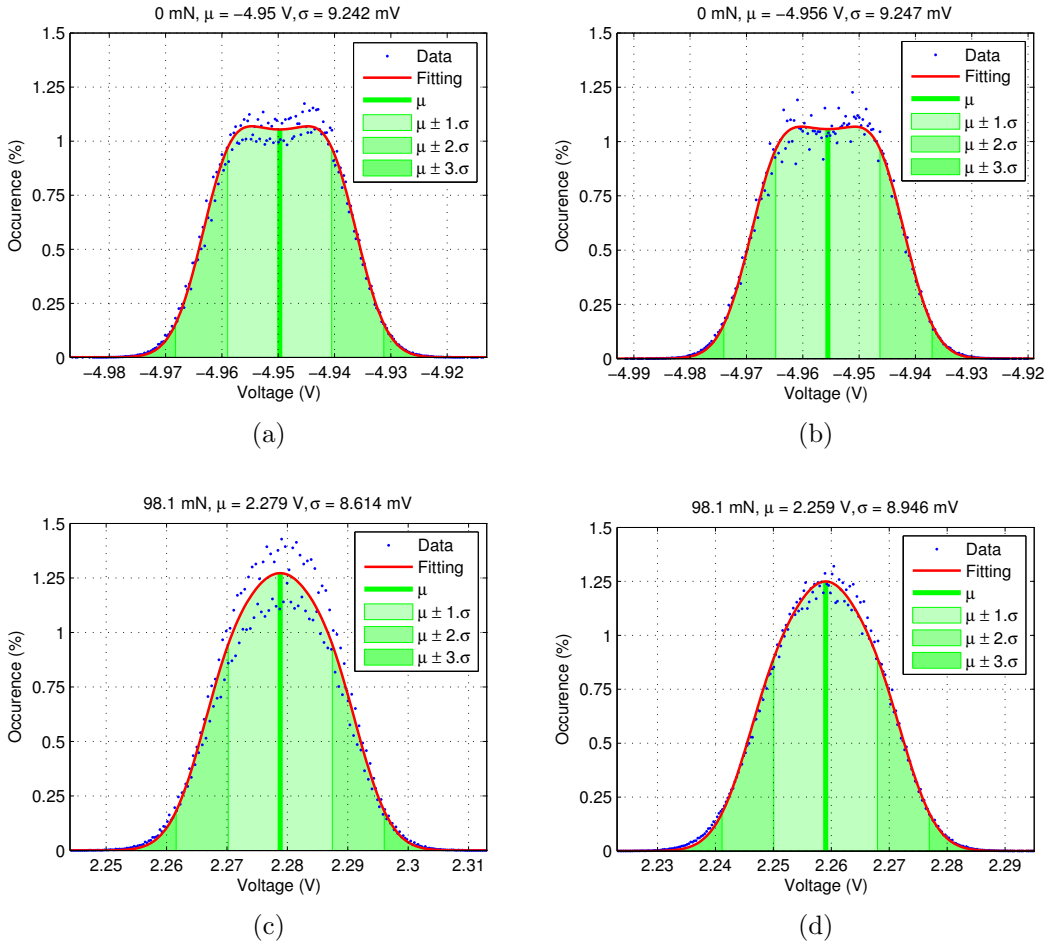

Figure B.1: Probability distribution for the isolated load cell at 0 (a, b) and 10 g (c, d) loads over 10^6 points sampled at 25 kHz.

Case	Kurtosis	Skewness (%)	Coefficients			R^2	Probability (%)		
			a	b	c		$\pm\sigma$	$\pm 2\sigma$	$\pm 3\sigma$
(a)	2.322	-2.715	0.7802	1.632	0.7488	0.9947	63.6	97.3	99.7
(b)	2.327	-2.520	0.7765	1.619	0.7496	0.9938	63.7	97.3	99.7
(c)	2.601	-3.987	0.6894	1.365	0.9199	0.9818	65.6	96.6	99.5
(d)	2.641	-5.688	0.6550	1.339	0.9063	0.9969	65.9	96.4	99.4

Table B.1: Statistics and curve fitting parameters for the probability distribution of the isolated load cell.

Appendix C

Full Test Rig Calibration

C.1 Calibration Method and Equipment

At the bottom end of the lever of the test rig, a stainless steel rod is placed and fitted with different masses made of stainless steel or Perspex. The two default masses are made of standard steel and weigh around 250 g together. However, in order to ensure a better control over the verticality and zero-thrust loading of the load cell, different masses were manufactured. Moreover, in the first design, the platform was composed of an aluminium plate coated with Kapton and PVC. Since the aluminium core could affect the results, by interacting with the electric field, it was decided to use a 5 mm thick acrylic tray instead, thus adding mass on the upper part of the lever. The different masses are showed in picture Figure C.1. Using a standard scale, it was determined that the accuracy of the masses is nearly 10% for the perspex weights, ± 1 g for the stainless steel masses up to 50 g, and ± 2 g for the 100 g weights. However, as these masses are only used in order to set the verticality of the lever, and set the zero thrust load, this error does not directly affect the results.

The calibration is realised using two weights hangers of mass 10 g (±9.72%). The hangers are attached to a string via small pulleys. The hangers are attached at the front and back of the rig, allowing to transform the vertical force into a horizontal load. A string links the two hangers together, and is glued (super-glue and PVC tape) at 37 mm above the blade edge (no amplification). As a result, by assuming the friction in the pulleys is negligible, the force recorded by the load cell, should simply be the hung mass times the standard gravitational constant. Several calibration weights can be placed on the hangers: 1 g (±8.11%), 2 g (±4.34%) and 5 g (±2.61%).

C.2 Linearity

Over a week, 17 series of measurements were realised. Every series consists of a voltage reading v from the load cell, for calibration inputs of 0 to 10 g by step of 1 g. The voltage at 0 g $v(0\text{g})$ is used as a reference. For a voltage $v(m)$ obtained for a mass m, the voltage difference Δv is utilised to determine the increase in the voltage due to the

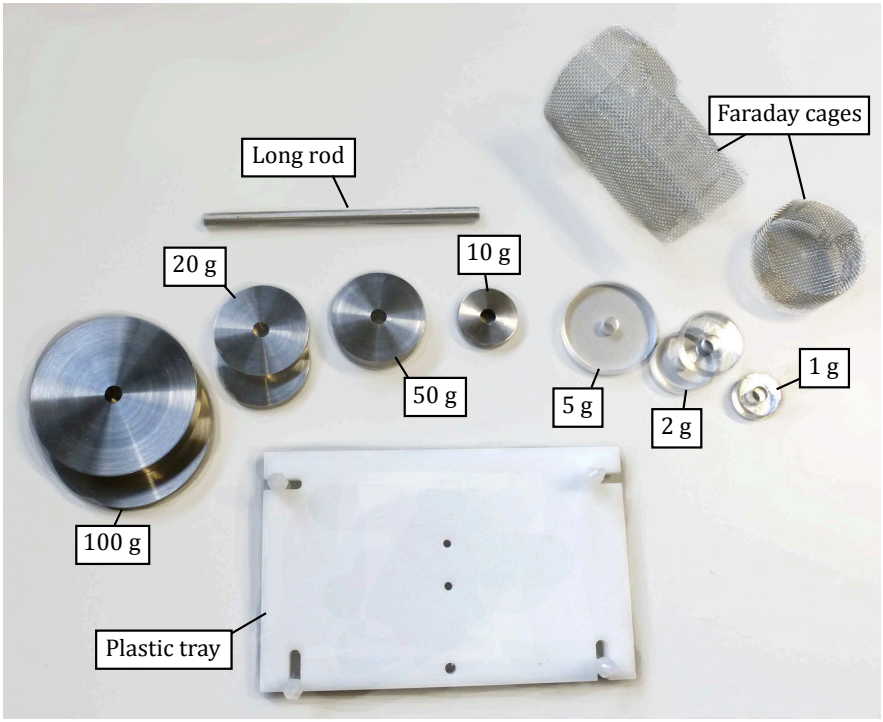

Figure C.1: Different calibration weights used to adjust the reference load.

load:

$$\Delta v = v(m) - v(0\text{g}) \tag{C.1}$$

A standard linear regression is performed on the data between point m and 0 g, in order to estimate the gain of the load cell G in mN/V. A point measured with the test rig is first scaled down using Equation C.1, and the voltage difference is multiplied by the gain of the load cell in a second time. The measured force is plotted against the input mass in Figure C.2. For clarity, all 17 points were not drawn on the graph. The vertical error bars correspond to three standard deviations from the average, and the horizontal error bars were derived from the manufacturer data for the calibration masses (see previous section). However, four series taken on the same day have been added. Both the fast response (within a few seconds after placing the weights) and slow response (a few minutes after placing the masses) were recorded. Fast responses are typically slightly higher than slow responses, by an almost constant amount for each data series. Therefore, as long as the recording time is constant between the different measurements, the slope is hardly affected by the response time. Series number three shows the difference between fast or slow responses for one dataset. For this data series, the mass was placed, then the fast response was recorded, and after waiting, the slow response was captured as well. A linear fitting of the data was realised, and according to Newton's law of gravitation, the force is expected to be 9.81 m/s^2 times the mass. From all the data acquired, it was found to be closer to 9.80 m/s$^2\pm$ 0.060. This 0.1% difference can be explained by the inaccuracy in the mounting leading to a reduction of the force, or friction occurring in the pulleys. For a single data series, the slope

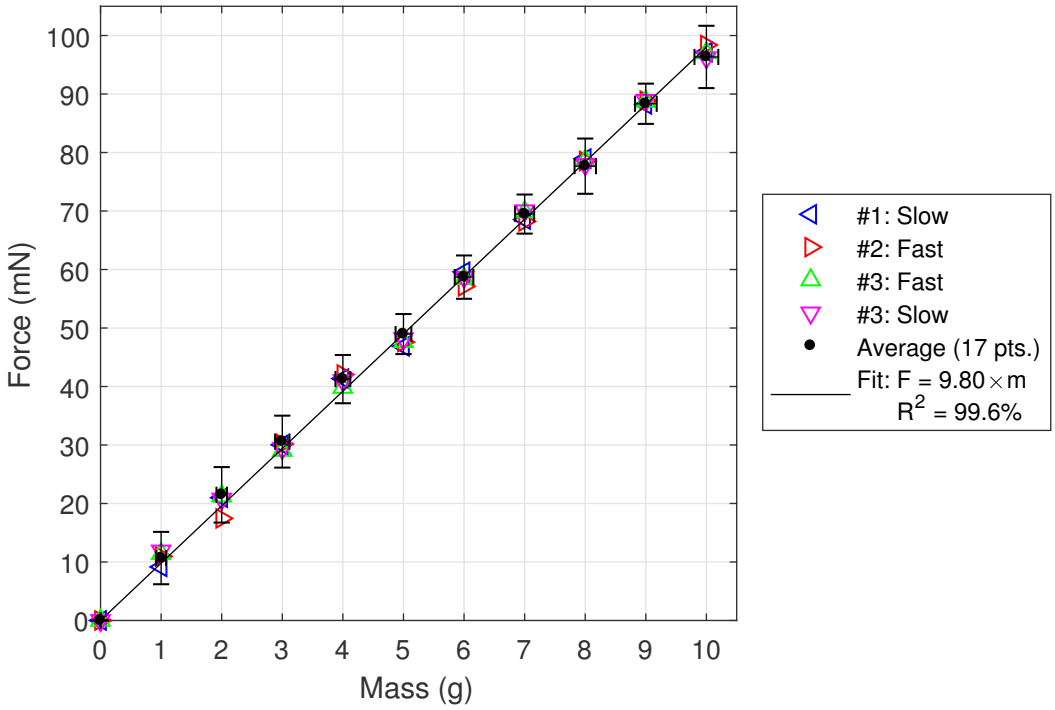

Figure C.2: Calibration and force determination over 17 points.

uncertainty was typically 0.087 m/s^2, with a maximum of 0.143 m/s^2, and a minimum of 0.045m/s^2. As a result, the gain could be determined with an accuracy of 0.5 to 1.5%.

C.3 Choice of the Calibration Process

As acquiring one of the previous data series takes a relatively long time, it was decided to determine a faster way to derive the gain of the load cell. The zero-input voltage must still be measured, as it sets the reference voltage. However, a smaller number of carefully chosen points can lead to a good estimation of the gain in a shorter time. As a result, seven series were chosen and the system gain was calculated with its accuracy. The results are shown in Figure C.3.

As can it be seen, the gain can change significantly within one day (series 1 to 2). After some maintenance realised by the manufacturer, the cell was fitted again in the rig, with a new gain varying between 11 and 13 mN/V. In Figure C.3, the acronyms "ZI" and "NZI" respectively refers to zero and non-zero intercept, depending whether the regression was forced to be purely proportional (zero output at zero input) or simply linear (free intercept at zero input). As the unloaded lever represented an output of up to 2 g on the load cell, it was preferred not to input masses over 8 g, even though the safe range of the device (+ 50%) would allow it.

The slope was separately calculated for all 17 points, and based only on 2 to 3 points. Using the 0 g input (red markers on the figure) could be argued as being a 2-point regression, since the mathematical model already assumes a zero output at

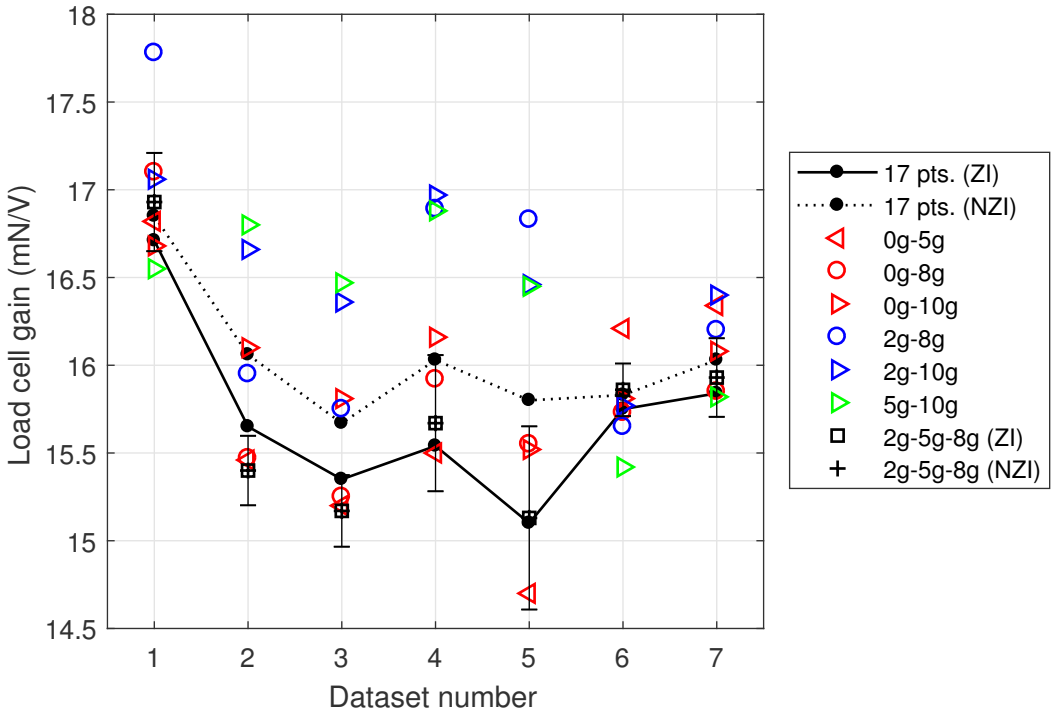

Figure C.3: Gain of the system for several calibration processes.

zero input. Other 2-point regressions show high disparities (blue and green markers). However, when recording three points (2, 5 and 8 g), the slope typically agrees with the full sample results. One major difference lies in the fact that forcing or not the zero intercept does not seem to impact the results for the 3-point procedure. At the contrary, when using a full sample (i.e. all 17 points), forcing the zero intercept tends to underestimate the gain compared to a free intercept case. It can thus be concluded that the zero intercept is usually overestimated.

Consequently, a linear regression calculated over three points was chosen. Every calibration will consist in the measurement of the reference voltage first (0 g), followed by measurements at 2, 5 and 8 g. Let v_i be the signal conditioner output voltage number i, m_i be the calibration mass number i and g_0 be the standard gravitational acceleration, assuming a null zero intercept, a standard regression can be led:

$$G = g_0 \cdot \frac{\sum_1^n v_i \cdot m_i}{\sum_1^n v_i^2} \quad , \tag{C.2}$$

where G corresponds to the system gain in mN/V. The standard error on the slope can also be derived:

$$\sigma = \sqrt{\frac{1}{n-2} \frac{\sum_1^n (g_0 \cdot m_i - G \cdot v_i)^2}{\sum_1^n (v_i - \bar{v})^2}} \quad , \tag{C.3}$$

$\bar{v}$ representing the mean value of the output voltage.

Equations C.2 and C.3 were both implemented in the acquisition software, so that real time estimation of the gain and its accuracy are displayed. The processing program was designed so that up to four calibration series could be recorded. Thus, the error on

the gain can usually be reduced by doing two calibrations before acquiring the thrust of a DBD, plus one to two calibrations afterwards.

Appendix D

Average Test Conditions

The following tables provide the mean atmospheric conditions for each run. The means are obtained over the three tests performed for each run. The run numbers can be found in Table A.2. Table D.1 provides a summary of the errors presented in Section 4.2.6, and their calculated confidence intervals for the means obtained over three values. Table D.2 shows the means and standard deviations of the atmospheric pressure p_0, temperature T_0 and humidity H_0 for every runs.

Parameters		p_0	T_0	H_0
Standard errors	**Single point**	4 hPa	0.4 °C	3 % of humidity
	Mean over 3 points	2.31 hPa	0.23 °C	1.73 % of humidity
Confidence interval (t-value = 3.18)		7.35 hPa	0.73 °C	5.50 % of humidity

Table D.1: Standard errors and confidence intervals of the atmospheric conditions measurements (runs detailed in Table A.2).

Run	p_0	(hPa)	T_0	(°C)	H_0	(%)
order	Mean	Dev.	Mean	Dev.	Mean	Dev.
1	1006.7	± 0.6	21.6	± 0.1	47.3	± 0.6
2	1017.0	± 0.0	21.8	± 0.2	62.0	± 0.0
3	1018.3	± 2.1	22.3	± 0.2	60.7	± 1.5
4	1013.3	± 0.6	22.9	± 0.2	58.0	± 1.0
5	998.7	± 2.5	22.2	± 0.2	50.7	± 7.5
6	1010.3	± 5.5	22.0	± 0.1	54.7	± 4.7
7	1013.7	± 0.6	22.4	± 0.2	56.3	± 0.6
8	1010.0	± 0.0	22.8	± 0.2	56.7	± 4.0
9	1011.3	± 0.6	23.4	± 0.1	64.0	± 2.6
10	1009.3	± 2.3	23.7	± 0.3	57.0	± 2.6
11	1002.3	± 11.7	22.9	± 0.3	58.3	± 2.5
12	1010.0	± 2.6	23.3	± 0.1	62.7	± 7.4
13	1018.0	± 7.5	21.7	± 0.5	50.3	± 11.0
14	1007.3	± 9.0	22.0	± 0.1	59.3	± 10.1
15	1006.0	± 4.4	22.1	± 0.3	52.7	± 12.4
16	1008.7	± 3.2	21.5	± 0.1	51.3	± 2.1
17	1018.3	± 0.6	20.9	± 0.1	39.7	± 4.0
18	1017.3	± 0.6	20.9	± 0.1	50.7	± 9.2
19	986.3	± 3.1	19.8	± 0.2	30.0	± 9.5
20	1001.0	± 3.5	21.3	± 0.2	42.3	± 4.2
21	986.0	± 5.2	21.2	± 0.1	43.3	± 2.9
22	1019.7	± 8.4	20.9	± 0.4	26.0	± 3.5
23	1005.3	± 10.7	20.8	± 0.1	33.7	± 2.9
24	1008.0	± 6.9	20.9	± 0.1	34.7	± 8.6
25	998.3	± 11.8	20.8	± 0.2	39.7	± 4.9
26	997.0	± 2.0	21.0	± 0.1	53.3	± 1.5
27	1003.3	± 0.6	21.1	± 0.1	46.7	± 0.6
28	1009.0	± 6.9	21.3	± 0.3	48.3	± 4.0
29	1017.3	± 0.6	22.4	± 0.1	50.3	± 1.5
30	1004.3	± 5.5	21.3	± 0.2	48.7	± 1.2
31	1004.7	± 0.6	20.6	± 0.1	41.0	± 2.6
32	1015.0	± 2.6	21.1	± 0.1	42.7	± 4.6

Table D.2: Mean and standard deviation of the test conditions over the repeats (runs detailed in Table A.2).

Appendix E

Error Analysis of the Aerodynamic Measurements

This appendix presents the error analysis of the total pressure measurements that are discussed in Section 8.2.

The x and z locations of each measurement have an uncertainty of 0.02 mm. The velocity recording system (capillary probe, tubing and anemometer) was observed to have an accuracy of 2% of the measurements (see Section 4.3). The atmospheric conditions are obtained within 4 hPa, 0.4°C and 3% of relative humidity.

Equation 8.2 is the difference of two integrals. The error of the x location of the measurement can be neglected in comparison to the error of the z location, since the step in the z direction between two successive measurements is of the order of tenths of millimetres compared several millimetres in the x direction.

Equation 8.2 can be viewed as the difference of two forces F_{rear} and F_{front}:

$$T_A = F_{\text{rear}} - F_{\text{front}} \ . \tag{E.1}$$

The integrals are performed numerically using the trapezoidal rule. Using the standard propagation of error, and because the errors of F_{rear} and F_{front} are equal, the error of the thrust is the error of the force multiplied by the square-root of two. As seen in Section 4.2.7, the uncertainty of an integral calculated with a trapezoidal rule can be approximated as the uncertainty of a mean. The minimal number of observations for each x location is ten z locations. Therefore, if σ_T is the uncertainty of the thrust, it can be expressed as:

$$\sigma_T \approx \sigma_F \sqrt{\frac{2}{10}} = \frac{\sigma_F}{\sqrt{5}} \ , \tag{E.2}$$

where $F_x(\Delta z)$ is the force per unit span generated over one vertical step of Δz and is measured with an error σ_F. $F_x(\Delta z)$ can be expressed as:

$$F_x(\Delta z) = \rho_0 \, u^2 \, \Delta z \ . \tag{E.3}$$

It can be noticed that the forces F_{rear} and F_{front} from which the thrust is derived are only averages of $F_x(\Delta z)$ over the ten steps of height Δz. As a result, their uncertainty is only $\sigma_F/\sqrt{10}$. The step size Δz is the difference between two position. Consequently, with the standard propagation of the error, its uncertainty $\sigma_{\Delta z}$ is the error of a z position σ_z (0.02 mm) multiplied by the square-root of two:

$$\sigma_{\Delta z} = \sigma_z\sqrt{2} \approx 0.028 \text{ mm}. \tag{E.4}$$

The velocity has an error of 2% of the value. The only remaining uncertainty belongs to the density. As previously expressed, Equation 3.1 was employed in order to account for the effect of the humidity. It can be summed up as:

$$\rho_0 = \frac{A}{T_0}\left(p_0 - B \cdot H_0 \cdot e_S\right) \ , \tag{E.5}$$

with A and B two constants, T_0 the temperature in K, p_0 the pressure in Pa, H_0 the relative humidity in %, and e_S the saturation vapour pressure given by:

$$e_S = C \cdot \exp\left(-\frac{D}{T_0}\right) \ , \tag{E.6}$$

with C and D two constants. As a result, the density is obtained through the formula:

$$\rho_0 = \frac{A}{T_0}\left(p_0 - B \cdot C \cdot H_0 \cdot \exp\left(-\frac{D}{T_0}\right)\right) \ , \tag{E.7}$$

where:

$$\begin{aligned} A &= 0.0034847 \ , \\ B &= 0.003796 \ , \\ C &= 1.7526 \times 10^{11} \ , \\ D &= 5315.56 \ . \end{aligned}$$

With the propagation of uncertainty, the error σ_ρ of the density can be derived from the errors of the pressure σ_p, humidity σ_H and temperature σ_θ with the formula:

$$\sigma_\rho = \sqrt{\left(\frac{\partial\rho_0}{\partial p_0}\,\sigma_p\right)^2 + \left(\frac{\partial\rho_0}{\partial H_0}\,\sigma_H\right)^2 + \left(\frac{\partial\rho_0}{\partial T_0}\,\sigma_\theta\right)^2} \ . \tag{E.8}$$

The partial derivatives can be calculated thanks to Equation E.7:

$$\frac{\partial\rho_0}{\partial p_0} = \frac{A}{T_0} \ , \tag{E.9}$$

$$\frac{\partial\rho_0}{\partial H_0} = -\frac{A \cdot B \cdot C}{T_0} \cdot \exp\left(-\frac{D}{T_0}\right) \ , \tag{E.10}$$

$$\begin{aligned}\frac{\partial \rho_0}{\partial T_0} &= -\frac{A \cdot p_0}{T_0^2} - A \cdot B \cdot C \cdot H_0 \cdot \frac{\partial}{\partial T_0}\left(\frac{1}{T_0}\exp\left(-\frac{D}{T_0}\right)\right) \ , \\ &= -\frac{A \cdot p_0}{T_0^2} + \frac{A \cdot B \cdot C \cdot H_0}{T_0^2} \cdot \left(1 + \frac{D}{T_0}\right) \cdot \exp\left(-\frac{D}{T_0}\right) \ . \end{aligned} \tag{E.11}$$

In order to find the maximum error, the three partial derivatives needs to be maximised. This can be done by using the minimal temperature, or maximum pressure and maximum humidity. Throughout the test campaigns, the smallest recorded temperature was 19.6°C (292.8 K), the highest measured pressure was 1,025 hPa (102,500 Pa) and the greatest recorded humidity was 71%. Given the values of the constant (see Equation E.7), it can be approximated that:

$$\begin{aligned}\frac{\partial \rho_0}{\partial p_0} &\approx 1.2 \times 10^{-5} \text{ kg/m}^3\text{/Pa} \ , \\ \frac{\partial \rho_0}{\partial H_0} &\approx -1.0 \times 10^{-4} \text{ kg/m}^3\text{/\%} \ , \\ \frac{\partial \rho_0}{\partial T_0} &\approx -3.7 \times 10^{-3} \text{ kg/m}^3\text{/K} \ . \end{aligned}$$

Considering the uncertainties of the temperatures σ_θ of 0.4 K, of the pressure σ_p of 400 Pa, and of the humidity σ_H of 3%, the error of the density can be calculated using Equation E.7:

$$\sigma_\rho \approx 5.0 \times 10^{-3} \text{ kg/m}^3.$$

Finally, the uncertainty of the velocity σ_u of 2% of the measurement can be replaced by an upper bound. Throughout the experiment, the recorded velocity never exceeded 4 m/s, giving a maximum error σ_u of 0.08 m/s.

Using Equation E.3, the uncertainty of the force derived over one step in the y direction is:

$$\begin{aligned}\sigma_F &= \sqrt{\left(\frac{\partial F}{\partial \rho_0}\,\sigma_\rho\right)^2 + \left(\frac{\partial F}{\partial u}\,\sigma_u\right)^2 + \left(\frac{\partial F}{\partial \Delta z}\,\sigma_{\Delta z}\right)^2} \ , \\ &= \sqrt{\left(u^2 \cdot \Delta z \cdot \sigma_\rho\right)^2 + \left(2 \cdot u \cdot \rho_0 \cdot \Delta z \cdot \sigma_u\right)^2 + \left(u^2 \cdot \rho_0 \cdot \sigma_{\Delta z}\right)^2} \ . \end{aligned} \tag{E.12}$$

Given a maximum velocity of 4 m/s, a maximum density of 1.211 kg/m^3 and a maximum step size of 0.5 mm, the inaccuracy for the force per unit span F is:

$$\sigma_F \approx 0.55 \text{ mN/m}.$$

Finally, the error of F can be used in Equation E.2 to determine the uncertainty of the thrust per unit span:

$$\sigma_T \approx 0.25 \text{ mN/m}.$$

It can be remarked the error on the force per unit span at one x location over the full

height of the wall jet (such as F_{rear} or F_{front}) is $\sigma_F/\sqrt{10} \approx 0.17$ mN/m. In addition the mass flow rate $\mathring{m}$ that goes through a cross section of span L (span of the electrode: 10 cm) and of height z (height of the wall jet) can be expressed as:

$$\mathring{m} = \rho_0 \cdot u \cdot L \cdot z \ . \tag{E.13}$$

By neglecting the inaccuracy of the span of the electrodes, the propagation of error leads to:

$$\frac{\sigma_{\mathring{m}}}{\mathring{m}} = \sqrt{\left(\frac{\sigma_\rho}{\rho_0}\right)^2 + \left(\frac{\sigma_u}{u}\right)^2 + \left(\frac{\sigma_z}{z}\right)^2} \ . \tag{E.14}$$

With the maximums of 1.211 kg/m^3, 4 m/s and 5 mm, the mass flow rate can be measured with a 2.1% accuracy (lower or equal to 0.051 g/s).

Appendix F

Complete Set of Aerodynamic Measurements

The present appendix presents the full set of aerodynamic results. Section F.1 provides the wall jet profiles recorded with DBD-1 and DBD-2 at different voltages and frequencies. Section F.2 contains the chord-wise evolutions of the maximum induced velocity $u_{\max}$ and of the wall jet thickness $y_{1/2}$ for DBD-1 and DBD-2 for the same voltages and frequencies. For the same actuators, under the same conditions, the evolutions of the mass flow rate and induced force can be found respectively in Section F.3 and Section F.4.

F.1 Wall Jet Profiles

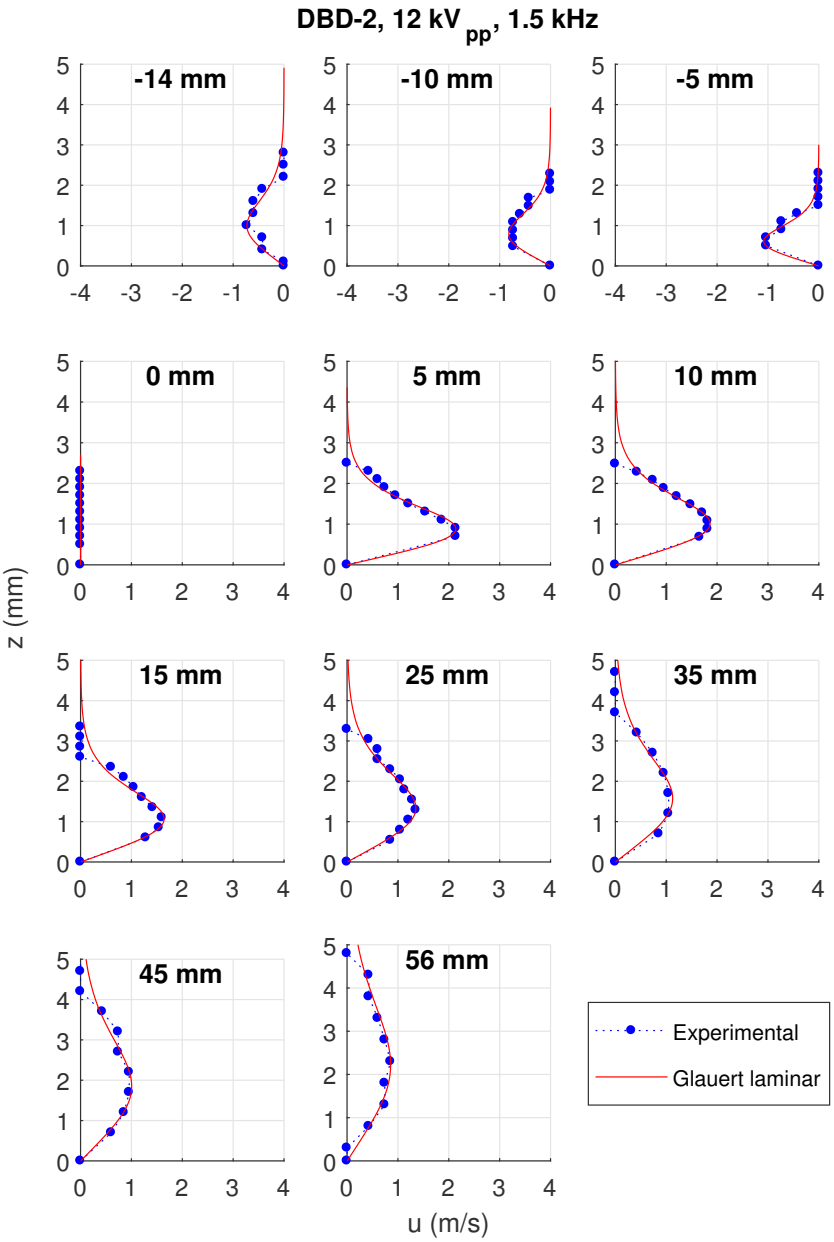

Figure F.1: Wall jet profiles for DBD-2 at 12 kV_{pp} and 1.5 kHz at different x locations.

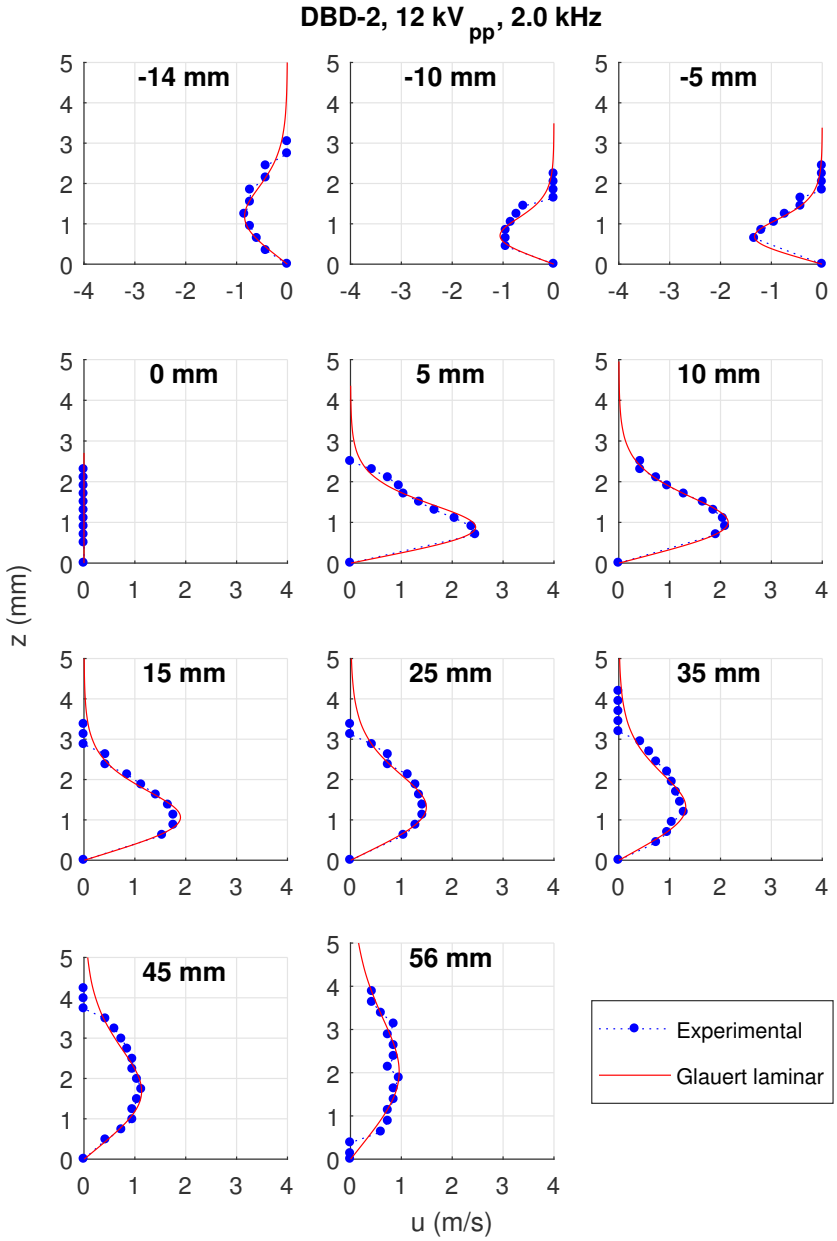

Figure F.2: Wall jet profiles for DBD-2 at 12 kV_{pp} and 2.0 kHz at different x locations.

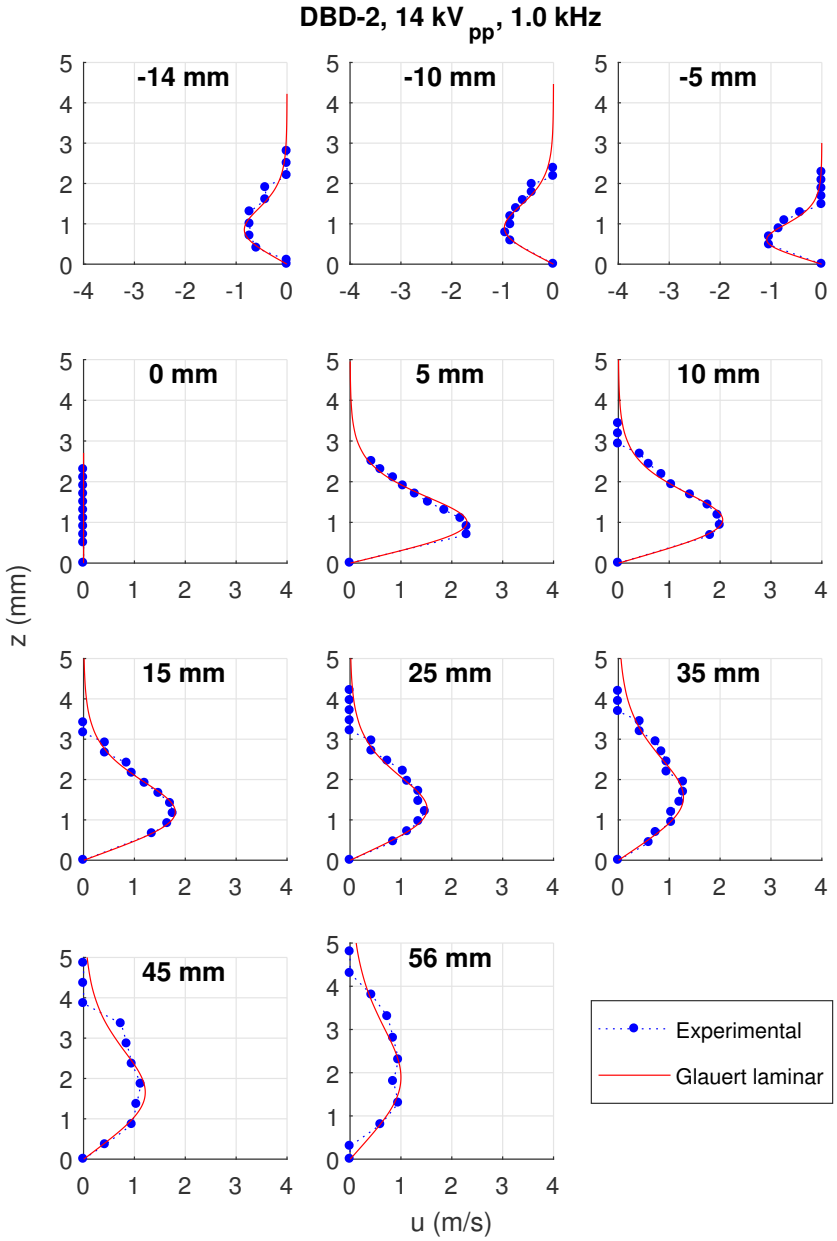

Figure F.3: Wall jet profiles for DBD-2 at 14 kV_{pp} and 1.0 kHz at different x locations.

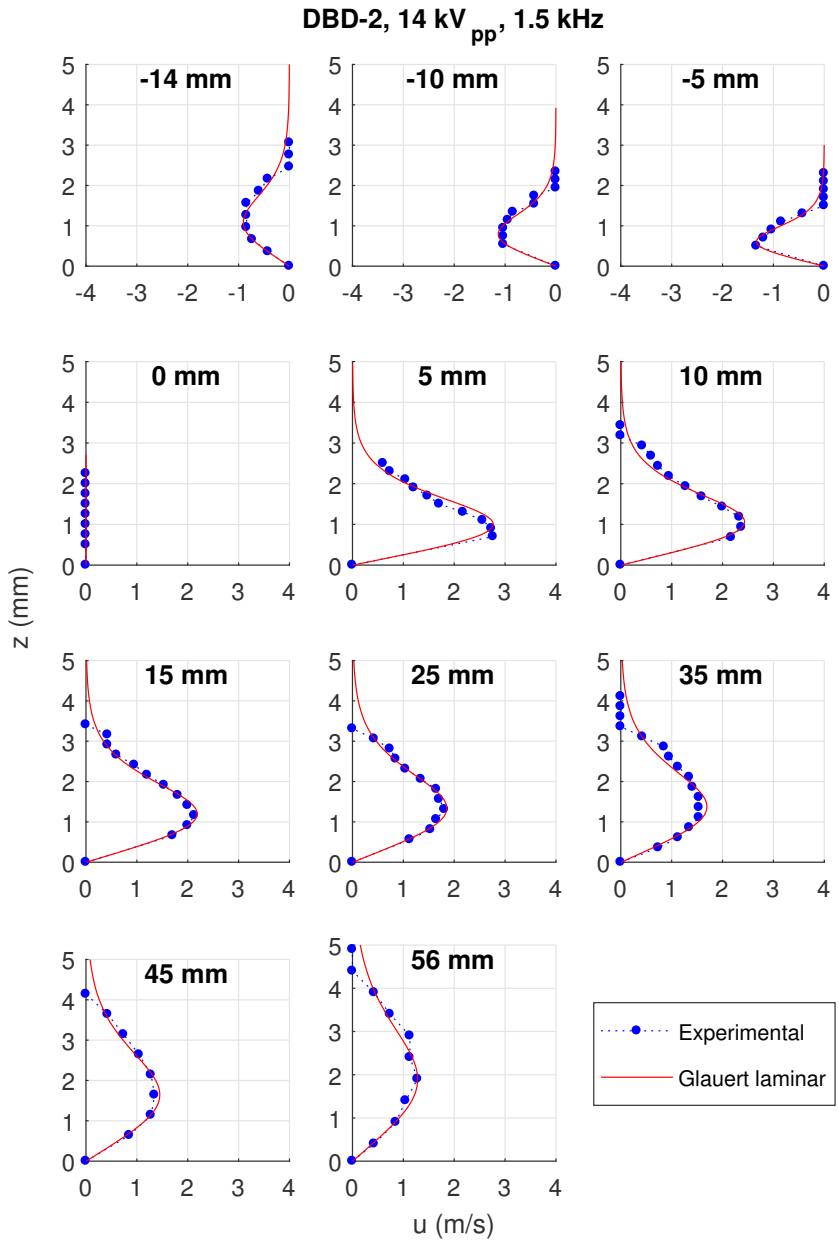

Figure F.4: Wall jet profiles for DBD-2 at 14 kV_{pp} and 1.5 kHz at different x locations.

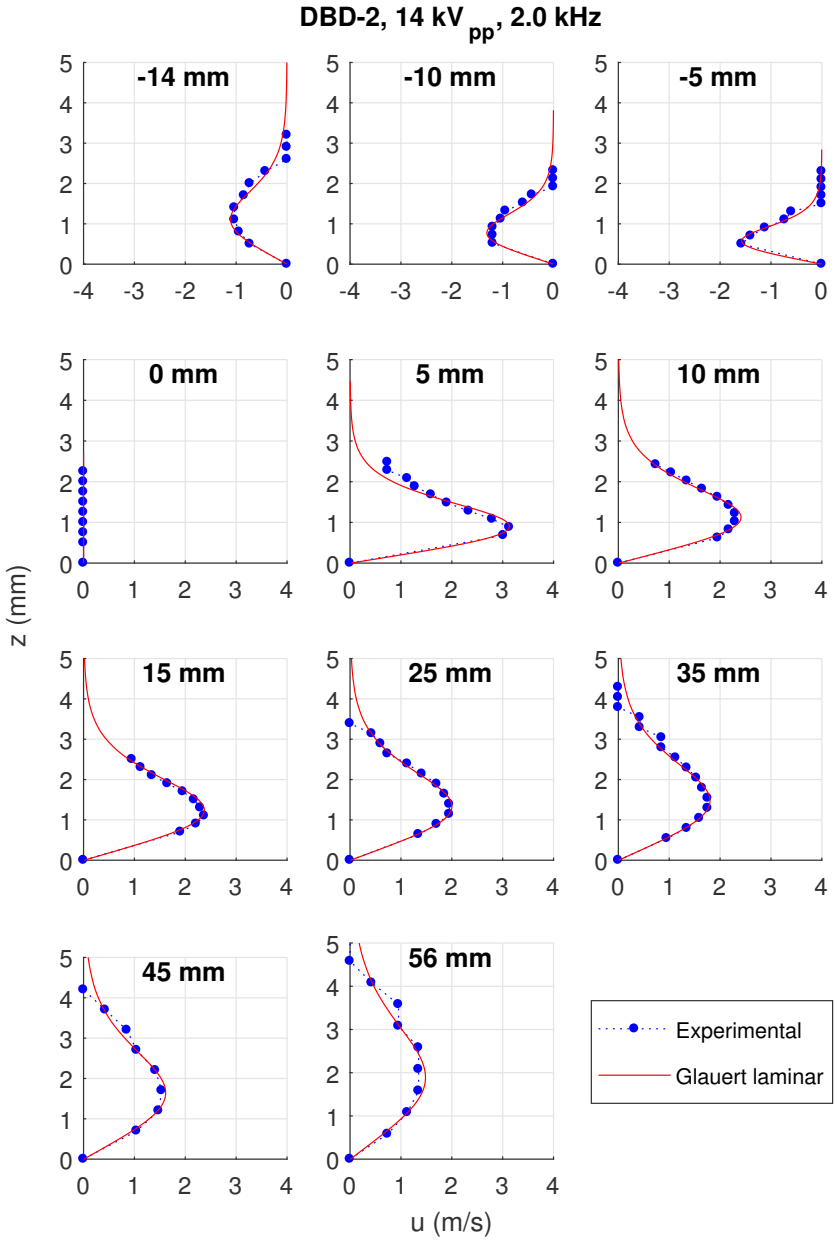

Figure F.5: Wall jet profiles for DBD-2 at 14 kV_{pp} and 2.0 kHz at different x locations.

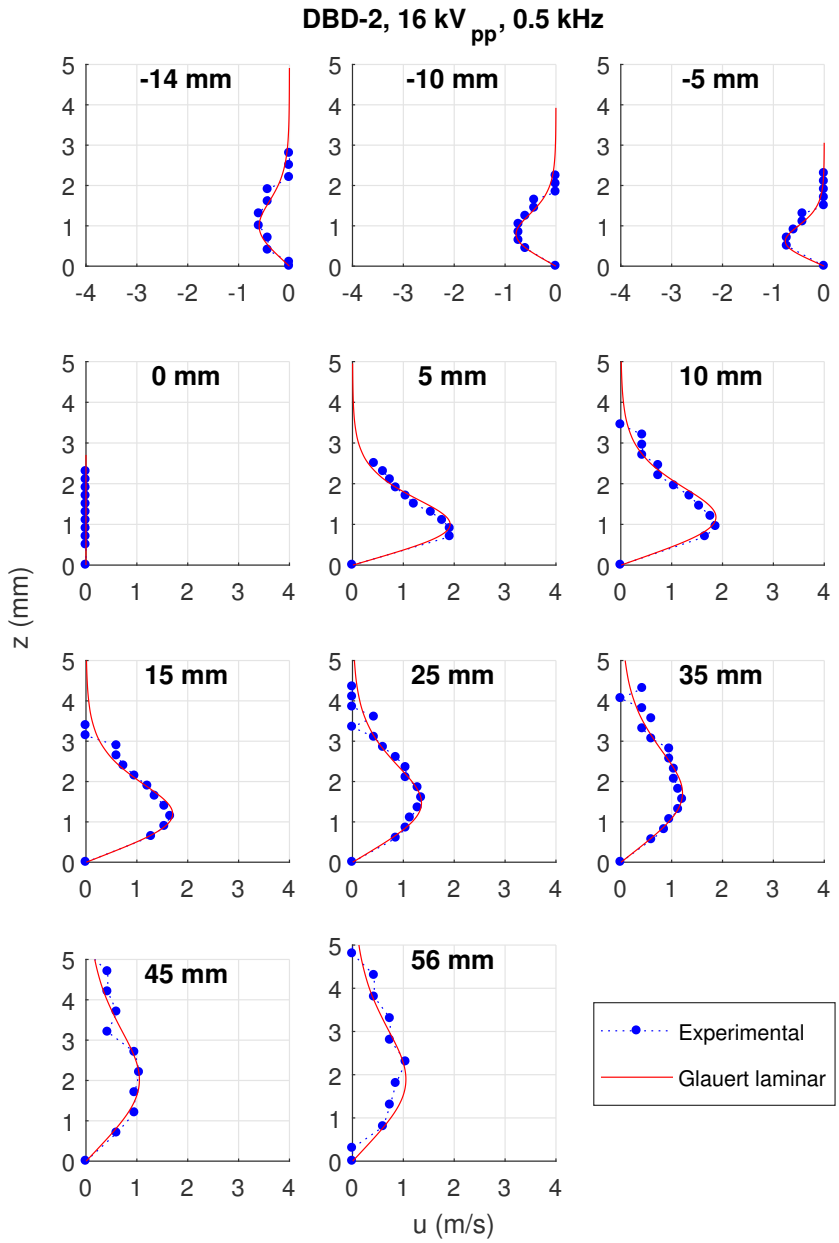

Figure F.6: Wall jet profiles for DBD-2 at 16 kV_{pp} and 0.5 kHz at different x locations.

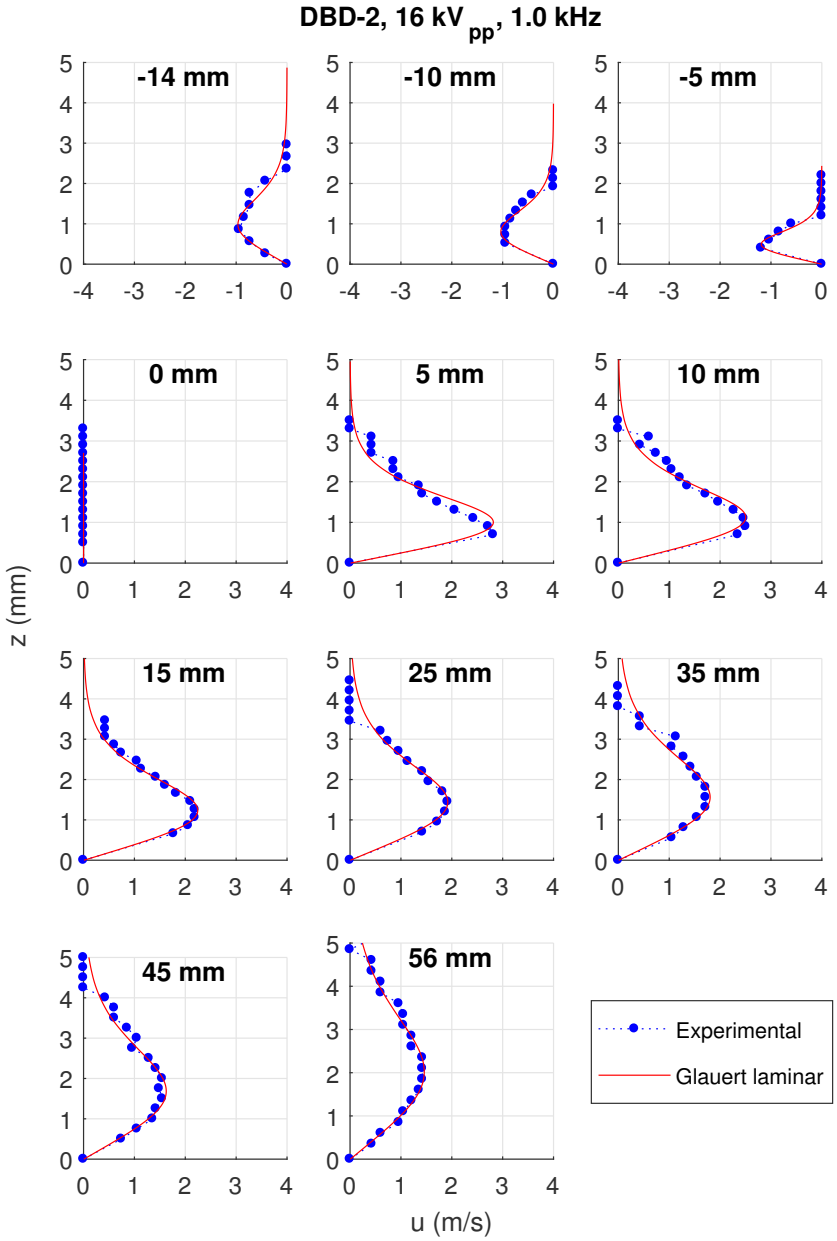

Figure F.7: Wall jet profiles for DBD-2 at 16 kV_{pp} and 1.0 kHz at different x locations.

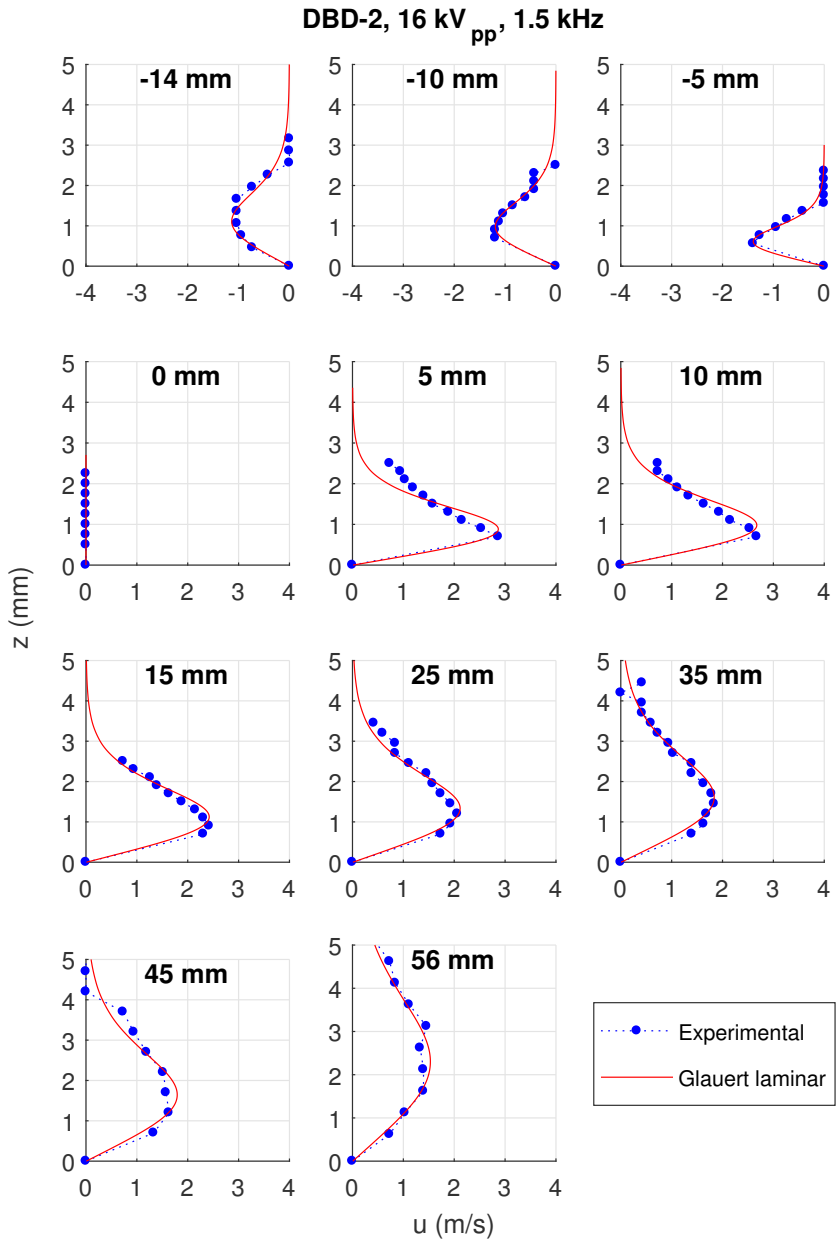

Figure F.8: Wall jet profiles for DBD-2 at 16 kV_{pp} and 1.5 kHz at different x locations.

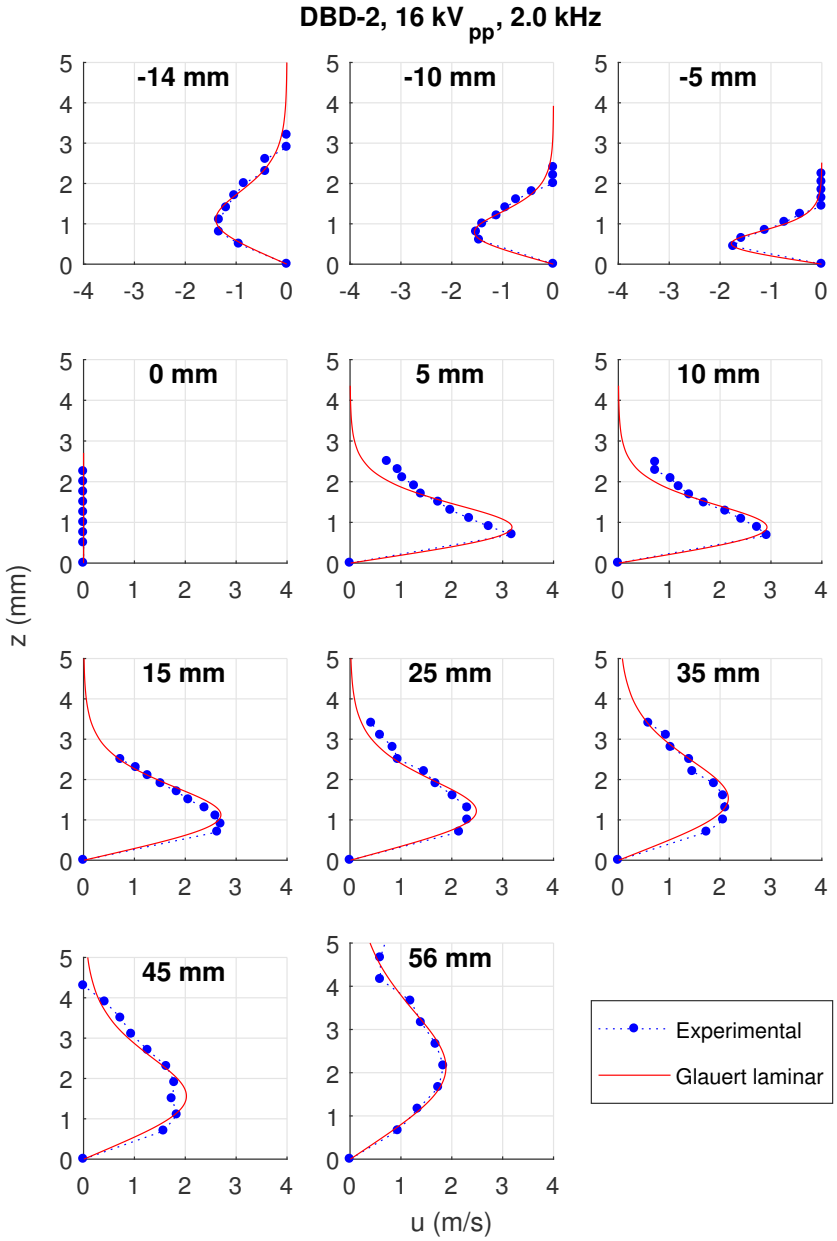

Figure F.9: Wall jet profiles for DBD-2 at 16 kV_{pp} and 2.0 kHz at different x locations.

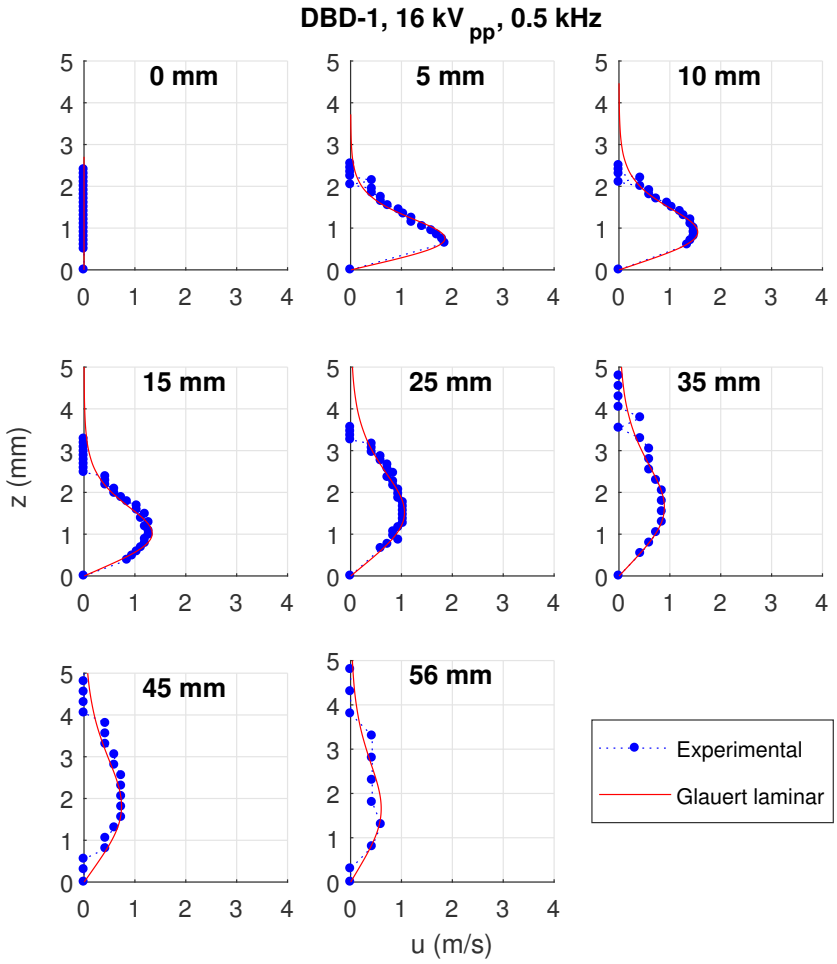

Figure F.10: Wall jet profiles for DBD-1 at 16 kV_{pp} and 0.5 kHz at different x locations.

F.2 Maximum Velocity and Wall Jet Thickness

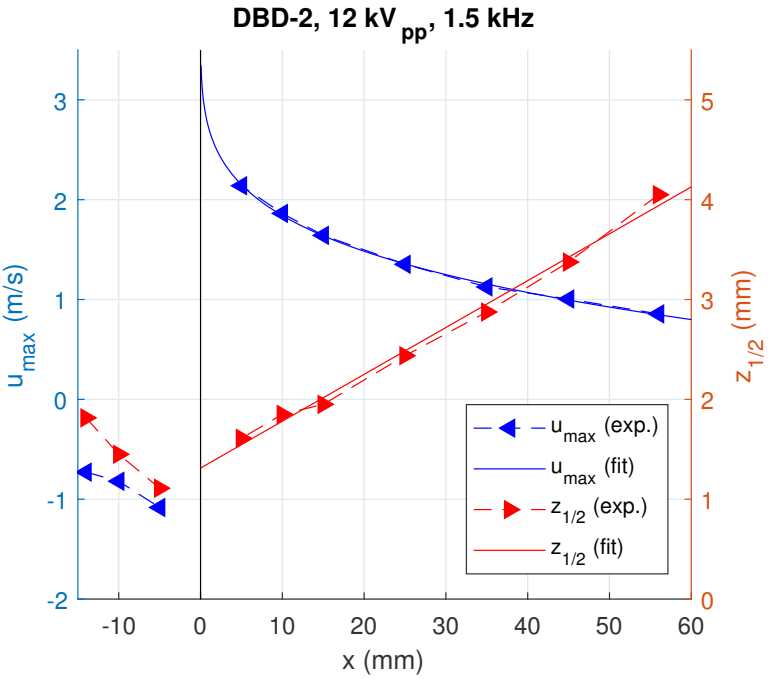

Figure F.11: Evolution of the maximum velocity and of the thickness of the wall jet for DBD-2 at 12 kV_{pp} and 1.5 kHz.

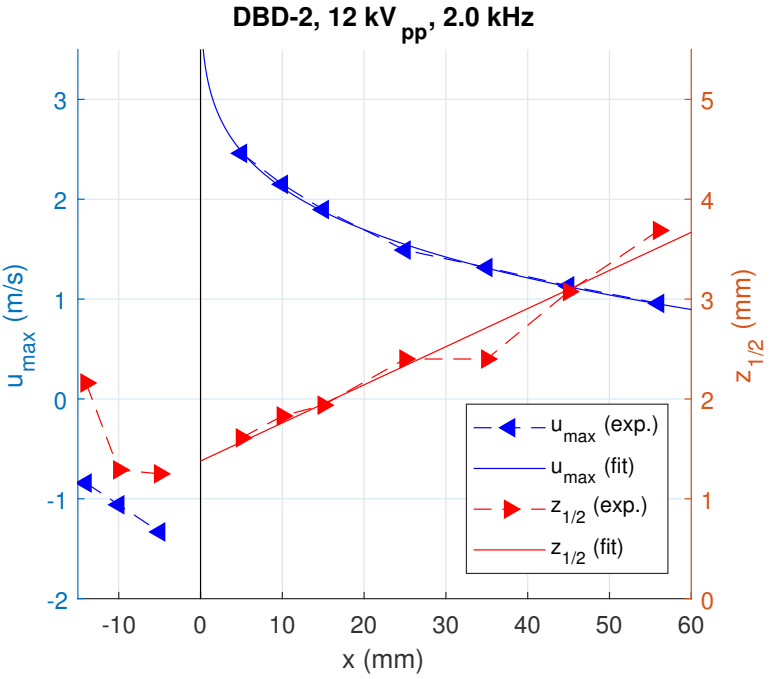

Figure F.12: Evolution of the maximum velocity and of the thickness of the wall jet for DBD-2 at 12 kV_{pp} and 2.0 kHz.

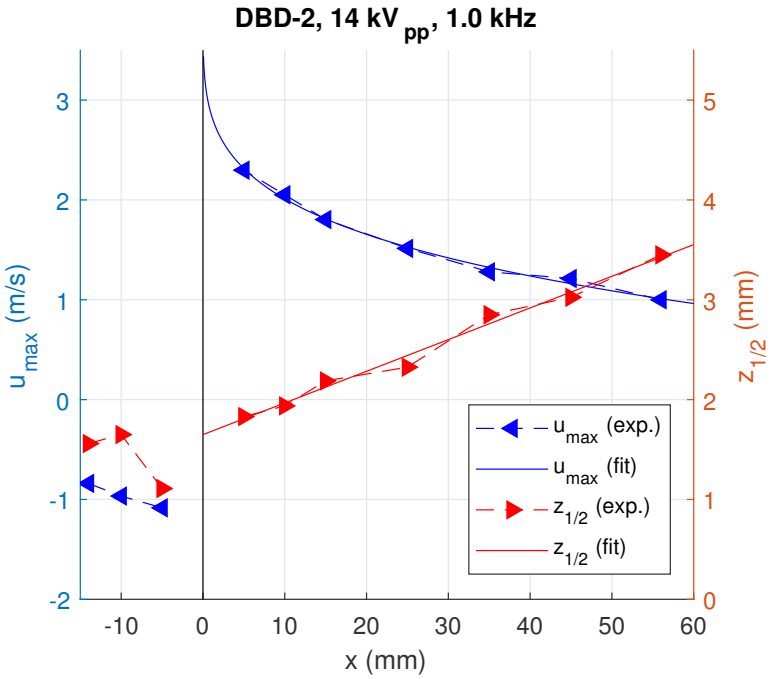

Figure F.13: Evolution of the maximum velocity and of the thickness of the wall jet for DBD-2 at 14 kV_{pp} and 1.0 kHz.

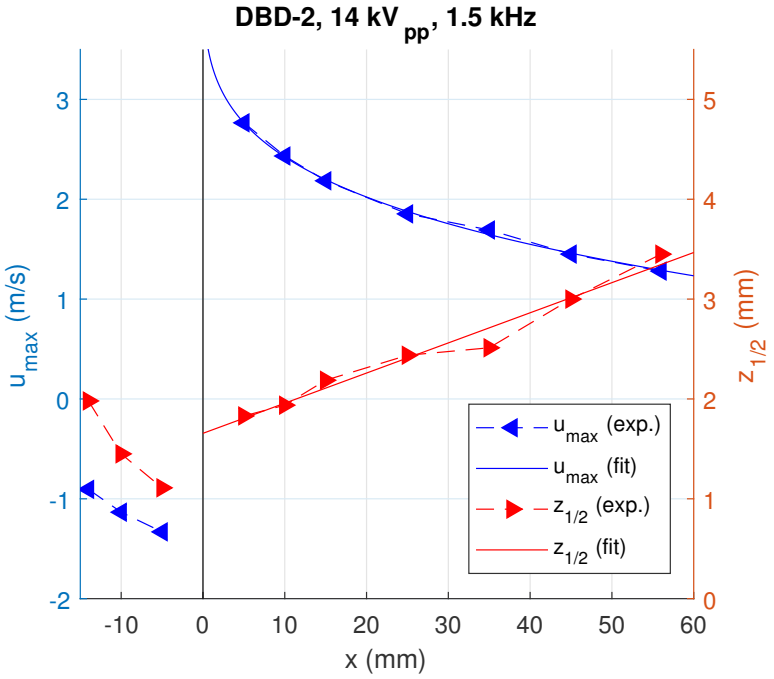

Figure F.14: Evolution of the maximum velocity and of the thickness of the wall jet for DBD-2 at 14 kV_{pp} and 1.5 kHz.

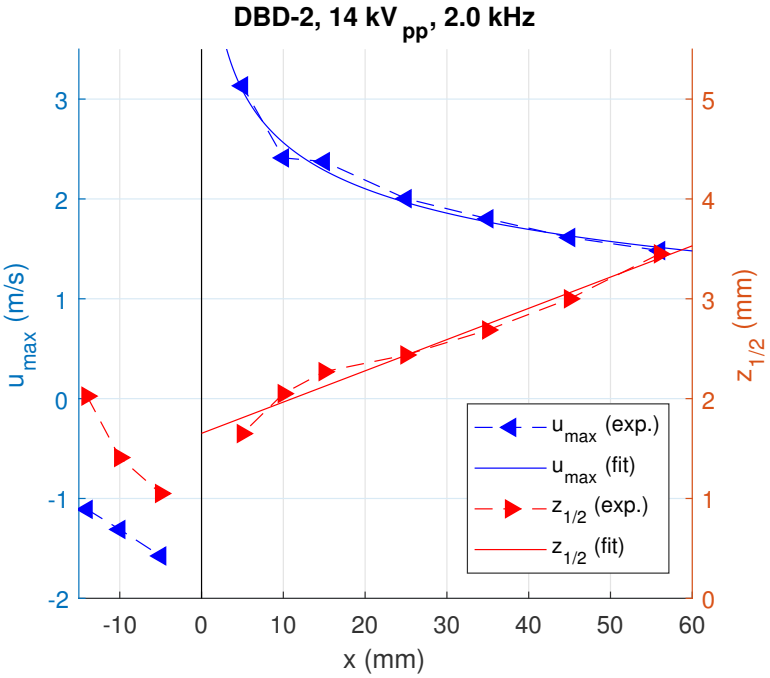

Figure F.15: Evolution of the maximum velocity and of the thickness of the wall jet for DBD-2 at 14 kV_{pp} and 2.0 kHz.

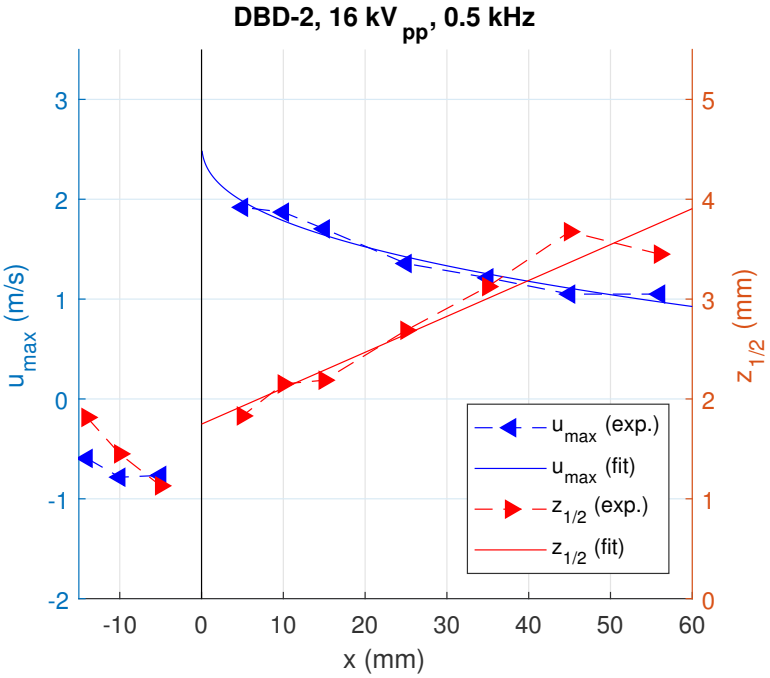

Figure F.16: Evolution of the maximum velocity and of the thickness of the wall jet for DBD-2 at 16 kV_{pp} and 0.5 kHz.

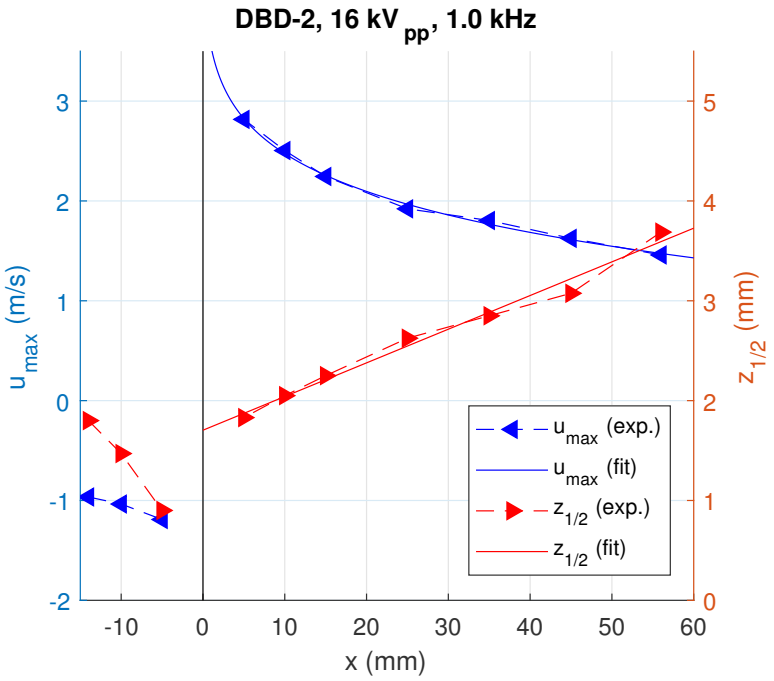

Figure F.17: Evolution of the maximum velocity and of the thickness of the wall jet for DBD-2 at 16 kV_{pp} and 1.0 kHz.

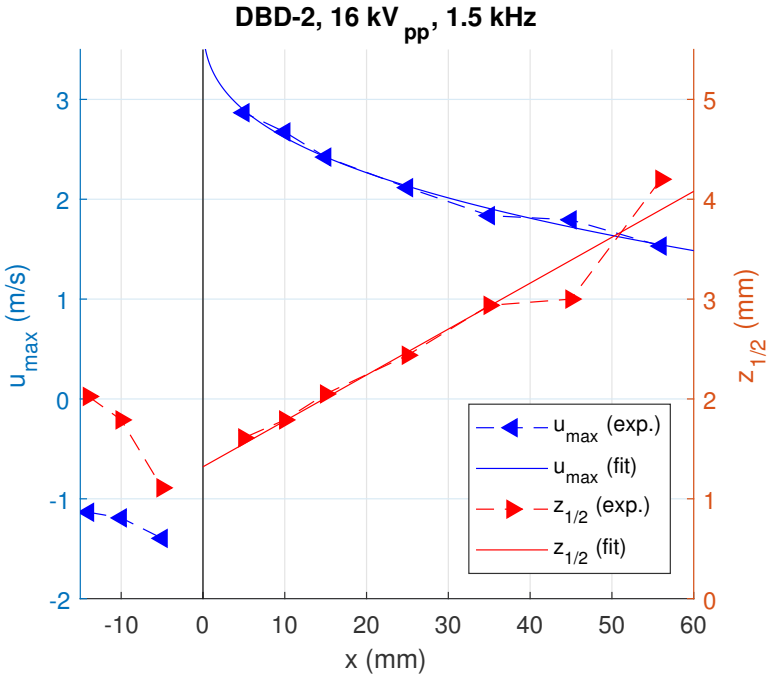

Figure F.18: Evolution of the maximum velocity and of the thickness of the wall jet for DBD-2 at 16 kV_{pp} and 1.5 kHz.

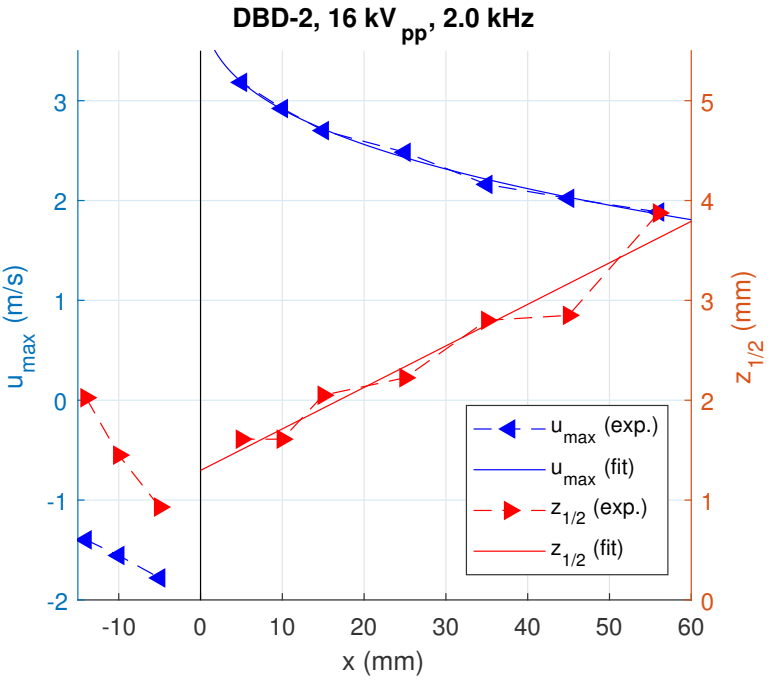

Figure F.19: Evolution of the maximum velocity and of the thickness of the wall jet for DBD-2 at 16 kV_{pp} and 2.0 kHz.

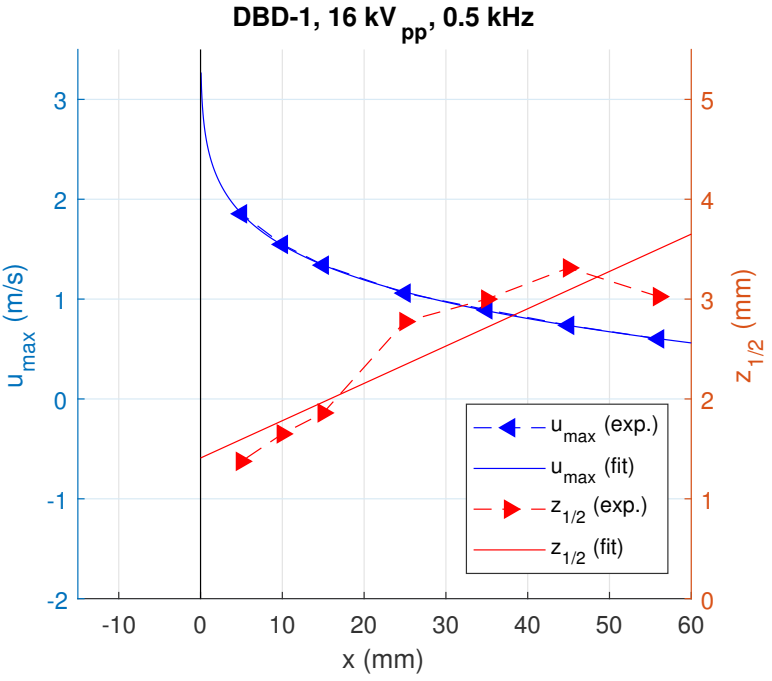

Figure F.20: Evolution of the maximum velocity and of the thickness of the wall jet for DBD-1 at 16 kV_{pp} and 0.5 kHz.

F.3 Mass Flow Rate

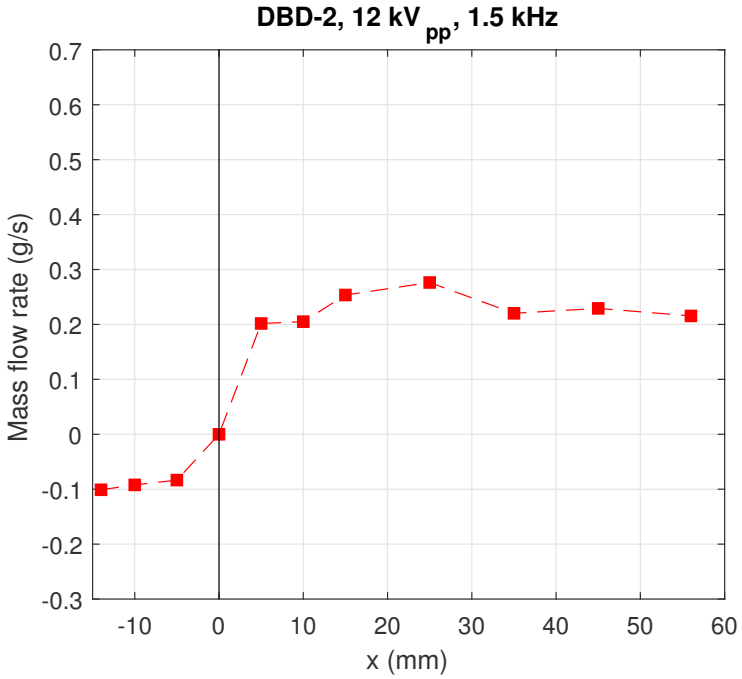

Figure F.21: Evolution of the mass flow rate of the wall jet for DBD-2 at 12 kV_{pp} and 1.5 kHz.

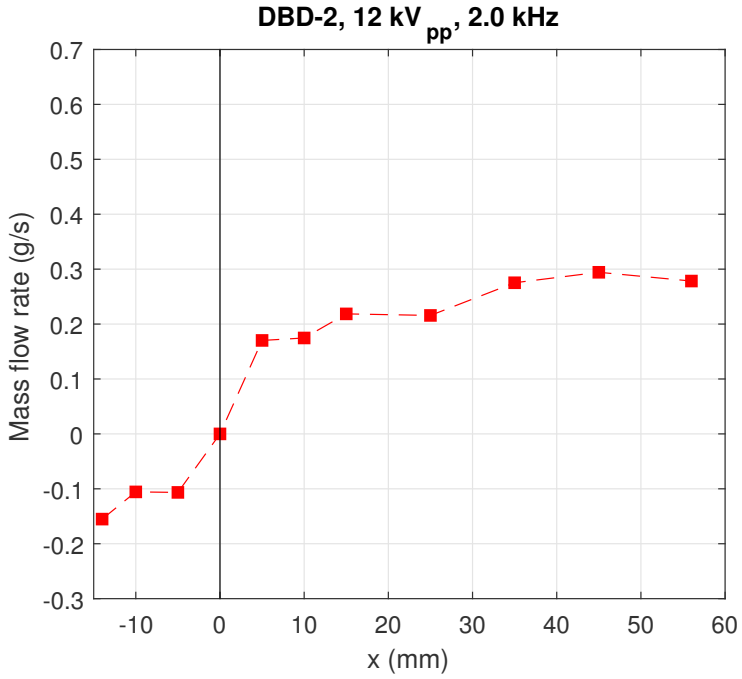

Figure F.22: Evolution of the mass flow rate of the wall jet for DBD-2 at 12 kV_{pp} and 2.0 kHz.

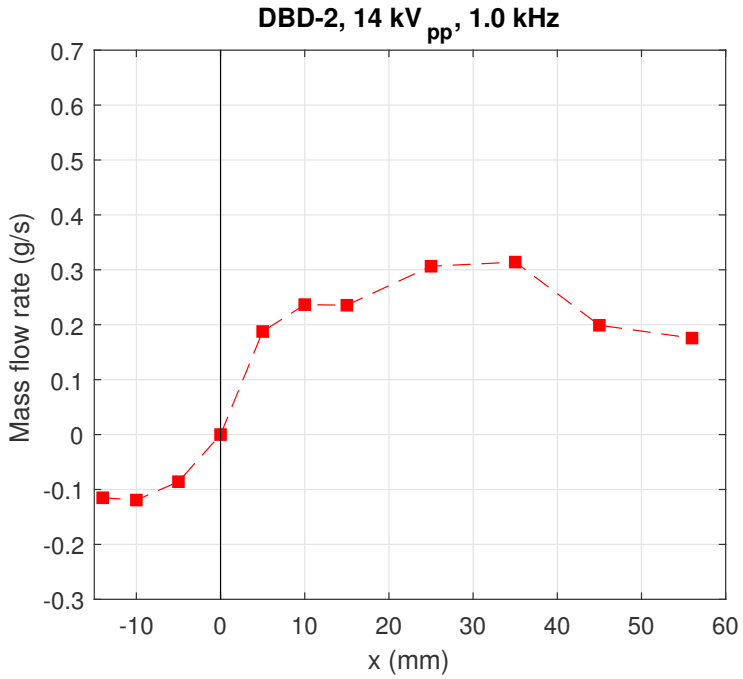

Figure F.23: Evolution of the mass flow rate of the wall jet for DBD-2 at 14 kV_{pp} and 1.0 kHz.

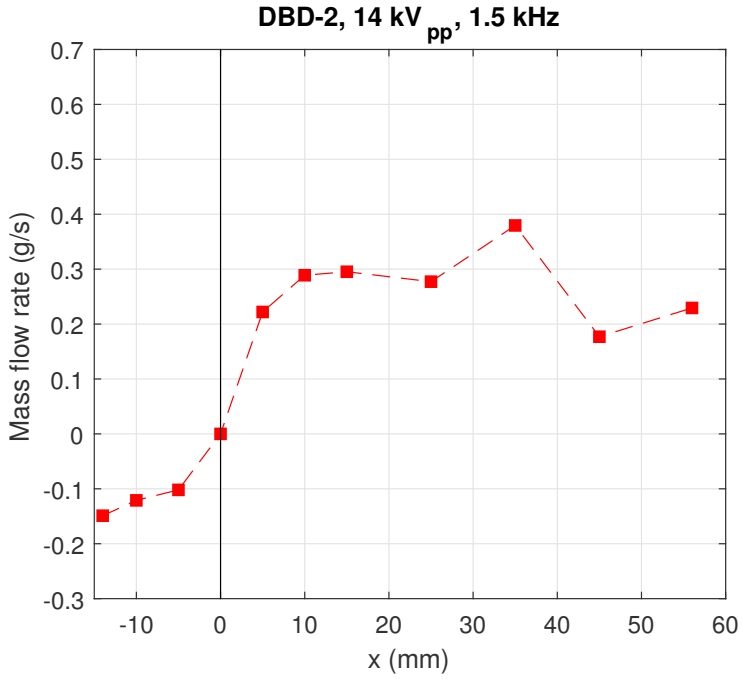

Figure F.24: Evolution of the mass flow rate of the wall jet for DBD-2 at 14 kV_{pp} and 1.5 kHz.

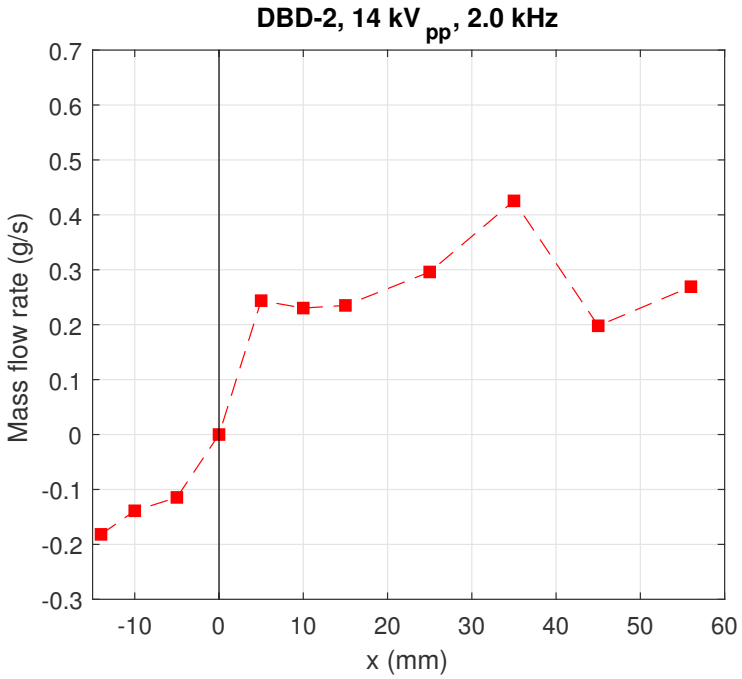

Figure F.25: Evolution of the mass flow rate of the wall jet for DBD-2 at 14 kV_{pp} and 2.0 kHz.

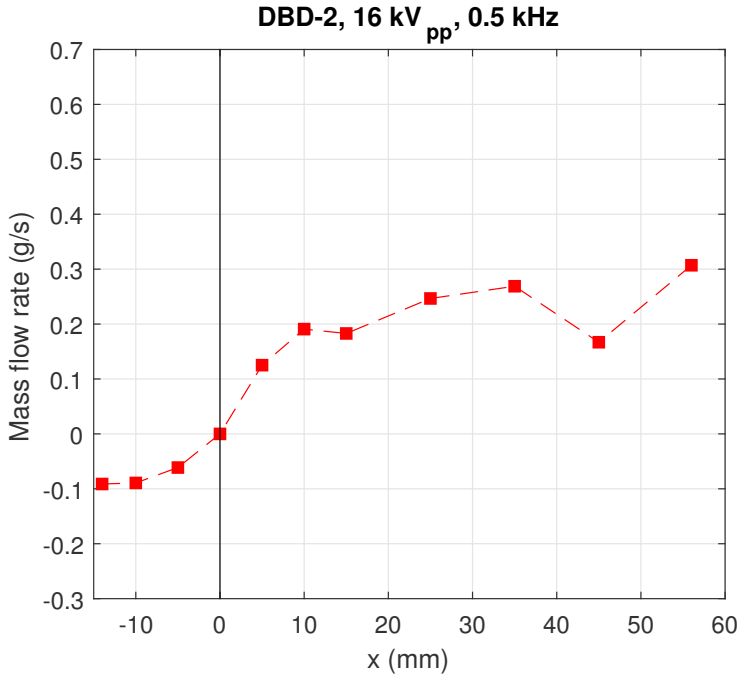

Figure F.26: Evolution of the mass flow rate of the wall jet for DBD-2 at 16 kV_{pp} and 0.5 kHz.

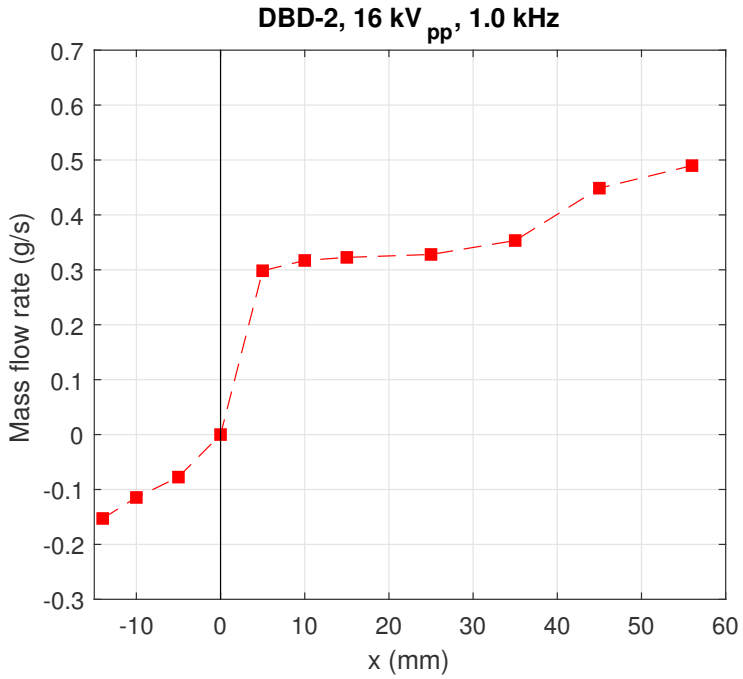

Figure F.27: Evolution of the mass flow rate of the wall jet for DBD-2 at 16 kV_{pp} and 1.0 kHz.

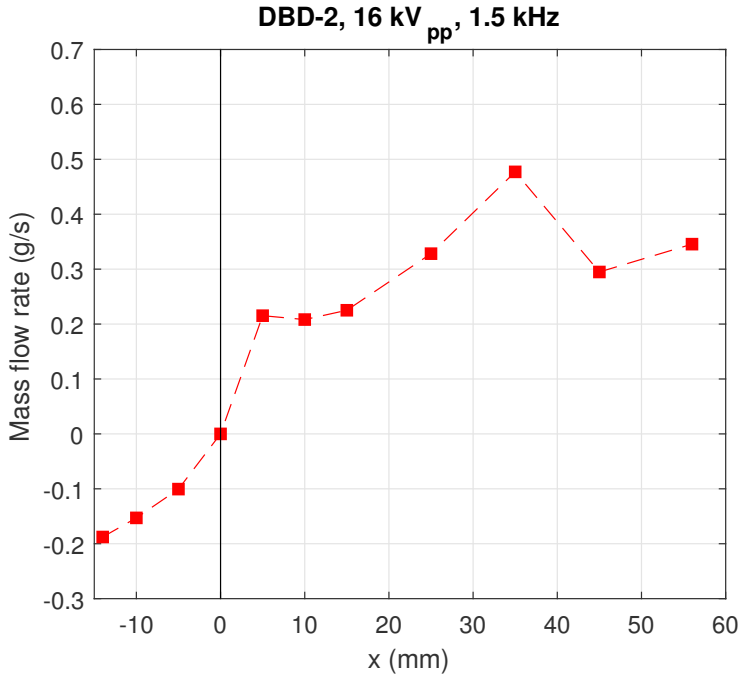

Figure F.28: Evolution of the mass flow rate of the wall jet for DBD-2 at 16 kV_{pp} and 1.5 kHz.

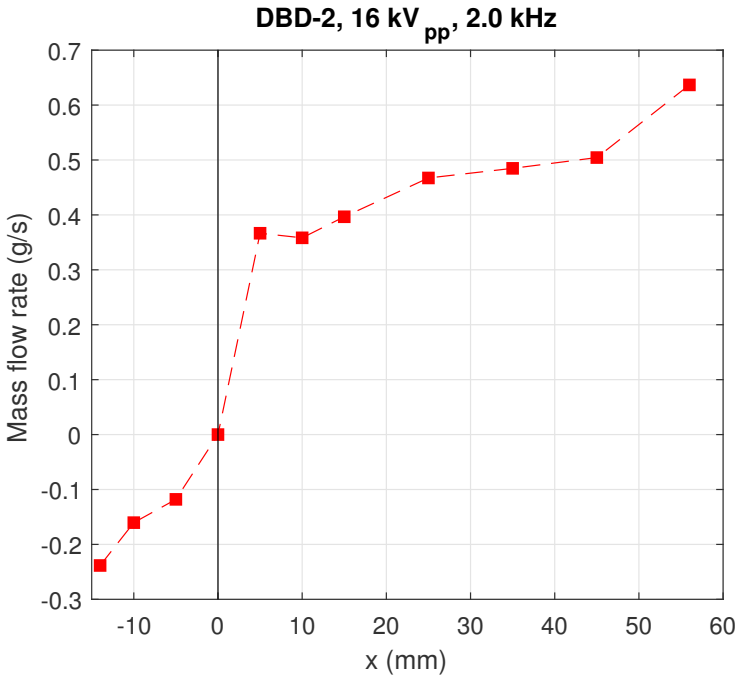

Figure F.29: Evolution of the mass flow rate of the wall jet for DBD-2 at 16 kV_{pp} and 2.0 kHz.

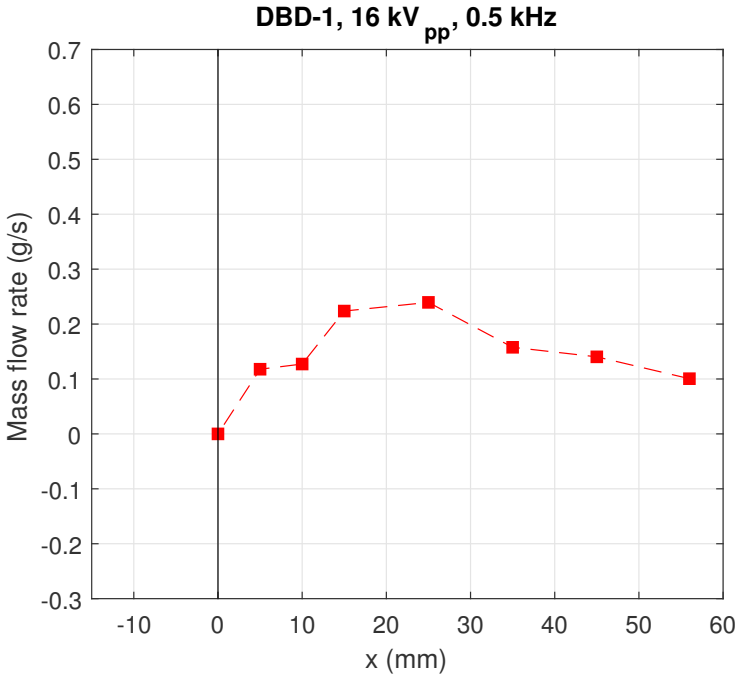

Figure F.30: Evolution of the mass flow rate of the wall jet for DBD-1 at 16 kV_{pp} and 0.5 kHz.

F.4 Force per Unit Span

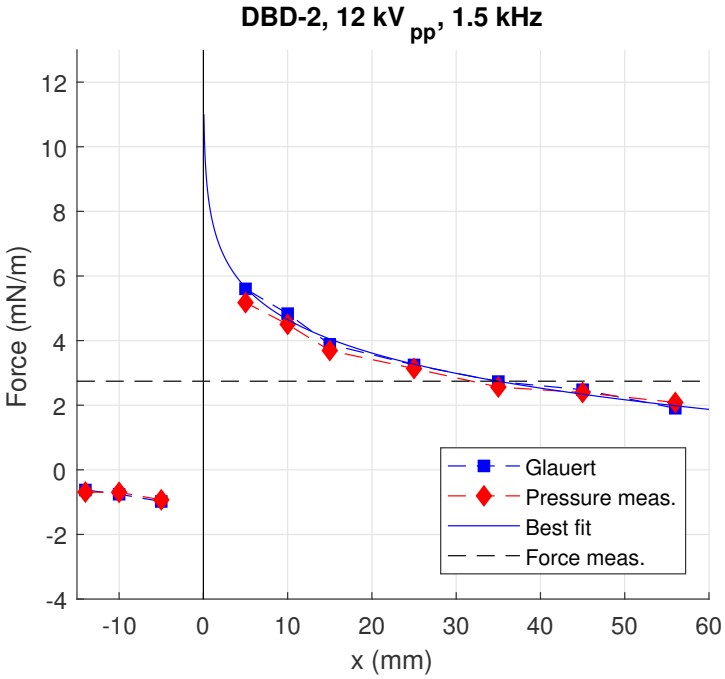

Figure F.31: Evolution of the force per unit span of the wall jet for DBD-2 at 12 kV_{pp} and 1.5 kHz.

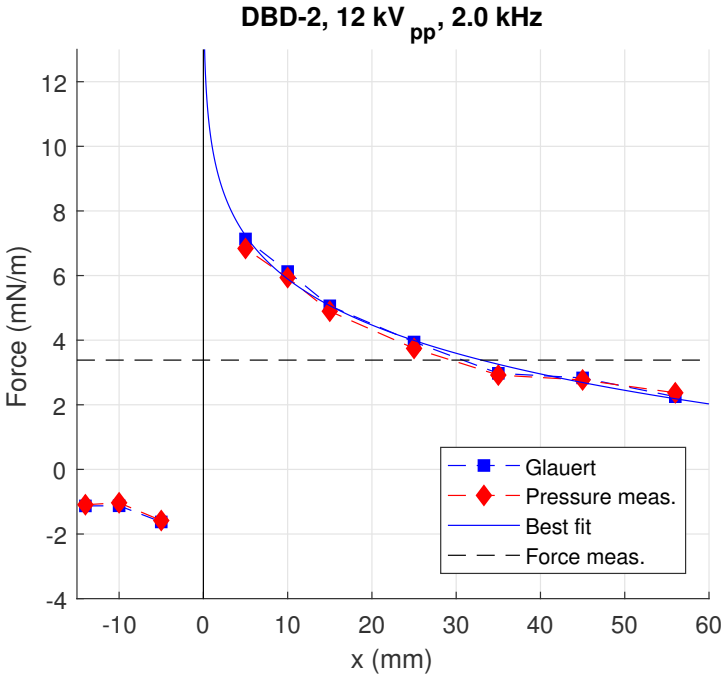

Figure F.32: Evolution of the force per unit span of the wall jet for DBD-2 at 12 kV_{pp} and 2.0 kHz.

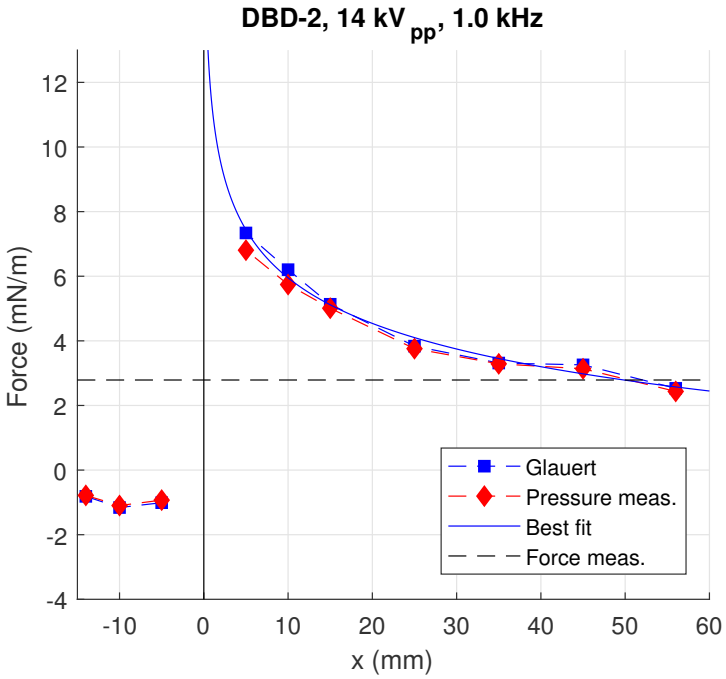

Figure F.33: Evolution of the force per unit span of the wall jet for DBD-2 at 14 kV_{pp} and 1.0 kHz.

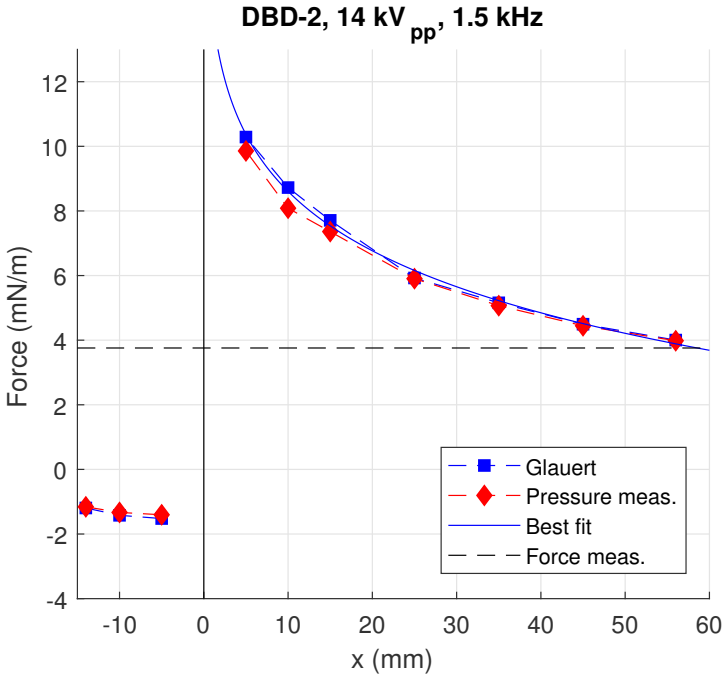

Figure F.34: Evolution of the force per unit span of the wall jet for DBD-2 at 14 kV_{pp} and 1.5 kHz.

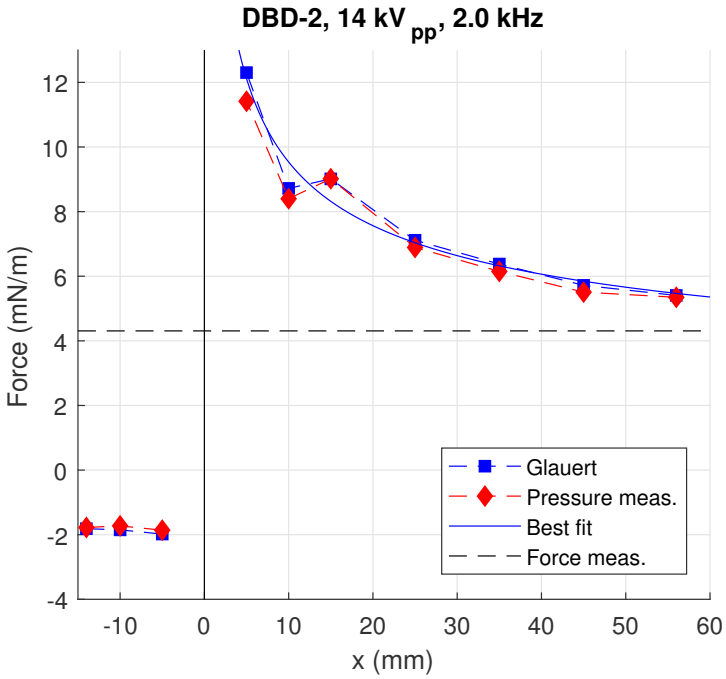

Figure F.35: Evolution of the force per unit span of the wall jet for DBD-2 at 14 kV_{pp} and 2.0 kHz.

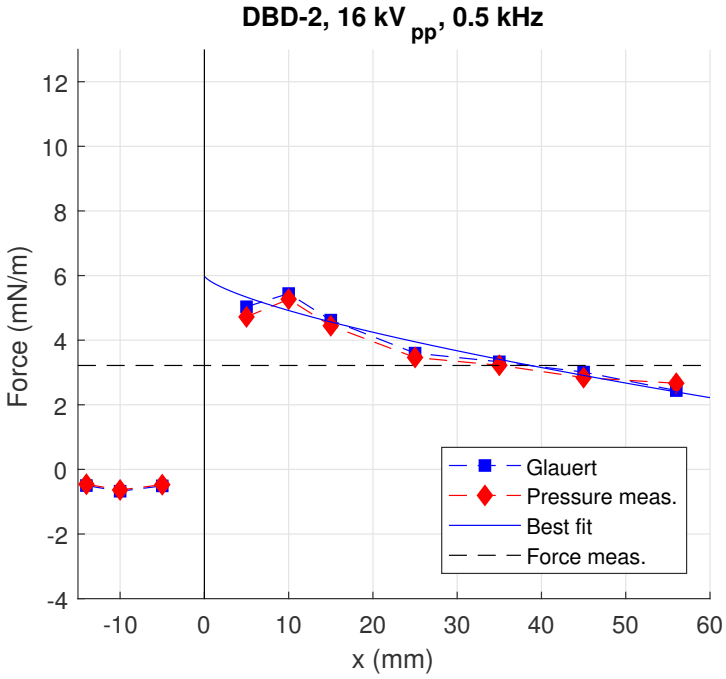

Figure F.36: Evolution of the force per unit span of the wall jet for DBD-2 at 16 kV_{pp} and 0.5 kHz.

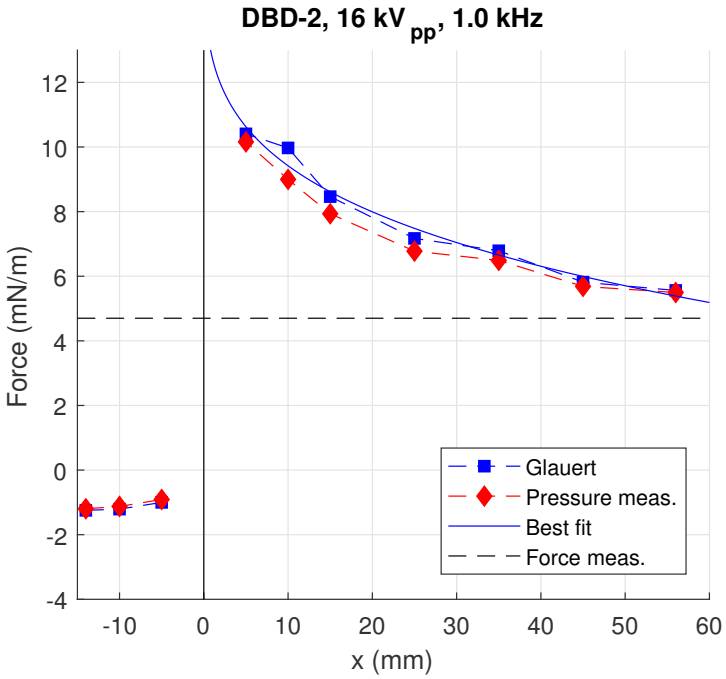

Figure F.37: Evolution of the force per unit span of the wall jet for DBD-2 at 16 kV_{pp} and 1.0 kHz.

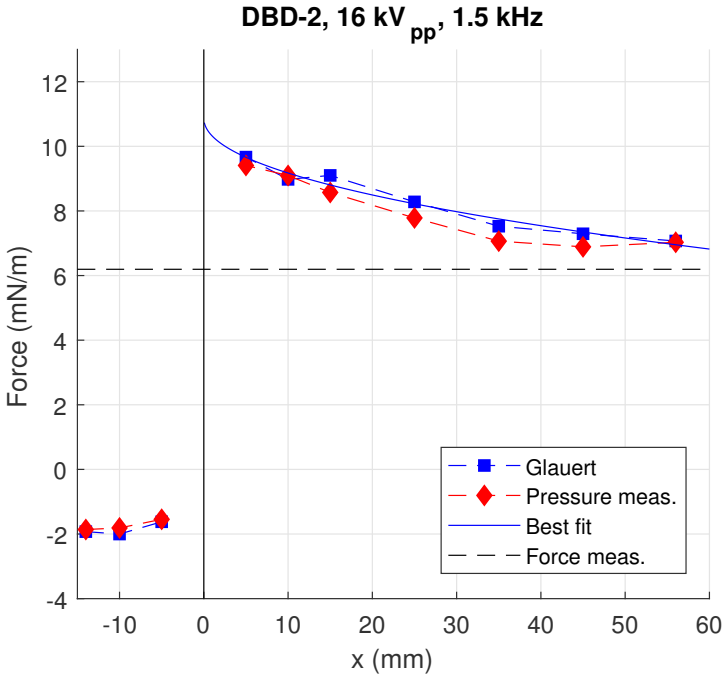

Figure F.38: Evolution of the force per unit span of the wall jet for DBD-2 at 16 kV_{pp} and 1.5 kHz.

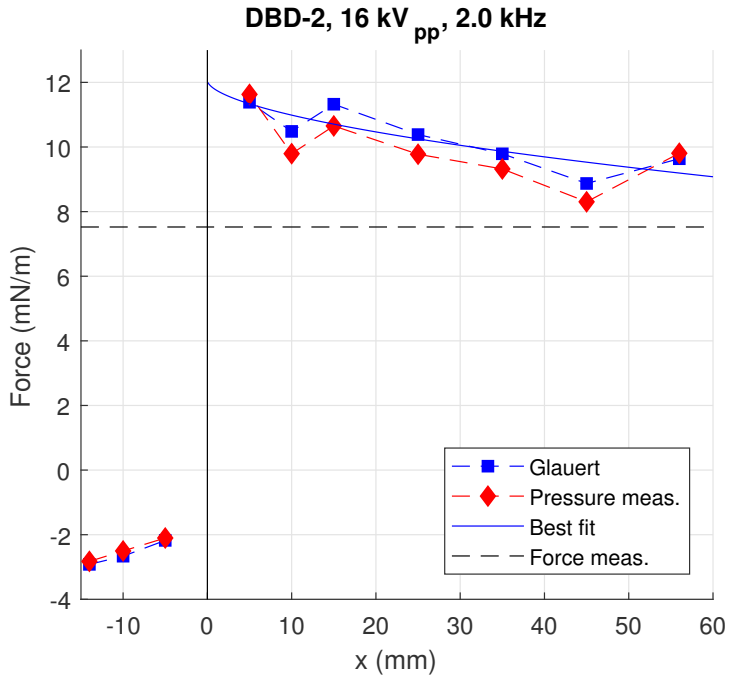

Figure F.39: Evolution of the force per unit span of the wall jet for DBD-2 at 16 kV_{pp} and 2.0 kHz.

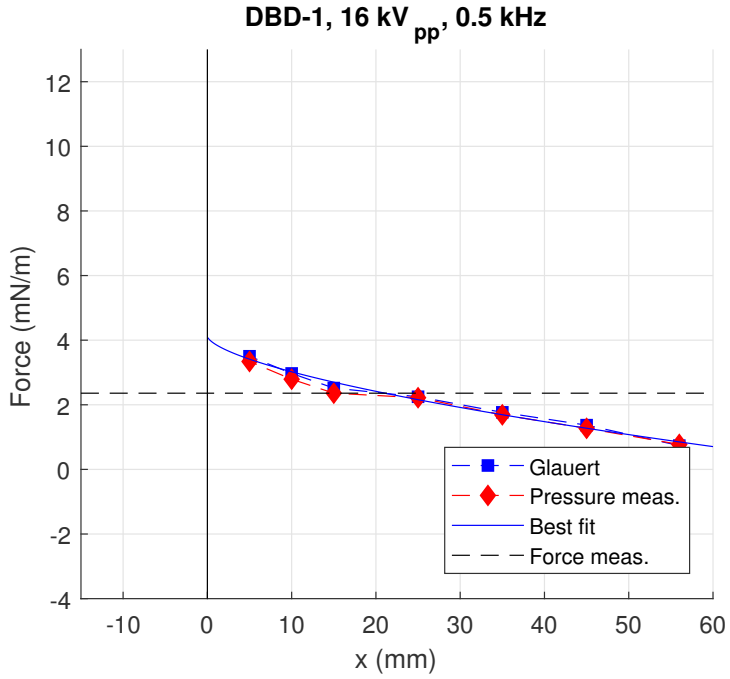

Figure F.40: Evolution of the force per unit span of the wall jet for DBD-1 at 16 kV_{pp} and 0.5 kHz.